Title
Using Self-Assembly to Control Nanoscale Morphology in Semiconducting Polymers for Application in Organic Photovoltaics

Author
Ferreira, Amy Susan

Publication Date
2015

Peer reviewed|Thesis/dissertation

UNIVERSITY OF CALIFORNIA

Los Angeles

Using Self-Assembly to Control Nanoscale Morphology in Semiconducting Polymers for Application in Organic Photovoltaics

A dissertation submitted in partial satisfaction of the requirements

for the degree Doctor of Philosophy in Chemistry

by

Amy Susan Ferreira

2015

ABSTRACT OF THE DISSERTATION

Using Self-Assembly to Control Nanoscale Morphology in Semiconducting Polymers for Application in Organic Photovoltaics

by

Amy Susan Ferreira

Doctor of Philosophy in Chemistry

University of California, Los Angeles, 2015

Professor Sarah H. Tolbert, Chair

Organic photovoltaics (OPVs) represent a promising alternative to silicon based photovoltaics because of they are lower cost and easier to process then current technology. A typical OPV consists of a semiconducting polymer that acts as the electron donor and primary photoabsorber combined with an electron acceptor, often a C_{60} fullerene derivative. Due to the low exciton diffusion length in organic blends, the two components must be blended on a fine enough length scale to enable efficient electron transfer. However, the components still need to be separated enough to maintain high conductivity in the pure domains for the extraction of the carriers. It can be difficult to create such a demanding structure and optimal morphology

reproducibly. This work focuses on controlling the semiconducting polymer through self-assembly as a way to tune the overall nanoscale architecture of a blended system.

In the first part of this dissertation, the effect of changing the crystallinity and orientation of semiconducting polymers will be examined as a way to tune the nanoscale morphology of a polymer/fullerene blend. The resulting device performance will be analyzed to gain further understanding of the optimal morphology required to maximize efficiency. Three polymer systems are used to explore how small changes in the crystallinity, regioregularity, and chain conformation can dramatically alter the resulting OPV device performance. Additionally, the changes in polymer morphology with two fullerene incorporation techniques, blend casting and sequential processing, will be compared. Since polymer morphology and characteristics can be determined, it will be shown that the processing method can be selected to match each intrinsic polymer, which are often more difficult to control.

In the second part, self-assembly will be used as a method to precisely direct the polymer morphology in films and solution. It will be shown that through the use of an inorganic host, individual chains can be straightened to dramatically increase the hole mobility in the polymer backbone. The ability to straighten polymer chains will be further expanded upon by using solution self-assembly to create a 3D conductive polymer network. Upon the addition of fullerene to this network, an energy cascade can be created to enable efficient charge separation through the formation of stable polarons.

This dissertation of Amy Susan Ferreira is approved.

Daniel Neuhauser

Yang Yang

Sarah H. Tolbert, Committee Chair

University of California, Los Angeles

2015

To my loving fiancé and family who have always supported me

TABLE OF CONTENTS

LIST OF FIGURES

CHAPTER 2. Crystallinity Effects in Sequentially Processed and Blend-Cast Bulk-Heterojunction Polymer/Fullerene Photovoltaics

CHAPTER 6. On the Structure and Conductivity of Semiconducting Polymer Hydrogels

APPENDIX A. Composition Effect in BC-BHJ Solar Cells

APPENDIX C. Dammin Bead Models

LIST OF TABLES

LIST OF ABBREVIATIONS AND SYMBOLS

Å	Ångström
a.u.	Arbitrary units
AFM	Atomic force microscopy
BC	Blend-cast
BHJ	Bulk heterojunction
$C_{60}(PI)_n$	C_{60}-N,N-dimethylpyrrolidinium iodide
CPE	Conjugated polyelectrolyte
cryoEM	Cyrogenic transmission electron microscopy
Da	Dalton
DIO	Diiodooctane
ET	Electron transfer
eV	Electron volt
FET	Field-effect transistor
FF	Fill factor
FWHM	Full width at half maximum
G'	Elastic storage modulous
G"	Viscous Loss Modulous
GIWAXS	Grazing incidence wide angle X-ray scattering
HOMO	Highest occupied molecular orbital
ITO	Indium-doped tin oxide
J_{sc}	Short circuit current density

LUMO	Lowest occupied molecular orbital
MEH-PPV	Poly[2-methoxy-5-(2'-ethylhexyloxy)-p-phenylene vinylene]
MeOH	Methanol
MW	Molecular weight
OPV	Organic photovoltaic
P3HT	Poly(3-hexylthiophene-2,5-diyl)
PBDTTT-C	Poly[4,8-bis-(2-ethylhexyloxy)-benzol[1,2-b:4,5-b']dithiophene-2,6-diyl-alt-4-(2-ethylhexyloxy-1-one)thieno[3,4-b]thiophene-2,6-diyl]
PCBM	[6,6]-phenyl-C_{61}-butyric-acid-methyl-ester
PCE	Power conversion efficiency
PDI	Polydispersity index
PEDOT:PSS	Poly(ethylene-dioxythiophene):poly(styrenesulfonic acid)
PFT	Poly(fluorine-alt-thiophene)
PL	Photoluminescence
RBO	Random poly(3-butylthiophene-co-3-octylthiophene)
RR	Regioregularity
SAXS	Small angle X-ray scattering
SCLC	Space-charge limited current
SqP	Sequential-processed
THF	Tetrahydrofuran
TRMC	Time-resolved microwave conductivity
UV-Vis	Ultraviolet-Visible
V_{OC}	Open-circuit voltage

ACKNOWLEDGEMENTS

This dissertation would not have been possible without the love and support of John Thomas, my future husband and partner in life. He has always supported me and pushed me to keep working towards the degree. Without his encouragement, I'm not sure I would have. I look forward to taking our next steps together in our new life and new careers. I would also like to thank my family for always being there and supporting me through all of my school endeavors.

I have been fortunate to be able to work for Prof. Sarah Tolbert, who not only guides her students but also inspires us to be better. She always finds time to help or offer advice on not only experiments and data interpretation, but also on future career options, presentation skills, and writing. Her guidance has helped me really become a scientist and chemist rather than just a student.

I would like to thank my fellow students in the Tolbert group, many of whom have taken the time to teach me to use equipment and preform experiments. I would especially like to thank Rachel Huber, who I worked side-by-side with on many of these projects as well as working long hours at the Stanford Synchrotron together.

Much of the work done for this dissertation was a collaborative effort. I would like to thank all of my collaborators and colleagues that have helped create some really good science. Ben Schwartz has been like a co-advisor and has always been available to talk about data interpretation and future experiments. The students and post-docs in the Schwartz group have also been pivotal in enabling the correlation of structure with device physics by making many of the solar cell devices I have worked with. The students and post-docs of the Rubin group have also helped by making novel fullerenes and polymers, which allowed our group to look at new systems.

I would like to thank the beam line scientists and the Stanford Synchrotron for the use of their facilities to perform X-ray experiments. Much of my dissertation research has revolved around understanding the structure of polymers through the use of x-ray scattering and the use of these facilities had greatly helped push my research further. I would also like to thank the National Science Foundation (NSF) funded Clean Green Integrative Graduate Education Research Traineeship (IGERT) for not only providing funding but for also enabling me to learn about the field of green energy. The fellowship taught me about the many types of energy production and storage, which has really helped me put my research into perspective.

I wish to thank my committee members, Professors Daniel Neuhauser and Yang Yang, for their help and support in writing this dissertation. I would also like to thank Professor Richard Kaner for serving on my oral committee. Finally, I would like to thank Professors Arlene Russell and Brent Corbin for providing letters of recommendation.

Previous Publications and Contributions of Co-Authors

Chapter 2 is a version of: Amy Ferreira, Guang Zhang, Rachel Huber, Shane Boyd, Christine Luscombe, Sarah H. Tolbert, Benjamin J. Schwartz, "Crystallinity Effects in Sequentially Processed and Blend-Cast Bulk-Heterojunction Polymer/Fullerene Photovoltaics." *J. Phys. Chem. C*, 2014, 118, 18424-18435. Guang made prepared the x-ray samples and devices and measured the device performances. Rachel and I worked together on collecting the x-ray data and Shane synthesized the RR-P3HT. Guang, Rachel, and I contributed equally to the writing of the manuscript and Professor Tolbert, Professor Schwartz, and Professor Luscombe helped edit the manuscript.

Chapter 3 is a version of: Amy Ferreira, Jordan Aguirre, Selvam Subramaniyan, Samson Jenekhe, Benjamin J. Schwartz, Sarah H. Tolbert, "Aspects of Polymer Synthesis and

Processing that Control OPV Device Performance: Regioregularity, Swelling and Morphology Optimization using Random Poly(3-butylthiophene-co-3-octylthiophene) Polymers." Jordan fabricated films and devices and measured absorbance, *J-V* characteristics for each, and performed the swelling studies. Selvam synthesized all of the RBOX polymers. Jordan and I both contributed equally to writing the manuscript. Professor Tolbert, Professor Schwartz, and Professor Jenekhe all helped edit the manuscript. The manuscript has been submitted to Advanced Energy Materials and is awaiting response.

Chapter 4 is a version of: Amy Ferreira, Taylor Aubry, Jordan Aguirre, Steven Hawks, Matthew Fontana, Benjamin J. Schwartz, Sarah H. Tolbert, "Sequential Processing as an Additive-free Method for Retaining the Face-on Polymer Orientation in PBDTTT-C-based Photovoltaics." Taylor, Jordan, and Matthew optimized and measured *J-V* characteristics of sequentially processed samples. I wrote the manuscript and Professor Tolbert and Professor Schwartz edited it. The manuscript will be submitted shortly after filing this dissertation.

Chapter 5 is a version of: Amy Ferreira, Christopher Tassone, Hirokatsu Miyata, Sarah H. Tolbert, "Ultra-High Mobility Semiconducting Polymers Produced through Confinement in Silica Nanopores." Dr. Miyata prepared the polyimide substrates. Christopher optimized the original FET fabrication. I wrote most of the manuscript, Christopher and Professor Tolbert edited it. The manuscript with be submitted shortly after filing this dissertation.

Chapter 6 is a version of: Rachel Huber, Amy Ferreira, Jordan Aguirre, Daniel Kilbride, Daniel Toso, Kenneth Mayoral, Thomas Mason, Hong Zhou, Nikos Kopidakis, Yves Rubin, Benjamin J. Schwartz, Sarah H. Tolbert, "On the Structure and Conductivity of Semiconducting Polymer Hydrogels." Rachel performed rheology studies with the help of Kenneth. Jordan and Nikos collected the TRMC data. Daniel Kilbride synthesized the PFT

and Daniel Toso took the cryo-EM images. Rachel and I contributed equally preparing samples for TEM and x-ray, collecting x-ray scattering, and writing the manuscript. Professor Tolbert, Professor Rubin, Professor Schwartz, and Professor Mason all helped edit the manuscript. The manuscript will be submitted for publication shortly after filing this dissertation.

Chapter 7 is a version of: Amy Ferreira, Rachel Huber, Robert Thompson, Daniel Kilbride, Nicholas Knutson, Lekshmi Dev, Daniel Toso, Hong Zhou, Yves Rubin, Benjamin J. Schwartz, Sarah H. Tolbert, "Long-Lived Photoinduced Polaron Formation in Conjugated Polyelectrolyte/Fullerene Assemblies." *Science*, 2015, 348, 1340-1343. Daniel Kilbride synthesized the PFT and Robert and Nicholas synthesized the fullerenes. Lekshmi collected the ultrafast data and Daniel Toso collected the cyro-EM images. Rachel and I contributed equally in this work, collected the fluorescence, absorbance, EPR, and SAXS data, and wrote the manuscript. Professor Zhou, Professor Schwartz, and Professor Tolbert helped edit the manuscript.

Professor Sarah Tolbert directed the research presented in this dissertation. This work was supported by: National Science Foundation (NSF); Clean Green Integrative Graduate Education Research Traineeship; California NanoSystems Institute (CNSI); Department of Energy (DOE); and University of California, Los Angeles Graduate Division. Portion of this research were performed at the Stanford Synchrotron Radiation Lightsource, a national user facility operated by Stanford University on behalf of the U.S. Department of Energy, Office of Basic Science.

VITA

Amy Susan Ferreira obtained her B.S. in Chemistry at the University of California, Riverside in 2009. While there she performed undergraduate research with Prof. Valentine I. Vullev in the Department of Biochemistry and received the Chancellors Award for Excellence in Undergraduate Research. She began her PhD work in Prof. Sarah H. Tolbert's group in 2009. She received the Clean Green Integrative Graduate Education Research Traineeship (IGERT) which provided support for two years in addition to training experiences in the field of clean energy. While working on her degree, she also was a facilitator for the Program for Excellence in Education and Research (PEERS), which provides extra workshops for underrepresented minorities in physical and life sciences. In addition to running workshops, Amy also actively participated in the California Nanosystems Institute (CNSI) High School Nanoscience program, where she acted as lead in teaching a superhydrophobics-based experiment to both high school teachers and high school students.

SELECT PUBLICATIONS AND PRESENTATIONS

Hwang, Y.; Courtright, A.; **Ferreira, A.**; Tolbert, S. H.; Jenekhe, S. A. "7.7% Efficient All-Polymer Solar Cells" *Advanced Materials* **2015**, doi:10.1002/adma.20151604.

Ferreira, A.; Huber, R.; Thompson, R.; Kilbride, D.; Knutson, N.; Devi, L.; Toso, D.; Zhou, H.; Rubin, Y.; Schwartz, B. J.; Tolbert, S. H. "Long-Lived Photoinduced Polaron Formation in Conjugated Polyelectrolyte/Fullerene Assemblies" *Science* **2015**, *348*, 1340-1343.

Aguirre, J.; Hawks, S.; **Ferreira, A.**; Yee, P.; Subramaniyan, S.; Jenekhe, S.; Tolbert, S. H.; Schwartz, B. J. "Sequential Processing for Organic Photovoltaics: Design Rules for Morphology Control by Tailored Semi-Orthogonal Solvent Blends" *Advanced Energy Materials* **2015**, *5*, 1402020.

Ferreira, A.; Zhang, G.; Huber, R.; Boyd, S.; Luscombe, C.; Tolbert, S. H.; Schwartz, B. J. "Crystallinity Effects in Sequentially Processed and Blend-Cast Bulk-Heterojunction Polymer/Fullerene Photovoltaics" *J. Phys. Chem. C.* **2014**, *118*, 18424-18435.

Aguirre, J.; **Ferreira, A.**; Ding, H.; Jenekhe, S.; Kopidakis, N.; Asta, M.; Pilon, L.; Rubin, Y.; Tolbert, S. H.; Schwartz, B. J.; Dunn, B.; Ozolins, V. "Panoramic View of Electrochemical Pseudocapacitor and Organic Solar Cell Research in Molecularly Engineered Energy Materials (MEEM)" *J. Phys. Chem. C.* **2014**, *118*, 19505-19523.

Hawks, S.; Aguirre, J.; Schelhas, L.; Thompson, R.; Huber, R.; **Ferreira, A.**; Zhang, G.; Herzing, A.; Tolbert, S. H.; Schwartz, B. J. "Comparing Matched Polymer:Fullerene Solar Cells Made by Solution-Sequential Processing and Traditional Blend Casting: Nanoscale Structure and Device Performance" *J. Phys. Chem. C.* **2014**, *118*, 17413-17425.

"Self-Assembling Semiconducting Polymers – Rods and Gels from Electronic Materials," Oral presentation at Energy Frontiers Research Centers (EFRC) Blue Team teleconference, Los Angeles, Ca, May 2013.

"Optimizing Morphology in Organic Photovoltaic Devices by Controlling Polymer Crystallinity," Oral and poster presentation at 243rd ACS National Meeting, San Diego, Ca March 2012.

"Amphiphilic Semiconducting Polymers for Photovolatic Applications" and "Control of Nanoscale Architecture in Polymer-based Solar Cells by Sequentially Processing," Oral and poster presentation at Energy Frontier Research Centers (EFRC) Review Meeting, Aurora, Co, January 2012.

"Optimizing Nanoscale Architecture in Semiconducting Polymers," Poster presentation at External Advisory Board Meeting, California Nanosystem Institute, Los Angeles, Ca, July 2011.

CHAPTER 1

Introduction

Organic photovoltaics (OPVs) having been of growing interest due to their low cost and potential ease of processing compared to their silicon counterparts.[1–4] Dramatic advances have already been made in this field, with overall power conversion efficiencies surpassing 10%.[5–7] These devices typically consist of a semiconducting polymer that acts as the primary photoabsorber and a C_{60} fullerene derivative as the electron acceptor. Upon excitation with light, an electron is transferred from the polymer's highest occupied molecular orbital (HOMO) to its lowest unoccupied molecular orbital (LUMO) to create an electron-hole pair, or exciton. This exciton must travel to a polymer:fullerene interface, so that the electron can be transferred to the LUMO of the fullerene, leaving a hole on the polymer. The free carriers created can subsequently be collected as charge through their respective electrodes. If the exciton is not able to reach an interface, it will recombine and give off light or heat instead of useful current. In order to prevent this recombination, the polymer and the fullerene must be intermixed on a length scale smaller than the exciton diffusion length, which is about 10-20 nm.[8] However, a purely mixed system, with no pure polymer or fullerene domains, would not be ideal since semiconducting polymers have very low mobilities in their amorphous form. Pure domains increase the mobility of each component and create conduction pathways that enable the extraction of the free carriers out of the system as current.[9–11] This intermixed morphology of the polymer and fullerene is called a bulk heterojunction (BHJ) and it can be difficult to controllably make.[12,13]

There have been several routes used to create an optimal BHJ morphology. In most

systems, the polymer and fullerene are co-dissolved in solution and subsequently spun cast onto a conductive substrate. These blend cast systems typically are too mixed to have the proper conduction needed, so many pre- and/or post-treatments are often performed to drive the phase separation of the components. Such treatments include the use of solvent additives[14–16] during deposition or the use of thermal[17–19] or solvent annealing[20,21] after deposition. Each of these methods is highly uncontrollable and relies on the spontaneous de-mixing of the polymer and fullerene, which is very sensitive to the precise processing conditions used.

Another method that has been used is sequential processing.[22–28] In this case, the polymer layer is deposited first and then a fullerene layer is deposited on top. The fullerene is then intercalated into the amorphous regions of the polymer either. This can be accomplished either through the use of solvent additives in the initial fullerene solution that acts to swell the underlying polymer film[25,29–34] or by thermal annealing after the fullerene has been cast[13,29,31,35,36] to yield a similar BHJ architecture. This processing method has been shown to be more reproducible and more controllable than traditional blend casting.[37] However, this method has not been fully explored as route to further control the semiconducting polymer morphology.

This work is divided into six research chapters and will look at several ways in which the morphology of the semiconducting polymer can be tuned and controlled. In the first three chapters (Chapter 2-4), the synthetic properties, such as regioregularity and side-chain length, of the semiconducting polymers will be taken advantage of in two main processing techniques to understand and optimize the BHJ morphology. The second half (Chapters 5-7) will focus on use self-assembly to direct polymer morphology to increase the overall mobility of the polymer.

To begin to study ways in which the morphology of the polymer component can be controlled, in Chapter 2 we will look at the effect of changing the polymer's regioregularity has

on both blend cast and sequential processed films. The orientation of the polymer side-chains determines its regioregularity where a highly regioregular polymer has perfect orientation of the side-chains and a polymer with low regioregularity has many side-chain orientation defects. The presence of these defects prevents the polymer from being able to pack as well and crystallize easily, thus a polymer with a low regioregularity is also significantly more amorphous.[38–40] Changing the regioregularity of a polymer can have dramatic effects on the BHJ morphology in blend cast systems.[12,41–43] Overall, we show that having a low regioregularity, and thus a lower propensity to crystallize, prevents the proper polymer:fullerene phase separation when using this processing technique. However, for sequential processing the presence of more amorphous polymer regions is advantageous as it allows the fullerene to intercalate into the polymer while leaving the crystalline regions intact.[25,44] In Chapter 2, we use the widely studied polymer poly(3-hexylthiophene) (P3HT) combined with the fullerene phenyl-C_{61}-butyric-acid-methyl-ester (PCBM) as a test system. By comparing P3HTs with low and high regioregularities, we show that having a high regioregularity drives the phase separation in blend casting, but hinders fullerene intercalation in sequential processing. Thus the processing technique can be selected to best match the intrinsic ability of the polymer to crystallize, which could be extended to non-P3HT systems.

Another way to control the morphology of a polymer:fullerene blend is to tune the composition of the polymer's solubilizing side-chains rather than control the regioregularity of the polymer.[45,46] It has been shown that changing the length or branching of the side chains on the polymer backbone can change the overall morphology and subsequent device performance obtained.[47–50] However, many of these studies do not hold the regioregularity of the polymer constant in the comparisons. Building off of our knowledge of the dramatic effect regioregularity can have on the morphology of a polymer, in Chapter 3 we look at changing both the average side

chain length and regioregularity. To control these properties while leaving the electronic polymer properties unchanged, we use a series of polythiophene copolymers, where the ratio between butyl and octyl side chains is varied. We again will use both the sequential processing and blend casting techniques to show that regioregularity is the dominate factor over side chain length in determining the overall crystallinity of the polymer within a device and the overall device performance. We will also show through swelling studies, that the ability of a polymer to swell with solvent predicts the performance in both blend cast and sequential processed devices. Overall, this chapter will show that regioregularity is a powerful tool that can be used to tune polymer morphology in a blend.

Even though regioregularity does play an important role in determining the crystallinity of a polymer within a blended system, another way in which the morphology of an OPV can be optimized is by changing the orientation of the polymer chains within crystalline domains.[51,52] In many polymers, there is a favorable interaction between the polymer side-chains and the underlying substrate. As such, these polymers adopt an edge-on orientation in which the hole must hop from one chain to the next to travel out of plane and be extracted.[53–55] However, the hole mobility is greatly increased if the hole is able to travel through the π-π conjugation of the semiconducting polymer backbone instead.[56] By improving the interaction between the polymer backbone and the substrate, it has been possible to force pure polymers to lie face-on, making use of the conjugation for conduction.[47,57–60] In Chapter 4, we will look at how the orientation of the polymer changes with processing technique. Due to favorable interactions between the polymer and a fullerene, the orientation of a face-on polymer is not preserved in simple blend casting. Through the use of sequential processing, we are able to maintain the polymer orientation and show that the overall device performance can be improved.

The use of sequential processing over blend casting does indeed affect the morphology of a polymer within a blended system, but control over the precise polymer morphology can enable a greater understanding of the ways in which OPVs can be further improved. To do this, we switch to a polymer-only system rather than a polymer:fullerene blend. In Chapter 4, we made use of the increase in conduction along the π-π stacking direction, however conduction along the polymer chain should be 100x greater than its inter-chain counterpart.[61–63] Thus, instead of simply causing greater crystallization or changes in polymer orientation, in Chapter 5 we wish to fully straighten-out the semiconducting backbone of the polymer and measure the effect on the hole mobility. Through the use of self-assembly we can create an insulating, silica host matrix. This host is a series of stacked, 1-dimensional tubes, each of which can only hold a few polymer chains.[64–66] The polymer's backbone must be fully straightened, without any kinks, to reside in these close-fit tubes. By measuring the hole mobility of a crystalline and amorphous polymer in this matrix, we can show that the low mobility typically obtained for amorphous polymers is due to the presence of kinks causing traps in a polymer film. Thus by straightening out the polymer chains, we are able to take advantage of the high intrinsic hole mobility of the polymer, which is a route to further increase performance in an OPV.

While an inorganic host matrix does straighten out the polymer chains, it is not a practical method for controlling the polymer morphology in real devices since it contains a large amount of insulating material. In Chapter 6, we expand the use of self-assembly but rather than creating a host, we can control the assembly of polymer chains in solution. Conjugated polyelectrolytes, which have a π-conjugated backbone and ionic pendant groups[67–70], have been used to create a variety of nanostructures in solution.[71–75] For our study, we use poly(fluorine-alt-thiophene) (PFT) which forms rod-like micelles in water with the semi-conducting backbone straightened along the

long-axis of the rod.[74] In this way, we are able to straighten the polymer chains without the use of a host matrix. In addition to simply forming rods, we can form a hydrogel at low polymer concentrations. We show that the hydrogel is formed by the bridging of polymer chains between the rod-shaped micelles, creating a 3-dimensional conductive polymer network in solution, which could have a variety of electronic applications.

Building-off of our single-component 3D conductive network, in Chapter 7, we look at adding a water soluble fullerene derivative as an electron acceptor to further move towards the creating of a water processable OPV. The placement of the solubilizing groups on the fullerene can be used as a way to direct the self-assembly of the fullerene with the amphiphilic polymer. By placing groups on the same side of the fullerene ball (cis-oid), the fullerene inserts into the interior of the polymer micelle and enables efficient electron transfer. If instead the groups are placed on opposite sides of the fullerene ball (trans-oid), the fullerene still co-assembles with the polymer, but resides on the outside of the micelle, which prevents charge recombination. By combining the fullerene isomers, we can create an energy cascade in which the fullerene inside separates the charges and transfers the electron to the fullerene on the outside. The electron is then stabilized by the water environment and is not able to recombine with the hole on the polymer, thus creating long lived polarons (or free carriers) in solution that remain stable for an unprecedented amount of time. This energy cascade additionally could help improve efficiency in a water processable photovoltaic devices.

By being able to control polymer orientation and morphology, we are able to optimize existing devices and further understand how to improve future applications. In Chapter 8, the results of this work will be summarized and the impacts this work has on the OPV field will be discussed. Additionally, the future directions of utilizing self-assembly as a means of controlling

polymer and fullerene morphology within devices will be examined. Finally, the appendices located at the end contain further information about effect of polymer:fullerene ratio on device performance (Appendix A), precise silica pore synthesis and subsequent field-effect transistor fabrication (Appendix B), detailed parameters for modeling the amphiphilic polymer from Chapter 6 (Appendix C), and detailed sample preparation using poly(fluorine-alt-thiophene) (Appendix D).

1.1 References

(1) Green, M. A.; Emery, K.; Hishikawa, Y.; Warta, W.; Dunlop, E. D. Solar Cell Efficiency Tables (version 42). *Progess Photovoltaics Res. Appl.* **2013**, *21*, 827–837.

(2) He, Z.; Zhong, C.; Su, S.; Xu, M.; Wu, H.; Cao, Y. Enhanced Power-Conversion Efficiency in Polymer Solar Cells Using an Inverted Device Structure. *Nat. Photonics* **2012**, *6*, 591–595.

(3) Deibel, C.; Dyakonov, V. Polymer–Fullerene Bulk Heterojunction Solar Cells. *Rep. Prog. Phys* **2010**, *73*, 096401.

(4) Helgesen, M.; Søndergaard, R.; Krebs, F. C. Advanced Materials and Processes for Polymer Solar Cell Devices. *J. Mater. Chem.* **2010**, *20*, 36.

(5) Li, G.; Zhu, R.; Yang, Y. Polymer Solar Cells. *Nat. Photonics* **2012**, *6*, 153–161.

(6) You, J.; Chen, C.-C.; Hong, Z.; Yoshimura, K.; Ohya, K.; Xu, R.; Ye, S.; Gao, J.; Li, G.; Yang, Y. 10.2% Power Conversion Efficiency Polymer Tandem Solar Cells Consisting of Two Identical Sub-Cells. *Adv. Mater.* **2013**, *25*, 3973–3978.

(7) You, J.; Dou, L.; Yoshimura, K.; Kato, T.; Ohya, K.; Moriarty, T.; Emery, K.; Chen, C.-C.; Gao, J.; Li, G.; et al. A Polymer Tandem Solar Cell with 10.6% Power Conversion Efficiency. *Nat. Commun.* **2013**, *4*, 1446.

(8) Shaw, P. E.; Ruseckas, A.; Samuel, I. D. W. Exciton Diffusion Measurements in Poly(3-Hexylthiophene). *Adv. Mater.* **2008**, *20*, 3516–3520.

(9) Halls, J. J. M.; Walsh, C. A.; Greenham, N.; Marseglia, E. A.; Friend, R.; Moratti, S. C.; Holmes, A. Efficient Photodiodes from Interpenetrating Polymer Networks. *Nature* **1995**, *376*, 498–500.

(10) Shaheen, S. E.; Brabec, C. J.; Sariciftci, N. S.; Padinger, F.; Fromherz, T.; Hummelen, J. C.

2.5% Efficient Organic Plastic Solar Cells. *Appl. Phys. Lett.* **2001**, *78*, 841–843.

(11) Halls, J. J. M.; Pichler, K.; Friend, R. H.; Moratti, S. C.; Holmes, A. B. Exciton Diffusion and Dissociation in a poly(p-phenylenevinylene)/C60 Heterojunction Photovoltaic Cell. *Appl. Phys. Lett.* **1996**, *68*.

(12) Collins, B. A.; Tumbleston, J. R.; Ade, H. Miscibility, Crystallinity, and Phase Development in P3HT/PCBM Solar Cells: Toward an Enlightened Understanding of Device Morphology and Stability. *J. Phys. Chem. Lett.* **2011**, *2*, 3135–3145.

(13) Yu, G.; Gao, J.; Hummelen, J. C.; Wudl, F.; Heeger, A. J. Polymer Photovoltaic Cells: Enhanced Efficiencies via a Network of Internal Donor-Acceptor Heterojunctions. *Science (80-.).* **1995**, *270*, 1789–1791.

(14) Peet, J.; Soci, C.; Coffin, R. C.; Nguyen, T. Q.; Mikhailovsky, A.; Moses, D.; Bazan, G. C. Method for Increasing the Photoconductive Response in Conjugated Polymer/fullerene Composites. *Appl. Phys. Lett.* **2006**, *89*, 252103–252105.

(15) Peet, J.; Kim, J. Y.; Coates, N. E.; Ma, W. L.; Moses, D.; Heeger, A. J.; Bazan, G. C. Efficiency Enhancement in Low-Bandgap Polymer Solar Cells by Processing with Alkane Dithiols. *Nat. Mater.* **2007**, *6*, 497–500.

(16) Lee, J. K.; Ma, W. L.; Brabec, C. J.; Yuen, J.; Moon, J. S.; Kim, J. Y.; Lee, K.; Bazan, G. C.; Heeger, A. J. Processing Additives for Improved Efficiency from Bulk Heterojunction Solar Cells. *J. Am. Chem. Soc.* **2008**, *130*, 3619–3623.

(17) Ma, W.; Yang, C.; Gong, X.; Lee, K.; Heeger, A. J. Thermally Stable, Efficient Polymer Solar Cells with Nanoscale Control of the Interpenetrating Network Morphology. *Adv. Funct. Mater.* **2005**, *15*, 1617–1622.

(18) Kim, K.; Liu, J.; Namboothiry, M. A. G.; Carroll, D. L. Roles of Donor and Acceptor Nanodomains in 6% Efficient Thermally Annealed Polymer Photovoltaics. *Appl. Phys. Lett.* **2007**, *90*, 163511.

(19) Verploegen, E.; Mondal, R.; Bettinger, C. J.; Sok, S.; Toney, M. F.; Bao, Z. Effects of Thermal Annealing Upon the Morphology of Polymer-Fullerene Blends. *Adv. Funct. Mater.* **2010**, *20*, 3519–3529.

(20) Zhao, Y.; Xie, Z.; Qu, Y.; Geng, Y.; Wang, L. Solvent-Vapor Treatment Induced Performance Enhancement of poly(3-Hexylthiophene):methanofullerene Bulk-Heterojunction Photovoltaic Cells. *Appl. Phys. Lett.* **2007**, *90*, 43503–43504.

(21) Jo, J.; Na, S.-I.; Kim, S.-S.; Lee, T.-W.; Chung, Y.; Kang, S.-J.; Vak, D.; Kim, D.-Y. Three-Dimensional Bulk Heterojunction Morphology for Achieving High Internal Quantum Efficiency in Polymer Solar Cells. *Adv. Funct. Mater.* **2009**, *19*, 2398–2406.

(22) Ayzner, A. L.; Tassone, C. J.; Tolbert, S. H.; Schwartz, B. J. Reappraising the Need for Bulk Heterojunctions in Polymer/Fullerene Photovoltaics: The Role of Carrier Transport in All-Solution-Processed P3HT/PCBM Bilayer Solar Cells. *Journal of Physical Chemistry C* **2009**, *113*, 20050–20060.

(23) Gevaerts, V. S.; Koster, L. J. A.; Wienk, M. M.; Janssen, R. A. J. R. A. J. Discriminating between Bilayer and Bulk Heterojunction Polymer:Fullerene Solar Cells Using the External Quantum Efficiency. *ACS Appl. Mater. Interfaces* **2011**, *3*, 3252–3255.

(24) Moon, J. S.; Takacs, C. J.; Sun, Y.; Heeger, A. J. Spontaneous Formation of Bulk Heterojunction Nanostructures: Multiple Routes to Equivalent Morphologies. *Nano Lett.* **2011**, *11*, 1036–1039.

(25) Treat, N. D.; Brady, M. A.; Smith, G.; Toney, M. F.; Kramer, E. J.; Hawker, C. J.; Chabinyc, M. L. Interdiffusion of PCBM and P3HT Reveals Miscibility in a Photovoltaically Active Blend. *Adv. Energy Mater.* **2011**, *1*, 82–89.

(26) Ayzner, A. L.; Doan, S. C.; de Villers, B.; Schwartz, B. J.; Tremolet de Villers, B. Ultrafast Studies of Exciton Migration and Polaron Formation in Sequentially Solution-Processed Conjugated Polymer/Fullerene Quasi-Bilayer Photovoltaics. *J. Phys. Chem. Lett.* **2012**, *3*, 2281–2287.

(27) Hawks, S. A.; Aguirre, J. C.; Schelhas, L. T.; Thompson, R. J.; Huber, R. C.; Ferreira, A. S.; Zhang, G.; Herzing, A. A.; Tolbert, S. H.; Schwartz, B. J. Comparing Matched Polymer:Fullerene Solar Cells Made by Solution-Sequential Processing and Traditional Blend Casting: Nanoscale Structure and Device Performance. *Journal of Physical Chemistry C* **2014**, *118*, 17413–17425.

(28) Zhang, G.; Huber, R.; Ferreira, A.; Boyd, S. D.; Luscombe, C. K.; Tolbert, S. H.; Schwartz, B. J. Crystallinity Effects in Sequentially Processed and Blend Cast Bulk-Heterojunction Polymer/Fullerene Photovoltaics. *Journal of Physical Chemistry C* **2014**, *118*, 18424-18435.

(29) Lee, K. H.; Schwenn, P. E.; Smith, A. R. G.; Cavaye, H.; Shaw, P. E.; James, M.; Krueger, K. B.; Gentle, I. R.; Meredith, P.; Burn, P. L. Morphology of All-Solution-Processed "Bilayer" Organic Solar Cells. *Adv. Mater.* **2011**, *23*, 766–770.

(30) Loiudice, A.; Rizzo, A.; Latini, G.; Nobile, C.; de Giorgi, M.; Gigli, G.; Mathew, X. Graded Vertical Phase Separation of Donor/acceptor Species for Polymer Solar Cells. *Sol. Energy Mater. Sol. Cells* **2012**, *100*, 147–152.

(31) Nardes, A. M.; Ayzner, A. L.; Hammond, S. R.; Ferguson, A. J.; Schwartz, B. J.; Kopidakis, N. Photoinduced Charge Carrier Generation and Decay in Sequentially Deposited Polymer/Fullerene Layers: Bulk Heterojunction vs Planar Interface. *Journal of Physical Chemistry C* **2012**, *116*, 7293–7305.

(32) Kim, D. H.; Mei, J.; Ayzner, A. L.; Schmidt, K.; Giri, G.; Appleton, A. L.; Toney, M. F.;

Bao, Z. Sequentially Solution-Processed, Nanostructured Polymer Photovoltaics Using Selective Solvents. *Energy Environ. Sci.* **2014**, *7*, 1103–1109.

(33) Aguirre, J. C.; Hawks, S. A.; Ferreira, A.; Yee, P.; Subramaniyan, S.; Jenekhe, S. A.; Tolbert, S. H.; Schwartz, B. J. Sequential Processing for Organic Photovoltaics: Design Rules for Morphology Control by Tailored Semi-Orthogonal Solvent Blends. *Adv. Energy Mater.* **2015**, *5*, 1402020.

(34) Liu, Y.; Lui, F.; Wang, H. W.; Nordlund, D.; Sun, Z.; Ferdous, S.; Russell, T. P. Sequential Deposition: Optimization of Solvent Swelling for High-Performance Polymer Solar Cells. *ACS Appl. Mater. Interfaces* **2014**, *7*, 653–661.

(35) Collins, B. A.; Gann, E.; Guignard, L.; He, X.; McNeill, C. R.; Ade, H. Molecular Miscibility of Polymer−Fullerene Blends. *J. Phys. Chem. Lett.* **2010**, *1*, 3160–3166.

(36) Lee, K. H.; Zhang, Y.; Burn, P. L.; Gentle, I. R.; James, M.; Nelson, A.; Meredith, P. Correlation of Diffusion and Performance in Sequentially Processed P3HT/PCBM Heterojunction Films by Time-Resolved Neutron Reflectometry. *J. Mater. Chem. C* **2013**, *1*, 2593–2598.

(37) Aguirre, J. C.; Ferreira, A.; Ding, H.; Jenekhe, S. A.; Kopidakis, N.; Asta, M.; Pilon, L.; Rubin, Y.; Tolbert, S. H.; Schwartz, B. J.; et al. Panoramic View of Electrochemical Pseudocapacitor and Organic Solar Cell Research in Molecularly Engineered Energy Materials (MEEM). *Journal of Physical Chemistry C* **2014**, *34*, 19505–19523.

(38) Jiang, X. M.; Österbacka, R.; Korovyanko, O.; An, C. P.; Horovitz, B.; Janssen, R. A. J.; Vardeny, Z. V. Spectroscopic Studies of Photoexcitations in Regioregular and Regiorandom Polythiophene Films. *Adv. Funct. Mater.* **2002**, *12*, 587–597.

(39) Adachi, T.; Brazard, J.; Ono, R. J.; Hanson, B.; Traub, M. C.; Wu, Z.-Q.; Li, Z.; Bolinger, J. C.; Ganesan, V.; Bielawski, C. W.; et al. Regioregularity and Single Polythiophene Chain Conformation. *J. Phys. Chem. Lett.* **2011**, *2*, 1400–1404.

(40) Brown, P.; Thomas, D.; Köhler, A.; Wilson, J.; Kim, J.-S.; Ramsdale, C.; Sirringhaus, H.; Friend, R. Effect of Interchain Interactions on the Absorption and Emission of poly(3-Hexylthiophene). *Phys. Rev. B* **2003**, *67*, 064203.

(41) Kim, Y.; Cook, S.; Tuladhar, S. M.; Choulis, S. A.; Nelson, J.; Durrant, J. R.; Bradley, D. D. C.; Giles, M.; McCulloch, I.; Ha, C.-S.; et al. A Strong Regioregularity Effect in Self-Organizing Conjugated Polymer Films and High-Efficiency Polythiophene:fullerene Solar Cells. *Nat Mater* **2006**, *5*, 197–203.

(42) Mauer, R.; Kastler, M.; Laquai, F. The Impact of Polymer Regioregularity on Charge Transport and Efficiency of P3HT:PCBM Photovoltaic Devices. *Adv. Funct. Mater.* **2010**, *20*, 2085–2092.

(43) Kohn, P.; Rong, Z.; Scherer, K. H.; Sepe, A.; Sommer, M.; Müller-Buschbaum, P.; Friend, R. H.; Steiner, U.; Hüttner, S. Crystallization-Induced 10-Nm Structure Formation in P3HT/PCBM Blends. *Macromolecules* **2013**, *46*, 4002–4013.

(44) Rochester, C. W.; Mauger, S. A.; Moule, A. J. Investigating the Morphology of Polymer/Fullerene Layers Coated Using Orthogonal Solvents. *Journal of Physical Chemistry C* **2012**, *116*, 7287–7292.

(45) Babel, A.; Jenekhe, S. A. Alkyl Chain Length Dependence on the Field-Effect Carrier Mobility in Regioregular poly(3-Alkylthiophene)s. *Synth. Met.* **2005**, *148*, 169–173.

(46) Gadisa, A.; Oosterbaan, W. D.; Vandewal, K.; Bolse, J. C.; Bertho, S.; D'Haen, J.; Lutsen, L.; Vanderzande, D.; Manca, J. V. Effect of Alkyl Side-Chain Length on Photovoltaic Properties of poly(3-alkylthiophene)/PCBM Bulk Heterojunctions. *Adv. Funct. Mater.* **2009**, *19*, 3300–3306.

(47) Szarko, J. M.; Guo, J.; Liang, Y.; Lee, B.; Rolczynski, B. S.; Strzalka, J.; Xu, T.; Loser, S.; Marks, T. J.; Yu, L.; et al. When Function Follows Form: Effects of Donor Copolymer Side Chains on Film Morphology and BHJ Solar Cell Performance. *Adv. Mater.* **2010**, *22*, 5468–5472.

(48) Yang, L.; Zhou, H.; You, W. Quantitatively Analyzing the Influence of Side Chains on Photovoltaic Properties of Polymer−Fullerene Solar Cells. *Journal of Physical Chemistry C* **2010**, *114*, 16793–16800.

(49) Mei, J.; Bao, Z. Side Chain Engineering in Solution-Processable Conjugated Polymers. *Chem. Mater.* **2014**, *26*, 604–615.

(50) Yiu, A. T.; Beaujuge, P. M.; Lee, O. P.; Woo, C. H.; Toney, M. F.; Fréchet, J. M. J. Side-Chain Tunability of Furan-Containing Low-Band-Gap Polymers Provides Control of Structural Order in Efficient Solar Cells. *J. Am. Chem. Soc.* **2012**, *134*, 2180–2185.

(51) Piliego, C.; Holcombe, T. W.; Douglas, J. D.; Woo, C. H.; Beaujuge, P. M.; Fréchet, J. M. J. Synthetic Control of Structural Order in N-alkylthieno[3,4-C]pyrrole-4,6-Dione-Based Polymers for Efficient Solar Cells. *J. Am. Chem. Soc.* **2010**, *132*, 7595–7597.

(52) Cabanetos, C.; El Labban, A.; Bartelt, J. A.; Douglas, J. D.; Mateker, W. R.; Fréchet, J. M. J.; McGehee, M. D.; Beaujuge, P. M. Linear Side Chains in benzo[1,2-b:4,5-B']dithiophene-thieno[3,4-C]pyrrole-4,6-Dione Polymers Direct Self-Assembly and Solar Cell Performance. *J. Am. Chem. Soc.* **2013**, *135*, 4656–4659.

(53) Rivnay, J.; Steyrleuthner, R.; Jimison, L. H.; Casadei, A.; Chen, Z.; Toney, M. F.; Facchetti, A.; Neher, D.; Salleo, A. Drastic Control of Texture in a High Performance N-Type Polymeric Semiconductor and Implications for Charge Transport. *Macromolecules* **2011**, *44*, 5246–5255.

(54) Zhang, X.; Richter, L. J.; DeLongchamp, D. M.; Kline, R. J.; Hammond, M. R.; McCulloch, I.; Heeney, M.; Ashraf, R. S.; Smith, J. N.; Anthopoulos, T. D.; et al. Molecular Packing of High-Mobility Diketo Pyrrolo-Pyrrole Polymer Semiconductors with Branched Alkyl Side Chains. *J. Am. Chem. Soc.* **2011**, *133*, 15073–15084.

(55) Liu, F.; Gu, Y.; Jung, J. W.; Jo, W. H.; Russell, T. P. On the Morphology of Polymer-Based Photovoltaics. *J. Polym. Sci. Part B Polym. Phys.* **2012**, *50*, 1018–1044.

(56) Sirringhaus, H.; Brown, P. J.; Friend, R. H.; Nielsen, M. M.; Bechgaard, K.; Langeveld-Voss, B. M. W.; Spiering, A. J. H.; Janssen, R. A. J.; Meijer, E. W.; Herwig, P.; et al. Two-Dimensional Charge Transport in Self-Organized, High-Mobility Conjugated Polymers. *Nature* **1999**, *401*, 685–688.

(57) Hammond, M. R.; Kline, R. J.; Herzing, A. A.; Richter, L. J.; Germack, D. S.; Ro, H.-W.; Soles, C. L.; Fischer, D. A.; Xu, T.; Yu, L.; et al. Molecular Order in High-Efficiency Polymer/Fullerene Bulk Heterojunction Solar Cells. *ACS Nano* **2011**, *5*, 8248–8257.

(58) Chen, M. S.; Niskala, J. R.; Unruh, D. A.; Chu, C. K.; Lee, O. P.; Fréchet, J. M. J. Control of Polymer-Packing Orientation in Thin Films through Synthetic Tailoring of Backbone Coplanarity. *Chem. Mater.* **2013**, *25*, 4088–4096.

(59) Osaka, I.; Kakara, T.; Takemura, N.; Koganezawa, T.; Takimiya, K. Naphthodithiophene-Naphthobisthiadiazole Copolymers for Solar Cells: Alkylation Drives the Polymer Backbone Flat and Promotes Efficiency. *J. Am. Chem. Soc.* **2013**, *135*, 8834–8837.

(60) Osaka, I.; Saito, M.; Koganezawa, T.; Takimiya, K. Thiophene-Thiazolothiazole Copolymers: Significant Impact of Side Chain Composition on Backbone Orientation and Solar Cell Performances. *Adv. Mater.* **2014**, *26*, 331–338.

(61) Stoneham, A. M.; Ramos, M. M. D.; Almeida, A. M.; Correia, H. M. G.; Ribeiro, R. M.; Ness, H.; Fisher, A. J. Understanding Electron Flow in Conducting Polymer Films: Injection, Mobility, Recombination and Mesostructure. *J. Phys. Condens. Matter* **2002**, *14*, 9877–9898.

(62) Lan, Y.-K.; Yang, C. H.; Yang, H.-C. Theoretical Investigations of Electronic Structure and Charge Transport Properties in Polythiophene-Based Organic Field-Effect Transistors. *Polym. Int.* **2010**, *59*, 16–21.

(63) Prins, P.; Grozema, F.; Schins, J.; Savenije, T.; Patil, S.; Scherf, U.; Siebbeles, L. Effect of Intermolecular Disorder on the Intrachain Charge Transport in Ladder-Type Poly(p-Phenylenes). *Phys. Rev. B* **2006**, *73*, 045204.

(64) Molenkamp, W. C.; Watanabe, M.; Miyata, H.; Tolbert, S. H. Highly Polarized Luminescence from Optical Quality Films of a Semiconducting Polymer Aligned within Oriented Mesoporous Silica. *J. Am. Chem. Soc.* **2004**, *126*, 4476–4477.

(65) Cadby, A. A. J.; Tolbert, S. S. H. Controlling Optical Properties and Interchain Interactions in Semiconducting Polymers by Encapsulation in Periodic Nanoporous Silicas with Different Pore Sizes. *J. Phys. Chem. B* **2005**, *109*, 17879–17886.

(66) Miyata, H.; Noma, T.; Watanabe, M.; Kuroda, K. Preparation of Mesoporous Silica Films with Fully Aligned Large Mesochannels Using Nonionic Surfactants. *Chem. Mater.* **2002**, *14*, 766–772.

(67) Chi, C.; Mikhailovsky, A.; Bazan, G. C. Design of Cationic Conjugated Polyelectrolytes for DNA Concentration Determination. *J. Am. Chem. Soc.* **2007**, *129*, 11134–11145.

(68) Jiang, H.; Zhao, X.; Schanze, K. S. Effects of Polymer Aggregation and Quencher Size on Amplified Fluorescence Quenching of Conjugated Polyelectrolytes. *Langmuir* **2007**, *23*, 9481–9486.

(69) Jiang, H.; Taranekar, P.; Reynolds, J. R.; Schanze, K. S. Conjugated Polyelectrolytes: Synthesis, Photophysics, and Applications. *Angew. Chemie Int. Ed.* **2009**, *48*, 4300–4316.

(70) Thomas, A.; Houston, J. E.; Van den Brande, N.; De Winter, J.; Chevrier, M.; Heenan, R. K.; Terry, A. E.; Richeter, S.; Mehdi, A.; Van Mele, B.; et al. All-Conjugated Cationic Copolythiophene "rod–rod" Block Copolyelectrolytes: Synthesis, Optical Properties and Solvent-Dependent Assembly. *Polym. Chem.* **2014**, *5*, 3352.

(71) Wu, C.; Bull, B.; Szymanski, C.; Christensen, K.; McNeill, J. Multicolor Conjugated Polymer Dots for Biological Fluorescence Imaging. *ACS Nano* **2008**, *2*, 2415–2423.

(72) Tuncel, D.; Demir, H. V. Conjugated Polymer Nanoparticles. *Nanoscale* **2010**, *2*, 484–494.

(73) Stevens, A. L.; Kaeser, A.; Schenning, A. P. H. J.; Herz, L. M. Morphology-Dependent Energy Transfer Dynamics in Fluorene-Based Amphiphile Nanoparticles. *ACS Nano* **2012**, *6*, 4777–4787.

(74) Clark, A. P.-Z.; Shi, C.; Ng, B. C.; Wilking, J. N.; Ayzner, A. L.; Stieg, A. Z.; Schwartz, B. J.; Mason, T. G.; Rubin, Y.; Tolbert, S. H. Self-Assembling Semiconducting Polymers-Rods and Gels from Electronic Materials. *ACS Nano* **2013**, *7*, 962–977.

(75) Zaroslov, Y. D.; Gordeliy, V. I.; Kuklin, a. I.; Islamov, a. H.; Philippova, O. E.; Khokhlov, a. R.; Wegner, G. Self-Assembly of Polyelectrolyte Rods in Polymer Gel and in Solution: Small-Angle Neutron Scattering Study. *Macromolecules* **2002**, *35*, 4466–4471.

CHAPTER 2

Crystallinity Effects in Sequentially-processed and Blend-cast Bulk-heterojunction Polymer/Fullerene Photovoltaics

2.1 Introduction

In recent years, dramatic progress has been made in the field of organic photovoltaics (OPVs),[1,2] resulting in power conversion efficiencies (PCEs) of polymer/fullerene devices surpassing 10%.[3–6] This achievement is based mostly on traditional blend-cast (BC) bulk heterojunctions (BHJs),[7] in which an electron-donating polymer and electron-accepting fullerene are mixed together in a solution that is used to cast the active layer of the organic solar cell. The resulting film is then typically thermally or solvent annealed to promote phase separation of the polymer and fullerene, resulting in a conductive network for both electrons and holes as well as intermixed regions where a majority of charge separation occurs.[8–17] The morphology of BC BHJ films is dictated by multiple factors, including the donor/acceptor miscibility, the propensity of one or both materials to crystallize,[16,18–21] the relative solubilities of the two materials in the casting solution, the drying kinetics of the film, the presence of any solvent additives,[22–26] etc. Because the nm-scale morphology depends on so many of the details of how the film is cast, the device performance of BC BHJ solar cells is hypersensitive to the processing kinetics of the active layer.[7] Thus, for any new set of OPV materials, an Edisonian approach involving the fabrication of hundreds of BC devices is needed to find the processing conditions that lead to the optimal morphology and best device performance.

An alternative approach to preparing polymer/fullerene active layers for photovoltaic

applications has been to sequentially process the polymer and fullerene components in separate steps by depositing the materials from orthogonal solvents.[27] This sequential processing (SqP) technique has been studied by several groups in both polymer-fullerene[28–36] and small molecule-fullerene systems.[37] It is well established that even though the fullerene is deposited on top of the polymer layer, the resultant film still has a significant amount of fullerene dispersed through the polymer layer,[38] particularly after thermal annealing.[39–41] Not only are the PCEs of devices fabricated via SqP comparable to or better than the more traditional BC devices,[36,37,42–48] but the SqP method also provides several distinct advantages that could make it the preferred route for large-scale fabrication of polymer-based photovoltaics. First, films produced via SqP have a more reproducible morphology because SqP does not rely on kinetic control of the nm-scale structure, resulting in devices that behave more consistently (*cf*. Figure 2.1).[27,42,49] Second, since the two materials are deposited separately, one can optimize or otherwise deliberately alter the donor material (e.g., by chemical doping) either before[50–52] or after[53] it has been processed, without unwanted chemistry occurring with the electron-accepting material. Third, sequentially-processed films are guaranteed to have a fullerene network that is connected to the top of the film, avoiding issues with undesirable vertical phase separation that necessitate the use of an inverted device geometry. Finally, many solubility issues can be bypassed since one can separately choose optimal solvents for the donor and acceptor materials.[37,54] Thus, the SqP technique potentially opens the photovoltaic field to a variety of donor and acceptor materials that once were not usable due to compatibility issues between solvents and materials.

Although it is clear that the BHJ morphology of films produced via SqP is generally similar to that of BC films in that the fullerene is dispersed throughout the polymer, a variety of experiments have suggested that the details of the nm-scale distribution of the polymer and

fullerene differ between the two processing techniques. For example, ultrafast spectroscopic studies have shown that the dynamics of exciton quenching and polaron production are different in optically-matched sequentially-processed and BC films made from the workhorse materials poly(3-hexylthiophene) (P3HT) and [6,6]-phenyl-C_{61}-butyric-acid-methyl-ester (PCBM).[55] Moreover, nominally matched sequentially-procssed and BC photovoltaic devices show different behaviors upon thermal annealing.[42,48,49,56] Thus, one of the most important issues concerning solar cells fabricated via SqP is precisely how the nm-scale morphology is different from that in BC films, and what factors control the extent and distribution of fullerene interpenetration into the polymer underlayer.

In this chapter, we work to build an understanding of the fullerene distribution in P3HT/PCBM BHJ solar cells produced via both SqP and blend-casting. Our approach is to take advantage of a series of P3HTs with a narrow molecular weight distribution and precisely controlled regioregularity that allow us to explore how changing specific attributes of the polymer leads to differences in both the BHJ architecture and in the PV performance of sequentially-procssed and BC devices. It is well known that polymer regioregularity and polydispersity index (PDI) can have dramatic effects on the photovoltaic performance of BC BHJs,[57–63] and here we extend these studies to sequentially-processed devices, focusing in particular on how regioregularity affects the morphology and device performance of thermally annealed P3HT/PCBM active layers. In agreement with previous suggestions, we first find that PCBM deposited by sequential processing preferentially penetrates into the amorphous regions of the P3HT underlayer, leaving the crystalline regions of the polymer essentially intact.[40,56] We then show that too much polymer crystallinity is actually unfavorable for SqP photovoltaic devices because too little fullerene can penetrate around the crystallites, leading to over-phase separation

of the polymer and fullerene. In contrast, BC devices show the opposite behavior: highly regioregular (and thus more crystalline) P3HT provides better efficiencies than BC devices made from lower regioregularity P3HTs. We thus conclude that sequentially-processed and BC BHJ devices require different materials properties to achieve formation of their ideal active layer morphologies.

2.2 Results and Discussion

In this section, we begin by discussing the hole mobility of the three polymer batches we investigate in this work (Table 2.1). Although we find that polymer regioregularity and molecular weight do slightly affect hole transport, the differences we observe are subtle, suggesting that BHJ morphology is a much larger factor in determining device performance than the raw hole mobility of the bare polymer. We then use these different polymer batches to fabricate SqP and BC solar cells, and demonstrate that polymer regioregularity has the opposite effect for the two different processing techniques in terms of photovoltaic device efficiency. This result can be understood through a series of morphological studies, including thin film absorption, fluorescence quenching and grazing incidence X-ray scattering measurements, which allow us to directly explore the structural changes that occur upon thermal annealing and to define the optimal conditions needed to create ideal morphologies for BC and SqP solar cells.

2.2.1 Device Physics of BC and SqP Solar Cells

***2.2.1.1 Hole Mobility of Different P3HTs*:** Many groups have examined how the mobilities of P3HT films are controlled by different polymer properties, such as the regioregularity and/or molecular weight.[58,59,64–68] The generally accepted trend is that increasing regioregularity

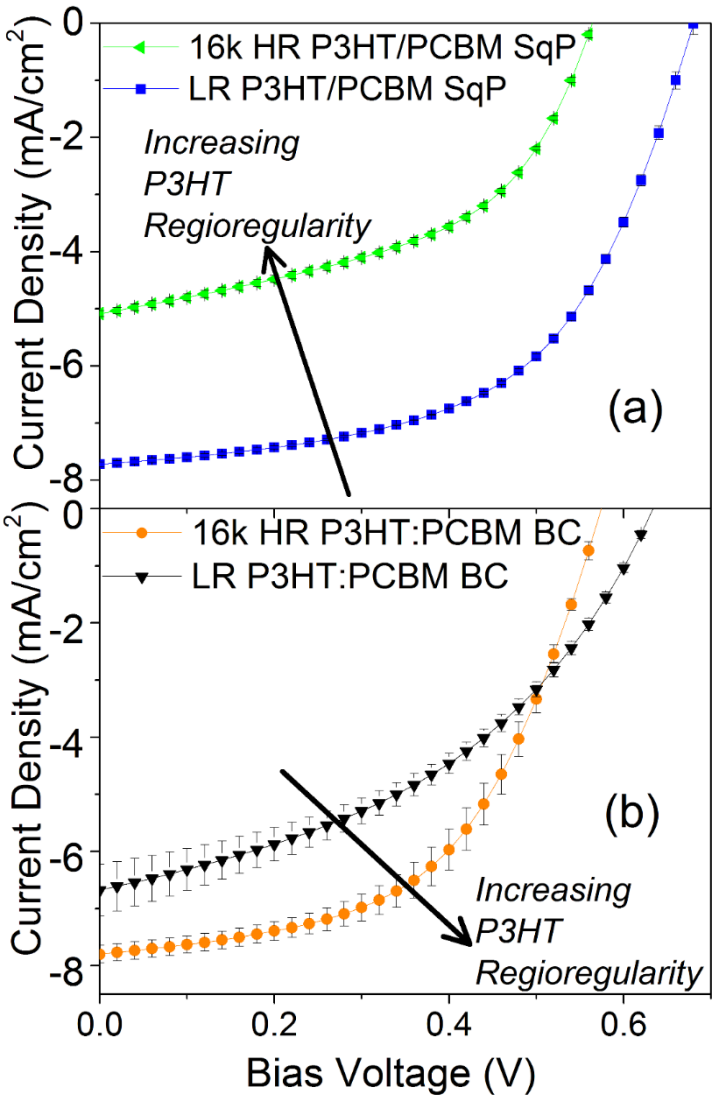

Figure 2.1. Current density versus applied bias for (a) ITO/poly(ethylene-dioxythiophene):poly(styrenesulfonic acid)(PEDOT:PSS)/P3HT/PCBM/Ca/Al sequentially-processed solar cells and (b) ITO/PEDOT:PSS/P3HT:PCBM/Ca/Al BC-BHJ solar cells under AM-1.5 illumination. The SqP active layer was made by spinning 5 mg/mL PCBM solution onto a 110 nm P3HT underlayer. All of the SqP and BC films were thermally annealed at 150 °C for 20 min prior to deposition of the cathode. The error bars show 1 standard deviation in measurements over at least 12 independent devices. Although error bars can be clearly seen in panel (b), they are comparable to or smaller than the symbols used to plot the data in panel (a), indicating that SqP devices are more reproducible than BC devices.

Table 2.1. Characteristics of P3HT used.

	M_n (kDa)	Regioregularity	PDI	Mobility (SCLC) ($cm^2\ V^{-1}\ s^{-1}$)
Low RR (LR) P3HT	~50-60	~94%	~2.20	1.6×10^{-5}
16k High RR (HR) P3HT	15.9	98%	1.18	3.4×10^{-5}
37k High RR (HR) P3HT	36.9	98%	1.19	1.3×10^{-5}

and increasing molecular weight lead to higher charge carrier mobilities,[66] although most such measurements are made on field-effect transistors (FETs).[69] Since the direction of charge transport for photovoltaic devices is perpendicular to that in FETs, we chose to examine the carrier mobilities in our P3HT batches in sandwich-structure devices so that our measurements would be directly relevant for the performance of these materials in solar cells.

We fabricated diodes from each batch of P3HT using an architecture of ITO/PEDOT:PSS/P3HT/Au to ensure that the majority carriers in the device are holes. We then fit the corresponding dark *J-V* curves using the space-charge limited current (SCLC) model, yielding the mobilities listed in Table 2.1. The 16k HR P3HT shows the highest hole mobility, a bit over twice that of the LR P3HT, which has a molecular weight of roughly 50 kDa. Surprisingly, the 37k HR P3HT shows the lowest mobility, even though it has the same regioregularity as the 16k HR batch but a higher molecular weight. These results indicate that P3HT hole mobility has a complex dependence on both regioregularity and molecular weight. We note, however, that the hole mobilities for all three P3HT batches all fall within a factor of 2.6. This suggests that when these different P3HTs are employed in photovoltaic devices, all else being equal, differences in hole mobility are not likely to explain any significant difference in device performance. This allows us to use these batches to understand how differences in regioregularity and molecular weight result in morphology differences that affect solar cell performance, and how these differences depend on the processing route chosen to make the BHJ active layer.

2.2.1.2 Comparing the Performance of SqP and BC Devices with Controlled P3HT Regioregularity and Fullerene Composition: To determine the effect of polymer regioregularity/crystallinity on the performance of the solar cells with different active-layer

processing methods, we constructed working photovoltaic devices with both SqP and BC active layers from both the 16k HR P3HT and LR P3HT batches. Figure 2.1 demonstrates the *J–V* characteristics of the devices under AM 1.5 solar illumination; the data plotted are the average *J–V* curves from at least twelve separate devices, and the error bars (which in some cases are smaller than the symbols used to plot the data) are ±1 standard deviation. The full *J–V* characteristics for all the devices we studied are detailed in Table 2. The data show clearly that even though SqP devices require one more spin-coating step than BC devices, SqP devices can be fabricated far more reproducibly. This is because SqP avoids the kinetic sensitivity of the BHJ morphology that is inherent with BC processing.[42]

The most interesting result from Figure 2.1 is the fact that the two P3HT batches show opposite performance trends, depending on the processing method used to make the devices. The SqP solar cells made with LR P3HT show *J–V* characteristics similar to those published previously,[27] with average open circuit voltage V_{oc} = 0.68 V, short circuit current J_{sc} = 7.2 mA cm^{-2}, fill factor *FF* = 56% and PCE = 2.9%. The HR P3HT batch, however, makes poorer SqP devices with J_{sc} values of only ~5.1 mA cm^{-2}, and PCE of only ~1.4%. In contrast, the HR P3HT:PCBM BC devices have a significantly higher J_{sc} and ~40% higher PCE compared to the BC devices fabricated with LR P3HT. Thus, the way polymer regioregularity/crystallinity affects device performance is not a simple material property, but instead depends on the route via which the active BHJ layer is processed.

To understand why changing the polymer regioregularity leads to opposite changes in performance for SqP and BC devices, we performed a series of control experiments to verify that the performance changes we observed did not result from changes in the polymer molecular weight or the polymer:fullerene composition of the active layer. Figure 2.2 and Table 2.2 summarize the

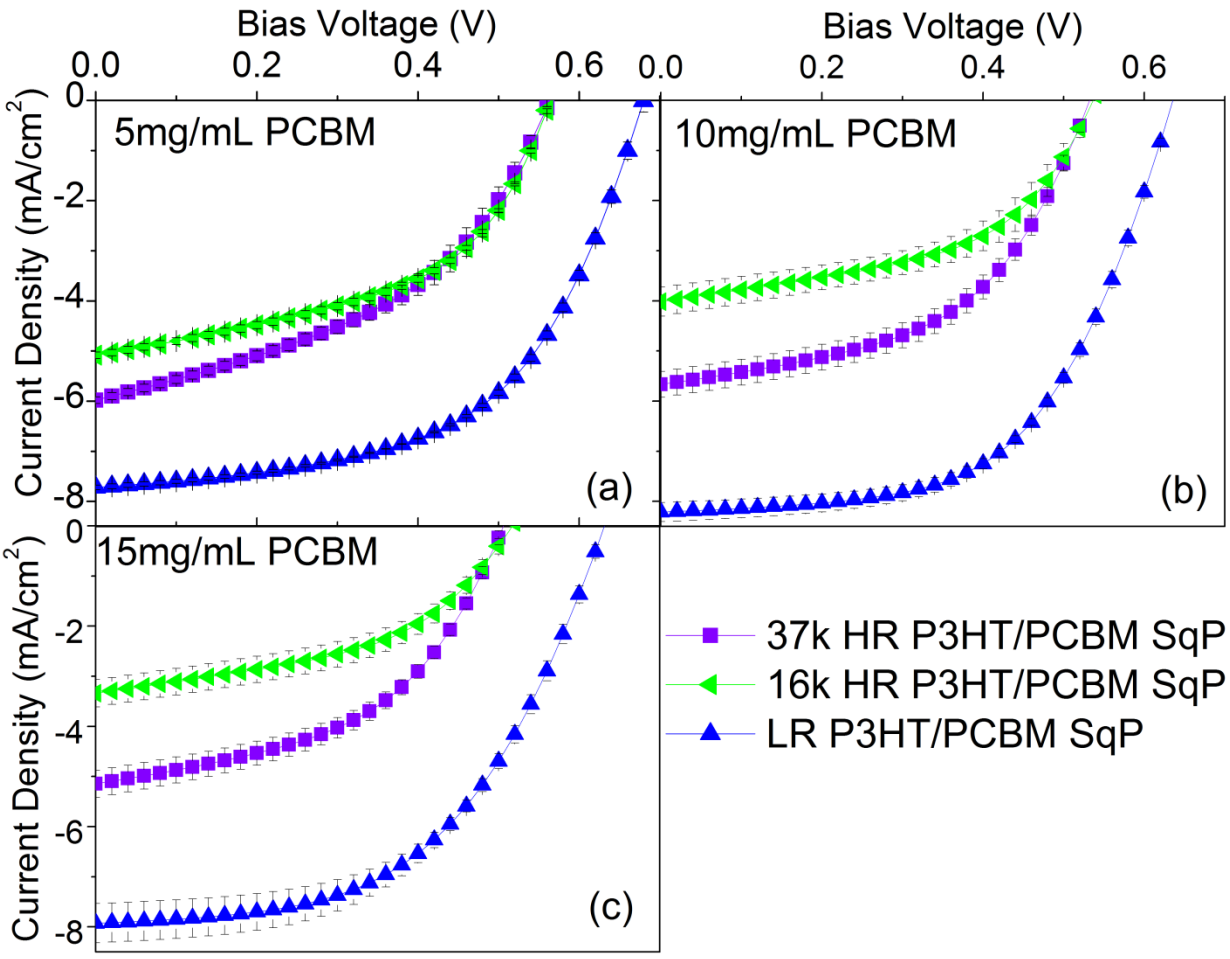

Figure 2.2. *E*ffect of molecular weight, regioregularity and film composition on the *J–V* characteristics of P3HT/PCBM devices made via SqP. LR P3HT (blue up-triangles) and two HR P3HTs with different molecular weights, e.g. 37k Da (violet squares) and 16 kDa (green left triangles) are used as underlayer. All P3HT underlayers were kept at ~110 nm. Three different concentrations of PCBM (5 mg/mL, 10 mg/mL and 15 mg/mL) were spun on top of the P3HT underlayers from DCM and the corresponding *J–V* curves are shown in panels (a), (b) and (c), respectively. The total thicknesses of the active layers are 155 nm, 169 nm and 185 nm with increasing PCBM solution concentratio, respectively. All samples were annealed at 150° C for 20 min before deposition of the Ca/Al cathode. The error bars show 1 standard deviation for measurements over at least 12 independent devices.

J–V characteristics of SqP solar cells made from the 16k HR P3HT (green triangles) and LR P3HT (blue squares), as well as the 37k HR P3HT (violet squares). The in-house synthesized 37k HR P3HT batch has the same high regioregularity and low PDI as the 16k HR P3HT, but a molecular weight closer to that of the commercial LR P3HT. The V_{oc} and *FF* of the 37k HR batch are similar to the 16k HR P3HT, but the overall PCE is higher, mainly due to increased J_{sc}. However, even though increasing the molecular weight improves the device performance, we see that the LR P3HT still shows superior performance for devices fabricated by SqP. Thus, for SqP devices, the overall performance is governed more by the degree of P3HT regioregularity instead of the polymer molecular weight.

In addition to polymer regioregularity, the performance of OPVs also depends sensitively on the overall polymer:fullerene composition,[43,70] a factor that is directly controlled using the ratio of polymer to fullerene in the casting solution in BC processing. In SqP, by contrast, the composition is indirectly controlled by the relative solution concentrations and spin speeds used to deposit each component of the active layer. Figure 2.2 thus illustrates the change in SqP solar cell performance with different polymer:fullerene compositions. In these experiments, we fixed the thickness of the P3HT underlayer and increased the concentration of the PCBM solution spun on top. We find that with increasing fullerene loading in SqP active layer, the LR P3HT-based devices show only slight variations in J_{sc}, with an optimal polymer/fullerene composition obtained when the PCBM overlayer is spun from a 10 mg/mL solution.[27] In contrast, the performance of the SqP devices based on HR P3HT continually decreases with increased PCBM loading. Thus, not only does increased P3HT regioregularity lead to poorer SqP device performance, the results also imply that the introduction of extra fullerene cannot be accommodated in pre-formed high-RR P3HT underlayers.

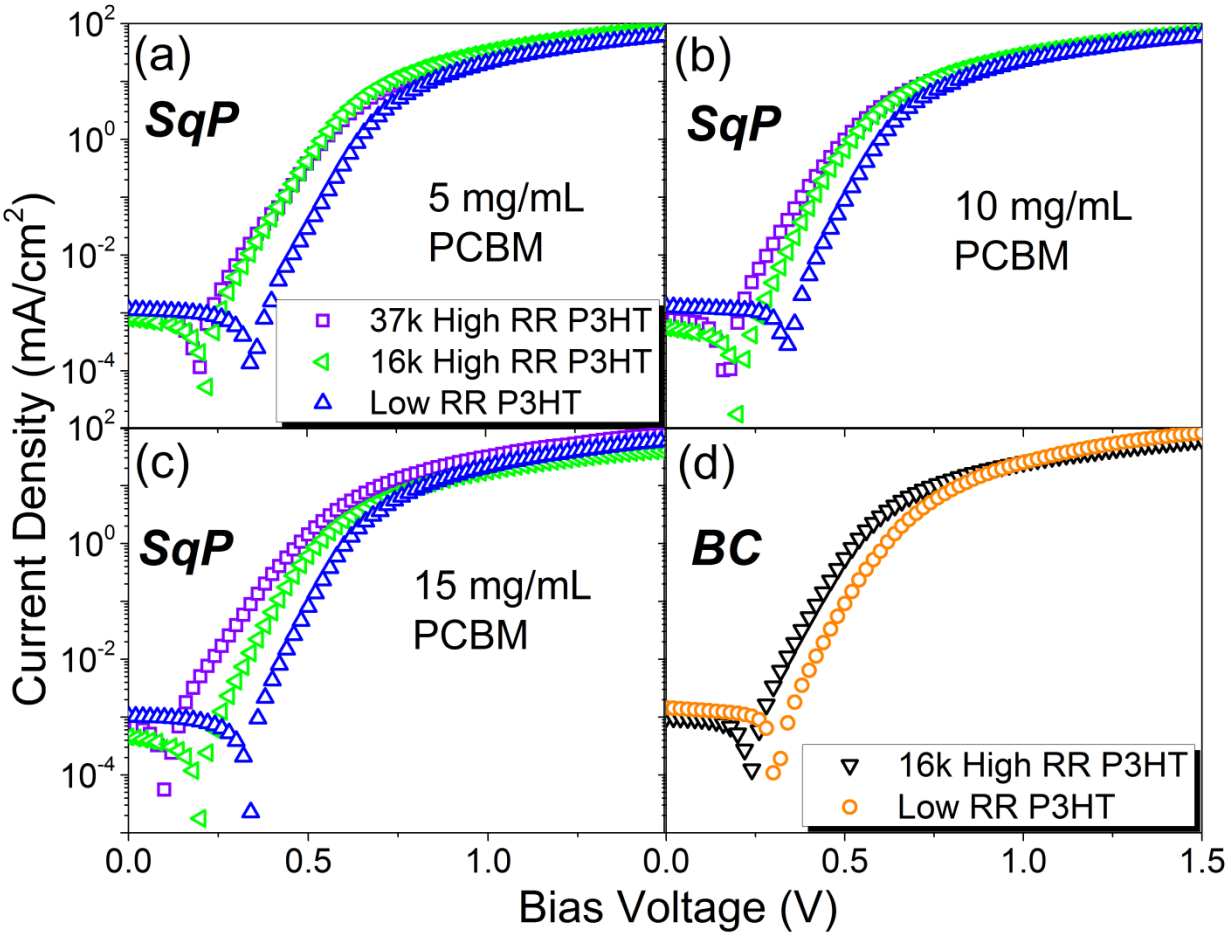

Figure 2.3. Dark *J-V* characteristics of the same SqP devices in Figure 2.2 and the same BC devices in Figure 2.1.

Table 2.2. Summary of Device Parameters

	V_{oc} (V)	J_{sc} (mA/cm^2)	*FF*	*PCE* (%)	n_{ideal} (Dark *J-V*)	R_{seires} (Ω-cm^2)	R_{shunt} (×10^5 Ω-cm^2)
37k HR P3HT/PCBM(5mg/mL) SqP	0.56 ±0.01	5.98 ±0.06	0.44 ±0.02	1.48 ±0.07	1.62 ±0.03	11.2 ±2.2	13.0 ±0.3
16k HR P3HT/PCBM(5mg/mL) SqP	0.56 ±0.01	5.08 ±0.06	0.50 ±0.01	1.43 ±0.02	1.62 ±0.03	8.8 ±0.7	7.8 ±0.0
LR P3HT/PCBM(5mg/mL) SqP	0.68 ±0.01	7.72 ±0.04	0.56 ±0.01	2.92 ±0.02	1.43 ±0.02	10.6 ±0.3	20.8 ±0.4
37k HR P3HT/PCBM(10mg/mL) SqP	0.53 ±0.01	5.67 ±0.26	0.51 ±0.01	1.52 ±0.09	1.88 ±0.03	12.3 ±2.2	12.6 ±0.0
16k HR P3HT/PCBM(10mg/mL) SqP	0.54 ±0.01	4.02 ±0.29	0.50 ±0.03	1.09 ±0.10	1.64 ±0.04	10.7 ±2.1	8.7 ±0.0
LR P3HT/PCBM(10mg/mL) SqP	0.64 ±0.01	8.21 ±0.19	0.57 ±0.01	2.97 ±0.03	1.40 ±0.04	10.9 ±2.1	14.8 ±0.2
37k HR P3HT/PCBM(15mg/mL) SqP	0.51 ±0.01	5.15 ±0.27	0.48 ±0.02	1.26 ±0.12	2.09 ±0.05	9.1 ±1.9	9.5 ±0.0
16k HR P3HT/PCBM(15mg/mL) SqP	0.515 ±0.01	3.34 ±0.27	0.47 ±0.02	0.82 ±0.08	1.64 ±0.05	18.3 ±1.9	10.0 ±0.0
LR P3HT/PCBM(15mg/mL) SqP	0.636 ±0.01	7.93 ±0.39	0.52 ±0.02	2.63 ±0.06	1.43 ±0.05	10.8 ±2.0	82.2 ±21
16k HR P3HT:PCBM BC	0.58 ±0.01	7.80 ±0.15	0.53 ±0.03	2.39 ±0.14	1.51 ±0.02	11.2 ±1.5	22.6 ±0.0
LR P3HT:PCBM BC	0.64 ±0.01	6.68 ±0.45	0.42 ±0.01	1.79 ±0.07	1.65 ±0.07	6.9 ±1.4	7.4 ±0.1

We also have performed identical experiments exploring the changes in device performance for different batches of P3HT with different fullerene compositions for BC devices. Since similar studies have been published previously the literature,[70–72] our results are shown in Appendix A. We find, in agreement with the literature, that increased P3HT regioregularity is beneficial to BC device performance. Surprisingly, however, we find that for BC devices made from the 16k HR P3HT, the optimal P3HT:PCBM weight ratio is 1:1.3, significantly higher than the 1:0.9 optimal ratio typically seen in the literature (with lower regioregular, commercially-available P3HT). Thus, for the HR-P3HT, the trend in fullerene loading for optimal BC devices also goes in the opposite direction as that for SqP devices.

2.2.1.3 The Effects of Polymer Regioregularity on BC and SqP Device Physics: To begin our exploration of why polymer regioregularity has opposite effects on solar cells fabricated via BC and SqP, we measured the dark *J–V* curves of the SqP and BC solar cells discussed above; the results are summarized in Figure 2.3 and Table 2.2.

Perhaps the most interesting parameter to consider for purposes of this study is the dark ideality factor. Typically the dark ideality factor falls into the range between 1 and 2, although numbers outside this range have been reported mainly due to resistivity effects.[73,74] Within the range of 1 and 2, a larger ideality factor is considered as a strong indication of increased trap-assisted recombination in the device, whereas lower ideality factors are more reflective of bimolecular recombination.[75–77] We derived the ideality factors for our SqP and BC devices in Table 2.2 from the slope of the linear regions in Figure 2.3; we find that the ideality factors mirror the trends in device performance. For SqP devices with a given fullerene concentration, the ideality factors for devices based on LR P3HT are consistently lower than those fabricated with

HR P3HTs. For BC devices, the opposite is true: the HR P3HT-based devices exhibit lower ideality factors than the LR P3HT-based devices. This implies that the polymer/fullerene interfacial trap distribution is quite different for the different BHJ morphologies formed through the two different processing techniques.

Based on the data presented above and the structural data presented below, we offer the following picture for the changes in device physics with polymer regioregularity. Low P3HT regioregularity typically leads to more amorphous regions in BHJ films made from the traditional blend-casting method. Since there are fewer crystalline polymer regions and more structural disorder, there is a greater degree of trap-assisted recombination. In contrast, increasing the polymer regioregularity in SqP devices causes the ideality factor to increase no matter what fullerene loading is used. This suggests that pre-existing P3HT underlayers can support only a certain amount of PCBM, an amount presumably limited by the fraction of the polymer that lies within amorphous regions. Thus, increasing the polymer regioregularity decreases the available space for fullerene intercalation, so that increased regioregularity leads to poorer device performance. If one tries to compensate for this by increasing the fullerene concentration in SqP devices, large-scale phase separation of the fullerene from the highly crystalline polymer network occurs (Figure 2.7), leading to an increase in the fraction of structural traps and thus trap-assisted recombination, as seen with the increased ideality factor.

Finally, we note that the devices made with different batches of P3HT also have slightly different V_{oc}'s. The trend that V_{oc} is lower in both SqP and BC devices with HR P3HT correlates with the concomitant red-shift of the absorption spectrum, described further below. This red-shift results from the fact that the highest occupied molecular orbital (HOMO) increases slightly in energy with increasing regioregularity of P3HT because of enhanced delocalization.[78,79] It is also

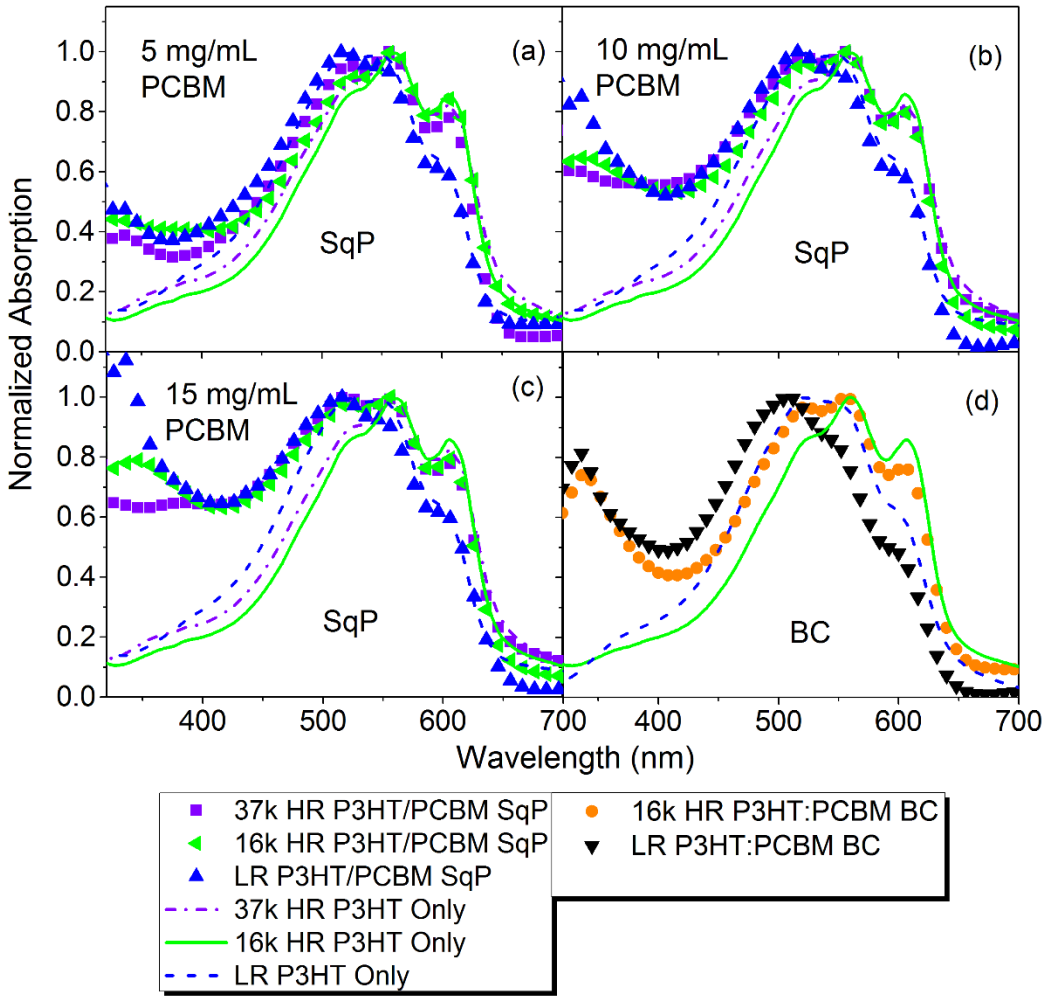

Figure 2.4. UV-visible absorption spectra of thin films made from different batches of pure P3HT (solid dashed and dash-dotted lines) and SqP P3HT/PCBM films (symbols) made from the same P3HTs with **(a)** 5 mg/mL PCBM, **(b)** 10 mg/mL PCBM and **(c)** 15 mg/mL PCBM spun on top; and **(d)** BC P3HT:PCBM films made from the same P3HTs. The pure P3HT films were 110 nm thick in all cases. All films were thermally annealed at 150 °C for 20 minutes and the spectra in both panels are normalized to the highest polymer optical density (i.e. highest OD red of 490 nm) for ease of comparison.

known that increasing the amount of trap-assisted recombination can result in decreased V_{oc}, particularly for devices with carrier mobilities similar to those used here.[80] Since we indeed find that HR P3HT shows more trap-assisted recombination in the SqP devices but less in BC devices, this can help us explain the fact that the V_{oc} decrease observed in BC devices (0.06 V) is smaller than that seen in SqP devices (>0.1 V): the recombination effect goes in the same direction as the HOMO level effect in determining V_{oc} for the SqP devices while the two effects partially compensate in BC devices.

2.2.2 Understanding How P3HT Crystallinity Affects the BHJ Architecture for SqP and BC OPVs

Now that we have shown that polymer regioregularity causes opposite effects in SqP and BC photovoltaic device performance, we turn in this section to study how regioregularity affects the active layer morphology in both SqP and BC films. To this end, we perform thin-film absorption, fluorescence quenching, and grazing incidence wide-angle X-ray scattering (GIWAXS) to examine differences in the active layer morphologies formed via SqP and BC.

2.2.2.1 UV-Vis and PL of SqP and BC Active Layers with Different P3HT Regioregularities: Figure 2.4 shows the UV-Visible absorption spectra of pure P3HT films from each of the different polymer batches as well as spectra for all of the SqP and BC active layers discussed above. The spectra of the pure LR P3HT (dashed curve) is shifted to the blue by about 13 nm compared to the HR P3HT (solid and dash-dotted curve), and the relative intensity of the vibronic peaks is also different. Both Spano[81,82] and others[83–85] have shown that the ratio of the intensity of the 0-0 peak ($A_{0\text{-}0}$) to the 0-1 peak ($A_{0\text{-}1}$) is directly related to the intermolecular

coupling and thus the crystallinity of P3HT. For our polymer batches, we observe higher $A_{0\text{-}0}/A_{0\text{-}1}$ ratios for the 37k and 16k HR P3HT than for the LR P3HT, indicating higher crystallinity in the HR P3HT films. The slight decrease of $A_{0\text{-}0}/A_{0\text{-}1}$ for the 37k HR P3HT sample compared to the 16k sample indicates the crystallinity of the polymers is slightly affected by their molecular weights. Despite this, the data suggest the polymer regioregularity is the most important factor in determining the film crystallinity.

The symbols in Figures 4(a)-(c) show the absorption spectra of the same P3HT films after sequential deposition of a PCBM overlayer and subsequent thermal annealing at 150 °C for 20 minutes. We find that for all three P3HT batches, the SqP film absorption is nearly identical to that of the pure polymer, indicating that the fullerene incorporated into the film through sequential processing induces little disruption to the crystalline polymer domains.

The band seen near 340 nm in the BHJ films in Figure 2.4 arises primarily from the absorption of PCBM, although there is some residual absorption of P3HT at this wavelength. Since the pure P3HT absorption at 340 nm is nearly identical for all three polymer batches, we can use the 340-nm peak intensity to roughly evaluate the PCBM content in each of the SqP films (but see Ref. 42). For SqP films with the PCBM overlayer cast from a 5 mg/mL solution, the fullerene content of the films is quite similar, suggesting that any of the underlayer films can accommodate the relatively modest amount of fullerene provided by the dilute solution. For SqP active layers produced using more concentrated PCBM solutions, however, the HR P3HT samples show much weaker fullerene absorption than LR P3HT sample. This confirms that higher crystallinity polymers are less able to incorporate fullerene during SqP; if there are fewer amorphous regions into which PCBM can penetrate into the bulk of the film, more of the fullerene is likely to simply spin off during deposition of the over-layer. In Figure 2.7 we show optical micrographs of these

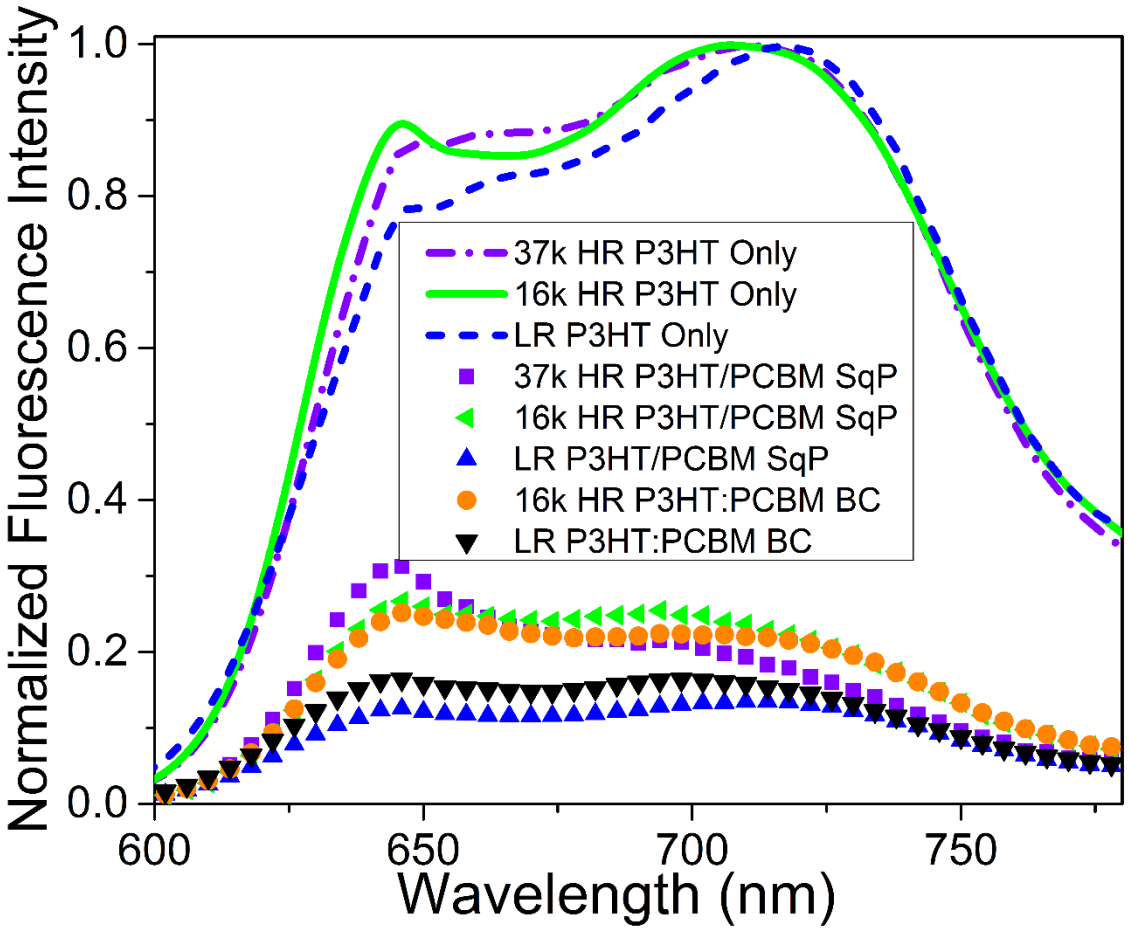

Figure 2.5. Photoluminescence (PL) spectra of thin films made from: pure P3HTs (same as Figure 2.4a), SqP P3HT/PCBM films (same as Figure 2.4a) and P3HT:PCBM BC films (same as Figure 2.4d). The measured PL intensities were divided by each film's optical density at 530 nm, the excitation wavelength used in this experiment. and then normalized to the highest PL value (that of the pure 16k HR P3HT film) to best illustrate the extent of PL quenching in the different samples.

films whose absorption spectra are shown Figure 2.4; the films made from HR P3HT batches with high PCBM concentrations spun on top show fullerene aggregates/crystals at the μm-length scale, consistent with the idea that sequentially-processed high crystallinity films cannot accommodate significant fullerene loadings.

Unlike the sequentially-processed films, whose absorption spectra do not change upon the addition of fullerene, the vibronic features in the absorption spectra of P3HT:PCBM BC films (Figure 2.4(d)) are strongly altered by the presence of fullerene. For the LR P3HT flim, the vibronic peaks have a dramatcially decreased intensity relative to the pristine P3HT, even after 20 minutes of thermal annealing at 150 °C. This suggests for LR P3HT, the presence of fullerene hinders the crystallization of P3HT during both the spin-coating and thermal annealing processes. In the case of the HR P3HT:PCBM BC films, although the A_{0-1}/A_{0-0} ratio does not remain constant as observed in the seqentially processed films, it does not decrease as strongly as in the LR P3HT:PCBM BC-BHJ films. Thus, this data suggests that even in BC films, the inherent crystallinity of HR P3HT can be better retained than that of LR P3HT.

In addition to UV-Visible spectroscopy, we also performed a series of photoluminescence (PL) quenching experiments of SqP and BC P3HT:PCBM films made from the different polymer batches, the results of which are shown in Figure 2.5. The PL spectra of the pure P3HT polymer films are similar, with only slight differences in the relative height of the 0-0 peak near 650 nm that reflect the changes in intermolecular coupling with the degree of polymer crystallinity,[81] in agreement with the UV-Visible data in Figure 2.4. Overall, the trends observed in BC and SqP films are very similar. HR samples show less PL quenching in all cases compared to LR samples, a result that indicates that the equilibrium (i.e. post-annealing) extent of polymer-fullerene mixing at the molecular scales is driven primarily by polymer regioregularity and not by the processing

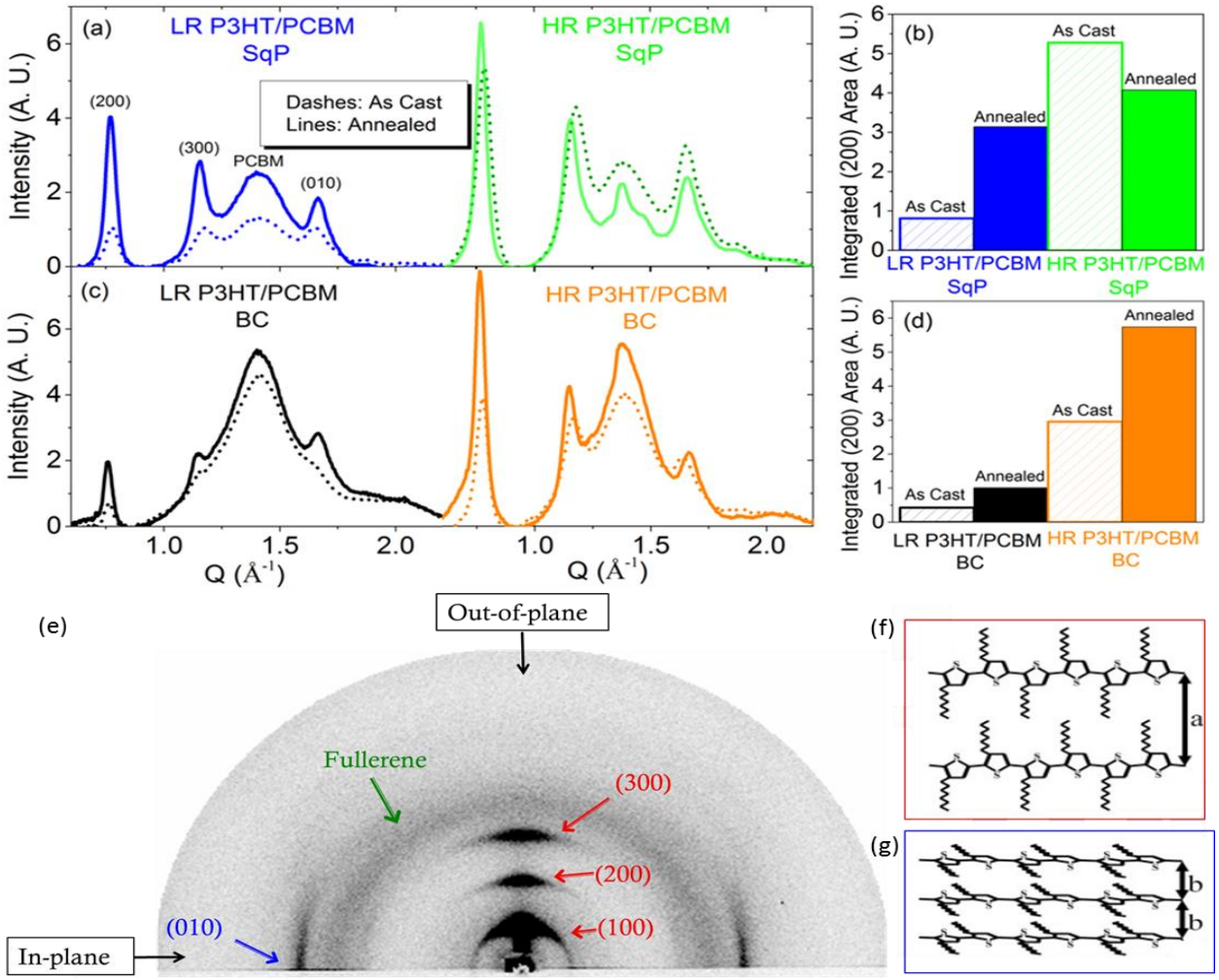

Figure 2.6. (a) Radially-integrated 2-D GIWAXS intensities for P3HT/PCBM sequentially processed active layers cast on a silicon substrate for LR and HR P3HT. In each case, the P3HT film thickness was 110 nm, and the PCBM over-layer was spun from a 5mg/mL solution. (b) Integrated peak area for the (200) polymer peak for SqP. (c) Integrated GIWAXS intensity for P3HT/PCBM BC films. (d) Integrated peak area for the (200) polymer peak for BC-BHJ films. Dashed lines indicate as-cast films and solid lines are after 20 min of thermal annealing at 150 °C for both (a) and (c). (e) 2-D GIWAXS of thermally annealed LR P3HT/PCBM SqP active layer and corresponding P3HT packing structures (f) and (g). The (100), (200), and (300) peaks correspond to the distance *a* and the (010) peak corresponds to the distance *b*.

Table 2.3. Summary of Parameters from GIWAXS

	(200) Peak Position ($Å^{-1}$)	(200) Peak Area (A. U.)	(200) FWHM[a] (A. U.)	(010) Peak Position ($Å^{-1}$)	(010) Peak Area (A. U.)	(010) FWHM[a] ($Å^{-1}$)
LR P3HT/PCBM SqP As Cast	0.778	8.1	6.6	1.657	10.9	10.7
LR P3HT/PCBM SqP Annealed	0.770	31.4	5.6	1.664	13.5	7.7
16k HR P3HT/PCBM SqP As Cast	0.787	52.8	6.9	1.655	35.4	10.0
16k HR P3HT/PCBM SqP Annealed	0.770	40.8	5.1	1.662	23.3	8.9
LR P3HT:PCBM BC As Cast	0.766	4.3	4.6	1.627	15.7	14.9
LR P3HT:PCBM BC Annealed	0.759	10.1	3.9	1.663	29.8	12.0
16k HR P3HT:PCBM BC As Cast	0.776	29.6	5.5	1.634	20.1	11.6
16k HR P3HT:PCBM BC Annealed	0.761	57.4	5.1	1.663	15.0	8.1

[a] *The full width at half maximum (FWHM) is inversely proportional to the coherence length, which is an estimate of the length over which the ordered crystalline packing is maintained.*

method. This result is particularly interesting in light of the facts that HR material produces the best BC devices while LR material gives SqP devices with the highest efficiency. The results thus emphasize how the same level of atomic-scale mixing must be accompanied by very different nanoscale architecture using the two different processing methods. For a separation-based process like BC, strong separation appears to drive the formation of an optimized nanoscale architecture. By contrast, for a mixing-based process like SqP, a strong driving force for mixing is needed to create that same ideal architecture.

2.2.2.2 Morphology of SqP and BC Films with Different Batches of P3HT Measured by X-Ray Diffraction: To directly investigate how changes in the P3HT regioregularity affect the polymer and fullerene crystallinity for the different processing routes used to make BHJs, we performed a series of two-dimensional (2-D) grazing incidence wide-angle X-ray scattering (GIWAXS) measurements. For these experiments, we used all the same processing methods described in the experimental section, but instead spun the active layer materials onto silicon substrates. Our GIWAXS measurements were performed at the Stanford Synchrotron Radiation Light Source on beamline 11-3 using a wavelength of 0.9742 Å. We should note that the absolute diffraction intensities cannot be compared between SqP and BC data sets because of different beam intensities during separate experimental runs; the relative intensities for a single processing method, however, can be meaningfully compared within each set. Below, we show only radially-integrated scattering data; the full 2-D GIWAXS diffraction pattern of LR P3HT/PCBM SqP is shown in Figure 2.6(e). The results from our GIWAXS measurement are summarized in Figure 2.6 and Table 2.3.

2.2.2.2.1 Polymer Diffraction in SqP Samples: We begin our discussion by examining the P3HT (200) peaks, located between 0.77 – 0.79 $Å^{-1}$, which arise from P3HT lamellar interchain stacking. The (200) peak is mostly distributed in the out-of-plane direction due to the dominant "edge-on" orientation of the P3HT chains relative to the substrate (see SI). For the as-cast SqP films (dashed curves), the integrated (200) peak area of the 16k HR P3HT is more than six times higher than that of the LR P3HT. The peak center of the HR P3HT is also positioned at higher Q than that of LR P3HT, which indicates more compact lamellar stacking for the HR P3HT. We note that in polymeric systems, the broadening of x-ray scattering peaks results from disorder in the polymer domains, rather than from the finite size of crystallites as seen in crystalline materials.[16,86,87] Thus, the FWHM or coherence lengths reported here are those derived from the Scherrer equation, even though the size of the crystalline polymer domains are likely smaller. In Table 2.3, the two P3HT batches show similar FWHM for the (200) peaks. From this data, we conclude that a larger fraction of the as-cast HR P3HT-based SqP samples is crystalline, but the crystallites in both films have similar coherence lengths. The HR samples also show closer packing than the LR P3HT-based samples, a fact that likely arises from increased ordering of the hexyl tails in the HR films.

The literature suggests that thermal annealing of SqP films serves the dual roles of facilitating fullerene diffusion into the polymer underlayer and helping to further crystalize amorphous polymer domains.[41,88] Indeed, the solid curves in Figure 2.6(a) show that for both batches of P3HT, annealing causes the (200) peaks to become sharper, indicating the formation of more ordered P3HT domains with larger structural coherence lengths. The change in the intensity of the (200) peak area upon thermal annealing, however, is quite different for the different SqP P3HT batches. For the LR P3HT, annealing increases the peak area by over a factor of three, a

result similar to previous studies on BC devices. Surprisingly, the peak area for the HR P3HT actually decreases upon thermal annealing, indicating that annealing this particular polymer/fullerene blend makes the film *less* crystalline. Further investigation reveals that unlike the LR P3HT, where annealing causes essentially no shift of the (200) peak, the HR P3HT (200) peak center also shifts slightly towards lower Q, indicating the d-spacing between the lamellar planes becomes larger after annealing. This likely results from small amount of PCBM diffusing into the P3HT crystallites.

We next turn to investigate the trends of the (010) peak, which corresponds to the polymer π-π stacking direction and is therefore important for charge delocalization and transport. We find that the same general trends with polymer regioregularity and thermal annealing observed for the (200) peak also hold in the (010) direction for our SqP films. For the LR P3HT, however, the increase in (010) peak area upon annealing is less dramatic than that observed for the (200) peak, but the decrease in (010) peak width upon annealing is greater. These data thus indicate that in the (010) direction, thermal annealing predominantly affects on the crystalline coherence length, likely from improvements in π-π stacking upon annealing. For the HR SqP P3HT samples, we saw that the diffraction peaks decrease in intensity upon thermal annealing, and that the decrease of the (010) peak area is slightly greater than the decrease seen in the (200) direction. Overall, the change in both peak with and peak area are qualitatively similar for the (010) and (200) peaks, suggesting that for SqP samples made with HR P3HT, diffusion of PCBM into the film reduces the extent of crystallinity in a fairly isotropic manner, likely by creating amorphous polymer regions where the fullerene can reside. This is in contrast to the LR samples, where annealing of paracrystalline disorder and fullerene diffusion are coupled in a more complex manner.

Clearly, the most significant difference between the two batches of SqP P3HT films is the

total amount of amorphous polymer. We believe that a certain amorphous fraction is necessary for the PCBM to penetrate into sequentially processed films. Even though the HR P3HT starts out highly crystalline with few amorphous regions, the thermally induced mixing that drives PCBM into the polymer underlayer actually disrupts the P3HT network by creating additional amorphous regions upon incorporation. This produces the surprising result of a polymer/fullerene sample that becomes less crystalline upon annealing.

2.2.2.2.2 Polymer Diffraction in BC Samples: In as-cast BC films, the BHJ is formed with the presence of both the polymer and the fullerene, leading to a different morphology than the case of SqP. Based on shifts in diffraction peaks, we find that there is more PCBM intercalation into the BC P3HT network in both the (200) and (010) directions for as-cast BC films relative to SqP films. After thermal annealing, a large amount of the PCBM in BC films is pushed out of the π-π interlayers, as evidenced by a sizable shift towards high Q for the (010) π-stacking peak. This (010) shift upon annealing does not occur with the SqP films. But perhaps more importantly, thermal annealing causes the crystallinity of both the HR and LR P3HT batches to increase when the film is prepared via BC. This provides one reason why the BC devices made from HR P3HT show superior performance compared to those made via SqP.

Another factor that could contribute to the change in device performance with regioregularity is the shape of the polymer crystallites. The widths of the (200) and (010) peaks indicate that the length of the HR P3HT crystallites are shorter than those of the LR P3HT in the (200) direction but longer in the (010) direction. Since the charge carrier transport in the π-π direction is important to the mobility of holes in OPV devices,[86] one might expect hole extraction in HR P3HT active layers to be more efficient than that in LR P3HT samples. Since the hole

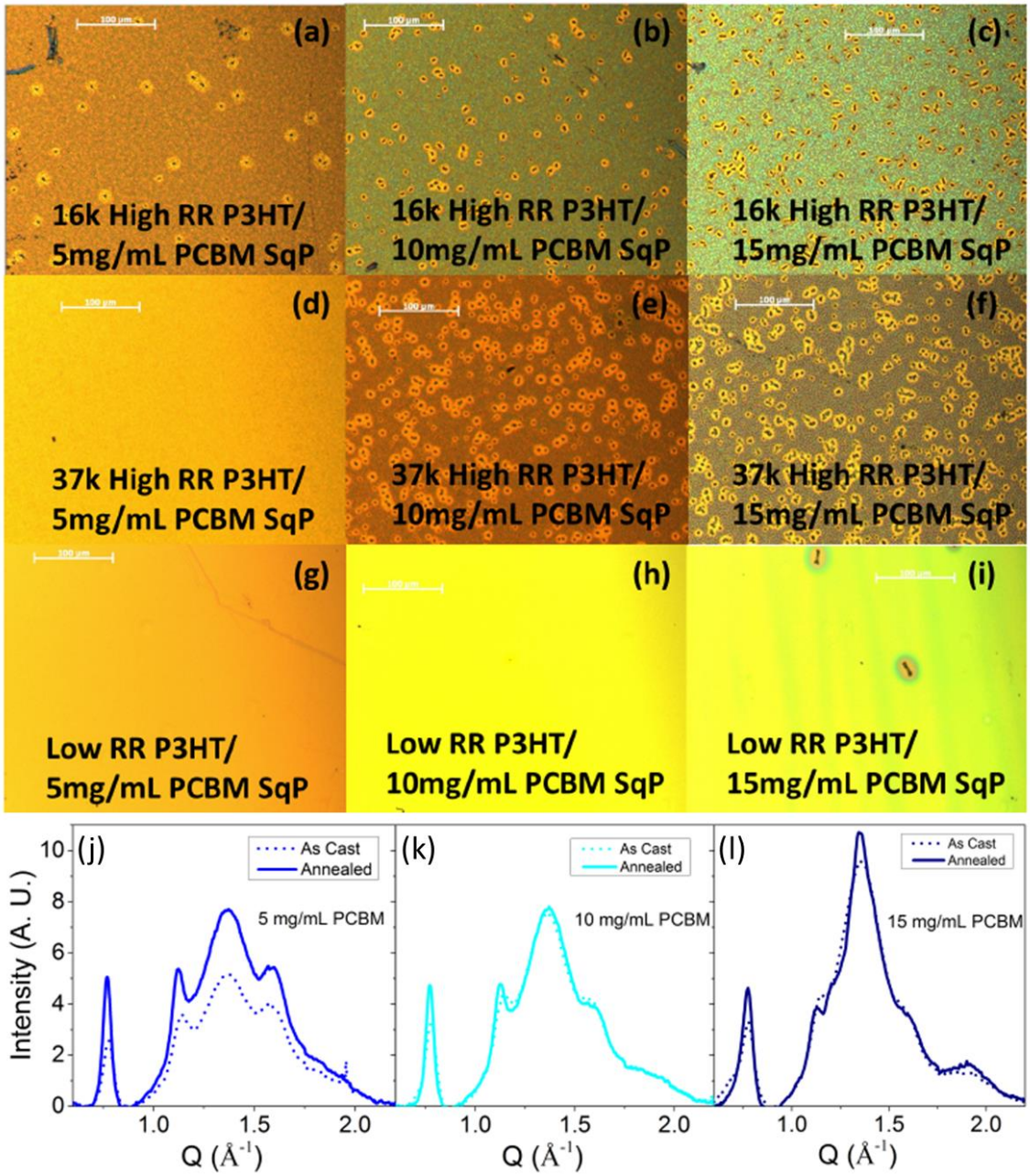

Figure 2.7. (a-i) Optical miscroscopy images of thermally annealed films with three batches of P3HTs and three different PCBM concentrations spun on top of each batch of them. The scale bar is 100 µm. (j-l) Integrated GIWAXS intensity for LR P3HT/PCBM SqP films with (j) 5 mg/mL, (k) 10 mg/mL and (l) 15 mg/mL PCBM spun on top of the P3HT underlayers. Dashed lines indicate as-cast films and solid lines are for films annealed at 150 °C for 20 min.

mobility in P3HT:PCBM blend films is typically lower than the electron mobility,[89] the HR P3HT provides a better mobility-matched active layer and therefore a device with higher fill factor[90] than the LR P3HT BC device, as seen in Figure 2.1.

2.2.2.2.3 Fullerene Diffraction in SqP and BC Samples: In addition to the changes in the crystallinity of the different batches of P3HT, Figure 2.6 also shows that thermal annealing leads to changes in the crystallinity of the PCBM. For example, the PCBM diffraction (at $q \sim 1.4$ Å^{-1}) in the LR P3HT SqP film shows a significant increase in intensity upon thermal annealing, but the peak remains broad. This is consistent with the formation of many small PCBM crystallites upon thermally annealing SqP LR P3HT films. In contrast, thermal annealing dramatically sharpens the PCBM peaks in the SqP films made with HR P3HT. This indicates that in highly crystalline P3HT, there are too few amorphous regions in which the PCBM can mix with the polymer, so that annealing forces the fullerenes to crystallize into a fewer, but significantly larger domains that are not consistent with an ideal BHJ architecture. These large domains may be accompanied by isolated fullerenes at grain boundaries, but those isolate fullerenes do not diffract and do not create effective conductive paths for photogenerated electrons. This hypothesis is supported by optical images, shown in the Figure 2.7, which reveal that after thermal annealing, there is optically-visible phase separation of the PCBM in the HR P3HT film.

All of these results make sense in the context of two ideas: first, that PCBM is miscible and mobile only in the amorphous regions of P3HT films,[40,42,89,93–96] and second, that P3HT only fully crystallizes in the absence of PCBM. The LR P3HT clearly possesses more amorphous regions as-cast, so in SqP films, there is ample opportunity for thermal annealing to cause PCBM to diffuse into the polymer underlayer and form semicrystalline aggregates, as well as for some of

the previously amorphous P3HT regions to crystallize. In highly crystalline as-cast polymers, on the other hand, there are almost no suitable amorphous spaces available for PCBM incorporation in SqP devices, so the polymer must partially disorder to make room for fullerene incorporation. Even with this disordering, the majority of the fullerene is still forced to aggregate into large, highly crystalline domains because it cannot mix into the already-crystalline regions of the polymer. In the case of BC films, the high propensity of the polymer to crystallize is important to help drive the phase separation of the polymer and the fullerene. In low regioregularity polymers, the P3HT cannot phase separate as easily, so an ideal interpenetrating BHJ network cannot be formed.

2.3 Conclusions

In summary, we have found that the effects of changing polymer regioregularity and thus crystallinity on active layer morphology and the photovoltaic device performance differ dramatically based on how the active layer is formed. PCBM disperses only into the amorphous regions after sequential processing onto P3HT films, so that controlling the amount of the amorphous phase has a direct impact on the subsequent device performance. SqP of P3HT with too high a polymer regioregularity results in highly crystalline films into which fullerenes cannot easily incorporate even after thermal annealing, leading to unfavorably large scale polymer/fullerene phase separation. SqP films made from P3HT with lower regioregularity possess more amorphous regions, which leads to a better polymer/fullerene network and thus more efficient solar cells. The effect of polymer crystallinity is reversed, however, if the active layer is fabricated through the traditional blend-cast method. The presence of PCBM in the mixed solution prevents P3HT from forming a highly crystalline network. Therefore, more highly regioregular

P3HT is favorable because of its stronger propensity to crystallize.

This work has revealed a fundamental mechanism difference for the formation of BHJ active layer morphology between SqP and BC. All of the structural and device performance data show that SqP and BC do not produce films with the same polymer/fullerene morphology, and that different materials parameters affect the film morphology in different ways for the two processing methods. This suggests that the two processing techniques are complementary, and that the appropriate choice of which processing method to use to achieve high efficiency solar cells depends on the details of the particular batch of polymer and fullerene being used.

2.4 Experimental

The key feature underpinning this work is the successful synthesis of P3HT with well-defined regioregularity and extremely narrow PDI.[95] In what is described below, we compare the behavior of three different batches of P3HT: commercial P3HT purchased from Rieke Metal Inc. (BASF Sepiolid^{TM} P100), which we denote as LR P3HT, and two in-house batches synthesized with 98% regioregularity and average molecular weights of about 16 kDa (PDI = 1.18) and 37 kDa (PDI = 1.19), denoted as HR P3HTs, where LR and HR stand for low regioregularity and high regioregularity, respectively. Each in-house batch was purified by successive Soxhlet extraction with MeOH, hexanes, and chloroform, which has been shown to reduce the level of impurities in the polymer to undetectable levels. The full characteristics of the three batches we focus on here are summarized in Table 2.1.

2.4.1 Sample Preparation: We fabricated SqP P3HT/PCBM solar cells by starting with prepatterned tin-doped indium oxide (ITO; TFD Inc.) coated substrates and cleaning them by

successive sonication in detergent solution, deionized water, acetone and isopropanol for 8 min each. After drying with blowing argon gas, we treated the ITO substrates with an air plasma (200mTorr, 15 min). A thin layer of PEDOT:PSS was then spin-coated onto the clean substrates in air at 5000 rpm for 60 s, and then the PEDOT:PSS-covered substrate was then baked at 140 °C for 20 min in a nitrogen atmosphere. P3HT solutions were prepared by dissolving 20 mg/mL of each batch of P3HT in *o*-dichlorobenzene (ODCB). The solutions were stirred at 60°C for at least two hours prior to being cooled to room temperature and spun onto PEDOT:PSS-covered substrates at spin speeds ranging from 1000 to 1200 rpm for 60 s for LR P3HT and 16k HR P3HT, and from 1400 to 1500 rpm for 60 s for 37k HR P3HT. After spin-coatingm the P3HT films were dried under active vacuum for at least 20 min prior to subsequent use. PCBM solutions were prepared by dissolving PCBM powder (Nano-C) in dichloromethane (DCM) at concentrations of 5 mg/mL, 10 mg/mL or 15 mg/mL and stirring at room temperature for at least 30 min. These solutions were spin-cast on top of the P3HT layer from the previous step at 4000 rpm for 10 s. Film thicknesses were measured after the deposition of each successive layer with a Dektak 150 Stylus Surface Profiler. The P3HT film thickness was kept to ~110 nm for each batch by adjusting the pin speed to account for the different solution viscosities. For thermally annealed samples, the films were heated to 150 °C for 20 min on a hot plate under argon atmosphere. Cathode deposition consisted of ~40 nm of Ca evaporated at rates below 1 Å/s followed by 70 nm of Al at ~2 Å/s. The resulting device active areas were 6.51 mm^2.

For BC bulk heterojunction (BHJ) devices, except for the active layer fabrication procedure, all the steps were identical to those for SqP devices. All of our blend solutions had polymer concentrations of 20 mg/mL in ODCB. Depending on the experiment, both 1:0.9 and 1:1.3 polymer:fullerene weight ratios were used. The solutions were stirred at 60 °C overnight on

a hot plate in a nitrogen atmosphere. The active layers for our BC devices were prepared by spin-coating the blend solutions in the speed range 1000 to 1200 rpm for 60 s for 16k HR P3HT:PCBM and LR P3HT:PCBM blends, ans at 1200 rpm for 60 s for 50k HR P3HT:PCBM blend to account for the higher viscosity of this solution. The resulting films had similar thickness of about 175 nm.

We note that no slow drying of solvent or solvent vapor treatments were performed on either the sequentially-processed or BC devices, even though such treatments are necessary to optimize the PCE for the P3HT/PCBM materials combination. Instead, we chose our spin-coating parameters to provide us with completely dry films after spinning. We made this choice to eliminate drying kinetics, which can cause marked variations in the performance of BC devices.[42,96] In this way, we were able to maintain our focus on how polymer properties such as regioregularity and molecular weight control variations in morphology and device performance.

2.4.2 Sample Characterization: The *J-V* curves shown were measured in an argon atmosphere using a Keithley 2400 source meter. A xenon arc lamp and an AM-1.5 filter were used as the excitation source, with the intensity calibrated to match 1 sun.

The films for all other measurements (GIWAXS, UV-Vis and PL quenching, as in Figures 2.4-2.6) were prepared using the identical procedures to those described above but without the deposition of a top electrode. The UV-Visible absorption spectra shown in Figure 2.4 were collected using a Lamba 25 UV-Vis Spectrophotometer. The steady-state PL measurements shown in Figure 2.5 were performed with a FluoroMax-3 (J-Y Horiba) fluorimeter. The PL spectra for all samples were collected in air at 22.5° with respect to the excitation beam with the sample positioned at 45° with respect to the excitation axis. The slit widths and integration times were kept constant during all of our measurements. All of the PL spectra displayed were normalized by

the optical density at our chosen excitation wavelength of 530 nm. The spectra were further corrected for the known wavelength variation of the detector and the monochromator responses. To better emphasize the PL quenching of the samples, the spectra of the pure P3HTs in Figure 2.5 were normalized to their highest PL values.

2-D grazing incidence wide angle X-ray scattering (GIWAXS) measurements were performed at the Stanford Synchrotron Radiation Lightsource (SSRL) on beamline 11-3 using a wavelength of 0.9742 Å. Samples were prepared using all of the same processing methods described above with the difference being the active layer was spun onto silicon substrates (with a native ~2 nm thick oxide layer). The diffraction patterns were collected on a 2-D image plate with the detector 400 mm from the sample center. The beam spot was approximately 150 μm wide and a helium chamber was used to improve signal-to-noise. The WxDiff software package was used to radially integrate scattering data. The integrated diffraction pattern for each sample was also fit to a series of Gaussian distributions using Igor.

2.5 References

(1) Deibel, C.; Dyakonov, V. Polymer–Fullerene Bulk Heterojunction Solar Cells. *Rep. Prog. Phys* **2010**, *73*, 096401.

(2) Helgesen, M.; Søndergaard, R.; Krebs, F. C. Advanced Materials and Processes for Polymer Solar Cell Devices. *J. Mater. Chem.* **2010**, *20*, 36.

(3) He, Z.; Zhong, C.; Su, S.; Xu, M.; Wu, H.; Cao, Y. Enhanced Power-Conversion Efficiency in Polymer Solar Cells Using an Inverted Device Structure. *Nat. Photonics* **2012**, *6*, 591–595.

(4) Li, G.; Zhu, R.; Yang, Y. Polymer Solar Cells. *Nat. Photonics* **2012**, *6*, 153–161.

(5) You, J.; Chen, C.-C.; Hong, Z.; Yoshimura, K.; Ohya, K.; Xu, R.; Ye, S.; Gao, J.; Li, G.; Yang, Y. 10.2% Power Conversion Efficiency Polymer Tandem Solar Cells Consisting of Two Identical Sub-Cells. *Adv. Mater.* **2013**, *25*, 3973–3978.

(6) You, J.; Dou, L.; Yoshimura, K.; Kato, T.; Ohya, K.; Moriarty, T.; Emery, K.; Chen, C.-C.; Gao, J.; Li, G.; et al. A Polymer Tandem Solar Cell with 10.6% Power Conversion Efficiency. *Nat. Commun.* **2013**, *4*, 1446.

(7) Yu, G.; Gao, J.; Hummelen, J. C.; Wudl, F.; Heeger, A. J. Polymer Photovoltaic Cells: Enhanced Efficiencies via a Network of Internal Donor-Acceptor Heterojunctions. *Science (80-.).* **1995**, *270*, 1789–1791.

(8) Kim, Y.; Choulis, S. A.; Nelson, J.; Bradley, D. D. C.; Cook, S.; Durrant, J. R. Device Annealing Effect in Organic Solar Cells with Blends of Regioregular poly(3-Hexylthiophene) and Soluble Fullerene. *Appl. Phys. Lett.* **2005**, *86*, 63502.

(9) Ayzner, A. L.; Wanger, D. D.; Tassone, C. J.; Tolbert, S. H.; Schwartz, B. J. Room to Improve Conjugated Polymer-Based Solar Cells: Understanding How Thermal Annealing Affects the Fullerene Component of a Bulk Heterojunction Photovoltaic Device. *Journal of Physical Chemistry C* **2008**, *112*, 18711–18716.

(10) Collins, B. A.; Gann, E.; Guignard, L.; He, X.; McNeill, C. R.; Ade, H. Molecular Miscibility of Polymer−Fullerene Blends. *J. Phys. Chem. Lett.* **2010**, *1*, 3160–3166.

(11) Chen, D.; Nakahara, A.; Wei, D.; Nordlund, D.; Russell, T. P. P3HT/PCBM Bulk Heterojunction Organic Photovoltaics: Correlating Efficiency and Morphology. *Nano Lett.* **2011**, *11*, 561–567.

(12) Parnell, A. J.; Cadby, A. J.; Mykhaylyk, O. O.; Dunbar, A. D. F.; Hopkinson, P. E.; Donald, A. M.; Jones, R. A. L. Nanoscale Phase Separation of P3HT PCBM Thick Films As Measured by Small-Angle X-Ray Scattering. *Macromolecules* **2011**, *44*, 6503–6508.

(13) Bartelt, J. A.; Beiley, Z. M.; Hoke, E. T.; Mateker, W. R.; Douglas, J. D.; Collins, B. A.; Tumbleston, J. R.; Graham, K. R.; Amassian, A.; Ade, H.; et al. The Importance of Fullerene Percolation in the Mixed Regions of Polymer-Fullerene Bulk Heterojunction Solar Cells. *Adv. Energy Mater.* **2013**, *3*, 364–374.

(14) Shoaee, S.; Subramaniyan, S.; Xin, H.; Keiderling, C.; Tuladhar, P. S.; Jamieson, F.; Jenekhe, S. A.; Durrant, J. R. Charge Photogeneration for a Series of Thiazolo-Thiazole Donor Polymers Blended with the Fullerene Electron Acceptors PCBM and ICBA. *Adv. Funct. Mater.* **2013**, *23*, 3286–3298.

(15) Li, G.; Shrotriya, V.; Huang, J.; Yao, Y.; Moriarty, T.; Emery, K.; Yang, Y. High-Efficiency Solution Processable Polymer Photovoltaic Cells by Self-Organization of Polymer Blends. *Nat Mater* **2005**, *4*, 864–868.

(16) Verploegen, E.; Mondal, R.; Bettinger, C. J.; Sok, S.; Toney, M. F.; Bao, Z. Effects of Thermal Annealing Upon the Morphology of Polymer-Fullerene Blends. *Adv. Funct. Mater.* **2010**, *20*, 3519–3529.

(17) Westacott, P.; Tumbleston, J. R.; Shoaee, S.; Fearn, S.; Bannock, J. H.; Gilchrist, J. B.; Heutz, S.; DeMello, J.; Heeney, M.; Ade, H.; et al. On the Role of Intermixed Phases in Organic Photovoltaic Blends. *Energy Environ. Sci.* **2013**, *6*, 2756–2764.

(18) Gomez, E. D.; Barteau, K. P.; Wang, H.; Toney, M. F.; Loo, Y.-L. Correlating the Scattered Intensities of P3HT and PCBM to the Current Densities of Polymer Solar Cells. *Chem. Commun. (Camb).* **2011**, *47*, 436–438.

(19) Guo, J.; Ohkita, H.; Benten, H.; Ito, S. Charge Generation and Recombination Dynamics in Poly (3-Hexylthiophene)/fullerene Blend Films with Different Regioregularities and Morphologies. *J. Am. Chem. Soc.* **2010**, *132*, 6154–6164.

(20) Cates, N. C.; Gysel, R.; Beiley, Z.; Miller, C. E.; Toney, M. F.; Heeney, M.; McCulloch, I.; McGehee, M. D. Tuning the Properties of Polymer Bulk Heterojunction Solar Cells by Adjusting Fullerene Size to Control Intercalation. *Nano Lett.* **2009**, *9*, 4153–4157.

(21) Watts, B.; Belcher, W. J.; Thomsen, L.; Ade, H.; Dastoor, P. C. A Quantitative Study of PCBM Diffusion during Annealing of P3HT:PCBM Blend Films. *Macromolecules* **2009**, *42*, 8392–8397.

(22) Peet, J.; Soci, C.; Coffin, R. C.; Nguyen, T. Q.; Mikhailovsky, A.; Moses, D.; Bazan, G. C. Method for Increasing the Photoconductive Response in Conjugated Polymer/fullerene Composites. *Appl. Phys. Lett.* **2006**, *89*, 252103–252105.

(23) Peet, J.; Kim, J. Y.; Coates, N. E.; Ma, W. L.; Moses, D.; Heeger, A. J.; Bazan, G. C. Efficiency Enhancement in Low-Bandgap Polymer Solar Cells by Processing with Alkane Dithiols. *Nat. Mater.* **2007**, *6*, 497–500.

(24) Lee, J. K.; Ma, W. L.; Brabec, C. J.; Yuen, J.; Moon, J. S.; Kim, J. Y.; Lee, K.; Bazan, G. C.; Heeger, A. J. Processing Additives for Improved Efficiency from Bulk Heterojunction Solar Cells. *J. Am. Chem. Soc.* **2008**, *130*, 3619–3623.

(25) Chang, L.; Jacobs, I. E.; Augustine, M. P.; Moulé, A. J. Correlating Dilute Solvent Interactions to Morphology and OPV Device Performance. *Org. Electron.* **2013**, *14*, 2431–2443.

(26) Chen, W.; Xu, T.; He, F.; Wang, W.; Wang, C.; Strzalka, J.; Liu, Y.; Wen, J.; Miller, D. J.; Chen, J.; et al. Hierarchical Nanomorphologies Promote Exciton Dissociation in Polymer/fullerene Bulk Heterojunction Solar Cells. *Nano Lett.* **2011**, *11*, 3707–3713.

(27) Ayzner, A. L.; Tassone, C. J.; Tolbert, S. H.; Schwartz, B. J. Reappraising the Need for Bulk Heterojunctions in Polymer− Fullerene Photovoltaics: The Role of Carrier Transport in All-Solution-Processed P3HT/PCBM Bilayer Solar. *Journal of Physical Chemistry C* **2009**, *113*, 20050–20060.

(28) Chen, D.; Liu, F.; Wang, C.; Nakahara, A.; Russell, T. P. Bulk Heterojunction Photovoltaic

Active Layers via Bilayer. *Nano Lett.* **2011**, *11*, 2071–2078.

(29) Gevaerts, V. S.; Koster, L. J. A.; Wienk, M. M.; Janssen, R. A. J. Discriminating between Bilayer and Bulk Heterojunction Polymer:Fullerene Solar Cells Using the External Quantum Efficiency. *ACS Appl. Mater. Interfaces* **2011**, *3*, 3252–3255.

(30) Moon, J. S.; Takacs, C. J.; Sun, Y.; Heeger, A. J. Spontaneous Formation of Bulk Heterojunction Nanostructures: Multiple Routes to Equivalent Morphologies. *Nano Lett.* **2011**, *11*, 1036–1039.

(31) Cho, S.-M.; Bae, J.-H.; Jang, E.; Kim, M.-H.; Lee, C.; Lee, S.-D. Solvent Effect of the Fibrillar Morphology on the Power Conversion Efficiency of a Polymer Photovoltaic Cell in a Diffusive Heterojunction. *Semicond. Sci. Technol.* **2012**, *27*, 125018.

(32) Gadisa, A.; Tumbleston, J. R.; Ko, D.-H.; Aryal, M.; Lopez, R.; Samulski, E. T. The Role of Solvent and Morphology on Miscibility of Methanofullerene and poly(3-Hexylthiophene). *Thin Solid FIlms* **2012**, *520*, 5466–5471.

(33) Thummalakunta, L. N. S. A.; Yong, C. H.; Ananthanarayanan, K.; Luther, J. P3HT Based Solution-Processed Pseudo Bi-Layer Organic Solar Cell with Enhanced Performance. *Org. Electron.* **2012**, *13*, 2008–2016.

(34) Wong, M. K.; Wong, K. Y. Investigation of the Factors Affecting the Power Conversion Efficiency of All-Solution-Processed "bilayer" P3HT:PCBM Solar Cells. *Synth. Met.* **2013**, *170*, 1–6.

(35) Li, H.; Qi, Z.; Wang, J. Layer-by-Layer Processed Polymer Solar Cells with Self-Assembled Electron Buffer Layer. *Appl. Phys. Lett.* **2013**, *102*, 213901.

(36) Yang, B.; Yuan, Y.; Huang, J. Reduced Bimolecular Charge Recombination Loss in Thermally-Annealed Bilayer Heterojunction Photovoltaic Devices with Large External Quantum Efficiency and Fill Factor. *Journal of Physical Chemistry C* **2014**, *118*, 5196–5202.

(37) Lin, Y.; Ma, L.; Li, Y.; Liu, Y.; Zhu, D.; Zhan, X. Small-Molecule Solar Cells with Fill Factors up to 0.75 via a Layer-by-Layer Solution Process. *Adv. Energy Mater.* **2014**, *4*, 1300626.

(38) Nardes, A. M.; Ayzner, A. L.; Hammond, S. R.; Ferguson, A. J.; Schwartz, B. J.; Kopidakis, N. Photoinduced Charge Carrier Generation and Decay in Sequentially Deposited Polymer/Fullerene Layers: Bulk Heterojunction vs Planar Interface. *Journal of Physical Chemisty C* **2012**, *116*, 7293–7305.

(39) Lee, K. H.; Schwenn, P. E.; Smith, A. R. G.; Cavaye, H.; Shaw, P. E.; James, M.; Krueger, K. B.; Gentle, I. R.; Meredith, P.; Burn, P. L. Morphology of All-Solution-Processed "Bilayer" Organic Solar Cells. *Adv. Mater.* **2011**, *23*, 766–770.

(40) Treat, N. D.; Brady, M. A.; Smith, G.; Toney, M. F.; Kramer, E. J.; Hawker, C. J.; Chabinyc, M. L. Interdiffusion of PCBM and P3HT Reveals Miscibility in a Photovoltaically Active Blend. *Adv. Energy Mater.* **2011**, *1*, 82–89.

(41) Lee, K. H.; Zhang, Y.; Burn, P. L.; Gentle, I. R.; James, M.; Nelson, A.; Meredith, P. Correlation of Diffusion and Performance in Sequentially Processed P3HT/PCBM Heterojunction Films by Time-Resolved Neutron Reflectometry. *J. Mater. Chem. C* **2013**, *1*, 2593–2598.

(42) Hawks, S. A.; Aguirre, J. C.; Schelhas, L. T.; Thompson, R. J.; Huber, R. C.; Ferreira, A. S.; Zhang, G.; Herzing, A. A.; Tolbert, S. H.; Schwartz, B. J. Comparing Matched Polymer:Fullerene Solar Cells Made by Solution-Sequential Processing and Traditional Blend Casting: Nanoscale Structure and Device Performance. *Journal of Physical Chemistry C* **2014**, DOI:10.1021/jp504560r.

(43) Dang, M.; Hirsch, L.; Wantz, G. P3HT: PCBM, Best Seller in Polymer Photovoltaic Research. *Adv. Mater.* **2011**, *23*, 3597–3602.

(44) Yang, C.; Heeger, A. Morphology of Composites of Semiconducting Polymers Mixed with C 60. *Synth. Met.* **1996**, *83*, 85–88.

(45) Wang, D. H.; Moon, J. S.; Seifter, J.; Jo, J.; Park, J. H.; Park, O. O.; Heeger, A. J. Sequential Processing: Control of Nanomorphology in Bulk Heterojunction Solar Cells. *Nano Lett.* **2011**, *11*, 3163–3168.

(46) Li, H.; Li, Y.; Wang, J. Optimizing Performance of Layer-by-Layer Processed Polymer Solar Cells. *Appl. Phys. Lett.* **2012**, *101*, 033907.

(47) Li, H.; Wang, J. Layer-by-Layer Processed High-Performance Polymer Solar Cells. *Appl. Phys. Lett.* **2012**, *101*, 263901–263905.

(48) Cheng, P.; Hou, J.; Li, Y.; Zhan, X. Layer-by-Layer Solution-Processed Low-Bandgap Polymer-PC 61 BM Solar Cells with High Efficiency. *Adv. Energy Mater.* **2014**, DOI: 10.1002/aenm.201301349.

(49) Loiudice, A.; Rizzo, A.; Latini, G.; Nobile, C.; de Giorgi, M.; Gigli, G. Graded Vertical Phase Separation of Donor/acceptor Species for Polymer Solar Cells. *Sol. Energy Mater. Sol. Cells* **2012**, *100*, 147–152.

(50) Loiudice, A.; Rizzo, A.; Biasiucci, M.; Gigli, G. Bulk Heterojunction versus Diffused Bilayer: The Role of Device Geometry in Solution P-Doped Polymer-Based Solar Cells. *J. Phys. Chem. Lett.* **2012**, *3*, 1908–1915.

(51) Tao, C.; Aljada, M.; Shaw, P. E.; Lee, K. H.; Cavaye, H.; Balfour, M. N.; Borthwick, R. J.; James, M.; Burn, P. L.; Gentle, I. R.; et al. Controlling Hierarchy in Solution-Processed Polymer Solar Cells Based on Crosslinked P3HT. *Adv. Energy Mater.* **2013**, *3*, 105–112.

(52) Yang, H. Y.; Kang, N. S.; Hong, J.-M.; Song, Y.-W.; Kim, T. W.; Lim, J. A. Efficient Bilayer Heterojunction Polymer Solar Cells with Bumpy Donor–acceptor Interface Formed by Facile Polymer Blend. *Org. Electron.* **2012**, *13*, 2688–2695.

(53) Chen, H.; Hu, S.; Zang, H.; Hu, B.; Dadmun, M. Precise Structural Development and Its Correlation to Function in Conjugated Polymer: Fullerene Thin Films by Controlled Solvent Annealing. *Adv. Funct. Mater.* **2013**, *23*, 1701–1710.

(54) Kim, D. H.; Mei, J.; Ayzner, A. L.; Schmidt, K.; Giri, G.; Appleton, A. L.; Toney, M. F.; Bao, Z. Sequentially Solution-Processed, Nanostructured Polymer Photovoltaics Using Selective Solvents. *Energy Environ. Sci.* **2014**, *7*, 1103–1109.

(55) Ayzner, A. L.; Doan, S. C.; Tremolet de Villers, B.; Schwartz, B. J. Ultrafast Studies of Exciton Migration and Polaron Formation in Sequentially Solution-Processed Conjugated Polymer/Fullerene Quasi-Bilayer Photovoltaics. *J. Phys. Chem. Lett.* **2012**, *3*, 2281–2287.

(56) Rochester, C. W.; Mauger, S. A.; Moule, A. J. Investigating the Morphology of Polymer/Fullerene Layers Coated Using Orthogonal Solvents. *Journal of Physical Chemistry C* **2012**, *116*, 7287–7292.

(57) Jiang, X.; Osterbacka, R.; Korovyanko, O.; An, C. P.; Horovitz, B.; Janssen, R. A. J.; Vardeny, Z. V. Spectroscopic Studies of Photoexcitations in Regioregular and Regiorandom Polythiophene Films. *Adv. Funct. Mater.* **2002**, *12*, 587–597.

(58) Kim, Y.; Cook, S.; Tuladhar, S. M.; Choulis, S. A.; Nelson, J.; Durrant, J. R.; Bradley, D. D. C.; Giles, M.; McCulloch, I.; Ha, C.-S.; et al. A Strong Regioregularity Effect in Self-Organizing Conjugated Polymer Films and High-Efficiency Polythiophene:fullerene Solar Cells. *Nat. Mater.* **2006**, *5*, 197–203.

(59) Mauer, R.; Kastler, M.; Laquai, F. The Impact of Polymer Regioregularity on Charge Transport and Efficiency of P3HT:PCBM Photovoltaic Devices. *Adv. Funct. Mater.* **2010**, *20*, 2085–2092.

(60) Adachi, T.; Brazard, J.; Ono, R. J.; Hanson, B.; Traub, M. C.; Wu, Z.; Li, Z.; Bolinger, J. C.; Ganesan, V.; Bielawski, C. W.; et al. Regioregularity and Single Polythiophene Chain Conformation. *J. Phys. Chem. Lett.* **2011**, *2*, 1400–1404.

(61) Collins, B. A.; Tumbleston, J. R.; Ade, H. Miscibility, Crystallinity, and Phase Development in P3HT/PCBM Solar Cells: Toward an Enlightened Understanding of Device Morphology and Stability. *J. Phys. Chem. Lett.* **2011**, *2*, 3135–3145.

(62) Brown, P. J.; Thomas, D. S.; Köhler, A.; Wilson, J. S.; Kim, J.-S.; Ramsdale, C. M.; Sirringhaus, H.; Friend, R. H. Effect of Interchain Interactions on the Absorption and Emission of poly(3-Hexylthiophene). *Phys. Rev. B* **2003**, *67*, 064203–064218.

(63) Kohn, P.; Rong, Z.; Scherer, K. H.; Sepe, A.; Sommer, M.; Müller-Buschbaum, P.; Friend,

R. H.; Steiner, U.; Hüttner, S. Crystallization-Induced 10-Nm Structure Formation in P3HT/PCBM Blends. *Macromolecules* **2013**, *46*, 4002–4013.

(64) Kline, R. J.; McGehee, M. D.; Kadnikova, E. N.; Liu, J.; Fréchet, J. M. J.; Toney, M. F. Dependence of Regioregular Poly (3-Hexylthiophene) Film Morphology and Field-Effect Mobility on Molecular Weight. *Macromolecules* **2005**, *38*, 3312–3319.

(65) Zhang, R.; Li, B.; Iovu, M. C.; Jeffries-el, M.; Cooper, J.; Jia, S.; Tristram-nagle, S.; Smilgies, D. M.; Lambeth, D. N.; Mccullough, R. D.; et al. Nanostructure Dependence of Field-Effect Mobility in Regioregular poly(3-Hexylthiophene) Thin Film Field Effect Transistors. *J. Am. Chem. Soc.* **2006**, *128*, 3480–3481.

(66) Noriega, R.; Rivnay, J.; Vandewal, K.; Koch, F. P. V; Stingelin, N.; Smith, P.; Toney, M. F.; Salleo, A. A General Relationship between Disorder, Aggregation and Charge Transport in Conjugated Polymers. *Nat. Mater.* **2013**, *12*, 1038–1044.

(67) Pingel, P.; Zen, A.; Abellón, R. D.; Grozema, F. C.; Siebbeles, L. D. A.; Neher, D. Temperature-Resolved Local and Macroscopic Charge Carrier Transport in Thin P3HT Layers. *Adv. Funct. Mater.* **2010**, *20*, 2286–2295.

(68) Brinkmann, M.; Rannou, P. Molecular Weight Dependence of Chain Packing and Semicrystalline Structure in Oriented Films of Regioregular Poly(3-Hexylthiophene) Revealed by High-Resolution Transmission Electron Microscopy. *Macromolecules* **2009**, *42*, 1125–1130.

(69) Kline, R. J.; McGehee, M. D.; Kadnikova, E. N.; Liu, J.; Fréchet, J. M. J. Controlling the Field-Effect Mobility of Regioregular Polythiophene by Changing the Molecular Weight. *Adv. Mater.* **2003**, *15*, 1519–1522.

(70) Müller, C.; Ferenczi, T. a. M.; Campoy-Quiles, M.; Frost, J. M.; Bradley, D. D. C.; Smith, P.; Stingelin-Stutzmann, N.; Nelson, J. Binary Organic Photovoltaic Blends: A Simple Rationale for Optimum Compositions. *Adv. Mater.* **2008**, *20*, 3510–3515.

(71) Baek, W.-H.; Yoon, T.-S.; Lee, H. H.; Kim, Y.-S. Composition-Dependent Phase Separation of P3HT:PCBM Composites for High Performance Organic Solar Cells. *Org. Electron.* **2010**, *11*, 933–937.

(72) Van Bavel, S. S.; Bärenklau, M.; de With, G.; Hoppe, H.; Loos, J. P3HT/PCBM Bulk Heterojunction Solar Cells: Impact of Blend Composition and 3D Morphology on Device Performance. *Adv. Funct. Mater.* **2010**, *20*, 1458–1463.

(73) Kirchartz, T.; Deledalle, F.; Tuladhar, P. S.; Durrant, J. R.; Nelson, J. On the Differences between Dark and Light Ideality Factor in Polymer: Fullerene Solar Cells. *J. Phys. Chem. Lett.* **2013**, *4*, 2371–2376.

(74) Street, R. A.; Krakaris, A.; Cowan, S. R. Recombination Through Different Types of

Localized States in Organic Solar Cells. *Adv. Funct. Mater.* **2012**, *22*, 4608–4619.

(75) Street, R. A.; Schoendorf, M.; Roy, A.; Lee, J. H. Interface State Recombination in Organic Solar Cells. *Phys. Rev. B* **2010**, *81*, 205307.

(76) Kirchartz, T.; Pieters, B. E.; Kirkpatrick, J.; Rau, U.; Nelson, J. Recombination via Tail States in Polythiophene:fullerene Solar Cells. *Phys. Rev. B* **2011**, *83*, 115209.

(77) Foertig, A.; Rauh, J.; Dyakonov, V.; Deibel, C. Shockley Equation Parameters of P3HT:PCBM Solar Cells Determined by Transient Techniques. *Phys. Rev. B* **2012**, *86*, 115302.

(78) Woo, C. H.; Thompson, B. C.; Kim, B. J.; Toney, M. F.; Fréchet, J. M. J. The Influence of poly(3-Hexylthiophene) Regioregularity on Fullerene-Composite Solar Cell Performance. *J. Am. Chem. Soc.* **2008**, *130*, 16324–16329.

(79) Veldman, D.; Meskers, S. C. J.; Janssen, R. A. J. The Energy of Charge-Transfer States in Electron Donor-Acceptor Blends: Insight into the Energy Losses in Organic Solar Cells. *Adv. Funct. Mater.* **2009**, *19*, 1939–1948.

(80) Tress, W.; Leo, K.; Riede, M. Optimum Mobility, Contact Properties, and Open-Circuit Voltage of Organic Solar Cells: A Drift-Diffusion Simulation Study. *Phys. Rev. B* **2012**, *85*, 155201.

(81) Clark, J.; Silva, C.; Friend, R.; Spano, F. Role of Intermolecular Coupling in the Photophysics of Disordered Organic Semiconductors: Aggregate Emission in Regioregular Polythiophene. *Phys. Rev. Lett.* **2007**, *98*, 206406.

(82) Spano, F. C. Modeling Disorder in Polymer Aggregates: The Optical Spectroscopy of Regioregular poly(3-Hexylthiophene) Thin Films. *J. Chem. Phys.* **2005**, *122*, 234701.

(83) Gierschner, J.; Mack, H.-G.; Lüer, L.; Oelkrug, D. Fluorescence and Absorption Spectra of Oligophenylenevinylenes: Vibronic Coupling, Band Shapes, and Solvatochromism. *J. Chem. Phys.* **2002**, *116*, 8596.

(84) Niles, E. T.; Roehling, J. D.; Yamagata, H.; Wise, A. J.; Spano, F. C.; Moule, A. J.; Grey, J. K. J-Aggregate Behavior in Poly-3-Hexylthiophene Nanofibers. *J. Phys. Chem. Lett.* **2012**, *3*, 259–263.

(85) Gao, Y.; Grey, J. K. Resonance Chemical Imaging of Polythiophene/fullerene Photovoltaic Thin Films: Mapping Morphology-Dependent Aggregated and Unaggregated C=C Species. *J. Am. Chem. Soc.* **2009**, *131*, 9654–9662.

(86) O'Connor, B. T.; Reid, O. G.; Zhang, X.; Kline, R. J.; Richter, L. J.; Gundlach, D. J.; DeLongchamp, D. M.; Toney, M. F.; Kopidakis, N.; Rumbles, G. Morphological Origin of Charge Transport Anisotropy in Aligned Polythiophene Thin Films. *Adv. Funct. Mater.*

2014, DOI: 10.1002/adfm.201303351.

(87) Reid, O.; Pensack, R.; Song, Y. Charge Photogeneration in Neat Conjugated Polymers. *Chem. Mater.* **2013**, DOI: 10.1021/cm4027144.

(88) Lee, K. H.; Schwenn, P. E.; Smith, A. R. G.; Cavaye, H.; Shaw, P. E.; James, M.; Krueger, K. B.; Gentle, I. R.; Meredith, P.; Burn, P. L. Morphology of All-Solution-Processed "Bilayer" Organic Solar Cells. *Adv. Mater.* **2011**, *23*, 766–770.

(89) Abbas, M.; Tekin, N. Balanced Charge Carrier Mobilities in Bulk Heterojunction Organic Solar Cells. *Appl. Phys. Lett.* **2012**, *101*, 073302.

(90) Kumar, A.; Liao, H.-H.; Yang, Y. Hole Mobility in Optimized Organic Photovoltaic Blend Films Obtained Using Extraction Current Transients. *Org. Electron.* **2009**, *10*, 1615–1620.

(91) Yin, W.; Dadmun, M. A New Model for the Morphology of P3HT/PCBM Organic Photovoltaics from Small-Angle Neutron Scattering: Rivers and Streams. *ACS Nano* **2011**, 4756–4768.

(92) Chen, H.; Hegde, R.; Browning, J.; Dadmun, M. D. The Miscibility and Depth Profile of PCBM in P3HT: Thermodynamic Information to Improve Organic Photovoltaics. *Phys. Chem. Chem. Phys.* **2012**, *14*, 5635–5641.

(93) Kozub, D. R.; Vakhshouri, K.; Orme, L. M.; Wang, C.; Hexemer, A.; Gomez, E. D. Polymer Crystallization of Partially Miscible Polythiophene/Fullerene Mixtures Controls Morphology. *Macromolecules* **2011**, *44*, 5722–5726.

(94) Chen, W.; Nikiforov, M. P.; Darling, S. B. Morphology Characterization in Organic and Hybrid Solar Cells. *Energy Environ. Sci.* **2012**, *5*, 8045–8074.

(95) Bronstein, H. A.; Luscombe, C. K. Externally Initiated Regioregular P3HT with Controlled Molecular Weight and Narrow Polydispersity. *J. Am. Chem. Soc.* **2009**, *131*, 12894–12895.

(96) Brabec, C. J.; Heeney, M.; McCulloch, I.; Nelson, J. Influence of Blend Microstructure on Bulk Heterojunction Organic Photovoltaic Performance. *Chem. Soc. Rev.* **2011**, *40*, 1185–1199.

CHAPTER 3

Aspects of Polymer Synthesis and Processing that Control OPV Device Performance: Regioregularity, Swelling and Morphology Optimization using Random Poly(3-butylthiophene-co-3-octylthiophene) Polymers

3.1 Introduction

Organic photovoltaics (OPVs) composed of semiconducting polymer donors have been of growing interest since efficiencies of over 10% have been reached.[1,2] Most devices are composed of blended systems with conjugated polymers as the primary photoabsorbers and fullerene derivatives, such as [6,6]-phenyl-C_{60}-butyric acid methyl ester (PCBM), as the electron acceptors. For such systems, the photovoltaic efficiency is highly correlated with the nm-scale morphology of the blended components.[3] Due to low exciton diffusion lengths, the polymer and fullerene must be mixed on a 10–20 nm length scale to enable excitons to be split into free carriers at the donor/acceptor interface.[4] However, the two components also must have separate domains to prevent recombination[5] and to allow the free carriers to travel to their respective electrodes.[6,7] Such an exact morphology, known as a bulk-heterojunction (BHJ),[8] can be difficult to create by traditional blend-casting (BC) methods in which the polymer and fullerene are co-dissolved in solution and then cast into a film on a conductive substrate. Blend-casting relies on spontaneous de-mixing of the two components during the drying process, and often requires a co-solvent or solvent additive.[9–11] Additional processing can also be performed after film formation by blend-casting, including thermal annealing[12–14] and/or exposure to solvent atmosphere[15,16] to further de-mix the two phases. The final blend-cast film morphology is highly sensitive to the processing

conditions and requires an Edisonian, trial-and-error approach to optimize the extent of phase separation.[17]

An alternate approach to blend-casting is sequential processing (SqP), in which a pure polymer film is cast and dried, and then the fullerene layer is deposited on top of the polymer film in a second step.[18–26] In SqP, the fullerenes incorporate into the amorphous regions of the polymer film because the fullerene-casting solvent swells the underlying polymer film,[21,26–32] creating a BHJ morphology that can be similar to that formed through blend-casting. Mixing can be further altered through thermal- or solvent-annealing post-deposition processes.[7,23,25,29,30] The SqP route tends to preserve the initial crystallinity and other structural aspects of the pure polymer film in the final BHJ morphology that is created, enabling fairly precise control over the BHJ architecture.[32-35]

Although SqP is generally a more controllable processing method, the morphology created in both blend-casting and SqP is highly sensitive to the propensity of the polymer to crystallize.[24] Many groups have looked at controlling the crystallinity of the polymer by tuning either the polymer side chains or the polymer molecular weight, both of which can alter the resulting BHJ architecture.[36,37] We have previously shown that for poly(3-hexylthiophene) (P3HT), polymer crystallinity shows opposite effects on the efficiency of devices fabricated by blend-casting and SqP, with increased crystallinity improving the efficiency of blend-cast devices but decreasing the efficiency of sequentially-processed devices.[24]

In this chapter, our initial goal was to further explore the extent to which polymer crystallinity and paracrystallinity control the performance of OPV devices fabricated using different processing methods. To controllably tune the polymer properties, we took advantage of a series of random copolymers, poly(3-butylthiophene-co-3-octylthiophene)s (RBO)s,[38] in which

the percentage of 3-butyl versus 3-octyl side chains could be varied over a large range (Fig. 1a). Our goal was to mimic the well-studied P3HT system, but to add a new means of tuning the average length of the polymer side chains (Fig. 3.1b) and thus the crystallinity and BHJ morphology without changing the system energetics. What we found, however, was that BHJ morphology and device performance were not primarily determined by the polymer side-chain composition, as we had expected, but instead primarily correlated with the regioregularity of each batch of polymer. This regioregularity resulted from the synthetic details of each batch of polymer samples and varied non-monotonically across the range of samples. Overall device performance and regioregularity were oppositely correlated with efficiency when optimizing OPV devices fabricated by SqP and blend-casting. We argue that this extraordinary sensitivity to regioregularity, which has been largely overlooked in the literature, arises because regioregularity is the strongest predictor of polymer swelling, which is an essential component in the formation of the BHJ morphology, particularly with fabrication via SqP.[31] Overall, we find that the steps taken to optimize BHJ formation with one type of processing results in highly non-ideal morphologies for the other, so that both types of processing conditions must be explored to find the globally optimum device architecture for any given set of materials.

3.2 Results and Discussion

We synthesized five RBO_X random co-polymers with butyl side-chain percentages of 20%, 34%, 50%, 61%, and 72% following procedures published previously.[38] The polydispersity index (PDI) and regioregularity, which are both known to affect the polymer crystallinity and structure,[3,43–46] were also measured and are summarized in Figs. 1c and d, respectively. Although we tried to synthesize the polymer samples in as similar a manner as possible, we were not able to

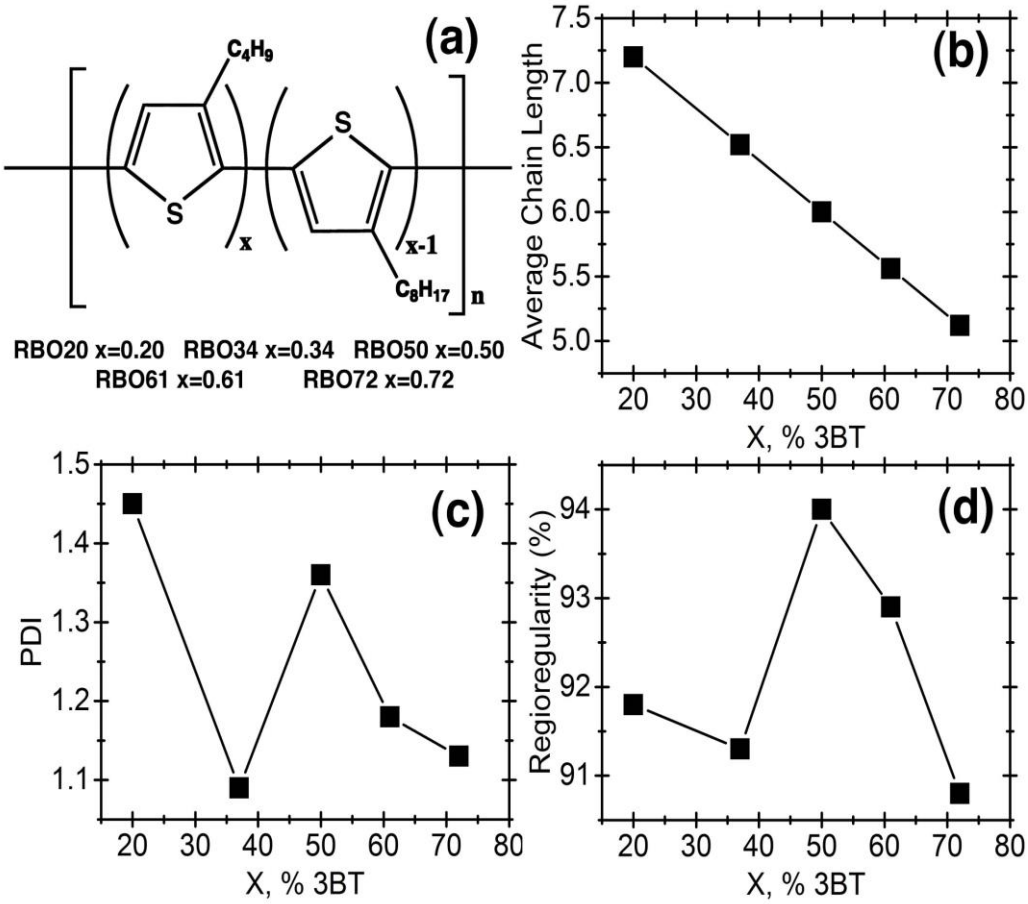

Figure 3.1. Characteristics of RBO_X used in this study: (a) chemical structure, (b) average chain length, (c) polydispersity index (PDI), (d) regioregularity.

precisely control the degree of regioregularity of each batch of polymer. Thus, RBO_{50} has the highest regioregularity of the five RBO_X polymers studied. RBO_{20} and RBO_{72}, in contrast, even though they have drastically different monomer compositions, have regioregularities that are quite similar. These latter two materials thus provide a means to isolate which factor is more important for controlling the BHJ morphology and device performance: regioregularity or average side chain length.

3.2.1 Device Performance for the RBO_X Series with Different Processing Conditions

To begin our study, we fabricated both blend-cast and sequentially-processed RBO_X:$PC_{71}BM$ BHJ devices using the various processing conditions summarized above. The average power conversion efficiency and full average *J-V* curves are plotted in Figure 3.2. It has been shown previously that kinetics of film formation are improved in blend-cast devices when slow-drying is used to increase the ability of the polymer to reorganize and crystallize, rather than being locked into a more amorphous, mixed architecture.[47] Our results for blend-cast samples (red squares) fit with this expectation, with the slow-dried samples (panel e) out-performing the fast-dried samples (panel f). Interestingly, for both drying conditions the blend-cast device that has the best efficiency was made using RBO_{50}, while RBO_{20} and RBO_{72} have the lowest efficiencies. We calculated the correlation factor for the device efficiencies with various characteristics of the different RBO_X polymer batches, and the results are summarized in Table 3.1. Perhaps the most striking feature is that the overall efficiency trend for the blend-cast devices with both drying conditions reflects the trend in regioregularity plotted in Figure 3.1(f): the correlation factors for both fast- and slow-dried blend-cast device efficiency with regioregularity are 0.75 and 0.95, respectively, suggesting that regioregularity is indeed an important factor in determining device

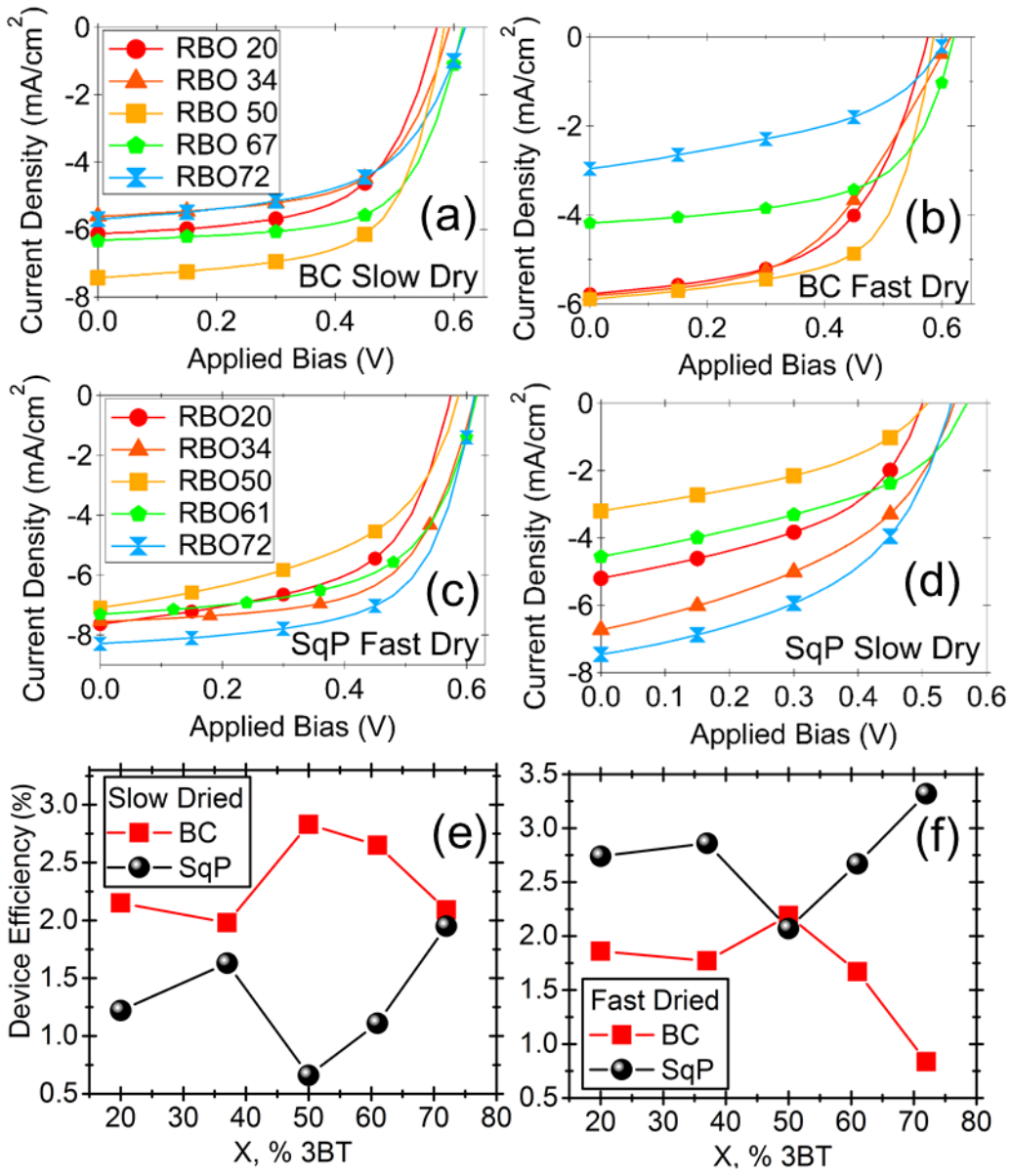

Figure 3.2. *J*-V curves for blend-cast (a, b) and SqP films (c,d) under slow-dried and fast-dried processing conditions. Photovoltaic device efficiency (%) for sequentially-processed and blend-cast RBO$_X$/PCBM films fabricated with the slow-dried method (e) and fast-dried method (f).

Table 3.1. Summary of Pearson product-moment correlation coefficients between $RBO_X/PC_{71}BM$ power conversion efficiency and RBO_X polymer properties.

Active Layer	Regioregularity	PDI	Average Side-Chain Length
Slow Dried SqP	-0.96	-0.65	-0.25
Slow Dried BC	0.95	0.35	-0.27
Fast Dried SqP	-0.94	-0.57	-0.28
Fast Dried BC	0.75	0.57	0.62

efficiency. The correlation between device efficiency and PDI was also calculated (Table 3.1), but the correlation factors were far lower; there is no apparent trend with average side-chain composition.

The other striking feature of Figure 3.2 is that the there is almost a complete anti-correlation between blend-cast and sequentially-processed devices (black circles, panels c and d) in terms of their efficiency. The sequentially-processed devices show an inverse effect of regioregularity, with a high anti-correlation factor (≤ -0.9; see Table 3.1); the RBO_{50} material gives the lowest device performance for SqP. Additionally, the trend in device performance with drying conditions is also reversed between blend-casting and SqP, where fast-drying the initial polymer film in SqP actually improves performance. The fact that the optimal polymer material and processing conditions give precisely opposite trends for SqP and blend-casting indicates that the overall kinetics of BHJ formation in these two fabrication processes is quite different.

3.2.2 Structural Studies of RBO_X:PCBM BHJ Active Layers

To understand precisely what it is about the processing conditions that leads to the correlation or anti-correlation of device performance for blend-casting and sequential processing, respectively, we performed grazing incidence wide-angle X-ray scattering (GIWAXS) studies on all of the BHJ active layers. To simplify the results, we examined the structure of pure polymer films, rather than sequentially-processed active layers. We have shown previously that PCBM intercalates primarily into the amorphous polymer regions during SqP, so that there is little change in X-ray-measurable polymer structure following sequential fullerene deposition.[48,49] The PCBM diffraction, however, overlaps the polymer diffractions and dramatically complicates analysis of the scattering data, as seen by the large peak at 1.4 nm^{-1} in Figure 3.3 (b and d). For blend-cast

films, data from both pure polymer films and blend-cast actives layers were considered because the blended films can show very different crystallinity than the pure polymer films.

Since we have previously seen that polymer crystallinity plays an important role in both blend-casting and sequential processing, we began by looking at the polymer crystallinity in both the lamellar (100) and π-π stacking (010) directions. To do this, we radially integrated our 2-D GIWAXS diffractograms to obtain 1-D data, as shown in Figure 3.3 for slow-dried pure RBO_X films (panel a) and slow-dried blend-cast films (panel b). The resulting 1-D data was fit to a series of Gaussians, where the peak area corresponds to the crystallinity and the peak width correlates to a Scherrer crystallite size or, more correctly, a domain correlation length.[39,50,51] The degree of paracrystalline disorder (*g*-factor) can also be calculated from the spread of the full width at half maximum (FWHM) of the lamellar peak, measured over multiple lattice overtones.[39] Since the analysis relies on multiple diffraction overtones, *g*-factors could not be calculated for the (010) or the fullerene peaks. The results for pure polymer films (black) and blend-cast films (red) are shown in Figures 3.3 e-h. From the data in Figure 3.3, we can readily see that the crystallinity and crystallite size do not follow a monotonic trend with side-chain length, as we would have expected based on the standard model of increased disorder associated with smaller side chains. This provides strong evidence that polymer crystallinity, and in turn the BHJ morphology, is not a very strong function of the side-chain length but is instead mostly dependent on other factors.

Looking at the crystallinity trends for the pure polymer films, we see very little change in the (010) peak area across the RBO_X series (Fig. 3.3g), but striking changes in the (100) peak area (Fig. 3e). We thus use the (100) peak area as a rough measure of the overall RBO_X crystallinity. By this measure, for sequentially-processed films with both drying conditions and for slow-dried blend-cast films, RBO_{50} has the highest crystallinity. The general trend is that pure polymer

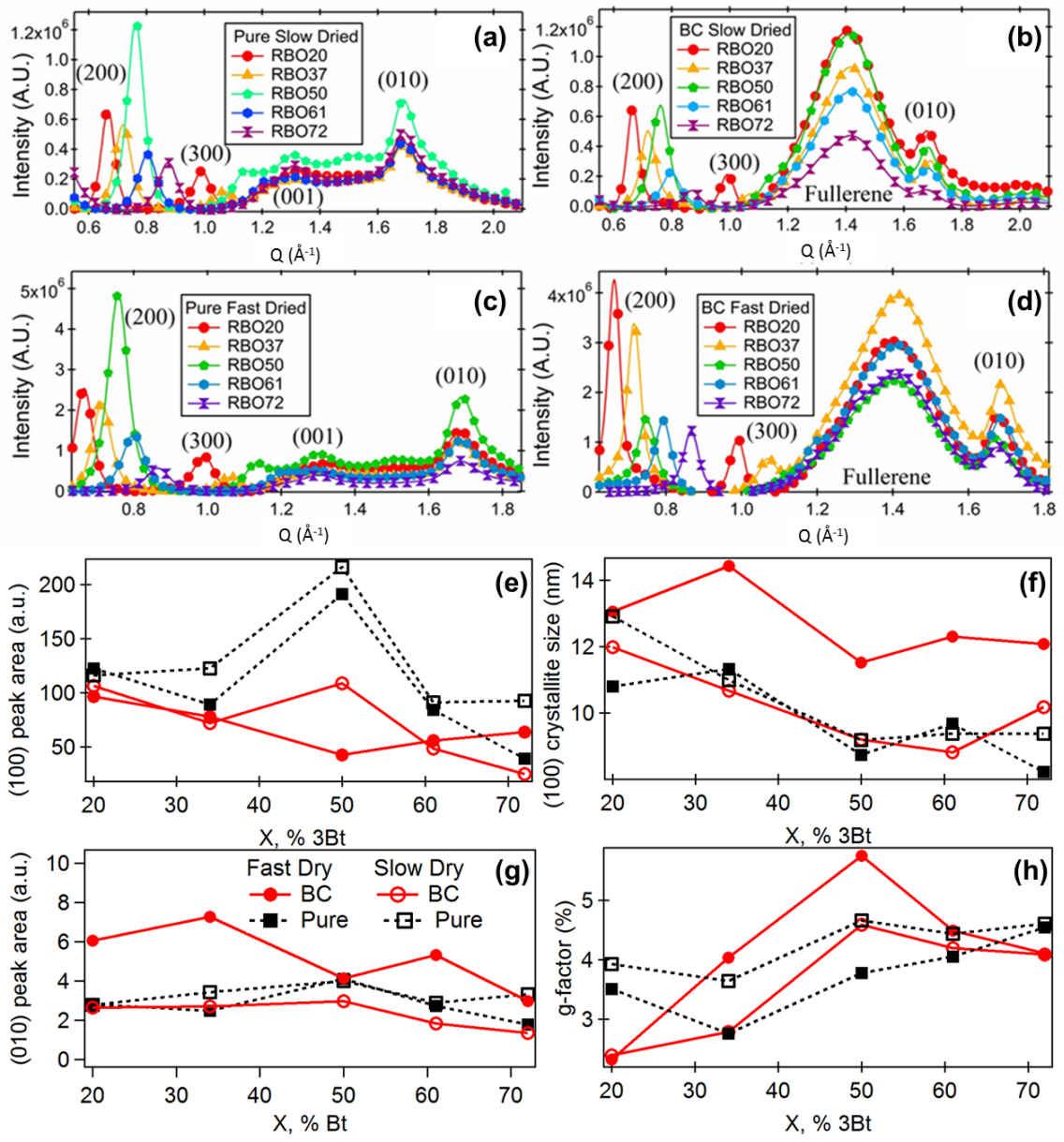

Figure 3.3. Integrated GIWAXS diffractograms for slow-dried (a, b) and fast-dried (c, d) pure and blend-cast films (b). Gaussian fits to GIWAXS lamellar (100) peak area (c), (100) crystallite size (d), (010) crystallite size (e) and paracrystalline disorder (f) for pure RBO_X films (black curves, symbols) and RBO_X/PCBM BHJs (red curves, symbols).

Table 3.2. Summary of Pearson product-moment correlation coefficients between different GIWAXS parameters of the RBO_X films used in this study and the RBO_X regioregularity (RR), polydispersity index (PDI), and side-chain length. All SqP correlations are using pure polymer diffraction, not BHJs.

Active layer	(100) peak area			(100) crystallite size			g-factor		
	RR	PDI	side-chain	RR	PDI	side-chain	RR	PDI	side-chain
Slow Dried SqP	0.72	0.47	-0.17	-0.37	0.47	-0.89	0.45	0.08	0.79
Slow Dried BC	0.54	0.80	-0.77	-0.59	0.34	-0.73	0.55	-0.17	0.84
Fast Dried SqP	0.82	0.70	-0.41	-0.23	0.04	-0.83	0.03	-0.01	0.79
Fast Dried BC	-0.64	0.20	-0.72	-0.55	-0.33	-0.61	0.63	-0.25	0.58

Table 3.3. Summary of Pearson product-moment correlation coefficients between $RBO_X/PC_{71}BM$ device power conversion efficiency and different GIWAXS parameters used in this study.

Active Layer	(100) Area		(010) Area		(100) Crystallite Size		(010) Crystallite Size		g-factor	
Slow Dried SqP		-0.71[a]		-0.27[a]		0.10[a]		-0.71[a]		-0.27[a]
Slow Dried BC	0.29	0.58[a]	0.21	0.35[a]	-0.75	-0.56[a]	0.36	0.52[a]	0.74	0.67[a]
Fast Dried SqP		-0.95[a]		-0.99[a]		0.00[a]		-0.88[a]		0.25[a]
Fast Dried BC	-0.08	0.89[a]	0.5	0.88[a]	0.06	0.41[a]	-0.85[a]	0.91[a]	0.20	-0.60[a]

[a] Data compared to pure polymer films

crystallinity correlates well with polymer regioregularity, correlates somewhat with polymer PDI, and does not correlate at all with chain composition, as summarized in Table 2.2. On the other hand, the extent of paracrystalline disorder, which is a measure of the long range coherence of the crystalline packing,[35,46–49] correlates well with the average side-chain length, with the shortest side-chain length causing the largest disorder, as expected. Since order in the backbone of the polymer is seen in the overall crystallinity, this correlation most likely reflects disorder within the side chains.

In contrast to the correlations found with pure polymer films, Table 3.2 shows that blend-cast RBO_X films show almost no correlation between polymer regioregularity and crystallinity. This is rather surprising given that it is generally accepted that increasing polymer regioregularity improves polymer π-π overlap by promoting inter-chain ordering.[54,55] Clearly, there is not a simple relationship between the synthetic parameters of the pure polymer and the polymer's crystallinity in a blended system. Instead, a large variety of both polymer and fullerene characteristics play a role in the de-mixing that occurs during the drying (and thermal or solvent annealing) of blend-cast films, so that there is no easy way to predict the final BHJ morphology.[17]

To better assess how polymer crystallinity is related to the BHJ morphology of blended films, we examined the correlation between device efficiency and each of the GIWAXS parameters discussed above. Table 3.3 shows the correlation of blend-cast and sequentially-processed device efficiency with both the blend-cast GIWAXS parameters and the pure polymer GIWAXS parameters across the RBO_X polymer series. The sequentially-processed device efficiencies strongly anti-correlate with the blend-cast device efficiencies, as expected based on our previous work showing that sequentially-processed devices need more amorphous regions for fullerene intercalation.[49] However, the blend-cast device efficiencies also correlate more strongly to the

crystallinity of the pure polymer than to the crystallinity of the blend-cast polymer/fullerene composite. This indicates that rather than studying the more complicated mixed systems using X-ray diffraction, the pure polymer morphology is a better predictor of the final BHJ morphology and device performance.

One surprising feature of Table 3.3 is the essentially complete lack of correlation between (100) crystallite size and device efficiency for either blend-cast or sequentially-processed RBO_X devices. Since large crystallites would prevent proper mixing, we expected that there would be an anti-correlation between crystalline domain size and device efficiency. The overall crystallinity is a combination of the crystallite size, the defect density within those crystallites, and the number of crystallites. Thus, the lack of correlation of device performance with crystallite size either indicates that as long a crystallites are below a certain size, which reasonable performance is observed, or more likely, that defects within a crystallite do not significantly affect performance, and so a broad range of apparent domain sizes can correlate with similar physical crystallite sizes and similar performance. In addition, although there is a correlation between paracrystalline disorder and side-chain length, the paracrystallinity also does not correlate with device efficiency. This argues that disorder in the side-chains (rather than the semiconducting polymer backbone) does not play a significant role for the performance of devices fabricated by either SqP or blend-casting. We have also seen that there is also a strong correlation between the shape of the UV-Visible absorption spectrum and device performance (data not shown), as the absorption spectrum accurately reflects the type of order that is important for charge transport through the BHJ device.[58]

3.2.3 Swelling Studies of Pure RBO_X Films

Even though the average side-chain length varies considerably across the RBO_X series, why

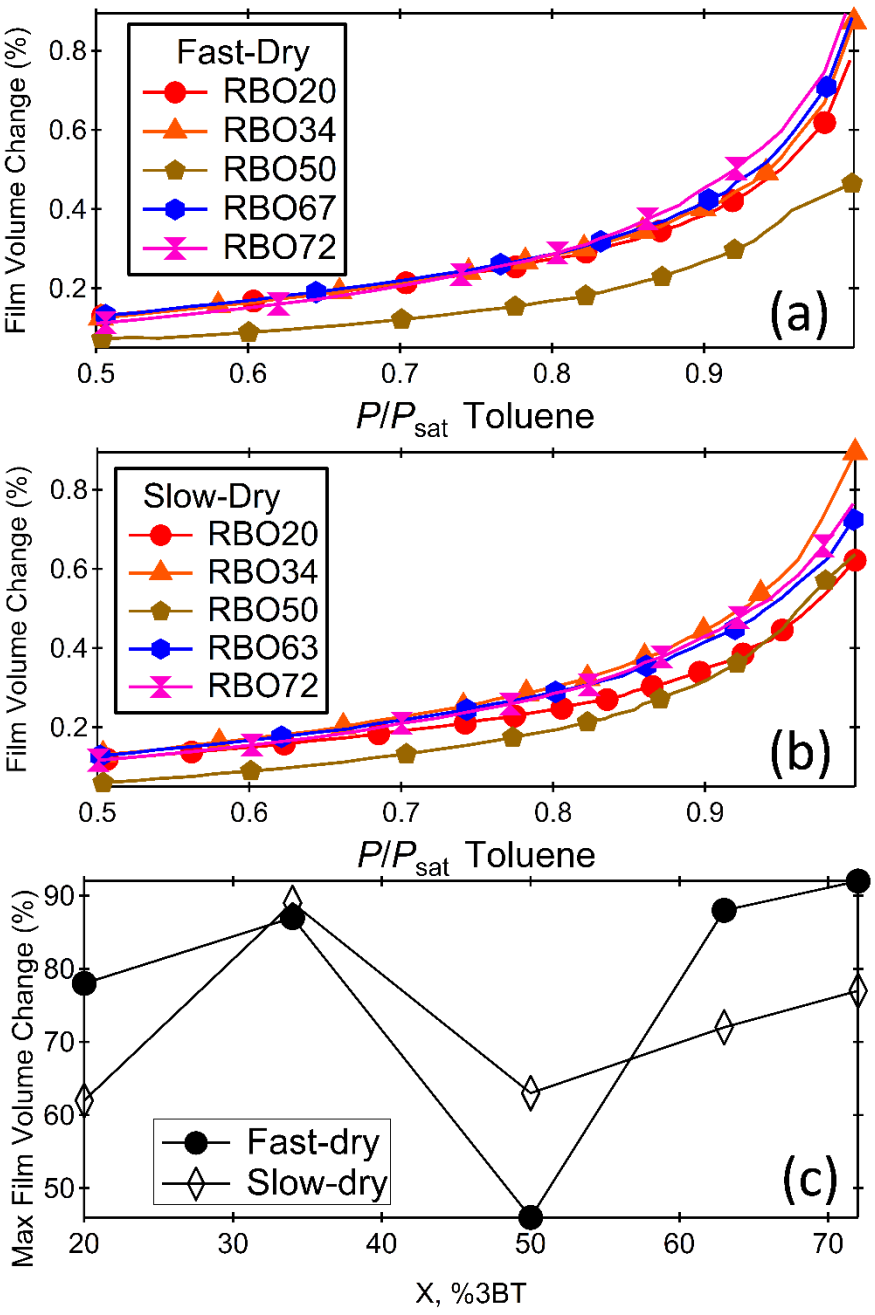

Figure 3.4. Ellipsometric porosimetry swelling profiles for fast-dried (a) and slow-dried (b) pure RBO_X films. (c) The maximum volume change of swelled pure RBO_X films taken at the saturation pressure of toluene (29 Torr).

Table 3.4. Summary of Pearson product-moment correlation coefficients between pure RBO_X polymer film swelling at the saturation pressure of toluene with different polymer properties, device efficiency and the various GIWAXS parameters used in this study.

Correlation to Swelling	Slow-Dried	Fast Dried
Regioregularity	-0.60	-0.81
PDI	-0.91	-0.63
Average Side-Chain Length	-0.21	-0.20
SqP Device Efficiency	0.70	0.89
BC Device Efficiency	-0.41	-0.69
SqP Paracrystallinity	-0.50	-0.01
SqP (100) Peak Area	-0.57	-0.47
SqP (100) Crystallite Size	-0.03	0.13
SqP (010) Peak Area	-0.37	0.26
SqP (010) Crystallite Size	-0.54	-0.84
BC Paracrystallinity	-0.19	-0.54
BC (100) Peak Area	-0.56	0.47
BC (100) Crystallite Size	-0.02	0.48
BC (010) Peak Area	-0.26	0.19
BC (010) Crystallite Size	-0.20	0.45

is it that the most important factors correlating with device efficiency are the polymer regioregularity and crystallinity in the pure film? We believe that answer is linked with how polymers of different regioregularity swell while being processing into BHJs. We have previously shown that polymer swelling is essential for producing high-efficiency photovoltaic devices fabricated through SqP.[31] We also believe that swelling plays an important role in the de-mixing of the polymer and fullerene during blend-casting. Our belief stems from the fact that the best blend-cast polymer/fullerene photovoltaic devices often make use of solvent additives, such as diiodooctane (DIO), during processing. It has been shown in the literature that DIO remains in the film following casting,[56] and that application of DIO to an already-prepared blend-cast film improves de-mixing and thus the BHJ morphology.[57] Thus, rather than DIO simply providing differential solubility of the two components,[8,58] DIO and related additives likely function by swelling the polymer, allowing for demixing to occur in a fashion that is not possible in an unswollen polymer film.

To understand how the regioregularity and crystallinity differences of the RBO_X polymers are related to swelling, we measured the extent of swelling in both slow-dried and fast-dried RBO_X films using spectroscopic ellipsometric porosimetry.[40,59–64] For these studies, we induced swelling by exposing the polymer films to controlled amounts of toluene vapor, which is a good solvent for all of the polymers in this series. Figure 3.4 (a) and (b) shows the resulting swelling profiles that occurred for each RBO_X using fast-drying and slow-drying. The maximum swelling of each film occurred at the saturation vapor pressure of toluene, 29 torr. Figure 3.4(c) shows the maximum swelling of both fast-dried and slow-dried films of the pure polymers across the RBO_X series, and Table 3.4 explores the correlations of swelling with various synthetic, structural and device parameters. The swelling of both fast-dried and slow-dried RBO_X films are anti-correlated to

regioregularity, with the most regioregular polymers being the least able to swell. This result is expected, since highly regioregular polymers should be more crystalline, leaving fewer amorphous regions to uptake solvent.[27,30,49,65–6852,53] We also see an anticorrelation between swelling and PDI, which we believe simply reflects that fact that for this batch of samples, the more regioregular polymers also tended to have higher PDIs. We find little correlation between the average side-chain length and the amount of swelling in the RBO_X films. If we expect swelling to be a major factor in controlling morphology, this again indicates that side-chain length is simply unimportant in determining the structure and performance of BHJ devices.

For the sequentially-processed devices, we observe a strong correlation between swelling and device efficiency for both the slow-dried and fast-dried polymer samples. This fits well with our previous work showing that swelling is the dominant factor that controls fullerene intercalation, BHJ morphology, and the performance of sequentially-processed devices.[31] Unexpectedly, we also see a modest anti-correlation between blend-cast device efficiency and pure polymer swelling in both the fast-dried (–0.69) and slow-dried (–0.41) cases. This provides strong evidence that swelling of a polymer film also plays a role in the kinetics of de-mixing that occurs during drying of blend-cast films. If the polymer is easily swollen, there is less driving force to cause phase separation of the polymer and the fullerene, creating a different BHJ morphology than would be obtained with a polymer that is difficult to swell. This correlation of de-mixing with swelling further is part of what complicates the x-ray diffraction observed from the mixed polymer/fullerene films, explaining why the best correlations are to the crystallinity of the pure polymer films. Thus, the crystallinity and swelling of pure polymers films, which are determined primarily by the polymer regioregularity, are much better predictors of the final blend-cast morphology than any parameter obtained through analysis of the BHJ film.

3.3 Conclusions

This work shows that it is the fundamental properties of conjugated polymer chains determined by their synthesis, such as the average chain regioregularity, dominate BHJ morphologies produced by both SqP and blend-casting. Moreover, because SqP and blend-casting produce optimized BHJ morphologies from fundamentally different starting points, factors such as polymer regioregularity control device performance and morphology from these two processing routes in opposite ways. A high amount of polymer regioregularity is needed for blend-cast devices in order to drive phase separation between polymers and fullerenes that were molecularly mixed in the solution used to cast the film.[37,71,59,60] When a high amount of polymer regioregularity is not present, other processing techniques that facilitate de-mixing must be used, such as thermal annealing[72] or the use of solvent additives[10,73] or solvent annealing,[74] the latter two of which work by swelling the polymer. In SqP, on the other hand, BHJ formation occurs only when the fullerene-casting solvent swells the underlying polymer film,[8,22,30,49] a process that is facilitated with polymer samples that have lower regioregularity and crystallinity.

The initial goal of this work was to use polymer average side-chain length to direct morphology formation in both blend-cast and sequentially-processed devices. What we found, however, is that the regioregularity of the polymer, which happened to vary from one batch to the next, is the primary polymer property responsible for determining BHJ morphology because of the way regioregularity impacts swelling and crystallinity. We also found that the crystallinity of the pure polymer films is a better predictor of device performance than any structural characteristic of the BHJ blends. We note that the polythiophene derivatives studied in this work, even those with lower regioregularity, tend to be highly crystalline, whereas more recent low bandgap, high-efficiency push-pull polymers tend to be much more amorphous. This suggests that regioregularity

effects like those observed here could be even more important with low bandgap materials that have relatively little crystallinity and thus little driving force for de-mixing with fullerenes in blend-cast devices; swelling of these materials is likely to be even more important for BHJ formation. This also suggests that the generally more amorphous low-bandgap polymers should be more amenable to SqP than blend-casting, even though most of the work in the literature with these materials has focused on blend-casting.

Finally, it is worth pointing out that the best sequentially-processed device from this series, fabricated with RBO_{72}, outperforms the most efficient blend-cast device from this series, made with RBO_{50}. This shows the danger in focusing solely on the blend-cast fabrication technique to screen novel photovoltaic materials. Though there is only a small difference in device efficiency in the best blend-cast and SqP devices, these two processing methods favor different polymers within the RBO_X series. What is particularly striking is that the best material for one processing method is the other's worst performer. Therefore, knowledge gained by studying a materials series solely through the blend-casting method could be misleading, particularly since the effects of regioregularity, swelling and crystallinity run in opposite direction for blend-casting and SqP. For the case of the RBO_X series, the highest-performing polymer RBO_{72} would have been entirely dismissed if only blend-cast films were studied. Clearly, it is necessary to consider multiple fabrication methods when screening new materials for photovoltaic performance.

3.4 Experimental

We refer to the individual RBO polymers we used in this work as RBO_X, where X is the percent of butyl-thiophene monomers in the polymer chain. The five random copolymers, poly(3-butylthiophene-co-3-octylthiophene)s[37] RBO_{20}, RBO_{34}, RBO_{50}, RBO_{61} and RBO_{72} with different

percentages of butyl chains 20%, 34%, 50%, 61%, and 72%, respectively, were synthesized and their corresponding regioregularities were measured to be 91.8%, 91.3%, 94.0%, 92.9%, 90.8%.

We fabricated the active photovoltaic device layers in this work using two basic processing conditions: 'slow-dried', in which the OPV film spin-coating is halted while the film is still wet,[38] and 'fast-dried', in which the active layer is spun until dry. All devices were fabricated on ITO substrates that were sequentially sonicated in baths of detergent, water, acetone, and isopropyl alcohol followed by UV ozone treatment for 10 minutes. 40 nm of poly(ethylenedioxythiophene):poly(styrenesulfonic acid) (PEDOT:PSS Clevios PVP AI 4083) was deposited onto ITO to form the hole collection layer.

For the blend-cast procedure, a 1:0.8 wt/wt RBO_X:$PC_{71}BM$ (Solenne, used as received) solution was made at a concentration of 20 mg/ml polymer/1,2 dichlorobenzene. This solution was deposited onto a PEDOT:PSS-coated substrate to produce films with a thickness of 115 ± 5 nm. Slow-dried films were allowed to fully dry in a N_2 atmosphere then thermally annealed at 110 ^oC for 5 minutes. The fast-dried films were thermally annealed at 150 ^oC for 10 minutes.

Sequentially-processed films were fabricated by depositing solutions of the pure RBO_X polymers onto PEDOT:PSS-coated substrates at 1000 rpm for 60 s (fast-dried) or 30 s (slow-dried). $PC_{71}BM$ was deposited onto the fully dry polymer layer by spin coating at 4000 rpm for 10 s. Both sequentially-processed and blend-cast processed films were thermally annealed at 150 ^oC for 10 minutes (fast-dried) or 110 ^oC for 5 minutes (slow-dried). 10 nm of Ca and 70 nm of Al were thermally evaporated (Angstrom Engineering) as cathodes.

Samples for GIWAXS were fabricated similarly to the photovoltaic devices with the exceptions that Si was used as the substrate (with a native ~2-nm thick oxide) instead of ITO on glass, and $PC_{61}BM$ (Nano-C) was substituted for $PC_{71}BM$. The thicknesses of all films were found

to be comparable using profilometry (Dektak). The polymer:fullerene ratio between blend-cast and sequentially-processed films using a given RBO_X donor was matched using the re-dissolved film absorption spectroscopy method detailed by Hawks *et al*.[23]

Photovoltaic performance was measured in an Ar atmosphere using a Keithly 2400 source meter and AM-1.5-filtered light from a xenon arc lamp equipped with a liquid light guide (Oriel). The incident light intensity on tested samples was adjusted to be 100 mW/cm^2 using a calibrated Si diode. All photovoltaic efficiencies were verified by comparing the measured short-circuit current to the integrated external quantum efficiency (EQE).

To determine correlations between different parameters, we used the Pearson product-moment correlation coefficient (r), given as:[39]

$$r = \frac{\sum(x - \bar{x})(y - \bar{y})}{\sqrt{\sum(x - \bar{x})^2 \sum(y - \bar{y})^2}}$$

where x and y are the data sets to be correlated. All correlation coefficients are given in Table 3.1.

Grazing-incidence wide-angle X-ray scattering (GIWAXS) measurements were performed at the Stanford Synchrotron Radiation Lightsource (SSRL) on beamline 11-3 using a wavelength of 0.9742 Å. The diffraction patterns were collected on a 2-D image plate with the detector 400 mm from the sample center. The beam spot was approximately 150 μm wide and a helium chamber was used to reduce air scatter and improve signal-to-noise. The WxDiff software package was used to radially integrate scattering data. The patterns shown in the main text are results average from three separate films. Each diffractogram was fit to a series of Gaussian curves. The increase in the full width at half maximum (FWHM) across the overtones of the (100) scattering planes was used to determine the *g*-factor, which is correlated to the paracrystalline disorder.[39] The

subsequent *g*-factors for each separate film were averaged together for the correlation calculations.

Polymer swelling was measured *in situ* using a PS-1000 Semilab ellipsometric porosimeter; experiments following the methods outlined by Huttner *et al.*[40] Pure polymer films were deposited onto silicon substrates with a native oxide layer using both the fast-dried and slow-dried methods described above . Ellipsometric measurements were taken at the approximate Brewster angle of silicon, 75°. The data were fit using the Semilab Spectroscopic Ellipsometry Analyzer (SEA) software, using a multi-layer model for the silicon substrate and the native oxide layer. The Cauchy model was used for the thin polymer film to fit the tan(Ψ) and cos(Δ) parameters directly measured by the ellipsometer. No significant differences were found in the fitting parameters when anisotropy (i.e., birefringence) in the polymer films was included in the model, so for simplicity the data presented here was fit assuming an isotropic (single *n* and *k*) polymer film.[41] To minimize contributions from the polymer absorption, we used the 800-1000 nm region for our fits. The (unswelled) film thicknesses measured by ellipsometry were confirmed by direct measurement with a Dektak profilometer. The swelling measurements used toluene vapor both because of its compatibility with the porosimeter instrument and because it is a good solvent for the RBO_X polymers that yields large volume changes during swelling. Vapor pressures were measured as relative pressure (P/P_{sat}), using the saturation pressure P_{sat} for toluene of 29 torr. The refractive indexes that we measured were validated using reported values.[18,42] Since the transparent region of the ellipsometry data was used for fitting, changes in the refractive index with swelling and solvent incorporation were fully taken into account.

3.5 References

(1) Green, M. A.; Emery, K.; Hishikawa, Y.; Warta, W.; Dunlop, E. D. Solar Cell Efficiency Tables (version 43). *Prog. Photovoltaics Res. Appl.* **2014**, *22*, 1–9.

(2) He, Z.; Zhong, C.; Su, S.; Xu, M.; Wu, H.; Cao, Y. Enhanced Power-Conversion Efficiency in Polymer Solar Cells Using an Inverted Device Structure. *Nat Phot.* **2012**, *6*, 591–595.

(3) Collins, B. A.; Tumbleston, J. R.; Ade, H. Miscibility, Crystallinity, and Phase Development in P3HT/PCBM Solar Cells: Toward an Enlightened Understanding of Device Morphology and Stability. *J. Phys. Chem. Lett.* **2011**, *2*, 3135–3145.

(4) Shaw, P. E.; Ruseckas, A.; Samuel, I. D. W. Exciton Diffusion Measurements in Poly(3-Hexylthiophene). *Adv. Mater.* **2008**, *20*, 3516–3520.

(5) Groves, C.; Marsh, R. A.; Greenham, N. C. Monte Carlo Modeling of Geminate Recombination in Polymer-Polymer Photovoltaic Devices. *J. Chem. Phys.* **2008**, *129*, -.

(6) Halls, J. J. M.; Walsh, C. A.; Greenham, N.; Marseglia, E. A.; Friend, R.; Moratti, S. C.; Holmes, A. Efficient Photodiodes from Interpenetrating Polymer Networks. *Nature* **1995**, *376*, 498–500.

(7) Shaheen, S. E.; Brabec, C. J.; Sariciftci, N. S.; Padinger, F.; Fromherz, T.; Hummelen, J. C. 2.5% Efficient Organic Plastic Solar Cells. *Appl. Phys. Lett.* **2001**, *78*, 841–843.

(8) Yu, G.; Gao, J.; Hummelen, J. C.; Wudl, F.; Heeger, A. J. Polymer Photovoltaic Cells: Enhanced Efficiencies via a Network of Internal Donor-Acceptor Heterojunctions. *Science (80-.).* **1995**, *270*, 1789–1791.

(9) Peet, J.; Soci, C.; Coffin, R. C.; Nguyen, T. Q.; Mikhailovsky, A.; Moses, D.; Bazan, G. C. Method for Increasing the Photoconductive Response in Conjugated Polymer/fullerene Composites. *Appl. Phys. Lett.* **2006**, *89*, 252103–252105.

(10) Peet, J.; Kim, J. Y.; Coates, N. E.; Ma, W. L.; Moses, D.; Heeger, A. J.; Bazan, G. C. Efficiency Enhancement in Low-Bandgap Polymer Solar Cells by Processing with Alkane Dithiols. *Nat Mater* **2007**, *6*, 497–500.

(11) Lee, J. K.; Ma, W. L.; Brabec, C. J.; Yuen, J.; Moon, J. S.; Kim, J. Y.; Lee, K.; Bazan, G. C.; Heeger, A. J. Processing Additives for Improved Efficiency from Bulk Heterojunction Solar Cells. *J. Am. Chem. Soc.* **2008**, *130*, 3619–3623.

(12) Ma, W.; Yang, C.; Gong, X.; Lee, K.; Heeger, A. J. Thermally Stable, Efficient Polymer Solar Cells with Nanoscale Control of the Interpenetrating Network Morphology. *Adv. Funct. Mater.* **2005**, *15*, 1617–1622.

(13) Kim, K.; Liu, J.; Namboothiry, M. A. G.; Carroll, D. L. Roles of Donor and Acceptor Nanodomains in 6% Efficient Thermally Annealed Polymer Photovoltaics. *Appl. Phys. Lett.* **2007**, *90*, 163511.

(14) Verploegen, E.; Mondal, R.; Bettinger, C. J.; Sok, S.; Toney, M. F.; Bao, Z. Effects of Thermal Annealing Upon the Morphology of Polymer-Fullerene Blends. *Adv. Funct. Mater.* **2010**, *20*, 3519–3529.

(15) Zhao, Y.; Xie, Z.; Qu, Y.; Geng, Y.; Wang, L. Solvent-Vapor Treatment Induced Performance Enhancement of poly(3-Hexylthiophene):methanofullerene Bulk-Heterojunction Photovoltaic Cells. *Appl. Phys. Lett.* **2007**, *90*, 43503–43504.

(16) Jo, J.; Na, S.-I.; Kim, S.-S.; Lee, T.-W.; Chung, Y.; Kang, S.-J.; Vak, D.; Kim, D.-Y. Three-Dimensional Bulk Heterojunction Morphology for Achieving High Internal Quantum Efficiency in Polymer Solar Cells. *Adv. Funct. Mater.* **2009**, *19*, 2398–2406.

(17) Heeger, A. J. 25th Anniversary Article: Bulk Heterojunction Solar Cells: Understanding the Mechanism of Operation. *Adv. Mater.* **2014**, *26*, 10–28.

(18) Ayzner, A. L.; Tassone, C. J.; Tolbert, S. H.; Schwartz, B. J. Reappraising the Need for Bulk Heterojunctions in Polymer/Fullerene Photovoltaics: The Role of Carrier Transport in All-Solution-Processed P3HT/PCBM Bilayer Solar Cells. *J. Phys. Chem. C* **2009**, *113*, 20050–20060.

(19) Gevaerts, V. S.; Koster, L. J. A.; Wienk, M. M.; Janssen, R. A. J. Discriminating between Bilayer and Bulk Heterojunction Polymer:Fullerene Solar Cells Using the External Quantum Efficiency. *ACS Appl. Mater. Interfaces* **2011**, *3*, 3252–3255.

(20) Moon, J. S.; Takacs, C. J.; Sun, Y.; Heeger, A. J. Spontaneous Formation of Bulk Heterojunction Nanostructures: Multiple Routes to Equivalent Morphologies. *Nano Lett.* **2011**, *11*, 1036–1039.

(21) Treat, N. D.; Brady, M. a; Smith, G.; Toney, M. F.; Kramer, E. J.; Hawker, C. J.; Chabinyc, M. L. Interdiffusion of PCBM and P3HT Reveals Miscibility in a Photovoltaically Active Blend. *Adv. Energy Mater.* **2011**, *1*, 82–89.

(22) Ayzner, A. L.; Doan, S. C.; Tremolet de Villers, B.; Schwartz, B. J. Ultrafast Studies of Exciton Migration and Polaron Formation in Sequentially Solution-Processed Conjugated Polymer/Fullerene Quasi-Bilayer Photovoltaics. *J. Phys. Chem. Lett.* **2012**, *3*, 2281–2287.

(23) Hawks, S. A.; Aguirre, J. C.; Schelhas, L. T.; Thompson, R. J.; Huber, R. C.; Ferreira, A. S.; Zhang, G.; Herzing, A. A.; Tolbert, S. H.; Schwartz, B. J. Comparing Matched Polymer:Fullerene Solar Cells Made by Solution-Sequential Processing and Traditional Blend Casting: Nanoscale Structure and Device Performance. *J. Phys. Chem. C* **2014**, *118*, 17413–17425.

(24) Zhang, G.; Huber, R.; Ferreira, A.; Boyd, S. D.; Luscombe, C. K.; Tolbert, S. H.; Schwartz, B. J. Crystallinity Effect in Sequentially Processed and Blend Cast Bulk-Heterojunction Polymer/Fullerene Photovoltaics. *J. Phys. Chem. C* **2014**, *118*, 18424-18435.

(25) Clark, J.; Silva, C.; Friend, R.; Spano, F. Role of Intermolecular Coupling in the Photophysics of Disordered Organic Semiconductors: Aggregate Emission in Regioregular Polythiophene. *Phys. Rev. Lett.* **2007**, *98*, 206406.

(26) Van Franeker, J. J.; Kouijzer, S.; Lou, X.; Turbiez, M.; Wienk, M. M.; Janssen, R. A. J. Depositing Fullerenes in Swollen Polymer Layers via Sequential Processing of Organic Solar Cells. *Adv. Energy Mater.* **2015**, n/a–n/a.

(27) Lee, K. H.; Schwenn, P. E.; Smith, A. R. G.; Cavaye, H.; Shaw, P. E.; James, M.; Krueger, K. B.; Gentle, I. R.; Meredith, P.; Burn, P. L. Morphology of All-Solution-Processed "Bilayer" Organic Solar Cells. *Adv. Mater.* **2011**, *23*, 766–770.

(28) Loiudice, A.; Rizzo, A.; Latini, G.; Nobile, C.; de Giorgi, M.; Gigli, G. Graded Vertical Phase Separation of Donor/acceptor Species for Polymer Solar Cells. *Sol. Energy Mater. Sol. Cells* **2012**,

100, 147–152.

(29) Nardes, A. M.; Ayzner, A. L.; Hammond, S. R.; Ferguson, A. J.; Schwartz, B. J.; Kopidakis, N. Photoinduced Charge Carrier Generation and Decay in Sequentially Deposited Polymer/Fullerene Layers: Bulk Heterojunction vs Planar Interface. *J. Phys. Chem. C* **2012**, *116*, 7293–7305.

(30) Kim, D. H.; Mei, J.; Ayzner, A. L.; Schmidt, K.; Giri, G.; Appleton, A. L.; Toney, M. F.; Bao, Z. Sequentially Solution-Processed, Nanostructured Polymer Photovoltaics Using Selective Solvents. *Energy Environ. Sci.* **2014**.

(31) Aguirre, J. C.; Hawks, S. A.; Ferreira, A.; Yee, P.; Subramaniyan, S.; Jenekhe, S. A.; Tolbert, S. H.; Schwartz, B. J. Sequential Processing for Organic Photovoltaics: Design Rules for Morphology Control by Tailored Semi-Orthogonal Solvent Blends. *Adv. Energy Mater.* **2015**, *5*, 1402020.

(32) Liu, Y.; Lui, F.; Wang, H. W.; Nordlund, D.; Sun, Z.; Ferdous, S.; Russell, T. P. Sequential Deposition: Optimization of Solvent Swelling for High-Performance Polymer Solar Cells. *ACS Appl. Mater. Interfaces* **2014**, *7*, 653–661.

(33) Collins, B. a.; Gann, E.; Guignard, L.; He, X.; McNeill, C. R.; Ade, H. Molecular Miscibility of Polymer−Fullerene Blends. *J. Phys. Chem. Lett.* **2010**, *1*, 3160–3166.

(34) Lee, K. H.; Zhang, Y.; Burn, P. L.; Gentle, I. R.; James, M.; Nelson, A.; Meredith, P. Correlation of Diffusion and Performance in Sequentially Processed P3HT/PCBM Heterojunction Films by Time-Resolved Neutron Reflectometry. *J. Mater. Chem. C* **2013**, *1*, 2593.

(35) Aguirre, J. C.; Ferreira, A.; Ding, H.; Jenekhe, S. A.; Kopidakis, N.; Asta, M.; Pilon, L.; Rubin, Y.; Tolbert, S. H.; Schwartz, B. J.; et al. Panoramic View of Electrochemical Pseudocapacitor and Organic Solar Cell Research in Molecularly Engineered Energy Materials (MEEM). *J. Phys. Chem. C* **2014**, *34*, 19505–19523.

(36) Babel, A.; Jenekhe, S. a. Alkyl Chain Length Dependence of the Field-Effect Carrier Mobility in Regioregular poly(3-Alkylthiophene)s. *Synth. Met.* **2005**, *148*, 169–173.

(37) Gadisa, A.; Oosterbaan, W. D.; Vandewal, K.; Bolse, J. C.; Bertho, S.; D'Haen, J.; Lutsen, L.; Vanderzande, D.; Manca, J. V. Effect of Alkyl Side-Chain Length on Photovoltaic Properties of poly(3-alkylthiophene)/PCBM Bulk Heterojunctions. *Adv. Funct. Mater.* **2009**, *19*, 3300–3306.

(38) Wu, P. T.; Ren, G.; Jenekhe, S. A. Crystalline Random Conjugated Copolymers with Multiple Side Chains: Tunable Intermolecular Interaction and Enhanced Charge Transport and Photovoltaic Properties. *Macromolecules* **2010**, *43*, 3306–3313.

(39) Pearson, K. Note on Regression and Inheritance in the Case of Two Parents. *Proc. R. Soc. London* **1895**, *58* , 240–242.

(40) Lilliu, S.; Agostinelli, T.; Pires, E.; Hampton, M.; Nelson, J.; Macdonald, J. E. Dynamics of Crystallization and Disorder during Annealing of P3HT/PCBM Bulk Heterojunctions. *Macromolecules* **2011**, *44*, 2725–2734.

(41) Huttner, S.; Sommer, M.; Chiche, A.; Krausch, G.; Steiner, U.; Thelakkat, M. Controlled Solvent

Vapour Annealing for Polymer Electronics. *Soft Matter* **2009**, *5*, 4206–4211.

(42) Ng, A.; Li, C. H.; Fung, M. K.; Djurišić, A. B.; Zapien, J. A.; Chan, W. K.; Cheung, K. Y.; Wong, W.-Y. Accurate Determination of the Index of Refraction of Polymer Blend Films by Spectroscopic Ellipsometry. *J. Phys. Chem. C* **2010**, *114*, 15094–15101.

(43) Hedley, G. J.; Ward, A. J.; Alekseev, A.; Howells, C. T.; Martins, E. R.; Serrano, L. A.; Cooke, G.; Ruseckas, A.; Samuel, I. D. W. Determining the Optimum Morphology in High-Performance Polymer-Fullerene Organic Photovoltaic Cells. *Nat Commun* **2013**, *4*.

(44) Jiang, X. M.; Österbacka, R.; Korovyanko, O.; An, C. P.; Horovitz, B.; Janssen, R. A. J.; Vardeny, Z. V. Spectroscopic Studies of Photoexcitations in Regioregular and Regiorandom Polythiophene Films. *Adv. Funct. Mater.* **2002**, *12*, 587–597.

(45) Mauer, R.; Kastler, M.; Laquai, F. The Impact of Polymer Regioregularity on Charge Transport and Efficiency of P3HT:PCBM Photovoltaic Devices. *Adv. Funct. Mater.* **2010**, *20*, 2085–2092.

(46) Adachi, T.; Brazard, J.; Ono, R. J.; Hanson, B.; Traub, M. C.; Wu, Z.-Q.; Li, Z.; Bolinger, J. C.; Ganesan, V.; Bielawski, C. W.; et al. Regioregularity and Single Polythiophene Chain Conformation. *J. Phys. Chem. Lett.* **2011**, *2*, 1400–1404.

(47) Kohn, P.; Rong, Z.; Scherer, K. H.; Sepe, A.; Sommer, M.; Müller-Buschbaum, P.; Friend, R. H.; Steiner, U.; Hüttner, S. Crystallization-Induced 10-Nm Structure Formation in P3HT/PCBM Blends. *Macromolecules* **2013**, *46*, 4002–4013.

(48) Turner, S. T.; Pingel, P.; Steyrleuthner, R.; Crossland, E. J. W.; Ludwigs, S.; Neher, D. Quantitative Analysis of Bulk Heterojunction Films Using Linear Absorption Spectroscopy and Solar Cell Performance. *Adv. Funct. Mater.* **2011**, *21*, 4640–4652.

(49) Hawks, S. A.; Aguirre, J. C.; Zhang, G.; Thompson, R.; Schelhas, L. T.; Harris, E.; Tolbert, S. H.; Schwartz, B. J. On the Composition of Sequentially Solution-Processed Polymer/Fullerene Organic Solar Cell Active Layers. *Submitted*.

(50) Zhang, G.; Ferreira, A.; Huber, R.; Boyd, S. D.; Luscombe, C. K.; Tolbert, S. H.; Schwartz, B. J. Crystallinity Effect in Sequentially-Processed P3HT/PCBM Photovoltaics. *Submitted*.

(51) Rogers, J. T.; Schmidt, K.; Toney, M. F.; Kramer, E. J.; Bazan, G. C. Structural Order in Bulk Heterojunction Films Prepared with Solvent Additives. *Adv. Mater.* **2011**, *23*, 2284–2288.

(52) Verploegen, E.; Miller, C. E.; Schmidt, K.; Bao, Z.; Toney, M. F. Manipulating the Morphology of P3HT–PCBM Bulk Heterojunction Blends with Solvent Vapor Annealing. *Chem. Mater.* **2012**, *24*, 3923–3931.

(53) Poelking, C.; Andrienko, D. Effect of Polymorphism, Regioregularity and Paracrystallinity on Charge Transport in Poly(3-Hexylthiophene) [P3HT] Nanofibers. *Macromolecules* **2013**, *46*, 8941–8956.

(54) Lilliu, S.; Agostinelli, T.; Verploegen, E.; Pires, E.; Hampton, M.; Al-Hashimi, M.; Heeney, M. J.; Toney, M. F.; Nelson, J.; Macdonald, J. E. Effects of Thermal Annealing upon the Nanomorphology

of poly(3-Hexylselenophene)-PCBM Blends. *Macromol. Rapid Commun.* **2011**, *32*, 1454–1460.

(55) Noriega, R.; Rivnay, J.; Vandewal, K.; Koch, F. P. V; Stingelin, N.; Smith, P.; Toney, M. F.; Salleo, A. A General Relationship between Disorder, Aggregation and Charge Transport in Conjugated Polymers. *Nat. Mater.* **2013**, *12*, 1–7.

(56) Sanyal, M.; Schmidt-Hansberg, B.; Klein, M. F. G.; Colsmann, A.; Munuera, C.; Vorobiev, A.; Lemmer, U.; Schabel, W.; Dosch, H.; Barrena, E. In Situ X-Ray Study of Drying-Temperature Influence on the Structural Evolution of Bulk-Heterojunction Polymer–Fullerene Solar Cells Processed by Doctor-Blading. *Adv. Energy Mater.* **2011**, *1*, 363–367.

(57) Shin, N.; Richter, L. J.; Herzing, A. A.; Kline, R. J.; DeLongchamp, D. M. Effect of Processing Additives on the Solidification of Blade-Coated Polymer/Fullerene Blend Films via In-Situ Structure Measurements. *Adv. Energy Mater.* **2013**, *3*, 938–948.

(58) Spano, F. C. Modeling Disorder in Polymer Aggregates: The Optical Spectroscopy of Regioregular poly(3-Hexylthiophene) Thin Films. *J. Chem. Phys.* **2005**, *122*, 234701–234715.

(59) Ye, L.; Jing, Y.; Guo, X.; Sun, H.; Zhang, S.; Zhang, M.; Huo, L.; Hou, J. Remove the Residual Additives toward Enhanced Efficiency with Higher Reproducibility in Polymer Solar Cells. *J. Phys. Chem. C.* **2013**, *117*, 14920-14928.

(60) Kong, J.; Hwang, I.-W.; Lee, K. Top-Down Approach for Nanophase Reconstruction in Bulk Heterojunction Solar Cells. *Adv. Mater.* **2014**, *26*, 6275–6283.

(61) Venkatesan, S.; Adhikari, N.; Chen, J.; Ngo, E. C.; Dubey, A.; Galipeau, D. W.; Qiao, Q. Interplay of Nanoscale Domain Purity and Size on Charge Transport and Recombination Dynamics in Polymer Solar Cells. *Nanoscale* **2014**, *6*, 1011–1019.

(62) Elbs, H.; Krausch, G. Ellipsometric Determination of Flory-Huggins Interaction Parameters in Solution. *Polymer (Guildf).* **2004**, *45*, 7935–7942.

(63) Ogieglo, W.; van der Werf, H.; Tempelman, K.; Wormeester, H.; Wessling, M.; Nijmeijer, A.; Benes, N. E. N-Hexane Induced Swelling of Thin PDMS Films under Non-Equilibrium Nanofiltration Permeation Conditions, Resolved by Spectroscopic Ellipsometry. *J. Memb. Sci.* **2013**, *437*, 313–323.

(64) Papanu, J. S.; Hess, D. W.; Soane, D. S.; Bell, A. T. Dissolution of Thin Poly(methyl Methacrylate) Films in Ketones, Binary Ketone/Alcohol Mixtures, and Hydroxy Ketones. *J. Electrochem. Soc.* **1989**, *136* , 3077–3083.

(65) Papanu, J. S.; Hess, D. W.; Soane (Soong), D. S.; Bell, A. T. Swelling of Poly(methyl Methacrylate) Thin Films in Low Molecular Weight Alcohols. *J. Appl. Polym. Sci.* **1990**, *39*, 803–823.

(66) Sirard, S. M.; Green, P. F.; Johnston, K. P. Spectroscopic Ellipsometry Investigation of the Swelling of Poly(Dimethylsiloxane) Thin Films with High Pressure Carbon Dioxide. *J. Phys. Chem. B* **2001**, *105*, 766–772.

(67) Stamatialis, D. F.; Sanopoulou, M.; Raptis, I. Swelling and Dissolution Behavior of Poly(methyl Methacrylate) Films in Methyl Ethyl Ketone/methyl Alcohol Mixtures Studied by Optical

Techniques. *J. Appl. Polym. Sci.* **2002**, *83*, 2823–2834.

(68) Chen, D.; Liu, F.; Wang, C.; Nakahara, A.; Russell, T. P. Bulk Heterojunction Photovoltaic Active Layers via Bilayer Interdiffusion. *Nano Lett.* **2011**, *11*, 2071–2078.

(69) Collins, B. a.; Gann, E.; Guignard, L.; He, X.; McNeill, C. R.; Ade, H. Molecular Miscibility of Polymer Fullerene Blends. *J. Phys. Chem. Lett.* **2010**, *1*, 3160–3166.

(70) Vohra, V.; Arrighetti, G.; Barba, L.; Higashimine, K.; Porzio, W.; Murata, H. Enhanced Vertical Concentration Gradient in Rubbed P3HT:PCBM Graded Bilayer Solar Cells. *J. Phys. Chem. Lett.* **2012**, *3*, 1820–1823.

(71) Vohra, V.; Higashimine, K.; Murakami, T.; Murata, H. Addition of Regiorandom Poly (3-Hexylthiophene) to Solution Processed Graded Bilayers to Tune the Vertical Concentration Gradient. *Appl. Phys. Lett.* **2012**, *173301*, 1–4.

(72) Kim, Y.; Cook, S.; Tuladhar, S. M.; Choulis, S. A.; Nelson, J.; Durrant, J. R.; Bradley, D. D. C.; Giles, M.; McCulloch, I.; Ha, C.-S.; et al. A Strong Regioregularity Effect in Self-Organizing Conjugated Polymer Films and High-Efficiency Polythiophene:fullerene Solar Cells. *Nat Mater* **2006**, *5*, 197–203.

(73) Chiu, M.-Y.; Jeng, U.-S.; Su, M.-S.; Wei, K.-H. Morphologies of Self-Organizing Regioregular Conjugated Polymer/Fullerene Aggregates in Thin Film Solar Cells. *Macromolecules* **2010**, *43*, 428–432.

(74) Treat, N. D.; Chabinyc, M. L. Phase Separation in Bulk Heterojunctions of Semiconducting Polymers and Fullerenes for Photovoltaics. *Annu. Rev. Phys. Chem.* **2014**, *65*, 59–81.

(75) Verploegen, E.; Mondal, R.; Bettinger, C. J.; Sok, S.; Toney, M. F.; Bao, Z. Effects of Thermal Annealing Upon the Morphology of Polymer/Fullerene Blends. *Adv. Funct. Mater.* **2010**, *20*, 3519–3529.

(76) Lou, S. J.; Szarko, J. M.; Xu, T.; Yu, L.; Marks, T. J.; Chen, L. X. Effects of Additives on the Morphology of Solution Phase Aggregates Formed by Active Layer Components of High-Efficiency Organic Solar Cells. *J. Am. Chem. Soc.* **2011**, *133*, 20661–20663.

(77) Tang, H.; Lu, G.; Li, L.; Li, J.; Wang, Y.; Yang, X. Precise Construction of PCBM Aggregates for Polymer Solar Cells via Multi-Step Controlled Solvent Vapor Annealing. *J. Mater. Chem.* **2010**, *20*, 683–688.

CHAPTER 4

Sequential Processing as an Additive-free Method for Retaining the Face-on Polymer Orientation in PBDTTT-C-based Photovoltaics

4.1 Introduction

Organic photovoltaics (OPVs) have been of interest due to their potentially low cost, ease of processing, and composition containing only earth-abundant elements. These devices typically consist of a semiconducting polymer as the primary photoabsorber and electron donor, paired with a fullerene derivative as the electron acceptor. Although reasonably high power conversion efficiencies (PCEs) can be obtained,[1,2] the overall device performance is highly sensitive to the morphology of the blended system.[3] To obtain optimal performance, the polymer and fullerene must have some separated domains to enable efficient charge collection,[4,5] but must also be mixed on length scales of less than ~20 nm to prevent exciton recombination prior to charge separation.[6] The primary way that this morphology is achieved is through blend casting, in which the polymer and fullerene are co-dissolved in solution and spun onto a conductive substrate to create a bulk heterojunction (BHJ) structure.[7] The polymer and fullerene must partially de-mix during film formation to form an interpenetrating network, a process that is often assisted by the use of solvent additives[8–10] or via post-treatment steps involving solvent[11,12] or thermal annealing.[13–15] This type of processing not only requires a blind Edisonian approach for optimization, but also prevents precise control of the nanoscale structure of the final film.

Another, more recently introduced, processing technique for forming polymer:fullerene BHJs is sequential processing (SqP).[16–23] In this method, the polymer film is formed first and then

the fullerene is cast on top of the polymer from a quasi-orthogonal solvent. In SqP, the fullerene-casting solvent is chosen to swell but not dissolve the polymer underlayer, allowing fullerenes to intercalate into the amorphous regions of the polymer;[20,24–29] fullerene intercalation also can be aided with a separate thermal annealing step.[7,26,30–32] The final result is again a BHJ-type structure. Since the fullerenes preferentially reside in the amorphous polymer domains that are easy to swell, SqP leaves any crystalline polymer domains almost untouched.[28] Thus, sequential processing offers more control over the polymer structure, which is easily tuned when the polymer film is first formed. Because of this, SqP also allows for the creation of more reproducible and scalable organic photovoltaic devices.[22,33]

It is well known that polymer crystallinity is directly correlated to the amount of de-mixing in blend-cast systems and the ability of fullerenes to diffuse into the polymer network in sequential-processed systems.[23] But in addition to the total polymer crystallinity, the polymer domain orientation (i.e., texture) can play a major role in hole extraction from the device.[34,35] Hole extraction is often the factor most limiting for OPV performance, as it directly influences both the short-circuit current and fill factor. Due to surface energetics, most semiconducting polymers prefer to lie with their side-chains parallel to the surface (edge-on), requiring holes to hop between polymer chains to be extracted from the electrode.[36–38] Thus, although it has been shown that the largest hole mobility is along the length of a semiconducting polymer chain (which would require a remarkably uncommon end-on polymer chain conformation to exploit in an OPV device),[39,40,41–44] the best readily-achievable mobility is for holes traveling between adjacent chain's π-conjugation networks; this can be achieved in OPV devices through face-on orientation of the polymer chains.[45]

For this reason, there has been much recent interest in determining whether the polymers

used in OPV devices lie either face-on or edge-on. Indeed, when conjugated polymers have a face-on orientation to the substrate electrode in working devices, both hole mobility and extraction are improved.[34,35,46–50,51] One semi-conducting polymer that is known to orient face-on when cast into films is poly[4,8-bis-(2-ethylhexyloxy)-benzol[1,2-b:4,5-b']dithiophene-2,6-diyl-alt-4-(2-ethylhexyloxy-1-one)thieno[3,4-b]thiophene-2,6-diyl] (PBDTTT-C), which has been used extensively with blend-cast processing to make high-performing OPV devices.[52–57] Although the performance of PBDTTT-C devices has been well optimized, the polymer crystallinity and domain orientation in BHJ blends has not been studied in depth.[52,53,56,58,59]

Herein, we present a detailed study of the crystallinity and orientation of PBDTTT-C polymer chains in both pure films and films blended with [6,6]-phenyl-C_{71}-butyric-acid-methylester ($PC_{71}BM$) in BHJ devices fabricated by both blend casting and sequential processing. We use two-dimensional grazing-incidence wide-angle X-ray scattering (GIWAXS) to understand the extent to which the polymer maintains its face-on orientation in BHJ blends using different processing methods. We find that blend-casting leads to isotropic orientation of the PBDTTT-C chains in BHJ active layers, but that the use of solvent additives such as diiodooctane can improve device performance by partially recovering the naturally-preferred face-on orientation. We also find that SqP preserves PBDTTT-C's intrinsic face-on orientation in BHJs, leading to superior device performance without need for the carefully-tuned use of solvent additives. Overall, we show that the ability to maintain a face-on polymer chain orientation via sequential processing directly improves device performance without the need for extensive additive optimization that is required with traditional blend casting.

4.2 Results and Discussion

For both our GIWAXS and device studies, commercially available PBDTTT-C was either used pure or combined with $PC_{71}BM$ for BHJs. Pure and blend-cast BHJ solutions were made at a concentration of 10 mg/mL polymer in *o*-dichlorobenzene, and all films were deposited by spin coating. For blend-cast BHJ active layers, the solutions were made with a 1:1.5 wt/wt PBDTTT-C:$PC_{71}BM$ blend. Sequentially-processed active layers were fabricated by first spin coating the pure PBDTTT-C solution and subsequently depositing the fullerene from a 10 mg/mL solution of $PC_{71}BM$ in a 1:1 blend of 2-chlorophenol:dichloromethane (2CP:DCM).[28] This procedure resulted in an optimized SqP composition of approximately 1:3.5 wt/wt PBDTTT-C:$PC_{71}BM$ (see SI).[22] Where noted, the diiodooctane (DIO) additive (3%) was added either to the blend-cast solution or to the polymer solution for the sequentially-processed samples. All films for all GIWAXS studies were cast onto silicon substrates to minimize substrate diffraction. Devices were fabricated from the same solutions with the structure: ITO/PEDOT:PSS/PBDTTT-C:$PC_{71}BM$:Ca/Al. Further details are given below in the Experimental section.

4.2.1 Orientation of PBDTTT-C Crystallites Measured by 2-D GIWAXS

4.2.1.1 The Face-on Structure of Pure PBDTTT-C Films: Two-dimensional grazing-incidence wide-angle X-ray scattering (GIWAXS) is a powerful tool that allows us to determine both the overall polymer crystallinity and the orientation of the crystalline domains. From the 2-D patterns, the extent of polymer orientation can be determined by looking at the intensity of the (100) lamellar stacking peak compared to the (010) π-π stacking peak, and examining both conventional out-of-plane scattering (i.e. looking at diffraction planes oriented parallel to the plane of the substrate), and in-plane scattering (i.e. focusing on diffraction planes oriented perpendicular to the plane of

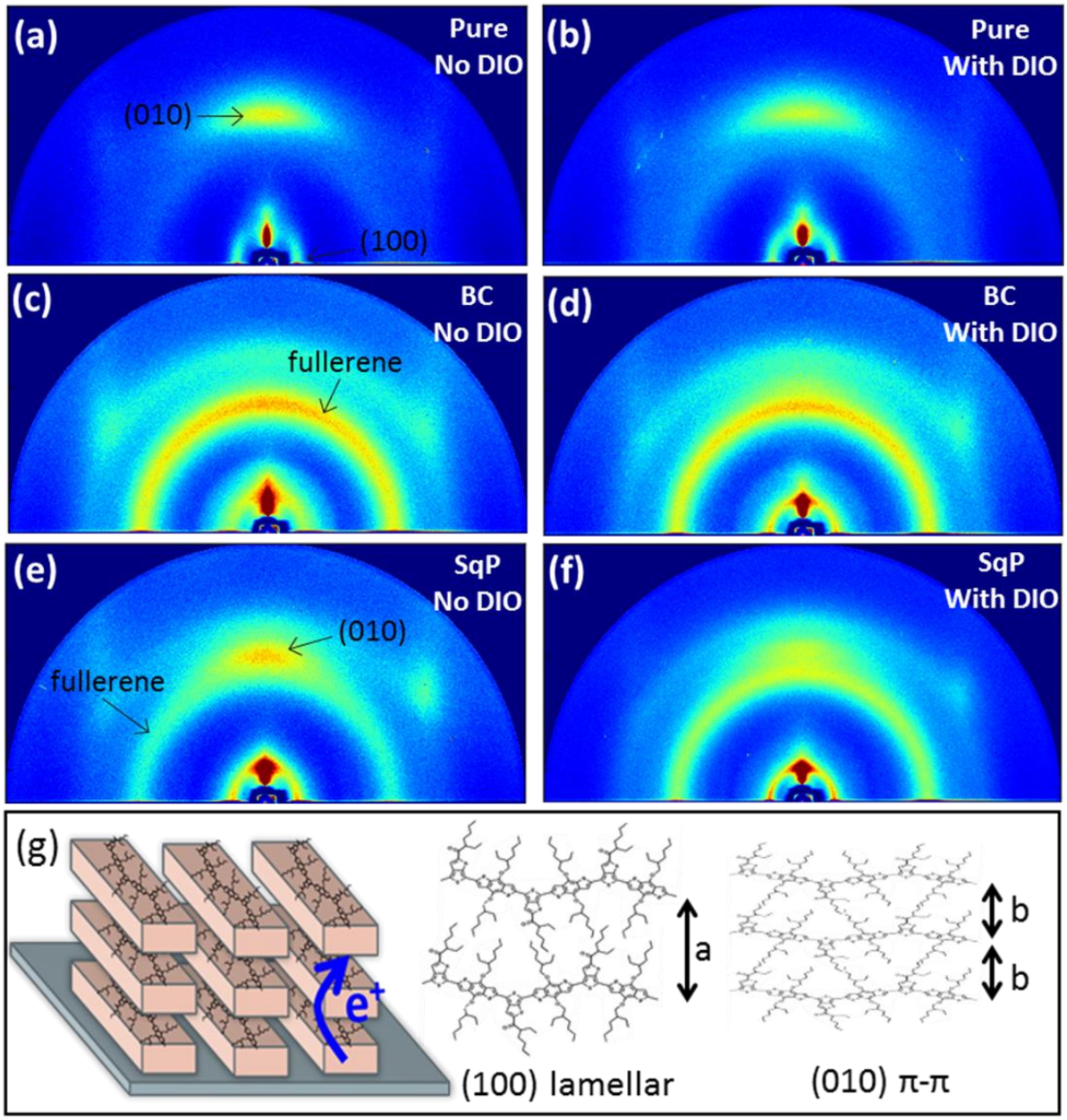

Figure 4.1. Raw GIWAXS diffractograms for pure polymer (a) and with DIO (b) showing face-on polymer orientation. Blend cast (c,d) and sequential processed (e,f) with and without DIO diffractograms exhibit isotropic fullerene orientation. Face-on polymer orientation is more pronounced for SqP films. Cartoon of face-on orientation and polymer chain orientation depicting the (100) and (010) stacking (g).

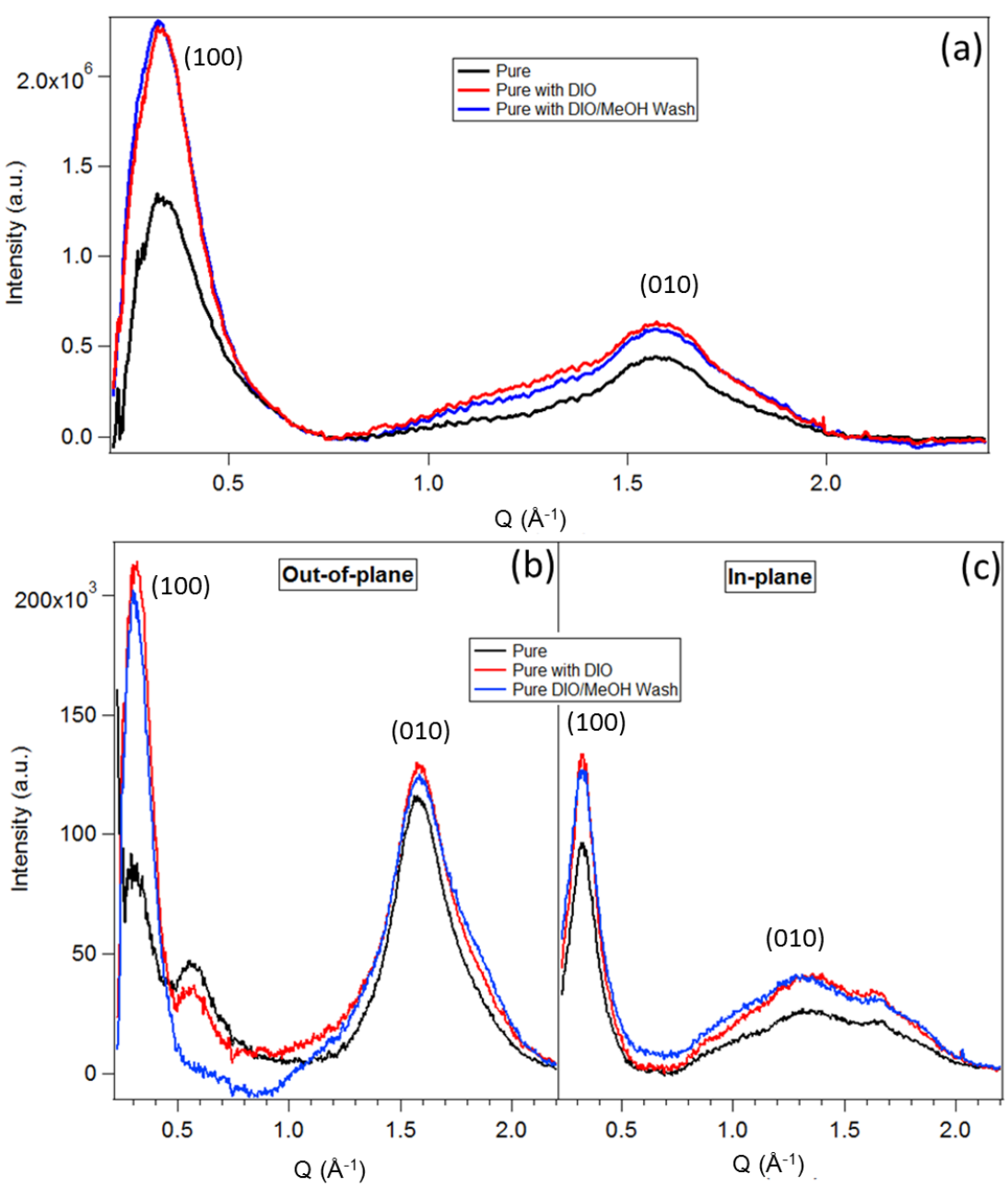

Figure 4.2. (a) Full integration of GIWAXS diffractograms for pure polymer showing the increase in crystallinity with the addition of DIO, where the black curves are pure polymer, red curves are polymer with 3% DIO and blue curves are after washing the DIO away with methanol. Face-on orientation shown by strong (010) diffraction out-of-plane (b) with very little intensity in-plane (c).

the substrate).

To study how the polymer structure changes with different processing conditions, we measured the 2-D scattering from blend-cast and sequentially-processed PBDTTT-C:$PC_{71}BM$ BHJ devices in addition to PBDTTT-C pure films, as shown in Figure 4.1 (a)-(f). From the raw diffractogram of the pure polymer (Figure 4.1a), the face-on orientation can clearly be seen, with the (100) lamellar peak located primarily in-plane and the (010) π-π stacking peak is primarily in the out-of-plane direction. A cartoon depicting this face-on orientation of the polymer chains in shown in Figure 4.1(g). The spots located at about 45-degrees are due to the silicon substrate and have been subtracted in the integrations discussed below.

The addition of DIO to blend-cast solutions of polymer and fullerene has been shown to improve the power conversion efficiency in a variety of systems.[52,59–61] Thus, we also looked at the effect of DIO on the structures of pure PBDTTT-C films and sequentially-processed BHJ films in addition to the well-studied blend-cast system with $PC_{71}BM$. The use of DIO in the pure polymer films does not seem to change the polymer orientation (Fig. 1b). For blend-cast and sequentially-processed BHJ films, however, a strong, amorphous fullerene scattering peak is observed near the polymer (010) peak. This fullerene scattering hinders our ability to visually determine the polymer orientation. As a result, more quantitative methods must be used to extract information on the polymer orientation within the BHJ films.

Beginning with pure PBDTTT-C films, we radially integrated the 2-D diffractograms shown in Figure 4.1 to obtain information on the overall crystallinity and crystallite size, as depicted in Figure 4.2(a). The pure polymer exhibits the characteristic (100) and (010) peaks, as expected, at $q \approx 0.33$ $Å^{-1}$ (19.0 Å) and 1.57 $Å^{-1}$ (4.0 Å), respectively. Upon the addition of DIO, a marked increase in the overall crystallinity of the pure polymer is observed. Although DIO is

typically thought of as a solubilizer for PBCM,[62–65] in this case it clearly acts to facilitate further crystallization in pure polymer films. This could be due to its low volatility compared to the polymer-casting solvent, as slower drying is known to create a more crystalline polymer film.

We next examined the results of performing a subsequent methanol wash of the pure polymer films cast with DIO, which has been shown to substantially improve the performance of blend-cast devices by removing any residual DIO solvent remaining in the films.[66] For the pure polymer films, however, we observed that methanol washing produces very little change over the DIO-treated films. In fact, neither methanol nor the 2-CP:DCM blend (the fullerene-casting solvent we used for sequential processing) significantly changed the polymer crystallinity or chain orientation.

In addition to information about the crystallinity, the extent of the polymer chain orientation in the pure polymer films can be better determined by directionally integrating the diffractograms. To look at the orientation, we took 10° integration slices in the out-of-plane (Figure 4.2b) and the in-plane (Figure 4.2c) directions. By comparing the out-of-plane and in-plane peaks, it is apparent that the PBDTTT-C chains in pure films lie mostly face on, with the π-π stacking occurring primarily in the out-of-plane direction at a q of 1.57 $Å^{-1}$. The addition of DIO causes a slight shift in this peak to higher *q* at 1.58 $Å^{-1}$, indicating tighter π-π packing, which should be favorable for conduction. We also see some (010) scattering intensity in the in-plane direction; this broad peak, shifted to lower *q* (centered at about 1.3 $Å^{-1}$) indicates the presence of some disordered, edge-on polymer chains that have a significantly larger π-π stacking distance within the pure film. Thus, while the chains in the pure film are not perfectly face-on, PBDTTT-C films do have an excess of face-on domains. And although DIO causes an increase in overall crystallinity, it does still maintain the orientation of the polymer, as observed in Figure 4.2(b). This

preservation of chain orientation makes PBDTTT-C a promising candidate for BHJ improvement for both blend-cast and sequentially-processed films.

4.2.1.2 Polymer Orientation in Blend-Cast PBDTTT-C with $PC_{71}BM$: Now that we have an understanding of the chain conformation and the effects of DIO on pure PBDTTT-C films, we turn to assessing whether or not this orientation is maintained during blend-casting with $PC_{71}BM$. The fully-integrated diffractograms for blend-cast BHJs are shown in Figure 4.3(a), which correspond to the 2-D images in Figure 4.2(c) and (d). The data shows both the lamellar polymer diffraction at 0.36 $Å^{-1}$ and several $PC_{71}BM$ scattering peaks located at 0.66 $Å^{-1}$, 1.34 $Å^{-1}$, and 1.89 $Å^{-1}$. In addition to increasing the polymer crystallinity, as expected, the use of DIO as a solvent additive also decreases the lamellar (100) polymer peak width. Since peak width is inversely proportional to the correlation length of the polymer domains, this means that DIO acts to create much larger and/or more crystalline PBDTTT-C domains.[46,67] This increase enables better hole conductivity through the polymer and is partially responsible for the increase in the overall current observed for the DIO treated blend-cast BHJ devices, whose properties are discussed below in Figure 4.5 and Table 4.1.

Unlike with the pure polymer films, we do see changes in the structure of DIO-added blend-cast BHJ films upon washing with methanol. Although the overall polymer crystallinity remains unchanged, methanol washing causes a significant increase in the fullerene crystallinity, as seen by the increase in the peak centered at about 1.3 $Å^{-1}$ in Fig. 3(a). The removal of DIO clearly enables $PC_{71}BM$ to pack better and form more crystalline domains, creating a better overall network. In addition to removing the DIO, the methanol wash also likely removes some of the residual blend-casting solvent as well.[66] We also looked at the effect of methanol washing a blend-cast film without any DIO additive, and an increase in fullerene crystallinity upon washing can

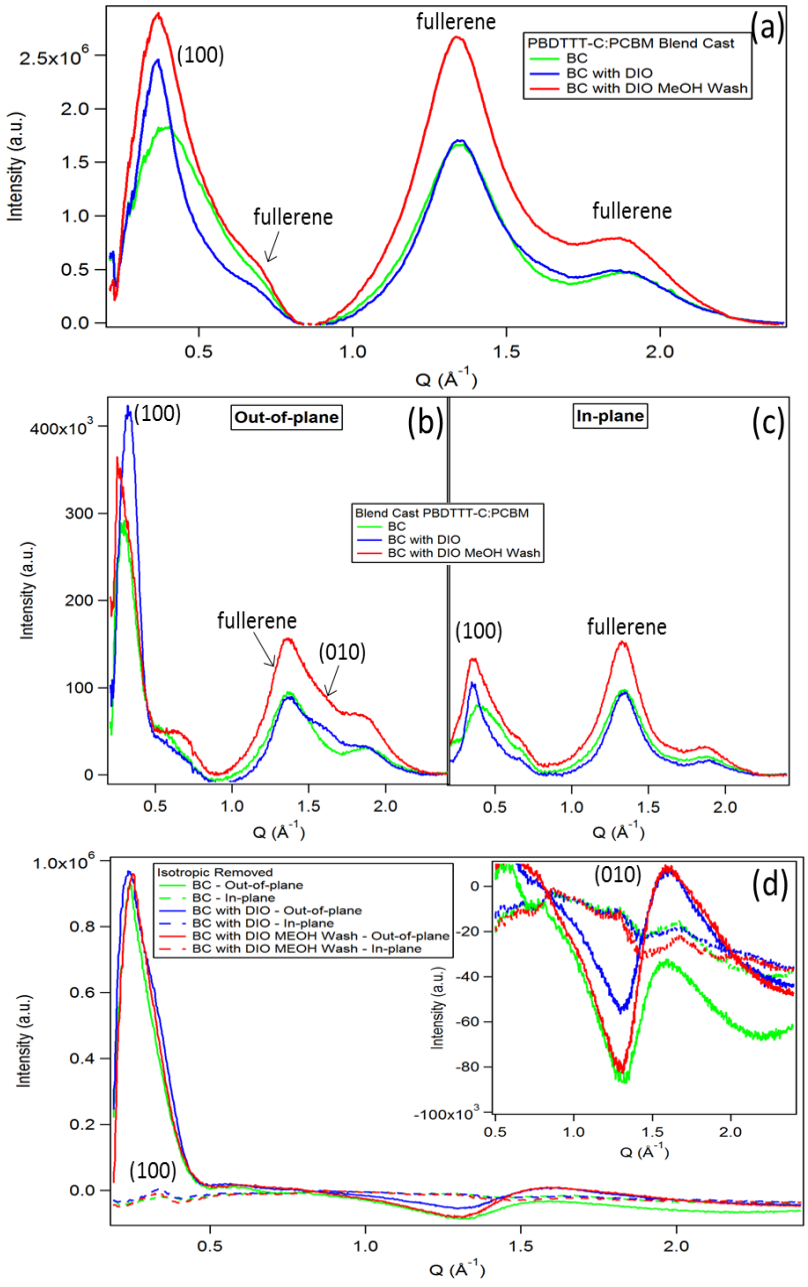

Figure 4.3. (a) Full integration of GIWAXS diffractograms for 1:1.5 PBDTTT-C:PCBM blend cast (BC) films without DIO (green), with 3% DIO (blue), and methanol washed (red). Isotropic fullerene orientation is observed by the equal intensity (b) out-of-plane and (c) in-plane. (d) Out-of-plane and in-plane diffraction after subtraction of isotropic fullerene, inset is a zoom in of the (010) polymer region.

also be observed (data not shown), though to a much lesser extent than in films prepared with DIO.

Similar to pure polymer, it is necessary to compare the in-plane and out-of-plane diffraction of our blend-cast BHJs to determine the polymer orientation, as plotted in Figure 4.3(b) and (c). In these panels, we see a large out-of-plane (100) lamellar stacking peak, which dominates the in-plane lamellar diffraction. This indicates that the polymer in blend-cast BHJs has an orientation that is more edge-on, rather than mostly face-on as it is for the pure polymer.

Unfortunately, the (010) π-π stacking peak is still largely obscured by the presence of the large, isotropic fullerene scattering centered at 1.34 $Å^{-1}$. For the sample with DIO, the (010) peak can be seen as a small shoulder, but the intensity in either sample is too small for quantitative analysis. To extract out the (010) π-π stacking peak from the fullerene peak, we took a 10° radial segment from the diffractogram centered at 45°, which contains scattering from any peaks with an isotropic orientation. Since the fullerene diffraction is isotropic, we subtracted the 45° segment from both the out-of-plane and in-plane data in Figure 4.3(b) and (c), respectively. This procedure should leave only the non-isotropic polymer diffraction. The results of these subtractions are shown in Figure 4.3(d), where we see that the lamellar peak for the blend-cast film is now lies entirely out-of-plane. This indicates that there are no preferentially in-plane oriented domains (i.e. face-on domains), but rather just isotropic polymer (which is subtracted away using the 45° data), and edge on polymer domains (which remain).

If we next focus on the region where the (010) π-π scattering peak should occur, the subtracted data are even more complex. For the in-plane direction, little non-isotropic scattering is observed. In the out-of-plane direction, by contrast, we do not see a distinct peak, but rather a derivative shape, where the intensity is uniformly less than the baseline. Since the (010) out-of-plane intensity is less than that of the isotropic (45°) diffraction, this is again an indication that the

PBDTTT-C is no longer face-on. The derivative shape arising from subtracting two peaks with different positions. For the pure polymer, we showed the existence of a more disordered π-π peak at lower q that occurred primarily in-plane, and a higher q out-of-plane peak corresponding to more ordered face on polymer. The derivative shape thus corresponds to a shift in peak position from high q (longer π-π distance) to low q (shorter π-π distance), but the fact that the whole subtracted shape has negative values indicates that there is both a peak shift and a decrease in the out-of-plane (010) scattering intensity relative to the isotropic peak. The combination of increased out-of-plane lamellar diffraction and decreased out-of-plane π-stacking intensity indicate that for blend-cast films without DIO, the polymer no longer has a face-on orientation.

Finally, we can compare the blend-cast BHJ films with and without DIO. When DIO additive is used in the casting solution, we see both a higher-intensity (100) lamellar peak in-plane, and a 45°-subtracted curve that is closer to the baseline in the (010) region (Figure 4.3c). Both of these indicate a slightly more of a face-on orientation of the polymer chains for the films cast with DIO. Thus, DIO must decrease the interaction between PBDTTT-C and $PC_{71}BM$, enabling the polymer to adopt more of its native, face-on orientation. This, in combination with the increased crystallite size discussed above, explains the increase in current and overall performance observed in blend-cast devices made with DIO (see Figure 4.5, below).

4.2.1.3 Polymer Orientation in Sequentially-Processed PBDTTT-C BHJs with $PC_{71}BM$: One goal in using naturally face-on oriented polymers is to be able to preserve this polymer orientation in BHJ devices blended with fullerene. We have shown above, however, that the face-on morphology is not well preserved by typical blend-casting techniques, even with the use of DIO. Thus, in this section we turn to assessing the morphology in sequentially-processed films. In

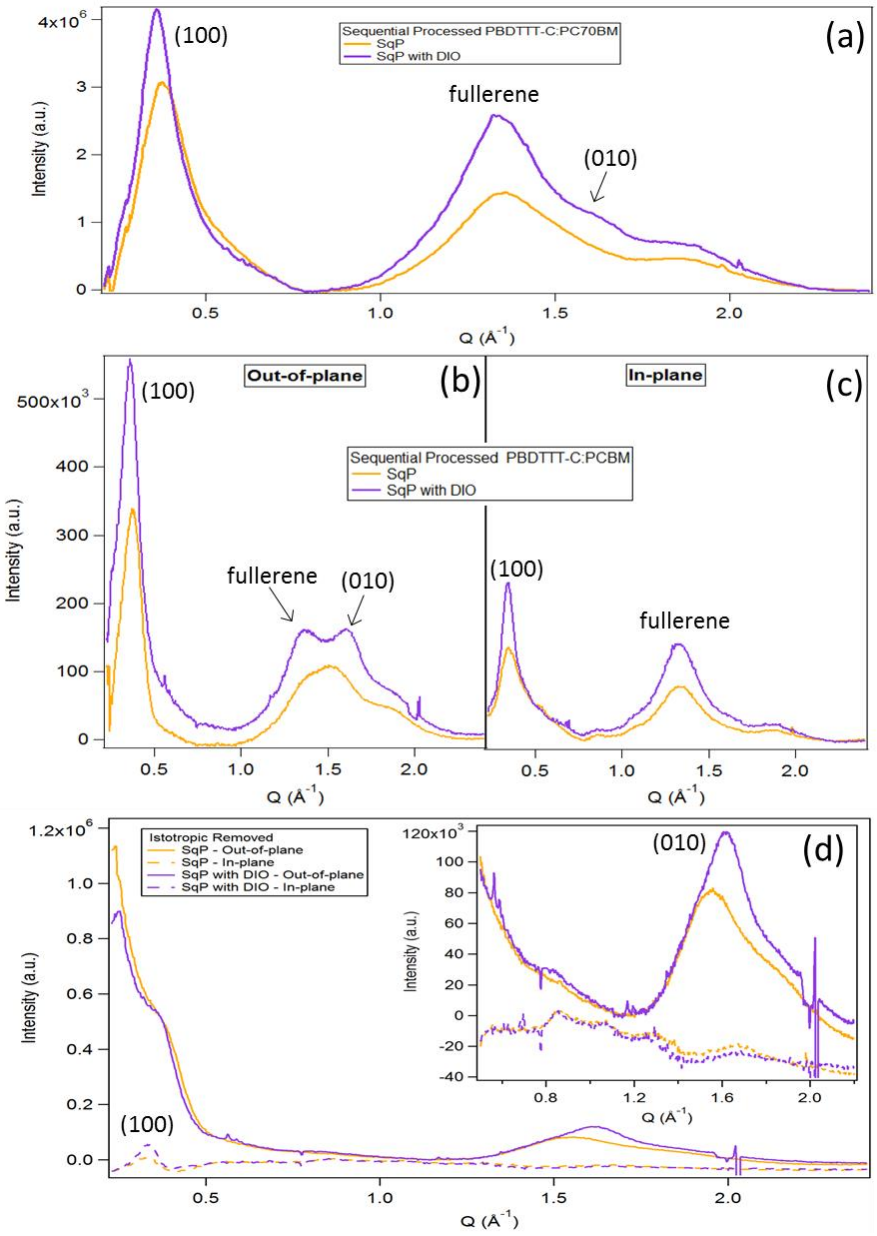

Figure 4.4. (a) Full integration of GIWAXS diffractograms for 1:1.5 PBDTTT-C:PCBM sequential processed (SqP) films, where the orange curves have no additive and the purple curves have 3% DIO in the polymer. (b) out-of-plane and (c) in-plane cuts showing polymer orientation. (d) Out-of-plane and in-plane diffraction after subtraction of isotropic fullerene, inset is a zoom in of the (010) polymer region.

previous work, we have argued that SqP preserves much of the morphology of the original polymer film,[22,23,28] so it is entirely possible that the net orientation could be different in blend-cast and sequentially-processed BHJs of the same materials.

Figure 4.4(a) shows radially-integrated 2-D GIWAXS diffractograms for PBDTTT-C films after BHJ formation by deposition of $PC_{71}BM$ via SqP. We note that in sequential processing, since the vapor pressure of DIO is so low, if DIO is used in the polymer casting solution, it likely remains in the film during the fullerene deposition stage. Consistent with what we saw above for pure polymer films, Fig. 4.4(a) shows that the addition of DIO to the polymer casting solution increases the polymer crystallinity in the sequentially-processed BHJs. The presence of DIO in the polymer solution also causes an increase in the intensity of the $PC_{71}BM$ scattering peak centered at 1.34 $Å^{-1}$. The increase of the fullerene scattering peak indicates that the DIO enables more $PC_{71}BM$ to diffuse into the polymer, likely because of enhanced polymer swelling. By dissolving away the SqP film,[22] we confirmed the samples had a higher fullerene content of 1:3.5 PBDTTT-C:$PC_{71}BM$ in comparison to the films fabricated by blend casting (1:1.5 PBDTTT-C:$PC_{71}BM$). As discussed below, this increase in fullerene content is beneficial to device performance, as seen through EQE (Figure 4.5b).

In comparison with the blend-cast BHJ films, the in- and out-of-plane diffraction of the sequentially-processed BHJ films (Figure 4.4, b and c) shows another pronounced difference in scattering anisotropy. The data clearly show a (010) scattering peak (shoulder) in the out-of-plane direction for the sequentially-processed films made with DIO in the polymer casting solution. The presence of this strong out-of-plane π-π peak means that the PBDTTT-C in the sequential processed BHJs is far more face-on than in its blend-cast counterparts. Additionally, more (100) lamellar intensity is observed in the in-plane direction for the sequentially-processed BHJs than

was seen with the blend-cast films.

Figure 4.4(d) shows the results of the same analysis as above, emphasizing the scattering anisotropy in the (010) peak by subtracting out the isotropic diffraction at 45°. Contrary to the blend-cast films, where the subtraction led to a derivative shape, the sequentially-processed PBDTTT-C:$PC_{71}BM$ BHJs instead show a distinct peak in the (010) region (inset of Figure 4d). As with the scattering from pure polymer films, this (010) peak exhibits a peak shift upon the addition of DIO, indicative of closer π-π stacking. This closer π-π packing should be highly beneficial for the hole mobility and overall device performance. Moreover, the (100) lamellar stacking scattering in the sequentially-processed BHJs shows more in-plane intensity than in the blend-cast samples, indicating a more face-on orientation as well. Thus, unlike with blend-cast BHJs, the SqP appears to preserve the strongly face-on polymer orientation found in the pure polymer samples.

4.2.2 Device Performance of Blend-Cast and Sequentially-Processed PBDTTT-C:$PC_{71}BM$ BHJs

To understand how all of the above structural observations are correlated with actual device performance, we fabricated OPVs with both blend-cast and sequentially-processed PBDTTT-C:$PC_{71}BM$ active layers, both with DIO as an additive and without; the results are summarized in Figure 4.5. As has been observed in previous work,[52,59–61] the addition of DIO during blend casting can improve overall device efficiency. Our blend-cast data fit with this expectation, as we observe an increase in overall power conversion efficiency from 4.4% to 5.0% upon the addition of 3% DIO (Figure 4.5(a) and Table 4.1). The boost in efficiency arises from a slight improvement in the fill factor and a large improvement in the short-circuit current, $-J_{SC}$, from 12.7 mA/cm^2 to 15.4

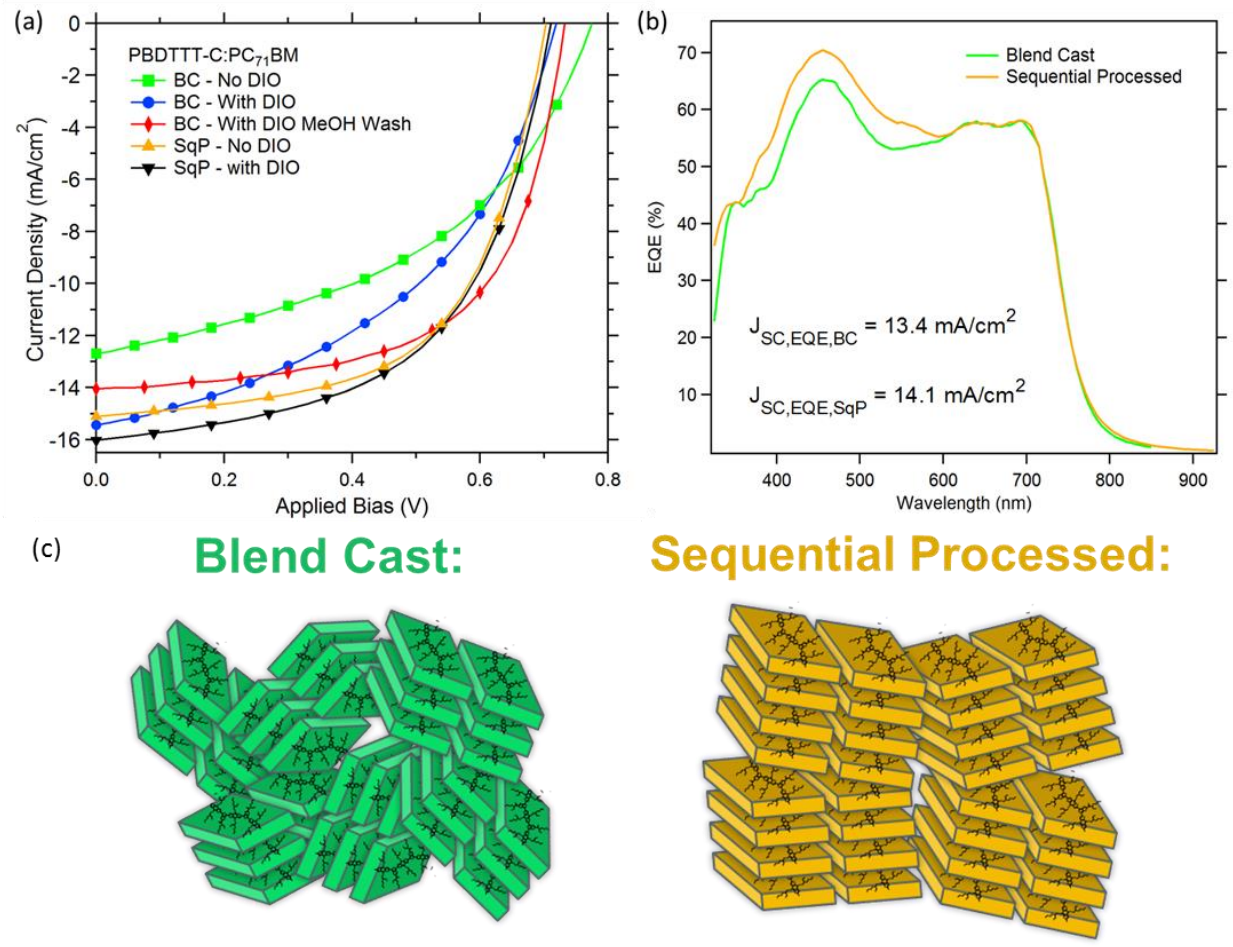

Figure 4.5. (a) *J-V* device curves for blend cast films without additives (green squares) and with DIO (blue circles). Additional improvement is seen with methanol washing the DIO films (red diamonds). Sequential processing without the use of additives (orange triangles) shows slight improvement over the blend cast films. All devices have the structure: ITO/PEDOT:PSS/PBDTTT-C:$BC_{71}BM$:Ca/Al. (b) External quantum efficiency (EQE) for blend cast and sequentially processed films without DIO, showing higher current with SqP. (c) Cartoon depicting the chain orientation within the polymer domains for blend cast (left) and sequentially processed (right), showing more disorder in the blend cast films.

Table 4.1. Summary of *J-V* Characteristics for the devices shown in Figure 4.5

Sample		**V_{oc} (V)**	**J_{sc} (mA/cm^2)**	**FF (%)**	**PCE (%)**
Blend Cast	no DIO	0.775	-12.7	45	4.4
	with DIO	0.719	-15.4	46	5.0
	with DIO/MeOH Wash	0.733	-14.0*	61	6.3
Sequentially Processed	no DIO	0.701	-15.1*	59	6.3
	with DIO/MeOH Wash	0.711	-16.0	56	6.3

*J_{SC} obtained from EQE for blend cast films with DIO/MeOH wash and SqP films without DIO are -13.4 mA/cm^2 and -14.1 mA/cm^2, respectively

mA/cm^2 for devices without and with DIO, respectively. Upon washing the blend-cast with DIO films with methanol, the PCE is further increased to 6.3% (6.1% EQE corrected) due to the more favorable rearrangement of the fullerene upon DIO removal, as discussed above.

Although this increase in PCE upon the addition of DIO was expected for blend-cast systems, we also see an increase when using sequential processing to create BHJ devices. Without the use of any additives, sequential processing produces a slight increase in J_{SC} compared to blend-cast active layers, which is verified by the external quantum efficiency measurements shown in Fig. 5b. The EQE also shows the effect of the increased fullerene content in the SqP devices by the increase in the peak centered at about 475 nm. We note that a similar improvement in J_{SC} with SqP compared to blend-casting has been seen with a related polymer, PBDTTT-C-T;[19] in the case of PBDTTT-C-T, however, the J_{SC} improvement was attributed to vertical phase separation, rather than to changes in the polymer domain orientation as we postulate here. For PBDTTT-C, besides the increase in current, we also see a significant enhancement of the fill factor with SqP, which increases to 57% from the 45% seen for blend-cast films. Even in comparison to the blend-cast device with DIO, our additive-free sequentially-processed device yields a PCE that is 0.5% higher. We believe that this improvement arises from the more favorable domain orientation in the sequentially-processed devices.

In contrast to the blend-cast films, however, the addition of DIO to the polymer layer does not have a large effect on the overall performance of sequentially-processed devices. The removal of the DIO after fullerene incorporation with a methanol wash, as was performed with the blend-cast samples, also yielded the same overall device performance (Figure 4.5a). To ensure the DIO in the polymer layers was not removed during SqP by the fullerene casting solvent, we additionally looked at SqP devices fabricated with 3% DIO in the fullerene solvent as well. Interestingly, these

devices still showed no improvement, even with methanol washing, over the SqP devices with no additives. As discussed above, the addition of DIO to the polymer casting solution does lead to increased X-ray scattering from fullerene. The lack of change in the PCE with DIO indicates that a slight increase in fullerene content and/or crystallinity is not important for device performance. Since PBDTTT-C maintains the same face-on orientation in both cases, we believe that orientation changes of the polymer are the key to DIO-based performance enhancements in blend-cast devices. It is also worth noting that some researchers have concluded that the mechanism of performance enhancement behind methanol washing is a favorable alteration of the buried PEDOT interface.[68–70] However, our SqP methanol washing results conclusively indicate that this is not the case, since there is little effect on performance with methanol washing. Instead, our results indicate that a methanol treatment improves performance by removing residual DIO, which consequently alters the blend cast morphology in a favorable manner.[66]

Comparing SqP with blend-casting, we can see that the morphology plays a significant role in the overall performance. For the blend-cast films, the isotropic orientation (Figure 4.5c) lead to a significant decrease in both the current and fill factor without the use of additive when compared to the face-on orientation of the SqP films. While the addition of DIO to the blend-cast films causes and increase in overall PBDTTT-C crystallinity, the improvement in device performance likely arises from the shift to a slightly more face-on polymer orientation. In contrast, sequential processing does not need the additional additive for improvement, as the most favorable polymer orientation is already obtained in a pure film without DIO.

4.3 Conclusions

In this work, we have shown that the face-on orientation of pure PBDTTT-C films is not

preserved when standard blend-casting techniques for creating BHJs with fullerenes are employed. The interactions of the polymer with $PC_{71}BM$ dominate the polymer-substrate interactions, leading to a loss of the natural face-on polymer orientation upon film formation. The addition of DIO does slightly restore the face-on tendency, but the effect is not dramatic.

By producing BHJ devices from PBDTTT-C using sequential processing, however, the face-on orientation of the polymer can be preserved, as summarized in the Figure 4.5(c). Sequential processing thus enables us to translate pure polymer properties and preserve them in blended BHJ films. The benefits of preserving the face-on polymer orientation are seen in device performance. Face-on orientation enables more efficient hole conduction through the polymer π-system, yielding a higher fill factor in OPV devices. Overall, even though the final device performance for this polymer/fullerene combination is similar for blend-cast and sequentially-processed devices, the structure of the polymer in the two devices is remarkably different. Additionally, for SqP, this device performance was obtainable without the use or optimization of solvent additives to drive the desired structure. This shows that there are a wide range of underlying BHJ architectures that can lead to good device performance, which explains why the intermixed BHJ-concept works.[22]

Overall, our work emphasizes that there are two distinct processing methods for creating OPV active layers that can be used to enhance different aspects of polymer structure and nanoscale morphology. By adding SqP alongside blend-casting to the OPV processing toolbox, researchers now have new ways to robustly and reproducibly create large-scale optimized low-cost polymer photovoltaic devices.

4.4 Experimental

The polymer poly[4,8-bis-(2-ethylhexyloxy)-benzol[1,2-b:4,5-b']dithiophene-2,6-diyl-alt-4-(2-ethylhexyloxy-1-one)thieno[3,4-b]thiophene-2,6-diyl] (PBDTTT-C) and [6,6]-phenyl-C_{71}-butyric-acid-methylester ($PC_{71}BM$) were purchased from Solarmer and used as received. All devices were fabricated on indium-doped tin oxide (ITO) substrates that were sequentially sonicated in baths of detergent, water, acetone, and isopropyl alcohol followed by UV ozone treatment for 20 minutes. Subsequently, 35 nm of poly(ethylenedioxythiophene): poly(styrenesulfonic acid) (PEDOT:PSS Clevios PVP AI 4083) was deposited onto the ITO to form the hole collection layer.

For the blend-casting procedure, a 1:1.5 wt/wt PBDTTT-C:$PC_{71}BM$ solution was made at a concentration of 10 mg/mL polymer in ODCB. Blend-cast solutions containing diiodooctane were made 3% v/v. Blend-cast solutions were deposited onto an ITO substrate (150 nm, 25 Ω/□) coated with a ~90-nm thick active-layer film. Sequentially-processed films were fabricated by depositing either a solution of pure PBDTTT-C or a solution with 3% v/v DIO, both at a concentration of 10 mg/mL ODCB, at 2500 rpm for 60 s. $PC_{71}BM$ was then deposited onto the fully dry polymer layer by spin coating at 2000 rpm for 60 s out of a 10 mg/mL solution in a 1:1 mixture of 2-chlorophenol:dichloromethane. The final PBDTTT-C:$PC_{71}BM$ ratio was determined by re-dissolving the SqP films in ODCB and fitting the absorbance profile to a linear combination of pure PBDTTT-C and pure $PC_{71}BM$ absorbance.[22] Both blend-cast and sequentially-processed films were fabricated into devices without further treatment by thermally evaporating 10 nm of Ca and 70 nm of Al as cathodes at a pressure of 1×10^{-6} Torr using an Ångstrom Engineering NexDep evaporator. The Ca layer was deposited at a rate of 0.5 Å/s to a thickness of 10 nm, and the Al layer was deposited at a rate of 1.5 Å/s to a thickness of 80 nm. Before exposing the devices to the

metals, ~10 nm of Ca was evaporated onto the shutter to ensure layer purity.

Photovoltaic performance was measured in an Argon atmosphere using a Keithley 2400 sourcemeter and AM-1.5 filtered light from a xenon arc lamp source equipped with a liquid light guide (Oriel). The incident light intensity on tested samples was adjusted to be 100 mW/cm^2 using a KG-5 calibrated Si diode. EQE measurements were collected using a chopped (23 Hz) monochromatic beam (Newport TLS-300X) measured across a 50 Ω resistor using a SR830 lock-in amplifier. Because the currents are low, the voltage across the resistor and therefore the device is also low, which means that short-circuit conditions are well-maintained at all times. Multiple long-wave-pass filters (90% transmission cut-on @ 345 nm, 605 nm, 850 nm, 1030 nm, and 1550 nm) were used during the measurement to remove high-energy light transmitted through the monochromator due to lower-order reflections. Each data point was taken from the amplitude readout of the lock-in and averaged for ~5 time constants.

2-D grazing incidence wide-angle X-ray scattering (GIWAXS) measurements were performed at the Stanford Synchrotron Radiation Lightsource (SSRL) on beam line 11-3 using a wavelength of 0.9742 Å. Diffraction patterns were collected on a 2-D image plate with a sample to detector distance of 400 mm and a spot size of roughly 150 μm. A helium chamber was utilized to increase the signal-to-noise. Blend-cast and sequentially-processed films for GIWAXS were prepared as above, except using silicon substrates (with a 1.8-nm SiO_2 native oxide layer) instead of ITO. Pure polymer films were spun onto PEDOT:PSS (35 nm) at 2000 rpm for 60 seconds from 10 mg/mL PBDTTT-C in ODCB. As above, solution samples with the DIO solvent additive were made 3% DIO v/v prior to spin coating.

For the analysis of the GIWAXS data, the 2-D diffraction for each sample was integrated using WxDiff. The limits of the integration were changed based on the orientation information

desired. To obtain a full integration of a diffractogram, the integration limits over chi were from 0° to 180°. For in-plane, out-of-plane, and 45° integration, the limits were 0°-10°, 80°-90°, and 40°-50°, respectively. The intensities on the opposite sides of the diffractogram (90°-180°) were also checked to ensure they were the same as the chosen limits. Each integration was background corrected for the substrate scattering by subtracting the scattering from a pure PEDOT:PSS films on silicon. The subtractions were performed on the raw scattering data to ensure no errors occurred.

4.5 References

(1) Green, M. A.; Emery, K.; Hishikawa, Y.; Warta, W.; Dunlop, E. D. Solar Cell Efficiency Tables (version 43). *Prog. Photovoltaics Res. Appl.* **2014**, *22*, 1–9.

(2) He, Z.; Zhong, C.; Su, S.; Xu, M.; Wu, H.; Cao, Y. Enhanced Power-Conversion Efficiency in Polymer Solar Cells Using an Inverted Device Structure. *Nat. Photonics* **2012**, *6*, 591–595.

(3) Collins, B. A.; Tumbleston, J. R.; Ade, H. Miscibility, Crystallinity, and Phase Development in P3HT/PCBM Solar Cells: Toward an Enlightened Understanding of Device Morphology and Stability. *J. Phys. Chem. Lett.* **2011**, *2*, 3135–3145.

(4) Halls, J. J. M.; Walsh, C. A.; Greenham, N.; Marseglia, E. A.; Friend, R.; Moratti, S. C.; Holmes, A. Efficient Photodiodes from Interpenetrating Polymer Networks. *Nature* **1995**, *376*, 498–500.

(5) Shaheen, S. E.; Brabec, C. J.; Sariciftci, N. S.; Padinger, F.; Fromherz, T.; Hummelen, J. C. 2.5% Efficient Organic Plastic Solar Cells. *Appl. Phys. Lett.* **2001**, *78*, 841–843.

(6) Shaw, P. E.; Ruseckas, A.; Samuel, I. D. W. Exciton Diffusion Measurements in Poly(3-Hexylthiophene). *Adv. Mater.* **2008**, *20*, 3516–3520.

(7) Yu, G.; Gao, J.; Hummelen, J. C.; Wudl, F.; Heeger, A. J. Polymer Photovoltaic Cells: Enhanced Efficiencies via a Network of Internal Donor-Acceptor Heterojunctions. *Science (80-.).* **1995**, *270*, 1789–1791.

(8) Peet, J.; Soci, C.; Coffin, R. C.; Nguyen, T. Q.; Mikhailovsky, A.; Moses, D.; Bazan, G. C. Method for Increasing the Photoconductive Response in Conjugated Polymer/fullerene Composites. *Appl. Phys. Lett.* **2006**, *89*, 252103–252105.

(9) Peet, J.; Kim, J. Y.; Coates, N. E.; Ma, W. L.; Moses, D.; Heeger, A. J.; Bazan, G. C. Efficiency Enhancement in Low-Bandgap Polymer Solar Cells by Processing with Alkane Dithiols. *Nat. Mater.* **2007**, *6*, 497–500.

(10) Lee, J. K.; Ma, W. L.; Brabec, C. J.; Yuen, J.; Moon, J. S.; Kim, J. Y.; Lee, K.; Bazan, G. C.; Heeger, A. J. Processing Additives for Improved Efficiency from Bulk Heterojunction Solar Cells. *J. Am. Chem. Soc.* **2008**, *130*, 3619–3623.

(11) Zhao, Y.; Xie, Z.; Qu, Y.; Geng, Y.; Wang, L. Solvent-Vapor Treatment Induced Performance Enhancement of poly(3-Hexylthiophene):methanofullerene Bulk-Heterojunction Photovoltaic Cells. *Appl. Phys. Lett.* **2007**, *90*, 43503–43504.

(12) Jo, J.; Na, S.-I.; Kim, S.-S.; Lee, T.-W.; Chung, Y.; Kang, S.-J.; Vak, D.; Kim, D.-Y. Three-Dimensional Bulk Heterojunction Morphology for Achieving High Internal Quantum Efficiency in Polymer Solar Cells. *Adv. Funct. Mater.* **2009**, *19*, 2398–2406.

(13) Ma, W.; Yang, C.; Gong, X.; Lee, K.; Heeger, A. J. Thermally Stable, Efficient Polymer Solar Cells with Nanoscale Control of the Interpenetrating Network Morphology. *Adv. Funct. Mater.* **2005**, *15*, 1617–1622.

(14) Kim, K.; Liu, J.; Namboothiry, M. A. G.; Carroll, D. L. Roles of Donor and Acceptor Nanodomains in 6% Efficient Thermally Annealed Polymer Photovoltaics. *Appl. Phys. Lett.* **2007**, *90*, 163511.

(15) Verploegen, E.; Mondal, R.; Bettinger, C. J.; Sok, S.; Toney, M. F.; Bao, Z. Effects of Thermal Annealing Upon the Morphology of Polymer/Fullerene Blends. *Adv. Funct. Mater.* **2010**, *20*, 3519–3529.

(16) Ayzner, A. L.; Tassone, C. J.; Tolbert, S. H.; Schwartz, B. J. Reappraising the Need for Bulk Heterojunctions in Polymer− Fullerene Photovoltaics: The Role of Carrier Transport in All-Solution-Processed P3HT/PCBM Bilayer Solar. *Journal of Physical Chemistry C* **2009**, *113*, 20050–20060.

(17) Gevaerts, V. S.; Koster, L. J. A.; Wienk, M. M.; Janssen, R. A. J. R. A. J. Discriminating between Bilayer and Bulk Heterojunction Polymer:Fullerene Solar Cells Using the External Quantum Efficiency. *ACS Appl. Mater. Interfaces* **2011**, *3*, 3252–3255.

(18) Moon, J. S.; Takacs, C. J.; Sun, Y.; Heeger, A. J. Spontaneous Formation of Bulk Heterojunction Nanostructures: Multiple Routes to Equivalent Morphologies. *Nano Lett.* **2011**, *11*, 1036–1039.

(19) Cheng, P.; Hou, J.; Li, Y.; Zhan, X. Layer-by-Layer Solution-Processed Low-Bandgap Polymer-PC 61 BM Solar Cells with High Efficiency. *Adv. Energy Mater.* **2014**, DOI: 10.1002/aenm.201301349.

(20) Treat, N. D.; Brady, M. A.; Smith, G.; Toney, M. F.; Kramer, E. J.; Hawker, C. J.; Chabinyc,

M. L. Interdiffusion of PCBM and P3HT Reveals Miscibility in a Photovoltaically Active Blend. *Adv. Energy Mater.* **2011**, *1*, 82–89.

(21) Ayzner, A. L.; Doan, S. C.; Tremolet de Villers, B.; Schwartz, B. J. Ultrafast Studies of Exciton Migration and Polaron Formation in Sequentially Solution-Processed Conjugated Polymer/Fullerene Quasi-Bilayer Photovoltaics. *J. Phys. Chem. Lett.* **2012**, *3*, 2281–2287.

(22) Hawks, S. A.; Aguirre, J. C.; Schelhas, L. T.; Thompson, R. J.; Huber, R. C.; Ferreira, A. S.; Zhang, G.; Herzing, A. A.; Tolbert, S. H.; Schwartz, B. J. Comparing Matched Polymer:Fullerene Solar Cells Made by Solution-Sequential Processing and Traditional Blend Casting: Nanoscale Structure and Device Performance. *Journal of Physical Chemistry C* **2014**, *118*, 17413–17425.

(23) Zhang, G.; Huber, R.; Ferreira, A.; Boyd, S. D.; Luscombe, C. K.; Tolbert, S. H.; Schwartz, B. J. Crystallinity Effects in Sequentially Processed and Blend Cast Bulk-Heterojunction Polymer/Fullerene Photovoltaics. *Journal of Physical Chemistry C* **2014**.

(24) Schwenn, P. E. P. P. E.; Gui, K.; Nardes, A. M.; Krueger, K. B.; Lee, K. H.; Mutkins, K.; Rubinstein-Dunlop, H.; Shaw, P. E.; Kopidakis, N.; Burn, P. L.; et al. A Small Molecule Non-Fullerene Electron Acceptor for Organic Solar Cells. *Adv. Energy Mater.* **2011**, *1*, 73–81.

(25) Loiudice, A.; Rizzo, A.; Latini, G.; Nobile, C.; de Giorgi, M.; Gigli, G. Graded Vertical Phase Separation of Donor/acceptor Species for Polymer Solar Cells. *Sol. Energy Mater. Sol. Cells* **2012**, *100*, 147–152.

(26) Nardes, A. M.; Ayzner, A. L.; Hammond, S. R.; Ferguson, A. J.; Schwartz, B. J.; Kopidakis, N. Photoinduced Charge Carrier Generation and Decay in Sequentially Deposited Polymer/Fullerene Layers: Bulk Heterojunction vs Planar Interface. *Journal of Physical Chemisty C* **2012**, *116*, 7293–7305.

(27) Kim, D. H.; Mei, J.; Ayzner, A. L.; Schmidt, K.; Giri, G.; Appleton, A. L.; Toney, M. F.; Bao, Z. Sequentially Solution-Processed, Nanostructured Polymer Photovoltaics Using Selective Solvents. *Energy Environ. Sci.* **2014**, *7*, 1103–1109.

(28) Aguirre, J. C.; Hawks, S. A.; Ferreira, A.; Yee, P.; Subramaniyan, S.; Jenekhe, S. A.; Tolbert, S. H.; Schwartz, B. J. Sequential Processing for Organic Photovoltaics: Design Rules for Morphology Control by Tailored Semi-Orthogonal Solvent Blends. *Adv. Energy Mater.* **2015**, *5*, 1402020.

(29) Liu, Y.; Lui, F.; Wang, H. W.; Nordlund, D.; Sun, Z.; Ferdous, S.; Russell, T. P. Sequential Deposition: Optimization of Solvent Swelling for High-Performance Polymer Solar Cells. *ACS Appl. Mater. Interfaces* **2014**, *7*, 653–661.

(30) Lee, K. H.; Schwenn, P. E.; Smith, A. R. G.; Cavaye, H.; Shaw, P. E.; James, M.; Krueger, K. B.; Gentle, I. R.; Meredith, P.; Burn, P. L. Morphology of All-Solution-Processed

"Bilayer" Organic Solar Cells. *Adv. Mater.* **2011**, *23*, 766–770.

(31) Collins, B. a.; Gann, E.; Guignard, L.; He, X.; McNeill, C. R.; Ade, H. Molecular Miscibility of Polymer Fullerene Blends. *J. Phys. Chem. Lett.* **2010**, *1*, 3160–3166.

(32) Tao, C.; Aljada, M.; Shaw, P. E.; Lee, K. H.; Cavaye, H.; Balfour, M. N.; Borthwick, R. J.; James, M.; Burn, P. L.; Gentle, I. R.; et al. Controlling Hierarchy in Solution-Processed Polymer Solar Cells Based on Crosslinked P3HT. *Adv. Energy Mater.* **2013**, *3*, 105–112.

(33) Aguirre, J. C.; Ferreira, A.; Ding, H.; Jenekhe, S. A.; Kopidakis, N.; Asta, M.; Pilon, L.; Rubin, Y.; Tolbert, S. H.; Schwartz, B. J.; et al. Panoramic View of Electrochemical Pseudocapacitor and Organic Solar Cell Research in Molecularly Engineered Energy Materials (MEEM). *Journal of Physical Chemistry C* **2014**, *34*, 19505–19523.

(34) Piliego, C.; Holcombe, T. W.; Douglas, J. D.; Woo, C. H.; Beaujuge, P. M.; Fréchet, J. M. J. Synthetic Control of Structural Order in N-alkylthieno[3,4-C]pyrrole-4,6-Dione-Based Polymers for Efficient Solar Cells. *J. Am. Chem. Soc.* **2010**, *132*, 7595–7597.

(35) Cabanetos, C.; El Labban, A.; Bartelt, J. A.; Douglas, J. D.; Mateker, W. R.; Fréchet, J. M. J.; McGehee, M. D.; Beaujuge, P. M. Linear Side Chains in benzo[1,2-b:4,5-B']dithiophene-thieno[3,4-C]pyrrole-4,6-Dione Polymers Direct Self-Assembly and Solar Cell Performance. *J. Am. Chem. Soc.* **2013**, *135*, 4656–4659.

(36) Rivnay, J.; Steyrleuthner, R.; Jimison, L. H.; Casadei, A.; Chen, Z.; Toney, M. F.; Facchetti, A.; Neher, D.; Salleo, A. Drastic Control of Texture in a High Performance N-Type Polymeric Semiconductor and Implications for Charge Transport. *Macromolecules* **2011**, *44*, 5246–5255.

(37) Zhang, X.; Richter, L. J.; DeLongchamp, D. M.; Kline, R. J.; Hammond, M. R.; McCulloch, I.; Heeney, M.; Ashraf, R. S.; Smith, J. N.; Anthopoulos, T. D.; et al. Molecular Packing of High-Mobility Diketo Pyrrolo-Pyrrole Polymer Semiconductors with Branched Alkyl Side Chains. *J. Am. Chem. Soc.* **2011**, *133*, 15073–15084.

(38) Liu, F.; Gu, Y.; Jung, J. W.; Jo, W. H.; Russell, T. P. On the Morphology of Polymer-Based Photovoltaics. *J. Polym. Sci. Part B Polym. Phys.* **2012**, *50*, 1018–1044.

(39) Osaka, I.; Takimiya, K. Backbone Orientation in Semiconducting Polymers. *Polymer (Guildf).* **2015**, *59*, A1–A15.

(40) Saeki, A.; Koizumi, Y.; Aida, T.; Seki, S. Comprehensive Approach to Intrinsic Charge Carrier Mobility in Conjugated Organic Molecules, Macromolecules, and Supramolecular Architectures. *Acc. Chem. Res.* **2012**, *45*, 1193–1202.

(41) Ma, J.; Hashimoto, K.; Koganezawa, T.; Tajima, K. End-on Orientation of Semiconducting Polymers in Thin Films Induced by Surface Segregation of Fluoroalkyl Chains. *J. Am. Chem. Soc.* **2013**, *135*, 9644–9647.

(42) Lu, G. H.; Li, L. G.; Yang, X. N. Achieving Perpendicular Alignment of Rigid Polythiophene Backbones to the Substrate by Using Solvent-Vapor Treatment. *Adv. Mater.* **2007**, *19*, 3594–3598.

(43) Coakley, K. M.; Srinivasan, B. S.; Ziebarth, J. M.; Goh, C.; Liu, Y.; McGehee, M. D. Enhanced Hole Mobility in Regioregular Polythiophene Infiltrated in Straight Nanopores. *Adv. Funct. Mater.* **2005**, *15*, 1927–1932.

(44) Aryal, M.; Trivedi, K.; Hu, W. W. Nano-Confinement Induced Chain Alignment in Ordered P3HT Nanostructures Defined by Nanoimprint Lithography. *ACS Nano* **2009**, *3*, 3085–3090.

(45) Sirringhaus, H.; Brown, P. J.; Friend, R. H.; Nielsen, M. M.; Bechgaard, K.; Langeveld-Voss, B. M. W.; Spiering, A. J. H.; Janssen, R. A. J.; Meijer, E. W.; Herwig, P.; et al. Two-Dimensional Charge Transport in Self-Organized, High-Mobility Conjugated Polymers. *Nature* **1999**, *401*, 685–688.

(46) Hammond, M. R.; Kline, R. J.; Herzing, A. A.; Richter, L. J.; Germack, D. S.; Ro, H.-W.; Soles, C. L.; Fischer, D. A.; Xu, T.; Yu, L.; et al. Molecular Order in High-Efficiency Polymer/Fullerene Bulk Heterojunction Solar Cells. *ACS Nano* **2011**, *5*, 8248–8257.

(47) Chen, M. S.; Niskala, J. R.; Unruh, D. A.; Chu, C. K.; Lee, O. P.; Fréchet, J. M. J. Control of Polymer-Packing Orientation in Thin Films through Synthetic Tailoring of Backbone Coplanarity. *Chem. Mater.* **2013**, *25*, 4088–4096.

(48) Osaka, I.; Kakara, T.; Takemura, N.; Koganezawa, T.; Takimiya, K. Naphthodithiophene-Naphthobisthiadiazole Copolymers for Solar Cells: Alkylation Drives the Polymer Backbone Flat and Promotes Efficiency. *J. Am. Chem. Soc.* **2013**, *135*, 8834–8837.

(49) Osaka, I.; Saito, M.; Koganezawa, T.; Takimiya, K. Thiophene-Thiazolothiazole Copolymers: Significant Impact of Side Chain Composition on Backbone Orientation and Solar Cell Performances. *Adv. Mater.* **2014**, *26*, 331–338.

(50) Szarko, J. M.; Guo, J.; Liang, Y.; Lee, B.; Rolczynski, B. S.; Strzalka, J.; Xu, T.; Loser, S.; Marks, T. J.; Yu, L.; et al. When Function Follows Form: Effects of Donor Copolymer Side Chains on Film Morphology and BHJ Solar Cell Performance. *Adv. Mater.* **2010**, *22*, 5468–5472.

(51) Proctor, C. M.; Love, J. A.; Nguyen, T.-Q. Mobility Guidelines for High Fill Factor Solution-Processed Small Molecule Solar Cells. *Adv. Mater.* **2014**, *26*, 5957–5961.

(52) Chen, H.-Y.; Lin, S.-H.; Sun, J.-Y.; Hsu, C.-H.; Lan, S.; Lin, C.-F. Morphologic Improvement of the PBDTTT-C and PC71BM Blend Film with Mixed Solvent for High-Performance Inverted Polymer Solar Cells. *Nanotechnology* **2013**, *24*, 484009.

(53) Hou, J.; Chen, H.-Y.; Zhang, S.; Chen, R. I.; Yang, Y.; Wu, Y.; Li, G. Synthesis of a Low Band Gap Polymer and Its Application in Highly Efficient Polymer Solar Cells. *J. Am. Chem.*

Soc. **2009**, *131*, 15586–15587.

(54) Huo, L.; Zhang, S.; Guo, X.; Xu, F.; Li, Y.; Hou, J. Replacing Alkoxy Groups with Alkylthienyl Groups: A Feasible Approach To Improve the Properties of Photovoltaic Polymers. *Angew. Chemie* **2011**, *123*, 9871–9876.

(55) You, J.; Chen, C.-C.; Dou, L.; Murase, S.; Duan, H.-S.; Hawks, S. A.; Xu, T.; Son, H. J.; Yu, L.; Li, G.; et al. Metal Oxide Nanoparticles as an Electron-Transport Layer in High-Performance and Stable Inverted Polymer Solar Cells. *Adv. Mater.* **2012**, *24*, 5267–5272.

(56) Chen, H.-Y.; Hou, J.; Zhang, S.; Liang, Y.; Yang, G.; Yang, Y.; Yu, L.; Wu, Y.; Li, G. Polymer Solar Cells with Enhanced Open-Circuit Voltage and Efficiency. *Nat. Photonics* **2009**, *3*, 649–653.

(57) Ho, P.-Y.; Sun, J.-Y.; Kao, S.-H.; Kao, C.-Y.; Lin, S.-H.; Lan, S.; Tseng, W.-H.; Wu, C.-I.; Lin, C.-F. The Effects of MoO3 Treatment on Inverted PBDTTT-C:PC71BM Solar Cells. *Sol. Energy Mater. Sol. Cells* **2013**, *119*, 235–240.

(58) Hawks, S. a.; Deledalle, F.; Yao, J.; Rebois, D. G.; Li, G.; Nelson, J.; Yang, Y.; Kirchartz, T.; Durrant, J. R. Relating Recombination, Density of States, and Device Performance in an Efficient Polymer:Fullerene Organic Solar Cell Blend. *Adv. Energy Mater.* **2013**, *3*, 1201–1209.

(59) Guo, X.; Zhang, M.; Ma, W.; Ye, L.; Zhang, S.; Liu, S.; Ade, H.; Huang, F.; Hou, J. Enhanced Photovoltaic Performance by Modulating Surface Composition in Bulk Heterojunction Polymer Solar Cells Based on PBDTTT-C-T/PC71 BM. *Adv. Mater.* **2014**, *26*, 4043–4049.

(60) Lou, S. J.; Szarko, J. M.; Xu, T.; Yu, L.; Marks, T. J.; Chen, L. X. Effects of Additives on the Morphology of Solution Phase Aggregates Formed by Active Layer Components of High-Efficiency Organic Solar Cells. *J. Am. Chem. Soc.* **2011**, *133*, 20661–20663.

(61) Chang, L.; Jacobs, I. E.; Augustine, M. P.; Moulé, A. J. Correlating Dilute Solvent Interactions to Morphology and OPV Device Performance. *Org. Electron.* **2013**, *14*, 2431–2443.

(62) Khatiwada, D.; Venkatesan, S.; Chen, J.; Chen, Q.; Adhikari, N.; Dubey, A.; Mitul, A. F.; Mohammad, L.; Sun, J.; Zhang, C.; et al. Morphological Evolution and Its Impacts on Performance of Polymer Solar Cells. *IEEE Trans. Electron Devices* **2015**, *62*, 1284–1290.

(63) Gu, Y.; Wang, C.; Russell, T. P. Multi-Length-Scale Morphologies in PCPDTBT/PCBM Bulk-Heterojunction Solar Cells. *Adv. Energy Mater.* **2012**, *2*, 683–690.

(64) Nagarjuna, G.; Venkataraman, D. Strategies for Controlling the Active Layer Morphologies in OPVs. *J. Polym. Sci. Part B Polym. Phys.* **2012**, *50*, 1045–1056.

(65) Liu, F.; Zhao, W.; Tumbleston, J. R.; Wang, C.; Gu, Y.; Wang, D.; Briseno, A. L.; Ade, H.; Russell, T. P. Understanding the Morphology of PTB7:PCBM Blends in Organic Photovoltaics. *Adv. Energy Mater.* **2014**, *4*, n/a – n/a.

(66) Ye, L.; Jing, Y.; Guo, X.; Sun, H.; Zhang, S.; Zhang, M.; Huo, L.; Hou, J. Remove the Residual Additives toward Enhanced Efficiency with Higher Reproducibility in Polymer Solar Cells. *Journal of Physical Chemistry C* **2013**, *117*, 14920–14928.

(67) Zusan, A.; Gieseking, B.; Zerson, M.; Dyakonov, V.; Magerle, R.; Deibel, C. The Effect of Diiodooctane on the Charge Carrier Generation in Organic Solar Cells Based on the Copolymer PBDTTT-C. *Sci. Rep.* **2015**, *5*, 8286.

(68) Zhou, H.; Zhang, Y.; Seifter, J.; Collins, S. D.; Lou, C.; Bazan, G. C.; Nguyen, T. Q.; Heeger, A. J. High-Efficiency Polymer Solar Cells Enhanced by Solvent Treatment. *Adv. Mater.* **2013**, *25*, 1646–1652.

(69) Zhang, K.; Hu, Z.; Duan, C.; Ying, L.; Huang, F.; Cao, Y. The Effect of Methanol Treatment on the Performance of Polymer Solar Cells. *Nanotechnology* **2013**, *24*, 484003.

(70) Tan, Z. K.; Vaynzof, Y.; Credgington, D.; Li, C.; Casford, M. T. L.; Sepe, A.; Huettner, S.; Nikolka, M.; Paulus, F.; Yang, L. et al. In-Situ Switching from Barrier-Limited to Ohmic Anodes for Efficient Organic Optoelectronics. *Adv. Funct. Mater.* **2014**, *24*, 3051–3058.

CHAPTER 5

Ultra-High Mobility Semiconducting Polymers Produced through Confinement in Silica Nanopores

5.1 Introduction

Semiconducting polymers are easily processed, opto-electronic materials that are finding applications in many low-cost devices, including LEDs and solar cells.[1–5] While progress is impressive, devices are limited by the low carrier mobilities found in polymeric materials compared to inorganic semiconductors such as silicon, and thus the need to couple organic devices to inorganic logic component.[1,6] The development of plastic integrated circuits could fundamentally change the way low-cost devices are utilized, allowing for truly disposable electronics or smart fabrics. Although many polymeric systems have already reached the mobility found in amorphous silicon,[7–11] much improvement can still be made.

In this manuscript, we show that enhanced carrier mobilities can be achieved in FETs fabricated from semiconducting polymers aligned by incorporation into the pores of surfactant-templated silica films. The silica serves to both isolate and elongate the polymers chains so that conductivity is dominated by intra-chain transport and chain disorder is suppressed. We fabricate FETs from two different aligned polymers, one highly crystalline and one amorphous, and obtain hole mobilities in the range from 1 to 10 $cm^2/V{\cdot}s$ for both systems. The similarity of the mobility values is quite surprising, given that the mobilities of the two polymers differ by 10x in pure polymer film form.[12,13]

To date, the highest carrier mobilities for polymer systems have been achieved in

homogeneous thin films of highly crystalline polymer, with transport limited by conductivity in the π-π stacking direction.[9,11,14] However, this inter-chain conductivity should be at least 100x slower that its intra-chain counterpart.[15–17] We thus hypothesize that in order to realize the theoretical limits of polymer conductivity, three objectives must be satisfied: macroscopic alignment of the polymer chains parallel to the conducting pathway, removal of all kinks which can serve as traps, and isolation of polymers in small bundles so that any remaining traps do not globally inhibit conductivity. Meeting all of these requirements should allow the mobility of amorphous polymers to match that of their highly crystalline counterparts, a result that would indicate that the intrinsic intra-chain conductivity of a polymer is not dependent upon polymer crystallinity.

The FET is the primary circuit component needed for integrated circuits and the voltage required to operate an FET is strongly dependent on the carrier mobility (μ) in the active material. While there have been many advancements in improving the mobility of semiconducting polymers[9,14,18] the overall mobility remains low compared to what is theoretically possible. Theoretical simulations on poly(phenylene vinylenes) (PPVs) find intra-chain hole and electron mobilites of 30-180 cm^2/Vs.[19] These simulations are bolstered by electrodeless microwave conductivity studies of PPV derivatives in solution which produce a local hole mobility μ_{hole}=300 cm^2/Vs.[17] As promising as these results are, for semiconducting polymers to be useful in integrated circuits, similar carrier mobilities must also be observed across macroscopic distances in the solid state.

5.2. Results and Discussion

To create high mobility polymer FETs, we build upon our previous work incorporating

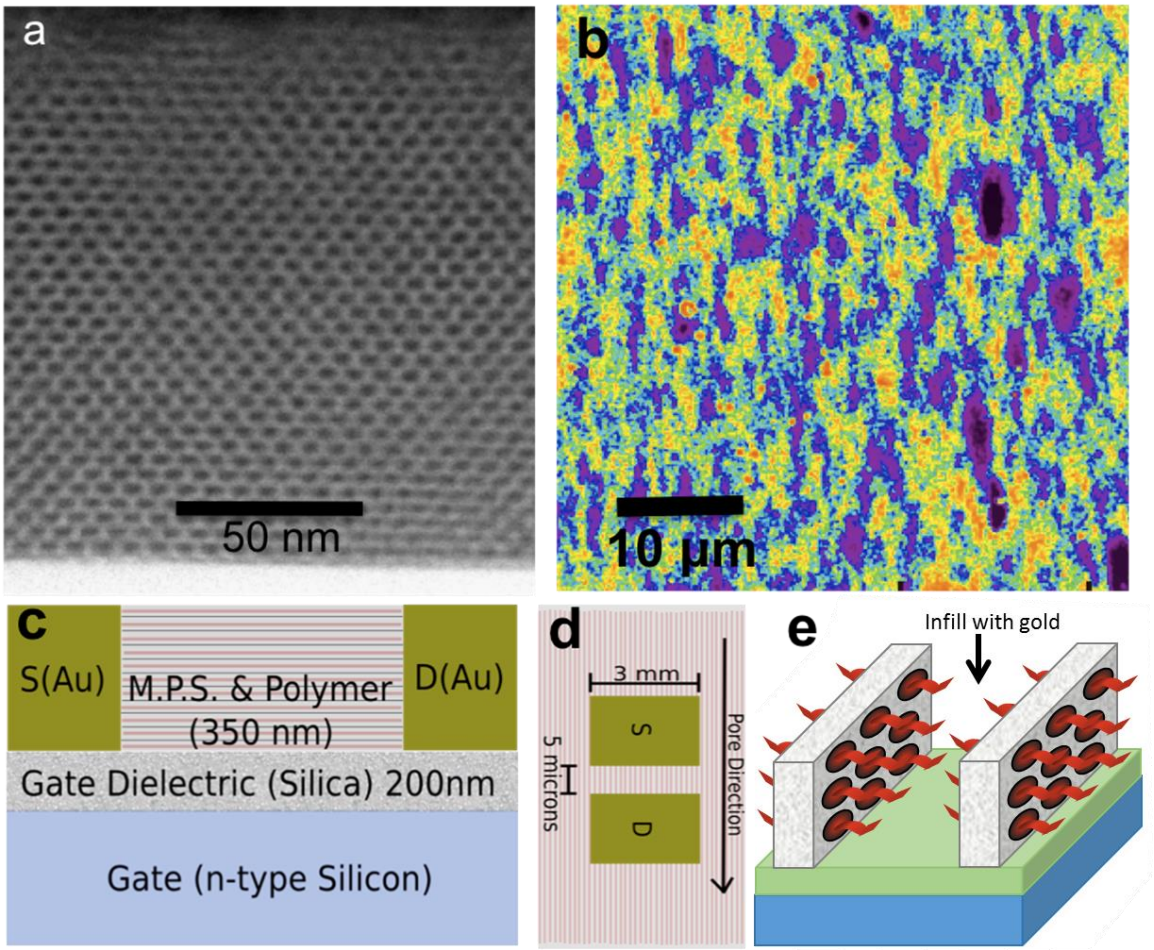

Figure 5.1. Film structure and schematic cartoon of FET device architecture. Part (a) shows an STEM image collected on a mesoporous silica film cut perpendicular to the pore alignment direction. The differential interference contrast (DIC) micrograph in part (b) shows that the film is composed of domains with an average size of 8 µm x 1 µm. The contrast on this image was enhanced in order to more clearly see the domain boundaries. The schematic diagram of the FET device cross-section in (c) shows that the S-D electrodes are patterned into the mesoporous silica:polymer composite. The top view (d) indicates that conductivity is measured parallel to the pore direction. A schematic of the composite following isotropic BOE etch is shown in (e), illustrating the polymer end dangling from the pore.

semiconducting polymers into the nanosized pores of a mesoporous silica host. We have previously shown that an aligned silica host can impart optical anisotropy to a semiconducting polymer.[20] Spectroscopic studies further show that both the number of chains per pore and polymer conformation is controlled by the pore size.[21] Based on those previous studies, the 5nm pores used here contain multiple elongated polymer chains per pore.[21]

The hydrothermally prepared mesoporous silica in this work forms continuous films with an ordered but compressed 2D hexagonal pore structure as confirmed by X-ray diffraction.[22] We can visualize this pore system using scanning transmission electron microscopy (STEM). Figure 5.1(a) shows an STEM image of a cross-sectional cut normal to the alignment direction and clearly shows the hexagonal array of 5 nm ellipsoidal pores.

Following the preparation of the host, polymer is incorporated into the matrix.[20] For this study we chose to examine the conductivity of two different polymer systems: poly[2-methoxy-5-(2'-ethylhexyloxy)-*p*-phenylene vinylene] (MEH-PPV) and poly(3-hexylthiophene-2,5-diyl) (P3HT). We chose P3HT because it exhibits high hole mobilities and is thus a good candidate to examine the ultimate extent to which hole mobilities can be improved through alignment and confinement. Conductivity in this system is also established to be limited by inter-chain transport.[14] MEH-PPV, by contrast, is a much less ordered system. Thin films of this polymer are comprised of very small crystallites, imbedded in a largely amorphous matrix,[23] making it difficult to correlate chain geometry with carrier transport.[24,25] Carrier motion through MEH-PPV films likely involves components of inter-chain transport, intra-chain transport, and trap-trap hopping. However, many theoretical studies have focused on PPV type polymers, providing an opportunity to directly compare theory and experiment. Moreover, because MEH-PPV thin films are largely amorphous, crystallization cannot be used to improve mobility. Space-confinement thus provides

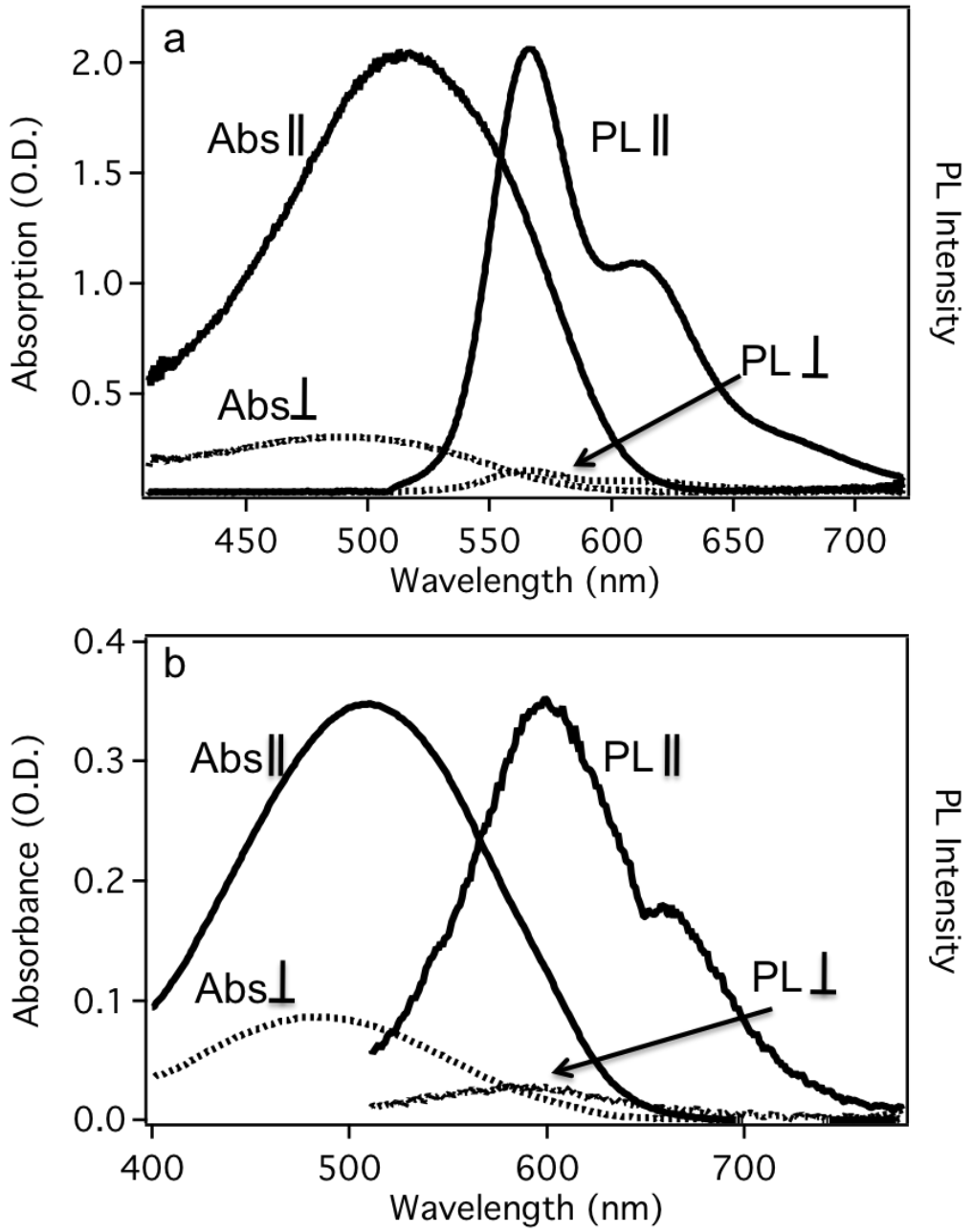

Figure 5.2. Polarized absorption (left curves and axes) and fluorescence (right curves and axes) obtained on aligned mesoporous silica films filled with MEH-PPV (a) and p3HT (b). Polarization is indicated on the graph and defined in the text.

a unique opportunity to dramatically improve mobility.

To ensure that our semiconducting polymers are well aligned in the silica host-matrix, polarized absorption and photoluminescence experiments were performed. Because absorption and fluorescence transition dipoles are oriented nearly parallel to the polymer chain axis, polarized optical studies can be used to characterize chain alignment.[26] Figure 5.2 shows polarized absorption and fluorescence for MEH-PPV (a) and P3HT (b) contained within nanoporous silica thin films. The parallel:perpendicular absorption ratio of 4.0 in the case of P3HT and 6.7 in the case of MEH-PPV indicates a high degree of polymer alignment. For both polymers, a red shift of the parallel absorption relative to both the perpendicular absorption and absorption from spin-cast films indicates that the host matrix both aligns the polymers chains and straightens and elongates them, leading to longer conjugation lengths parallel to the pores.[21] As expected, the red shift is greater for the non-crystalline MEH-PPV, where the polymer conformation is more dramatically changed by space confinement. The degree of alignment was also determined from the photoluminescence with the excitation and emission light polarized parallel and perpendicular to the pores. Here, we can define the ratio of the parallel polarized light divided by the perpendicularly polarized light as the anisotropic ratio, $I_{\parallel}:I_{\perp}$. Photoluminescence from both P3HT and MEH-PPV in pores also indicate alignment, with large anisotropic ratios of 8.0 and 20.5, respectively. Both P3HT and MEH-PPV thus appear to contain oriented and elongated chains in the mesoporous framework.

Field effect transistor devices were fabricated using highly doped, 0.005 Ω/cm^2, n-type silicon as a back gate electrode with a 200nm thermally grown SiO_2 top-layer as a gate insulator. Mesoporous silica filled with polymer was prepared using this *n*-Si/SiO_2 wafer as a substrate. Gold source and drain electrodes were patterned into the silica:polymer film as shown in the cross-

section schematic in Figure 5.1(c). To transfer the photolithographic pattern into the polymer incorporated mesoporous silica film, an anisotropic plasma etch was employed to etch through both the polymer and silica components of the composite. This was followed by a short buffered oxide sidewall etch to expose the polymer chains for metal evaporation, as illustrated in Figure 5.1(e). The source and drain electrodes were patterned with a 5 μm channel length and a width of 3 mm, oriented to collect current running parallel to the pores (Figure 5.1 d). Patterns oriented orthogonal to the pore direction were also fabricated as controls and showed no conductivity. FET devices with the conductive axis oriented along the pore direction but without incorporated polymers were also fabricated as controls, and again, these devices showed no conductivity. The channel length was chosen to be shorter than the average silica domain size of ~8 μm along the pores, as visualized by optical microscopy (Figure 5.1 b). Gold, which has a work function matched to the valence bands of both P3HT and MEH-PPV was chosen as the electrode material to ensure that holes were the electronic carrier.

Output characteristics for devices operating in enhancement mode are shown in Figure 5.3 (a) and (b) for MEH-PPV and P3HT devices, respectively. Both P3HT and MEH-PPV devices show field-effect behavior at extremely low gate voltage (V_g) application, ~1V. Devices also operate under extremely small source-drain bias, ~1V, which is a sign of the conductivity enhancement brought about by aligning the polymers.

While the low operating voltages are impressive, these devices show signs of two deviations from the "ideal" output characteristics for polymer transistors. First, a voltage shift, observable as a shift in the turn-on voltage as a function of V_g, is apparent in the output characteristics. This is commonly observed in polymer FETs and is due to a gate-voltage dependent contact resistance at the polymer/electrode interface.[27] Secondly, the output

characteristics show an asymmetry between positive and negative source-drain bias. In typical polymer FETs, the data is symmetric about the origin and both the first and third quadrants show FET behavior. This system, however, displays no FET behavior in the negative source-drain bias regime. This is indicative of a Schottky barrier limited current,[28–31] rather than the typically observed diffusion limited current.[31] Since both polymers show this unusual behavior, the mobility was modeled using both the stand diffusion limited model and a Schottky barrier model. Using the two methods combined enables us to validate the measured mobilities.

Transfer characteristics for MEH-PPV and P3HT devices operating with a 0.05V source-drain bias are shown in Figure 5.3 (c) and (d), respectively. Using the standard relationship between drain current (I_{DS}) and gate voltage in the linear regime,

$$\left.\frac{\partial I_{DS}}{\partial V_G}\right|_{Vds} = \frac{W}{L} C_i \mu_{FET} V_{DS},$$

the mobility, μ_{FET}, can be calculated.[31] Here C_i is the capacitance per unit area of the gate dielectric, which was calculated using the known permittivity of dense SiO_2; W and L are the channel width and length. From this relationship we are able to calculate a hole mobility of 1.5 cm^2/Vs for MEH-PPV devices and 10 cm^2/Vs for P3HT devices.

As mentioned above, however, the asymmetry in the FET output curves indicates that mobilities based on transfer characteristics may not be reliable. To further validate our high measured mobilities, we followed the method described by Zhang, et al, who looked at nanowire systems where the device properties are characterized by a high Schottky barrier.[28] Using the V_g=0 data, the resistance of the polymer was first determined first using the large S-D bias region of the output curves (5.5 – 7V for P3HT and 7 – 9.5V for MEH-PPV); the resistance is simply the slope in this region, Figure 5.4 (a) and (b). The zero-gate data is shown in Figure 5.4. From the resistance,

the conductivity can easily be determined from the length (l) and area (A) of the device using $\sigma = \frac{Rl}{A}$ where the thickness was taken to be the thickness of pure polymer within the pores. The conductivity for P3HT and MEH-PPV was found to be 1.33 Sm^{-1} and 0.97 Sm^{-1} respectively.

To get the mobility from the conductivity, the carrier density must also be calculated. In the intermediate bias region (2.5V – 5.5V for P3HT and 4 – 7V for MEH-PPV)), the Schottky barrier dominates and can be described by Equation 1.

$$lnI = lnS + lnJ_{SR} + V\left(\frac{q}{kT} - \frac{1}{E_0}\right) \quad (1)$$

Here J_{SR} is a correction to the current due to band energy levels, S is the contact area of the Schottky barrier and E_0 is the energy associated with the barrier. By plotting the logarithmic of current as a function of applied bias as shown in Figure 5.4 (c) and (d), E_0 can be obtained.

$$E_0 = E_{00}\coth\left(\frac{qE_{00}}{kT}\right) \quad (2)$$

$$E_{00} = \frac{\hbar}{2}\left[\frac{N_d}{m_p^*\varepsilon_s\varepsilon_0}\right]^{1/2} \quad (3)$$

The carrier concentration, N_d, can then be determined using Equations 2 and 3, where E_{00} is the energy at which the transition probability for tunneling is $1/e$ and ε_0 is the vacuum permittivity constant. The relative dielectric constant, ε_s, of the both polymers has been shown in literature to be 3.[32,33] The effective mass of a hole on the polymer chain, m_p^*, is required, but this differs from a bulk number since the bulk effective mass takes into the mass of the hole traveling both interchain and intrachain. From theory, the hole is much lighter when traveling intrachain on both polymers.[34–38] Since our system is just a few elongated polymer chains, the interchain hoping is greatly suppressed and therefore the intrachain number was used. The effective masses used were $0.185m_e$ for P3HT[34,35] and $0.10m_e$ for MEH-PPV.[36–38] For P3HT, the carrier density was found to be 3.4 x 10^{22} m^{-1}, leading to a mobility of 2.4 $cm^2/V{\cdot}s$. For MEH-PPV the carrier density and

mobility were found to be 1.1 x 10^{22} m^{-1} and 5.4 $cm^2/V \cdot s$ respectively.

To assess the validity of the Schottky barrier method, the barrier height and ideality factor were also calculated; the ideality factor represents the deviation from an ideal thermionic emission model. There is a large number of ways these can be calculated[28,30] but the simplest way is to use the low bias region of the zero-gate output curves.[30] By plotting the logarithm of current versus the applied bias, the barrier height, ϕ_b, and ideality factor, n, can be easily obtained from the intercept of the graph as in Equation 4.

$$I = AA^*T^2 exp\left(\frac{-q\phi_b}{kT}\right) exp\left(\frac{qV}{nkT}\right) \quad (4)$$

Here A is the area of the device and A^* is the effective Richardson constant. The barrier height and ideality constant for P3HT were found to be 0.65eV and 2.1, respectively. For MEH-PPV the barrier height was found to be 0.57eV and the ideality factor was 1.9. These values do represent a fairly high Schottky barrier, as expected for a barrier height limited current. Also, an ideality factor around 2 does indicate slight deviation from ideal thermionic emission but shows that overall the model being used is valid.

The mobility obtained using the transfer characteristics and the Schottky barrier method differ, since neither technique perfectly describes the physics of this unusual system. However, both methods confirm a large improvement in the carrier mobility for both polymers. Using either of the mobility values, the P3HT mobility is increased almost 100x from previous reports[14,39] while the MEH-PPV mobility is increased by nearly 10^4 over any report to date.[40]

These data represent a potential paradigm shift for plastic FETs, as they show that even amorphous semiconducting polymers can show high mobilities. It is relatively simple to understand this enhancement of $\mu_{hole,FET}$ in the case of P3HT. In previously fabricated FETs made with p3HT and other highly crystalline polymers, conductivity was limited by transport in the π-π

stacking direction.[9,15,16] By removing the need for carrier hoping along the π-stacks, the mobility should be significantly larger. Since P3HT is a fairly crystalline polymer, we expect the difference between inter- and intra-chain conductivity to be the dominant effect of confining P3HT in pores, and the results presented here are in good agreement with the predicted 100x difference in intra-chain and inter-chain mobility.[34–38]

For MEH-PPV, by contrast, confinement within the silica pores produces more dramatic changes. As previously stated, MEH-PPV is a largely amorphous polymer with conduction occurring via inter-chain hopping, trap-trap hopping, and intra-chain transport. Attempts to maximize conductivity in PPV FETs have focused on increasing the crystallinity,[41] but the low μ_{FET} observed previously suggest that carrier trapping limits the conductivity. In our system, pore straightening effectively eliminates traps arising from kinks within the polymer.[21] This effect adds to the alignment and the predominance of intra-chain transport also observed in P3HT.

While alignment and straightening of the polymer chains by the host matrix is clearly important to enhancing the mobility, that may not be the only reason for the large values observed here. Previous studies have attempted to achieve main chain alignment parallel to the conduction pathway through various rubbing techniques in Poly-9,9'-dioctyl-fluorene-co-bithiophene (F8T2).[18,42,8,43] These aligned films showed optical anisotropy similar to that observe here, yet the hole mobility was only 4.98×10^{-4} to 3.5×10^{-2} cm^2/Vs, depending on the alignment technique.[18,42,8,43] Alignment of p3HT has also been achieved by similar rubbing techniques[44–46] and through the use of an AFM tip,[7,47] however, the mobility obtained still remains below 0.02 cm^2/Vs.[7] Given that F8T2 is a fairly high mobility polymer, these results suggest that bulk aligned films are not equivalent to pore aligned films. It is likely that two additional effects come into play with the porous host. First, the isolation of polymer bundles within pores prevents a single trap

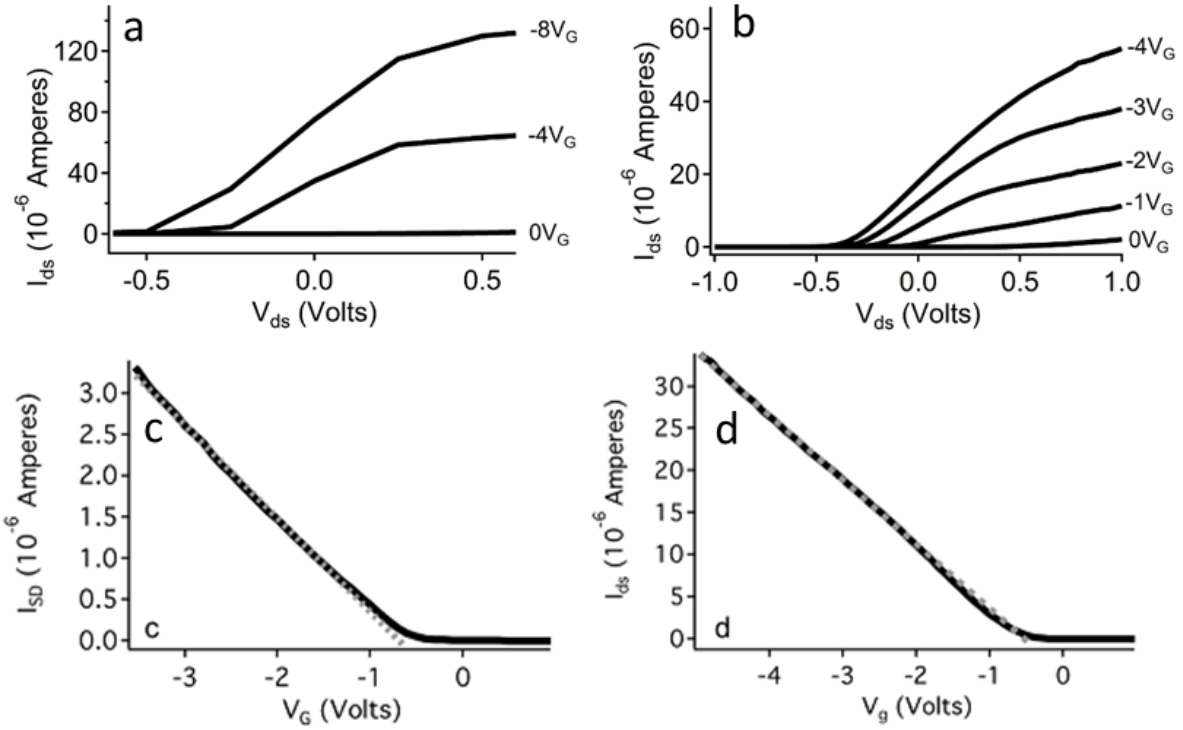

Figure 5.3. FET output characteristics for mesoporous silica films filled with MEH-PPV (a) and p3HT (b); FET transfer characteristics taken at 0.05V S-D bias for MEH-PPV (c) and p3HT (d), with fits shown as dotted grey lines.

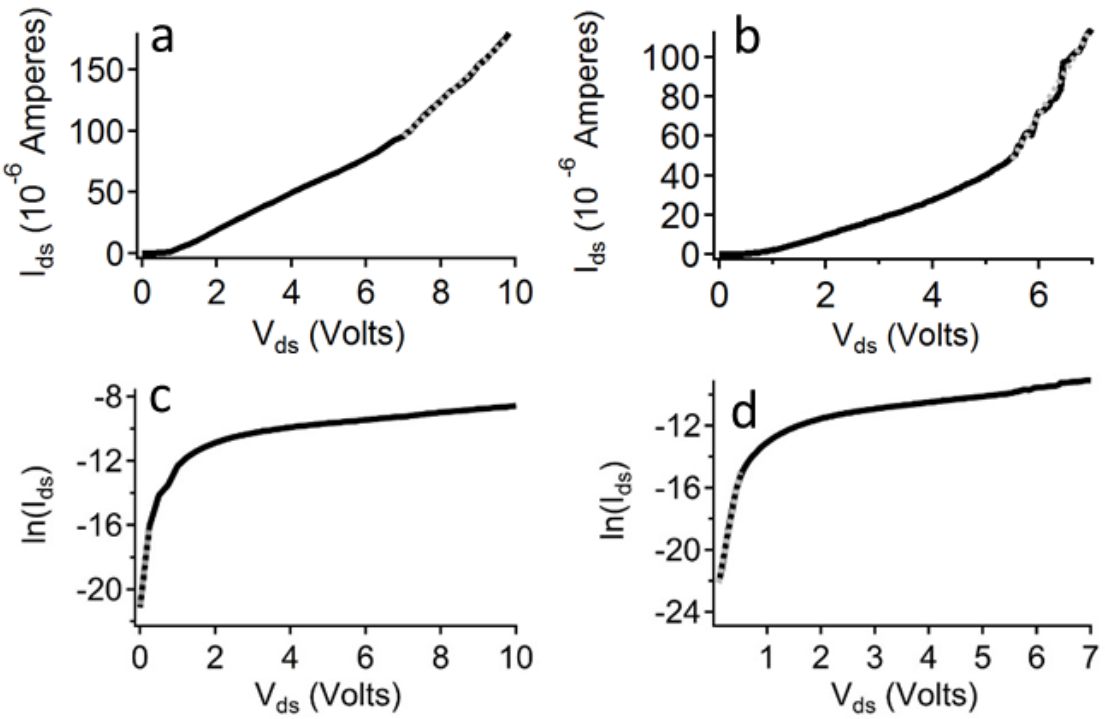

Figure 5.4. Zero-gate output characteristics for mesoporous silica films filled with MEH-PPV (a) and p3HT (b), fits for the resistance in the large bias region are shown by the grey dotted line; Logarithim of current versus S-D bias for MEH-PPV (c) and p3HT (d), fits for the barrier height and ideality factor are shown as grey dotted lines.

from harvesting carriers from a large volume of polymer. Secondly, even in highly oriented crystalline polymer systems, grain boundary resistance can affect μ_{FET}. Large grain boundary resistances can depress mobilities by up to 100x.[48] Because our pores are small, polymer chains likely form continuous aligned structures, rather than discrete crystalline domains. This continuous alignment may result in reduced domain boundary scattering and overall higher mobility.

A final alignment effect is depression of the threshold voltage, V_T, which is calculated from the intercept of a linear fit to the transfer characteristics, Figures 5.3 (c) and (d). We observe extremely small threshold voltages of 0.68V for MEH-PPV and 0.53V for P3HT. V_T is the voltage that must be applied to the gate electrode to create an accumulation layer.[31] In an ideal system with no physical or chemical defects, V_T will be zero. In polymer systems, intrinsic carriers typically arise from kinks, bends, or chemical defects within the polymer chains.[49,50] By straightening the polymer chains, we remove many of the intrinsic carriers present in a pure polymer film, thus forming an accumulation layer at very low applied gate voltage. Therefore, alignment and straightening of the polymer chains not only increases the carrier mobility, but also dramatically reduces the operating power of the device.

5.3 Conclusion

This work thus demonstrates that high intrinsic carrier mobilities in semiconducting polymers can be achieved. These mobilites are generated not by enhancing the inter-chain transport in crystalline materials, but instead by creating a system where transport is dominated by intra-chain conductivity and carriers are isolated into nanosized domains to minimize the effects of traps. The next step is to achieve similar mobilities in a pure polymer film. While this task may

seem daunting, self-assembly provides facile routes to related architectures in bulk polymer films.[51,52]

Regardless of whether these desirable polymer architectures are produced via space confinement, as described here, or though self-assembly, this work indicates that low power semiconducting polymer based integrated circuits may be achievable much sooner than previously expected. More broadly, many semiconducting polymer devices, including solar cells and LEDs, are currently limited by carrier mobility, and this work provides a practical route to overcoming those limits. Those devices, in combination with organic integrated circuits, open the door to completely organic electronics, such as all organic displays, smart fabrics, and disposable personal electronics.

5.4. Experimental

5.4.1 Polymer Incorporation: Polymer was incorporated into the silica matrix following the route described in reference 11. Regio-regular P3HT with a molecular weight of 50,000 Da was purchased from Rieke Metals. MEH-PPV with a molecular weight of 150,000 Da was purchased from American Dye Source.

5.4.2 Optical Characterization: Optical characterization was performed on polymer incorporated mesoporous silica (pMPS) films prepared on quartz substrates in order to minimize absorption and emission arising from the substrate. pMPS films on quartz substrates were prepared in an identical manner to FET devices. Absorption experiments were performed on a Perkin-Elmer Lambda 25 UV/Vis spectrometer. Photoluminescence was measured using a Coherent Innova argon ion laser (514 nm) as an excitation source. Fluorescence spectra were collected using an

Ocean Optics SD 2000 fiberoptic spectrometer, with a linear CCD. A Glan-Taylor polarizer was used to define the polarization of the incident beam and a half-wave plate was used to rotate this from horizontal to vertical in the laboratory frame. A second Glan-Taylor polarizer was then used to select the emission polarization. The integration of the total fluorescence intensity when excitation and emission are polarized parallel to the pore direction divided by the intensity when excitation and emission are perpendicular to the pores lets us define the anisotropic ratio as $I_{\parallel}:I_{\perp}$.

5.4.3 Electrical Characterization: In order to prevent breakdown of devices during electrical spectroscopy studies, FET devices were tested in an argon filled glove box under dark conditions. Testing was performed using two Keithley 2400 sourcemeters daisy chained together, with one Keithley controlling the source-drain bias and the other controlling the gate-source bias. In this configuration the source acts as a common ground for both Keithleys. Output curves and transfer characteristics were collected for multiple samples. Calibration was performed using a 2N5460 p-type MOSFET, Fairchild Semiconductor, as a standard.

5.5 References

(1) Forrest, S. R. The Path to Ubiquitous and Low-Cost Organic Electronic Appliances on Plastic. *Nature* **2004**, *428*, 911–918.

(2) De Boer, B.; Facchetti, A. Semiconducting Polymeric Materials. *Polym. Rev.* **2008**, *48*, 423–431.

(3) Schwartz, B. J. Conjugated Polymers as Molecular Materials: How Chain Conformation and Film Morphology Influence Energy Transfer and Interchain Interactions. *Annu. Rev. Phys. Chem.* **2003**, *54*, 141–172.

(4) Bujak, P.; Kulszewicz-Bajer, I.; Zagorska, M.; Maurel, V.; Wielgus, I.; Pron, A. Polymers for Electronics and Spintronics. *Chem. Soc. Rev.* **2013**, *42*, 8895–8999.

(5) Tremel, K.; Ludwigs, S. *P3HT Revisited – From Molecular Scale to Solar Cell Devices*;

Ludwigs, S., Ed.; Advances in Polymer Science; Springer Berlin Heidelberg: Berlin, Heidelberg, 2014; Vol. 265.

(6) Chuang, T.-K.; Troccoli, M.; Kuo, P.-C.; Jamshidi Roudbari, A.; Hatalis, M.; Spirko, J.; Klier, K.; Biaggio, I.; Voutsas, A. T.; Afentakis, T.; et al. Process Technology for High-Resolution AM-PLED Displays on Flexible Metal Foil Substrates. In *ECS Transactions*; ECS, 2006; Vol. 3, pp. 349–359.

(7) Derue, G.; Serban, D. A.; Leclère, P.; Melinte, S.; Damman, P.; Lazzaroni, R. Controlled Nanorubbing of Polythiophene Thin Films for Field-Effect Transistors. *Org. Electron.* **2008**, *9*, 821–828.

(8) Sirringhaus, H.; Wilson, R. J.; Friend, R. H.; Inbasekaran, M.; Wu, W.; Woo, E. P.; Grell, M.; Bradley, D. D. C. Mobility Enhancement in Conjugated Polymer Field-Effect Transistors through Chain Alignment in a Liquid-Crystalline Phase. *Appl. Phys. Lett.* **2000**, *77*, 406.

(9) McCulloch, I.; Heeney, M.; Bailey, C.; Genevicius, K.; Macdonald, I.; Shkunov, M.; Sparrowe, D.; Tierney, S.; Wagner, R.; Zhang, W.; et al. Liquid-Crystalline Semiconducting Polymers with High Charge-Carrier Mobility. *Nat. Mater.* **2006**, *5*, 328–333.

(10) Sirringhaus, H.; Tessler, N.; Friend, R. H. Integrated Optoelectronic Devices Based on Conjugated Polymers. *Science (80-.).* **1998**, *280*, 1741–1744.

(11) Kim, G.; Kang, S.-J.; Dutta, G. K.; Han, Y.-K.; Shin, T. J.; Noh, Y.-Y.; Yang, C. A Thienoisoindigo-Naphthalene Polymer with Ultrahigh Mobility of 14.4 cm(2)/V·s That Substantially Exceeds Benchmark Values for Amorphous Silicon Semiconductors. *J. Am. Chem. Soc.* **2014**, *136*, 9477–9483.

(12) Amorim, C. A.; Cavallari, M. R.; Santos, G.; Fonseca, F. J.; Andrade, A. M.; Mergulhão, S. Determination of Carrier Mobility in MEH-PPV Thin-Films by Stationary and Transient Current Techniques. *J. Non. Cryst. Solids* **2012**, *358*, 484–491.

(13) Von Hauff, E.; Dyakonov, V.; Parisi, J. Study of Field Effect Mobility in PCBM Films and P3HT:PCBM Blends. *Sol. Energy Mater. Sol. Cells* **2005**, *87*, 149–156.

(14) Sirringhaus, H.; Brown, P. J.; Friend, R. H.; Nielsen, M. M.; Bechgaard, K.; Langeveld-Voss, B. M. W.; Spiering, A. J. H.; Janssen, R. A. J.; Meijer, E. W.; Herwig, P.; et al. Two-Dimensional Charge Transport in Self-Organized, High-Mobility Conjugated Polymers. *Nature* **1999**, *401*, 685–688.

(15) Stoneham, A. M.; Ramos, M. M. D.; Almeida, A. M.; Correia, H. M. G.; Ribeiro, R. M.; Ness, H.; Fisher, A. J. Understanding Electron Flow in Conducting Polymer Films: Injection, Mobility, Recombination and Mesostructure. *J. Phys. Condens. Matter* **2002**, *14*, 9877–9898.

(16) Lan, Y.-K.; Yang, C. H.; Yang, H.-C. Theoretical Investigations of Electronic Structure and Charge Transport Properties in Polythiophene-Based Organic Field-Effect Transistors. *Polym. Int.* **2010**, *59*, 16–21.

(17) Prins, P.; Grozema, F.; Schins, J.; Savenije, T.; Patil, S.; Scherf, U.; Siebbeles, L. Effect of Intermolecular Disorder on the Intrachain Charge Transport in Ladder-Type Poly(p-Phenylenes). *Phys. Rev. B* **2006**, *73*, 045204.

(18) Kinder, L.; Kanicki, J.; Petroff, P. Structural Ordering and Enhanced Carrier Mobility in Organic Polymer Thin Film Transistors. *Synth. Met.* **2004**, *146*, 181–185.

(19) Correia, H. M. G.; Ramos, M. M. D. Modeling Charge Transport Properties of Cyano-Substituted PPV. *Mater. Sci. Eng. C* **2003**, *23*, 773–777.

(20) Molenkamp, W. C.; Watanabe, M.; Miyata, H.; Tolbert, S. H. Highly Polarized Luminescence from Optical Quality Films of a Semiconducting Polymer Aligned within Oriented Mesoporous Silica. *J. Am. Chem. Soc.* **2004**, *126*, 4476–4477.

(21) Cadby, A. J.; Tolbert, S. H. Controlling Optical Properties and Interchain Interactions in Semiconducting Polymers by Encapsulation in Periodic Nanoporous Silicas with Different Pore Sizes. *J. Phys. Chem. B* **2005**, *109*, 17879–17886.

(22) Miyata, H.; Noma, T.; Watanabe, M.; Kuroda, K. Preparation of Mesoporous Silica Films with Fully Aligned Large Mesochannels Using Nonionic Surfactants. *Chem. Mater.* **2002**, *14*, 766–772.

(23) Yang, C. Y.; Hide, F.; Díaz-García, M. A.; Heeger, A. J.; Cao, Y. Microstructure of Thin Films of Photoluminescent Semiconducting Polymers. *Polymer (Guildf).* **1998**, *39*, 2299–2304.

(24) Jeng, U.; Hsu, C.-H.; Sheu, H.-S.; Lee, H.-Y.; Inigo, A. R.; Chiu, H. C.; Fann, W. S.; Chen, S. H.; Su, A. C.; Lin, T.-L.; et al. Morphology and Charge Transport in Poly(2-Methoxy-5-(2‘-Ethylhexyloxy)-1,4-Phenylenevinylene) Films. *Macromolecules* **2005**, *38*, 6566–6574.

(25) Craig, I. M.; Tassone, C. J.; Tolbert, S. H.; Schwartz, B. J. Second-Harmonic Generation in Conjugated Polymer Films: A Sensitive Probe of How Bulk Polymer Crystallinity Changes with Spin Speed. *J. Chem. Phys.* **2010**, *133*, 044901.

(26) McBranch, D.; Campbell, I. H.; Smith, D. L.; Ferraris, J. P. Optical Determination of Chain Orientation in Electroluminescent Polymer Films. *Appl. Phys. Lett.* **1995**, *66*, 1175.

(27) Natali, D.; Fumagalli, L.; Sampietro, M. Modeling of Organic Thin Film Transistors: Effect of Contact Resistances. *J. Appl. Phys.* **2007**, *101*, 014501.

(28) Zhang, Z.; Yao, K.; Liu, Y.; Jin, C.; Liang, X.; Chen, Q.; Peng, L.-M. Quantitative Analysis of Current–Voltage Characteristics of Semiconducting Nanowires: Decoupling of Contact

Effects. *Adv. Funct. Mater.* **2007**, *17*, 2478–2489.

(29) Zhou, J.; Fei, P.; Gu, Y.; Mai, W.; Gao, Y.; Yang, R.; Bao, G.; Wang, Z. L. Piezoelectric-Potential-Controlled Polarity-Reversible Schottky Diodes and Switches of ZnO Wires. *Nano Lett.* **2008**, *8*, 3973–3977.

(30) Gholami, S.; Khakbaz, M. Measurement of I-V Characteristics of a PtSi /p-Si Schottky Barrier Diode at Low Temperatures. *World Acad. Sci. Eng. Technol.* **2011**, *57*, 1001–1004.

(31) Sze, S. M. *The Physics of Semiconductor Devices*; 1981.

(32) Watt, A.; Eichmann, T.; Rubinsztein-Duntop, H.; Meredith, P. Carrier Transport in PbS Nanocrystal Conducting Polymer Composites. *Appl. Phys. Lett.* **2005**, *87*, 253109.

(33) Park, J.; Yu, H.; Park, J.; Kim, B.; Lee, S. Non-Linear I– V Characteristics of MEH-PPV Patterned on Sub-Micrometer Electrodes. *Thin Solid FIlms* **2001**, *393*, 129–131.

(34) Siebbeles, L. D. a.; Grozema, F. C.; de Haas, M. P.; Warman, J. M. Effect of Backbone Structure on Charge Transport along Isolated Conjugated Polymer Chains. *Radiat. Phys. Chem.* **2005**, *72*, 85–91.

(35) Dag, S.; Wang, L.-W. Packing Structure of poly(3-Hexylthiophene) Crystal: Ab Initio and Molecular Dynamics Studies. *J. Phys. Chem. B* **2010**, *114*, 5997–6000.

(36) Pedersen, K. Characterisation of Semiconducting Polymers and Fabrication of OLEDs. *Aalborg Univ.* **2012**.

(37) Pedersen, T.; Johansen, P.; Pedersen, H. Particle-in-a-Box Model of One-Dimensional Excitons in Conjugated Polymers. *Phys. Rev. B* **2000**, *61*, 10504–10510.

(38) Ferretti, A.; Ruini, A.; Molinari, E.; Caldas, M. Electronic Properties of Polymer Crystals: The Effect of Interchain Interactions. *Phys. Rev. Lett.* **2003**, *90*, 086401.

(39) Wang, G.; Swensen, J.; Moses, D.; Heeger, A. J. Increased Mobility from Regioregular poly(3-Hexylthiophene) Field-Effect Transistors. *J. Appl. Phys.* **2003**, *93*, 6137.

(40) Muratsubaki, M. et al. Field-Effect Transistors Based on Poly(p-Phenylenevinylene) Derivatives. *Chem Lett* **2004**, *33*, 1480–1481.

(41) Huang, Y.-F.; Chang, C.-W.; Smilgies, D.-M.; Jeng, U.-S.; Inigo, A. R.; White, J. D.; Li, K.-C.; Lim, T.-S.; Li, T.-D.; Chen, H.-Y.; et al. Correlating Nanomorphology with Charge-Transport Anisotropy in Conjugated-Polymer Thin Films. *Adv. Mater.* **2009**, *21*, 2988–2992.

(42) Li, S. P.; Newsome, C. J.; Russell, D. M.; Kugler, T.; Ishida, M.; Shimoda, T. Friction Transfer Deposition of Ordered Conjugated Polymer Nanowires and Transistor Fabrication. *Appl. Phys. Lett.* **2005**, *87*, 062101.

(43) Gather, M. C.; Bradley, D. D. C. An Improved Optical Method for Determining the Order Parameter in Thin Oriented Molecular Films and Demonstration of a Highly Axial Dipole Moment for the Lowest Energy Π–π* Optical Transition in Poly(9,9- Dioctylfluorene-Co-Bithiophene). *Adv. Funct. Mater.* **2007**, *17*, 479–485.

(44) Abbas, M.; D'Amico, F.; Ali, M.; Mencarelli, I.; Setti, L.; Botentempi, E.; Gunnella, R. Rubbing Effects on the Structural and Optical Properties of poly(3-Hexylthiophene) Films - Abstract - Journal of Physics D: Applied Physics - IOPscience. *J. Phys. D* **2010**, *43*, 035103.

(45) Heil, H.; Finnberg, T.; von Malm, N.; Schmechel, R.; von Seggern, H. The Influence of Mechanical Rubbing on the Field-Effect Mobility in Polyhexylthiophene. *J. Appl. Phys.* **2003**, *93*, 1636.

(46) Vohra, V.; Arrighetti, G.; Barba, L.; Higashimine, K.; Porzio, W.; Murata, H. Enhanced Vertical Concentration Gradient in Rubbed P3HT:PCBM Graded Bilayer Solar Cells. *J. Phys. Chem. Lett.* **2012**, *3*, 1820–1823.

(47) Derue, G.; Coppée, S.; Gabriele, S.; Surin, M.; Geskin, V.; Monteverde, F.; Leclère, P.; Lazzaroni, R.; Damman, P. Nanorubbing of Polythiophene Surfaces. *J. Am. Chem. Soc.* **2005**, *127*, 8018–8019.

(48) Kline, R. J.; McGehee, M. D.; Kadnikova, E. N.; Liu, J.; Fréchet, J. M. J.; Toney, M. F. Dependence of Regioregular Poly (3-Hexylthiophene) Film Morphology and Field-Effect Mobility on Molecular Weight. *Macromolecules* **2005**, *38*, 3312–3319.

(49) Meisel, K. D.; Pasveer, W. F.; Cottaar, J.; Tanase, C.; Coehoorn, R.; Bobbert, P. A.; Blom, P. W. M.; de Leeuw, D. M.; Michels, M. A. J. Charge-Carrier Mobilities in Disordered Semiconducting Polymers: Effects of Carrier Density and Electric Field. *Phys. Status Solidi C* **2006**, *3*, 267–270.

(50) Liang, Z.; Nardes, A.; Wang, D.; Berry, J. J.; Gregg, B. A. Defect Engineering in Π-Conjugated Polymers. *Chem. Mater.* **2009**, *21*, 4914–4919.

(51) Huber, R. C.; Ferreira, A. S.; Thompson, R.; Kilbride, D.; Knutson, N. S.; Devi, L. S.; Toso, D. B.; Challa, J. R.; Zhou, Z. H.; Rubin, Y.; et al. Long-Lived Photoinduced Polaron Formation in Conjugated Polyelectrolyte-Fullerene Assemblies. *Science (80-.).* **2015**, *348*, 1340–1343.

(52) Clark, A. P.-Z.; Shi, C.; Ng, B. C.; Wilking, J. N.; Ayzner, A. L.; Stieg, A. Z.; Schwartz, B. J.; Mason, T. G.; Rubin, Y.; Tolbert, S. H. Self-Assembling Semiconducting Polymers-Rods and Gels from Electronic Materials. *ACS Nano* **2013**, *7*, 962–977.

CHAPTER 6

On the Structure and Conductivity of Semiconducting Polymer Hydrogels

6.1 Introduction

Conjugated polyelectrolytes (CPEs) are a class of polymers that consists of a π-conjugated backbone with ionic pendant groups.[1–4] Due to their charged side chains, CPEs can self-assemble into various motifs, including nanoparticles[5–7] and rods.[4,8,9] This assembly is driven by the kinetics of polymer aggregation in various solvents, and can result in changes of the polymer's physical and electronic properties, including the polymer's absorption[10,11] and conductivity.[8] Because assembly offers control over such properties, these materials have been integrated into organic photovoltaics,[12–14] sensors,[15,16] and have been used for biomedical imaging.[17–19]

CPEs also have the ability to form hydrogels if the building blocks self-assemble into extended structures, in much the same way as molecules like cetyl trimethyl ammonium bromide (CTAB) can be induced to form long worm-like micelles that result in gel formation.[20] Polymer hydrogels consist of a three-dimensional network held together either by chemical or physical means. A chemical hydrogel requires cross-linkers to create an interconnected network,[21–23] whereas a physical hydrogel network is held together by electrostatic interaction of charges, van der Waals forces, hydrogen bonds, etc.[24,25] The ≤10-nm structure of most gel networks is challenging to characterize through standard methods such as transmission electron microscopy (TEM) because these disordered networks lack both periodicity and electron density contrast, as they consist mainly of carbon. In this work, we use TEM to observe the existence of an interconnected network of rod-like micelles for a CPE. This is then complemented by solution-

phase small angle x-ray scattering (SAXS), Dammin bead modeling, and rheology measurements, all of which are indirect methods that we use to test hypothetical real-space models of the hydrogel's structure.

The gel structure of CPEs is essential to their implementation in electronic devices. For example, in organic photovoltaics (OPVs) a continuous nanostructured polymer network is required for extraction of charges out of the devices.[26] If discontinuous networks form due to polymer aggregation kinetics or phase separation from a second OPV component, then photogenerated current is lost. Thus, the advantage of forming fully interconnected gel networks from self-assembling CPE's is that this provides a route to create thermodynamically stable films with a beneficial function for optoelectronic devices.

In this study we show that the conjugated polyelectrolyte, poly(fluorene-alt-thiophene) (PFT; see Figure 6.1 for chemical structure), self-assembles into a network of cylindrical micelles in solution. Cryo-TEM provides a visualization of the polymer micelles that form in dilute solutions. Using solution SAXS in combination with Dammin bead modeling, we are able to determine the average size and shape of the micelles as well as the branching structure. Finally, through oscillatory mechanical rheometry, we measure the viscoelastic moduli and yielding behavior (*i.e.* the "break point") of the polymer network, and from the measured strength, we are able to postulate the types of connections that promotes gel network formation. We then show that the gels become stronger upon annealing with tetrahydrofuran (THF), and use Dammin bead modeling to visualize the increase in network connectivity and time-resolved microwave conductivity (TRMC) to show how THF annealing increases charge carrier mobility through the gel network.

6.2 Results and Discussion

The chemical structure of PFT is shown in Figure 6.1(a). This CPE can form micelles in water because of its amphiphilic character and because each monomer unit has an overall wedge-shape with a large hydrophilic volume because of the sp^3 carbon on the fluorene unit where the charged side chains attach.[8,32] These factors, combined with the fairly linear nature of the PFT backbone, allows PFT to assemble into rod-like micelles where the backbone of PFT runs along the long axis of the micelle, as shown by cartoon illustration in Figure 6.1(b) and as was characterized in detail for low molecular weight material in our previous work.[8] At concentrations as low as 1% wt/v, however, PFT forms a hydrogel, as seen in the photograph of the inverted vial shown in Figure 6.1(c). The molecular weight (MW) of PFT is critical to the formation of the gel network, thus size-selective precipitation was used to obtain both high and low MW fractions of the synthesized material (as described in Experimental). Unlike the high MW polymer, the low MW polymer does not form a gel network, indicating that the interactions between polymer micelles depends on the polymer chain length. Unless explicitly stated otherwise, all of the experiments described below use only the high MW polymer fraction.

6.2.1 Direct Structural Characterization of PFT Gels Using Cryo-EM and SAXS

Using cryo-electron microscopy on dilute solutions (cryo-EM, Figure 6.1d) we can observe both the micellar nature of the PFT assemblies and interconnections between those micelles, which should lead to hydrogel formation at higher concentrations. The cryo-EM samples were prepared by flash-freezing a droplet of PFT solution, as described above. The images produced show micelles that are both in the plane of the image, which appear as rods, and micelles standing on end, which appear as darker spots. From this data, we can approximately measure the diameter of

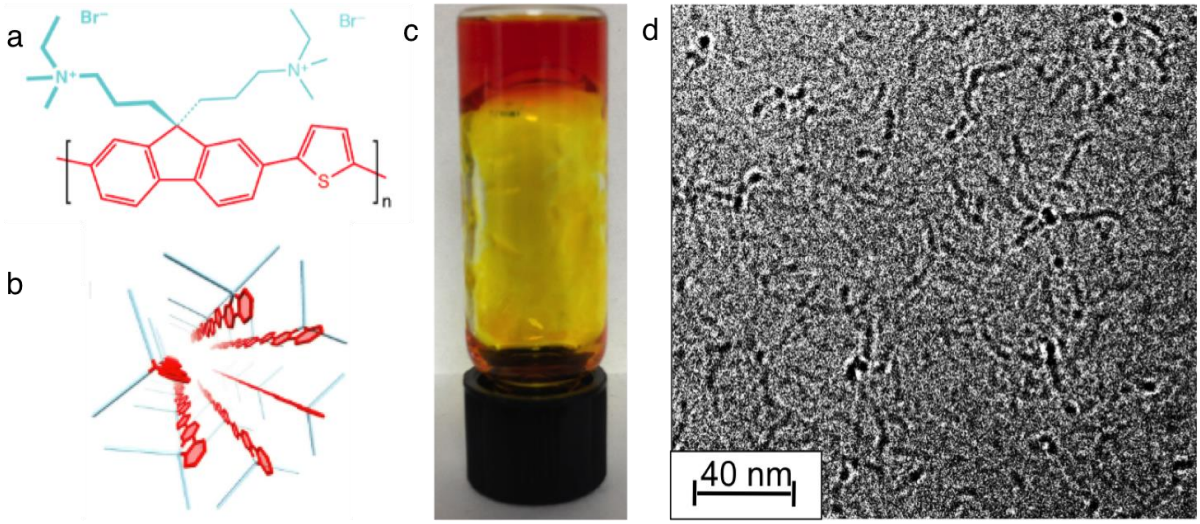

Figure 6.1. Properties of PFT. (a) Chemical structure of the PFT monomer. (b) Cartoon of an assembled PFT micelle based on SAXS and cryo-TEM data. (c) Photograph of an upside-down vial of a PFT hydrogel. (d) Cryo-TEM image of PFT micelles showing the bridging behavior even at dilute concentrations (1 mg/mL) (d).

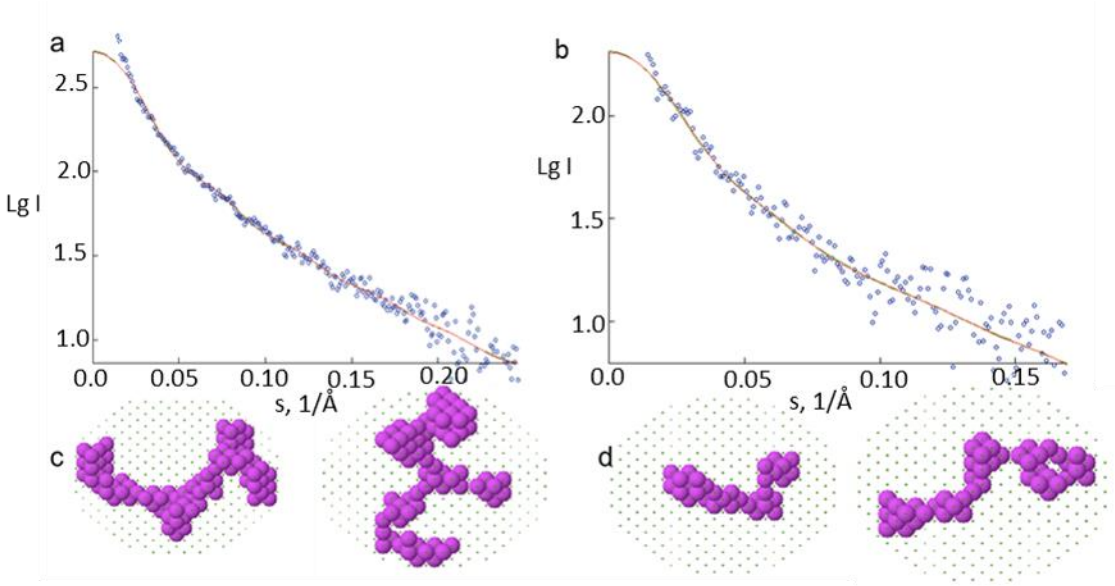

Figure 6.2. Fits of raw SAXS data to Dammin bead models for: (a) 1 mg/mL high-MW PFT samples and (b) 1mg/mL low-MW PFT samples. The corresponding bead models show a more bridged network for (c) the high-MW PFT sample, whereas (d) the low-MW PFT sample shows what appears to be single micelles that are not branched. Additional bead models are available in Appendix C.

the micelles to be about 4 nm, a size that correlates well with solution SAXS data we published previously.[8] The cryo-EM data provides clear evidence for PFT micelle formation and for the formation of interconnections between micelles, but because of the limited region that can be imaged at one time, it does not provide good statistical data on the average structure of the sample as a whole.

To further study the structure of the PFT micelle system we thus turned to solution SAXS. Solution SAXS has been used extensively to examine the nanometer scale structure of assemblies in solution.[33–35] By fitting the scattered intensity to a power law, $I = q^{-\alpha}$, we can relate the exponential slope, $-\alpha$, to the structure of the polymer in solution. Figure 6.2(a) shows that the scattering from PFT fits to two distinct slopes: $\alpha = 1.5$ at low q and $\alpha = 3.7$ at high q. The low-q slope of –1.5 is indicative of a rod-like shape at large distances, concomitant with the length of a rod; the high-q slope of –3.7 is indicative of a sphere-like shape, concomitant with the radius of the rod. This SAXS-determined rod-like shape correlates well with the micelle-shapes observed by TEM.

Along with the power-law analysis, the raw data can be fit using the software Gnom to enable smoothing of the data before the bead model analysis. The Dammin bead model fits this smoothed data and outputs a structure that may have caused the scattering data.[36] Comparing the bead models for high- and low-MW PFT (Figures 6.2 (b) and (c), respectively, with more bead model fits shown in Appendix C), indicates that the high-MW PFT has a more branched structure than the low-MW PFT. As stated above, the low MW polymer does not form a gel, while the high MW PFT does. From this data, we thus postulate that the low-MW polymer is present mostly in the form of discrete polymer micelles, while the high-MW PFT forms a branched network that enables gel formation. The base unit of this polymer hydrogel, as proven by TEM, SAXS, and the

Dammin bead modeling, is a rod-shaped polymer micelle.

6.2.2 Understanding Connections in the Gel Network via Rheology

With the basic structural element in hand, we now turn to rheology measurements to help determine how that polymer network is held together. Rheology is the study of the deformation or flow of matter, and one of the most useful techniques for studying the physics of a gel network.[37] The two components of the linear complex viscoelastic modulus, G^*, are the elastic storage modulus (G'), the in-phase real part, and the viscous loss modulus (G''), the 90° out-of-phase part. The storage modulus reflects the material's capacity to store energy resulting from shear excitations elastically, and the loss modulus reflects its capacity to dissipate energy.[38] Strictly speaking, G' and G'' are well defined only at very small strains (γ) in the linear response regime, but it is customary to measure these properties to very large strains beyond the yield point and still refer to them as G' and G'' even in the non-linear regime. Solids typically have $G' > G''$ over a large frequency (ω) range, extending to low frequencies. At fixed ω, constant behavior of $G'(\gamma)$ and $G''(\gamma)$ in the limit of small γ indicates linear behavior; at larger γ beyond the linear regime, a drop-off in $G'(\gamma)$ and peak in $G''(\gamma)$ signifies yielding behavior, beyond which dominantly viscous flow occurs at very high strains. By studying the viscoelastic response of a conjugated polyelectrolyte hydrogel under various strain and frequency studies, we can infer a great deal about the structure of the gel network.

We begin our rheology experiments with a gedanken model for the structure of the gel network and then attempt to prove or disprove that model. Given the micellar nature of PFT in solution, the very low concentrations where PFT begins to gel, and the fact that PFT has no significant potential to make either covalent or hydrogen bonds between polymer chains, we

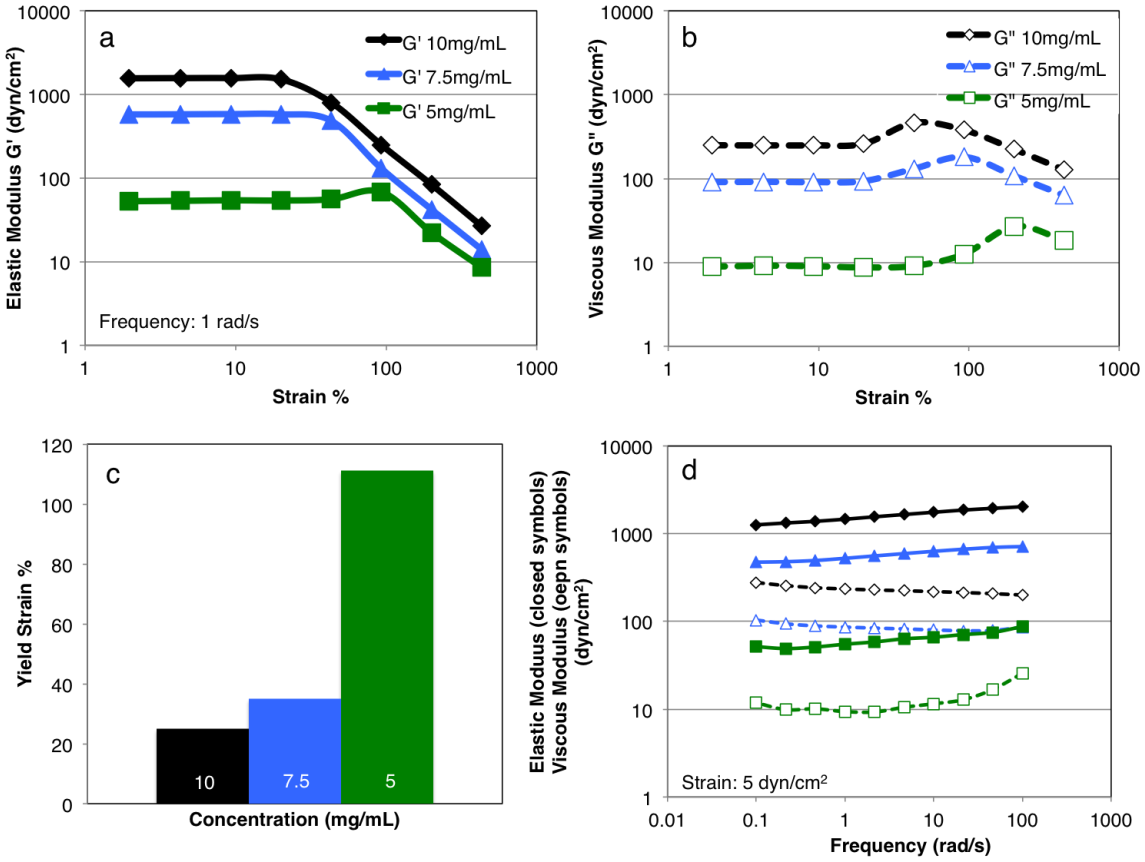

Figure 6.3. Mechanical shear rheometry measurements of gels with concentrations of 10, 7.5, and 5 mg/mL. (a) The strain-dependent elastic modulus and (b) the strain-dependent viscous modulus show that the most concentrated samples result in the strongest gel networks. (c) The yield strain (the point where enough strain has been applied to the system that it flows and is no long by definition a solid). (d) The frequency-dependent elastic and viscous moduli, showing the characteristics of hydrogels with robust networks.

hypothesize that it is the micelle formation itself that results in gel formation. For example, polymer chains can bridge between micelles, linking micelles together in much the same way that bridging actin fibers bridge between fiber bundles in actin gel networks.[39] We can describe these bridging polymer chains as "sticky ends" because in the absence of a second PFT micelle, a dangling polymer chain is likely to adopt a high energy, coiled conformation in aqueous solution, which would prefer to associate with another polymer micelle.

We can study the response of these PFT hydrogels under constant strain or constant frequency to help learn about the PFT network structure. Figure 6.3 (a) and (b) shows the values of $G'(\gamma)$ and $G''(\gamma)$ as a function of strain amplitude at a constant frequency of 1 rad/s for gels with concentrations of 10, 7.5 and 5 mg/mL. As expected, both the $G'(\gamma)$ and $G''(\gamma)$ values of the PFT gel increase as the polymer concentration increases, indicating that more concentrated gels have more interconnections. The elastic storage modulus for PFT shows a linear viscoelastic regime, where the modulus does not change with strain amplitude. The 10 mg/mL and 7.5 mg/mL samples both show a decrease at large strains in $G'(\gamma)$, which is known as yielding. These soft hydrogels yield at higher strains and then begins to flow at even higher strains where the non-linear $G''(\gamma)$ is significantly larger than the non-linear $G'(\gamma)$. In contrast, $G''(\gamma)$ begins with a linear viscoelastic regime but has an increase or peaks at high strains before decreasing similarly to $G'(\gamma)$.

Structurally, the elastic modulus reflects the number density of junctions in the polymer network, whereas the viscous modulus can reflect relaxation of elastic structures such as entanglements or connections that are being broken and formed dynamically under entropic microscopic excitations. The peak observed in $G''(\gamma)$ is indicative of the yield point of a dominantly elastic material, where the shear excitations far exceed entropic excitations and elements within the material are excited by the shear strain into shapes that are no longer similar

to those at thermal equilibrium. If the intramolecular interactions of the polymer micelles are disrupted, it should create more unbound "sticky ends", which should be loosely coiled due to steric constraints.[40] Because the 10 mg/mL and 7.5 mg/mL samples are too concentrated to allow the polymer chains to reorient, an increase in $G'(\gamma)$ at high γ is not observed before the material yields. This behavior is common in many polymer solutions and hydrogels.[41,42] In contrast, the 5 mg/mL samples show strain hardening in $G'(\gamma)$; this increase of both the elastic and viscous modulus is expected, because lower concentrations mean fewer connections between micelles and thus a weaker PFT network. When a large enough strain is applied to the system, it disrupts both the polymer micelles and the network. The polymer micelles can then reorient to bridge with other micelles in a more ideal configuration. In this case, we observe an increase in the number of junctions of this system. The observation of strain hardening in $G'(\gamma)$ thus supports the idea that bridging polymer chains are responsible for the formation of the PFT network.

Another important parameter that we can take from this polymer rheology study is the break point or failure point of the gel. The breakpoint of the hydrogel, shown in Figure 6.3(c), is the point where the strain amplitude applied to the system is sufficient to cause the network to break so that the entire system begins to flow.[43] In the case of PFT micelles, the bridging polymer chains would need to detach from one micelle and then align, allowing the samples to become liquid-like. There is only a slight difference between the break points for the 10 mg/mL and 7.5 mg/mL gels. However, the 5 mg/mL gel has a breakpoint that is more than twice as high as the 10 mg/mL and 7.5 mg/mL gels. This increase in breakpoint results from the lower density network that has the ability to dynamically reform junctions as strain is applied. Thus, the conclusions about the network from examining the break point of the gel agree well with the conclusions gleaned above from the elastic and viscous moduli.

Frequency-dependent measurements can be used to gain further insight about the nature of the gel. The frequency study in Figure 6.3(d) was performed at a constant strain amplitude of 5%, chosen to be in the plateau region for all gel samples. As in the strain amplitude measurements, we find that $G'(\omega)$ is always higher than $G''(\omega)$, proving that we have a solid-like gel. Also, as higher frequency oscillations are applied to the PFT gel, the slopes of the curves remain close to zero. This lack of response with increased frequency is also characteristic of physical gels because the network is strong enough to resist changes.[35] This implies that even though these are not exceptionally strong gels, the interactions that hold the gels together are quite robust. The viscous moduli for the 5 mg/mL sample does vary more with frequency than do the 10 mg/mL and 7.5 mg/mL samples, likely due to the fact that the 5 mg/mL is a much less connected gel, and so it is easier to reorient the micelles in this sample at high frequencies. These frequency measurements thus provide further information about the bridged PFT network.

6.2.3 THF Annealing of PFT Hydrogels

Studying the chemical factors that destroy these PFT hydrogels also can provide information about what holds them together. For example, the gel network is destroyed when PFT is exposed to THF.[44] Upon removal of the THF from the polymer system by thermal evaporation, the gel-network reforms. We hypothesize that this behavior arises because THF can enthalpically stabilize the coiled "sticky ends" of the bridging polymer chains, allowing the system to break the low entropy connections between micelles.

The THF annealing process of PFT gels can be followed by SAXS and analyzed with Dammin bead modeling as well as rheology. Figure 6.4 shows representative bead models for PFT samples before THF annealing, with THF present, and after removal of the THF (more bead

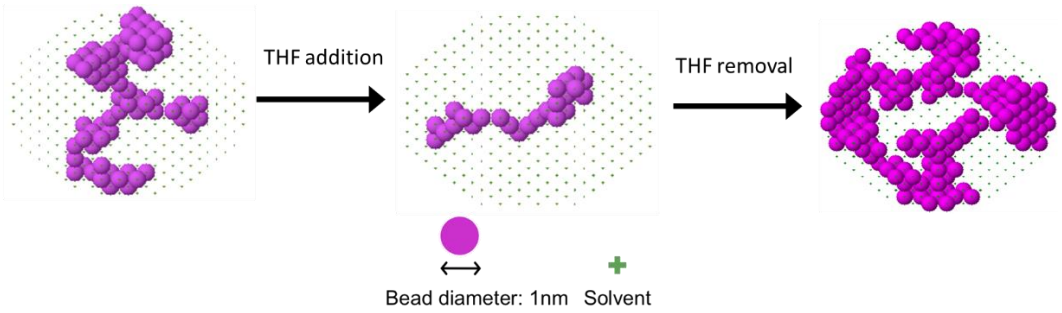

Figure 6.4. Dammin bead models of SAXS experiments (see Appendix C) on samples of high-MW PFT before THF annealing, during THF annealing, and after THF removal. Before THF annealing, the high-MW PFT shows a branched morphology. Upon addition of THF, however, the gel structure disassembles to either single PFT micelles or individual polymer chains. When THF is removed, the system shows an even higher polymer density that is representative of a more branched gel network.

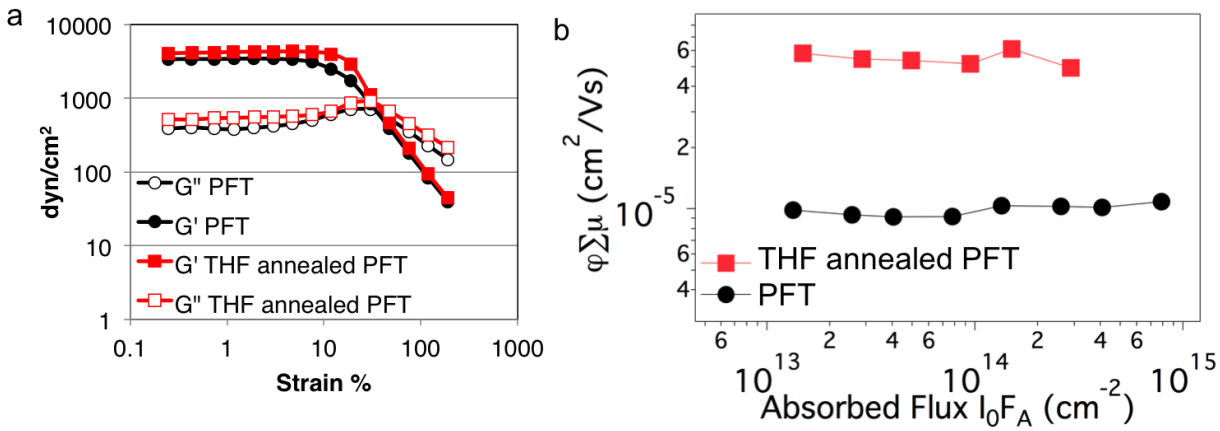

Figure 6.5. (a) Strain-dependent curves comparing high-MW PFT gels before (black) and after THF annealing (red). An increase is observed in both $G'(\gamma)$ and $G''(\gamma)$, suggesting a more robust network after THF annealing. (b) TRMC photoconductances measured on dried films cast from high-MW PFT solutions; films were cast before (black) and after THF annealing (red). Since the number of carriers created is not expected to change, the data shows that THF annealing provides an overall increase in carrier mobility.

models are available in Appendix C). The effect of adding THF on the micelle system is clearly observed by the loss of branching. The width of the structure decreases to approximately the width of a single bead, indicating that THF causes the solution to become either single solvated PFT chains or much smaller micelles. Upon removal of the THF, the PFT network becomes stronger, with the plateau modulus increasing from 3380 dyn/cm^2 to 4080 dyn/cm^2, as seen in Figure 6.5(a). Apparently, the gel network reforms in a more interconnected state than it is able to attain initially because network formation is kinetically limited when samples are first prepared. In agreement with this idea, Dammin modeling indicates that upon removal of the THF, both the branched structure and the width of the polymer micelles are restored (the raw scattering data with fit is available in Appendix C). Interestingly, the branching density increases, indicating that the post-annealed gel network contains more interconnected polymer micelles, compared to its pre-annealed counterpart. Thus, both the SAXS and rheological studies support the idea that THF annealed PFT gels have a more interconnected network.

If THF annealing increases the density of network connections, then it follows that THF annealing should also increase the conductivity of the PFT network. TRMC is a unique tool that allows for measurement of the photoconductivity of solid-state films without a need for electrical contacts.[45,46] In TRMC, photoinduced carriers are created by a laser pulse incident on the sample. These mobile carriers then absorb microwaves as they are induced to move by the microwave electric field, and the change in microwave power is measured. The change in microwave power is proportional to the local nm-scale photoconductivity of the sample, which is the product of the mobile carrier yield per photon absorbed, φ, and the sum of the mobilities of the carriers, $\Sigma\mu$ (the carriers in this case are both electrons and holes, as discussed in the experimental section).

Figure 6.5(b) shows that films produced from PFT solutions (diluted from gels) that have

been THF-annealed have a 6-fold increase in the $\varphi\Sigma\mu$ product. If we assume that the carrier yield is comparable in all of the PFT gel samples (a reasonable assumption, given their identical chemical nature and absorption of the pump laser), then the carrier mobility must be higher in the THF-annealed sample. We attribute this increased mobility both to the increased interconnectivity of the polymer network after THF annealing and to the decreased chain coiling in the THF-annealed samples (it has been shown that kinks and bends in polymer chains cause trap sites that reduce carrier mobility).[47,48] Furthermore, extending the conjugation length of the polymer by having longer straight sections can also increase the charge carrier mobility at microwave frequencies.[49] This data thus suggest that in addition to making more interconnections between micelles, THF annealing also increases the polymer ordering within micelles, a fact that is consistent with the observed increase in the plateau modulus.

6.2.4 Understanding Gel Network Structure via Mixing of Low- and High-MW PFT

Although all of the experiments described above provide information about the nature of these PFT hydrogels, they do not concretely prove that bridging polymer chains act as "sticky ends" that link micelles together. Thus, to further investigate this idea, we can take advantage of the fact that the polymer synthesis provides us with both high- and low-MW fractions (obtained by size selective precipitation, as discussed in the Experimental). To this end, we selectively recombined the high- and low-MW PFT with different ratios but maintaining the same overall polymer concentration. In this way, we can test how the low-MW PFT, which does not form a gel, interacts with the gel-forming high-MW PFT.

Figures 6.6(a) and (b) show the $G'(\gamma)$ and $G''(\gamma)$, respectively, for a series of samples that all have a total PFT concentration of 10 mg/mL but are made up of different fractions of low- and

high-MW polymer. The samples contain polymer ratios of 9 mg high-MW PFT to 1 mg low-MW PFT (9:1), 8 mg high-MW PFT to 2 mg low-MW PFT (8:2), and 7 mg high-MW PFT to 3 mg low-MW PFT (7:3). As a control, we also made a pure high-MW 10 mg/mL PFT sample (10) that has no low-MW PFT; this sample forms the strongest gel and thus provides a standard of comparison for the mixed-MW PFT samples. The figure shows clearly that there is an order of magnitude decrease in plateau modulus between the 10 mg/mL and the 9:1 samples, and another order of magnitude decrease between the 9:1 and 8:2 samples. The plateau modulus for the 7:3 sample is yet another four times lower than the 8:2 sample.

This dramatic decrease in the strength of the gel is caused not just by the decreasing amount of high-MW polymer, but also by the addition of the low-MW PFT. For example, the pure 7.5 mg/mL high-MW sample in Figure 6.3(a) has a $G'(\gamma)$ plateau value of 575 dyn/cm^2, where the 7:3 sample, which contains essentially the same amount of high-MW polymer, has a $G'(\gamma)$ plateau value of just 4.5 dyn/cm^2. We postulate that the reason for the decrease in gel strength is due to the fact that the low-MW polymer is able to cap the "sticky ends" of the high MW PFT micelle, allowing the high MW polymer to achieve an enthalpically favorable conformation without the entropic constraints of bridging between micelles.

We can obtain even more information about the mixed-MW samples by again focusing on the strain hardening observed in the elastic storage modulus. The pure 10 mg/mL PFT samples and the 9:1 samples show only yielding behavior, where the 8:2 and 7:3 samples show strain hardening at higher strains. This suggests that there are still sufficient interconnections in the 9:1 sample to prevent dynamical network reformation under strain. However, with the 8:2 and 7:3 samples, the ends of the micelles are capped with the low-MW PFT, so when strain is applied the low-MW PFT may transiently disengage from the high-MW PFT so that the "sticky ends" can

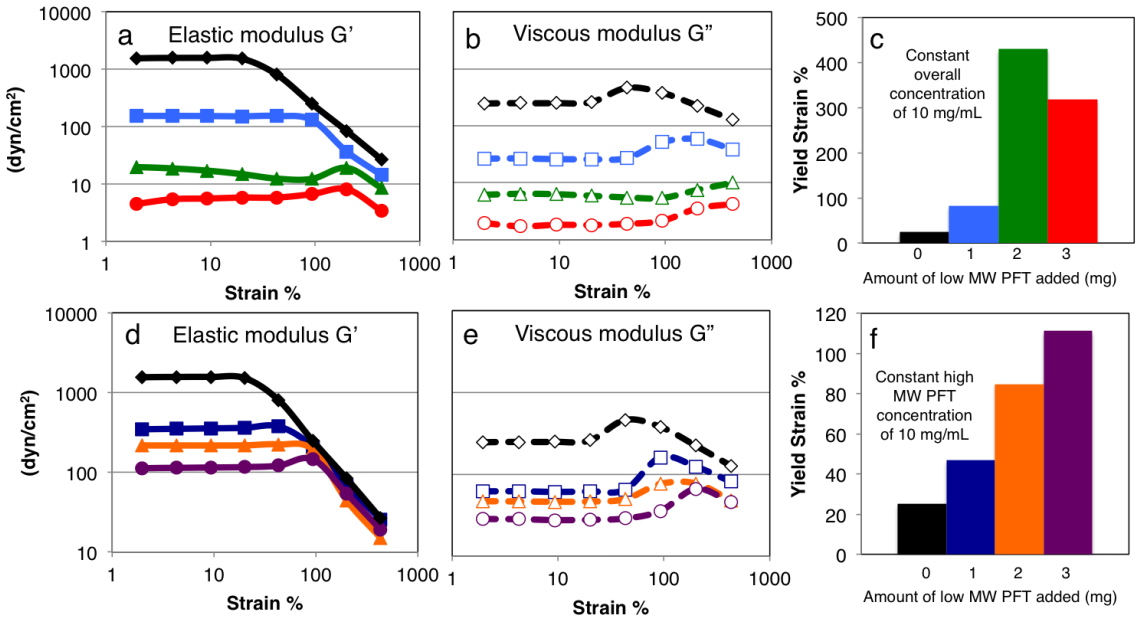

Figure 6.6. (a) Strain-dependent elastic modulus, (b) viscous modulus and (c) yield strain for PFT samples with a constant total concentration (10 mg/mL) but different ratios of low-MW PFT to high-MW PFT. As more low-MW PFT is added the hydrogel strength decreases, implying that the low-MW PFT is decreasing the amount of bridging polymer chains in the sample. (d) Strain-dependent elastic modulus, (e) viscous modulus and (f) yield strain for samples with a fixed concentration (10 mg/mL) of high-MW PFT combined with various amounts of low-MW PFT (1, 2 and 3 mg/mL). As low-MW PFT is added to high-MW PFT, the strength of the hydrogel decreases even though the overall polymer concentration is increasing.

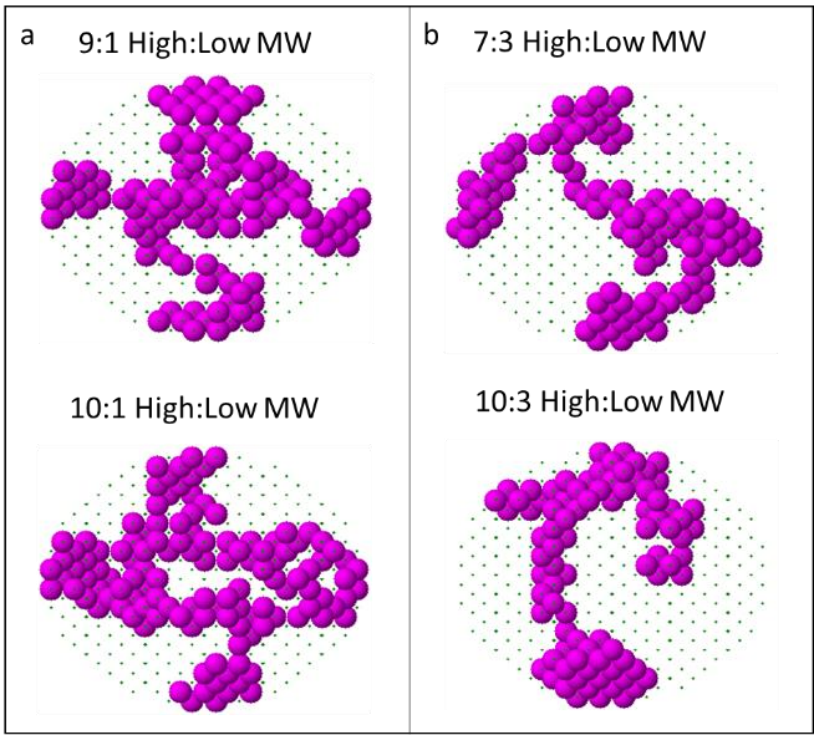

Figure 6.7. Dammin bead models of SAXS experiments for the same mixed high-MW/low-MW PFT samples whose rheology is explored in Figure 6.6. (a) Samples with a constant overall concentration, and (b) samples with a constant concentration of high-MW PFT. In both (a) and (b) the density of the bead models decreases as low-MW PFT is added to the high-MW PFT. This suggests that low-MW PFT caps the 'sticky ends' of the high-MW PFT micelles. In particular, the total polymer concentration of the 10:3 sample is quite a bit higher then the 10:1 sample, but the bead density is higher in the less concentrated sample that contains less low-MW polymer.

again bridge polymer micelles. The breakpoint, seen in Figure 6.6(c), actually increases from the 10 mg/mL samples to the 9:1 sample. The 8:2 and 7:3 breakpoints are similar, but as these are weak gels, we would expect an increase in the breakpoint relative to the pure the high-MW PFT gel studied in Figure 6.3(c).

Although the data presented above provides strong indication that low-MW PFT disrupts the nature of the gel network, the fact that the total amount of high-MW PFT is not constant in these samples complicates the issue. We thus performed a second set of experiments using a fixed concentration of high-MW PFT and a varying total polymer concentration. For this experiment, the concentration of high-MW PFT was kept at 10 mg/mL, and low-MW PFT was added in 1, 2, and 3 mg amounts (10:1, 10:2, 10:3).

As above, Figures 6.6 (d) and (e) show a decrease of $G'(\gamma)$ and $G''(\gamma)$ upon the addition of low-MW PFT, despite the fact that the total polymer concentration increases. The decrease of the elastic modulus after addition of 1 mg of low MW PFT is roughly an order of magnitude, although less than that observed in Figure 6.4(a) for the 9:1 sample. Indeed, the plateau moduli decrease as more low-MW PFT is added to the system. Normal yielding behavior at high strains in $G'(\gamma)$ is observed for the 10:1 and 10:2 samples, but the 10:3 sample shows slight strain hardening at high strains. It follows that the 10:1 and 10:2 samples still exhibit significant micelle bridging, as the ratio of low:high-MW PFT is not high enough to effectively break up the gel network. However, in the 10:3 samples, enough low-MW PFT is present to cap the ends of the polymer micelles and disrupt the network. The breakpoint in Figure 6.4(f) steadily increases as low-MW PFT is added, but the increase is not as large as in Figure 6.4(c). This data thus indicates that both the total concentration of high-MW polymer and the low-MW:high-MW ratio interplay to control the density of connections within the network.

The structural effects of adding low-MW PFT to high-MW PFT were further analyzed using solution SAXS and Dammin bead modeling on dilute 1mg/mL samples. Figure 6.7 shows the fits for the 9:1, 7:3, 10:1, and 10:3 high-MW:low-MW samples (see Appendix C for additional bead models). When comparing the 9:1 and 7:3 samples, we find that although the total polymer concentration is the same, the density of beads in the two models differs, indicating that in the 7:3 sample, a larger fraction of the polymer chains are individually dissolved (or form very small aggregates that are too small to see in the scattering vector range used for this experiment). The 9:1 sample contains a higher density of beads, indicating larger aggregates in solution and higher branching. The 10:1 and 10:3 samples show a similar trend, even though a higher bead density might have been expected for the 10:3 sample due to the higher total polymer concentration. Indeed, even though the 10:1 sample contains less polymer and the same amount of high-MW PFT as the 10:3 sample, a higher overall bead density is observed, again indicting larger aggregates with increased branching in solution for the 10:1 sample. This supports the idea that low-MW PFT caps the sticky ends of bridging high-MW PFT strands, resulting in less branching and more linear, single rod structures in samples containing more low-MW polymer.

6.3 Conclusions

In this study we examined the network structure of semiconducting polymer PFT hydrogels. TEM and SAXS were employed to examine the micellar building blocks of the hydrogel and Dammin models were used to analyze the solution SAXS data to visualize the network structure, all of which support the hypothesis of rod-like micelle building units. Rheology was used to examine interconnections within the gel network, and a combination of TRMC and rheology indicated that a more interconnected and potentially more ordered network was formed

after THF annealing of the gel. Bead models and rheology studies of mixed low-MW and high-MW PFT samples were used to further our understanding of the interactions that hold this semiconducting gel-network together. All of the data strongly supports a picture where the gel network is held together by polymer chains that bridge neighboring micelles, co-assembling with more than one micelle based on amphiphilic interactions. These bridging polymer chains, or "sticky ends" can be disrupted by either the addition of organic solvents or by adding low-MW polymers that can co-assemble with the "sticky ends" in a non-bridging fashion.

A key conclusion that comes from this work is the fact high-MW polymer chains bridge between micelles, offering the potential for facile electrical conductivity among the 3-D gel network. Although direct electrical measurements on the hydrogel network are complicated by the high conductivity of water, our TRMC results on dried gel networks show great promise for future device applications. The strongly interconnected nature of these conjugated polymer hydrogel networks could be ideal for a variety of polymer-based electronic devices as they rely on good conductivity in a heterostructured network.

6.4 Experimental

Polymer synthesis was performed as previously reported.[8] To further purify the PFT into high and low molecular weight fractions, 250 mg of PFT was dissolved in 5 mL of DMSO. Once dissolved, ethyl acetate was added to the PFT/DMSO solution until the polymer began to precipitate out of solution. Centrifugation was then used to pull the precipitated PFT out of the suspended solution. After pouring off the solution and drying the PFT, the solid that remained had a fairly high molecular weight, and for the rest of this paper, we refer to this fraction as high MW PFT. More ethyl acetate was added to the remaining solution and the rest of the polymer is

precipitated out of solution, producing the fraction that we refer to as low MW PFT.

Tetrahydrofuran (THF) annealing was performed by adding 0.05 mL of THF to 0.5 mL of H_2O with various amount of PFT. The PFT gel becomes a liquid upon addition of THF. The THF was then removed by heating and stirring at 80 ^oC for 4 hours.

Cryo-imaging grids for transmission electron microscopy were prepared by placing a small drop (~4 μl) of sample solution onto a glow-discharged holey-carbon mesh (Quantifoil 200 mesh grids) with 3.5-μm holes spaced 1-μm apart. The grids were then blotted and plunged immediately into liquid-nitrogen-cooled liquid ethane to rapidly freeze the samples in vitrified ice. The cryo-grids were visualized with an FEI Tecnai F20 transmission electron microscope with an accelerating voltage of 200 kV. Images were collected at ~50,000x magnification with a defocus of approximately 3 μm.

Small-angle X-ray scattering (SAXS) experiments were conducted at the Stanford Synchrotron Radiation Lightsource (SSRL) on Beamline 4-2. Using a syringe, 100 μL of each sample was loaded into a quartz capillary and held at 25 ^oC. Scattered X-rays (at 12 keV) were collected with a Rayonix MX225-HE detector (sample to detector distance = 1.7 m). The two-dimensional data was radially averaged to obtain one-dimensional scattering curves.

Raw solution SAXS data was fit and smoothed using Gnom and bead models were performed on the smoothed data using Dammin, a Monte-Carlo type modeling software that uses beads and solvent to create shapes that could have generated the experimental curves. The expert setting was used and the bead size was set to have a radius of 5 Å, corresponding to the width of a single polymer chain. The diameter of the sphere was set to be 140 Å. Each data set was run at least five times to ensure trends were reproducible Only a subset of the overall data is shown in the figures.

Rheological properties were measured on a Rheometrics RFS2 strain-controlled rheometer. The geometry used was the cone-and-plate for both strain-controlled and frequency-controlled experiments. Strain-controlled measurements were performed at a frequency of $\omega = 1$ rad/s and the frequency-controlled measurements were performed at a shear strain of $\gamma = 5\%$, corresponding to the linear response regime.

Flash-photolysis time-resolved microwave conductivity (TRMC) was used to measure photoconductivity via methods that have been previously reported.[27–30] Briefly, samples for microwave conductivity measurements were prepared onto 10 x 24 mm quartz substrates that were cleaned by subsequent ultrasonic baths in detergent, deionized water, acetone and isopropanol for 10 minutes each. Samples were placed into an X-band microwave cavity terminated with a grating that is transparent to optical excitations but reflective to microwaves. The samples were excited through the quartz substrates by a 5-ns, 500-nm laser pulse produced from an Optical Parametric Oscillator (Continuum Panther) pumped by the 355-nm harmonic of a Q-switched Nd:YAG laser (Continuum Powerlite) with a typical fluence of 0.56 mJ/cm^2. The intensity of the excitation was controlled by switchable neutral density filters. The photoinduced carries absorbed the incident microwaves, and the change in microwave power was measured and related to the conductance, ΔG, of the sample.[31] From ΔG, the product of the yield of the free charge carriers generated per photon absorbed, φ, with the sum of the mobilities of these carriers, $\Sigma\mu$, can be calculated as $\varphi\Sigma\mu = \Delta G/(\beta q_e I_0 F_A)$,[31] where I_0 is the photon flux of the excitation beam incident on the sample, F_A is the fraction of absorbed photons at the excitation wavelength, $\beta = 2.2$ is a geometric factor and q_e is the elementary charge.

6.5 References

(1) Chi, C.; Mikhailovsky, A.; Bazan, G. C. Design of Cationic Conjugated Polyelectrolytes for DNA Concentration Determination. *J. Am. Chem. Soc.* **2007**, *129*, 11134–11145.

(2) Jiang, H.; Zhao, X.; Schanze, K. S. Effects of Polymer Aggregation and Quencher Size on Amplified Fluorescence Quenching of Conjugated Polyelectrolytes. *Langmuir* **2007**, *23*, 9481–9486.

(3) Jiang, H.; Taranekar, P.; Reynolds, J. R.; Schanze, K. S. Conjugated Polyelectrolytes: Synthesis, Photophysics, and Applications. *Angew. Chem. Int. Ed. Engl.* **2009**, *48*, 4300–4316.

(4) Thomas, A.; Houston, J. E.; Van den Brande, N.; De Winter, J.; Chevrier, M.; Heenan, R. K.; Terry, A. E.; Richeter, S.; Mehdi, A.; Van Mele, B.; et al. All-Conjugated Cationic Copolythiophene "rod–rod" Block Copolyelectrolytes: Synthesis, Optical Properties and Solvent-Dependent Assembly. *Polym. Chem.* **2014**, *5*, 3352.

(5) Wu, C.; Bull, B.; Szymanski, C.; Christensen, K.; McNeill, J. Multicolor Conjugated Polymer Dots for Biological Fluorescence Imaging. *ACS Nano* **2008**, *2*, 2415–2423.

(6) Tuncel, D.; Demir, H. V. Conjugated Polymer Nanoparticles. *Nanoscale* **2010**, *2*, 484–494.

(7) Stevens, A. L.; Kaeser, A.; Schenning, A. P. H. J.; Herz, L. M. Morphology-Dependent Energy Transfer Dynamics in Fluorene-Based Amphiphile Nanoparticles. *ACS Nano* **2012**, *6*, 4777–4787.

(8) Clark, A. P.-Z.; Shi, C.; Ng, B. C.; Wilking, J. N.; Ayzner, A. L.; Stieg, A. Z.; Schwartz, B. J.; Mason, T. G.; Rubin, Y.; Tolbert, S. H. Self-Assembling Semiconducting Polymers-Rods and Gels from Electronic Materials. *ACS Nano* **2013**, *7*, 962–977.

(9) Zaroslov, Y. D.; Gordeliy, V. I.; Kuklin, a. I.; Islamov, a. H.; Philippova, O. E.; Khokhlov, a. R.; Wegner, G. Self-Assembly of Polyelectrolyte Rods in Polymer Gel and in Solution: Small-Angle Neutron Scattering Study. *Macromolecules* **2002**, *35*, 4466–4471.

(10) Nguyen, T.; Martini, I.; Schwartz, B. Controlling Interchain Interactions in Conjugated Polymers: The Effects of Chain Morphology on Exciton-Exciton Annihilation and Aggregation in MEH-PPV Films. *J. Phys. Chem. B* **2000**, *104*, 237–255.

(11) Martini, I. B.; Smith, A. D.; Schwartz, B. J. Exciton-Exciton Annihilation and the Production of Interchain Species in Conjugated Polymer Films : Comparing the Ultrafast Stimulated Emission and Photoluminescence Dynamics of MEH-PPV. *Phys. Rev. B* **2004**, *69*, 1–12.

(12) Seo, J.; Gutacker, A.; Sun, Y. Improved High-Efficiency Organic Solar Cells via Incorporation of a Conjugated Polyelectrolyte Interlayer. *J. …* **2011**, *133*, 8416–8419.

(13) Costa, T.; Marques, A. T.; Se, J.; Melo, S. De; Thomas, A. W.; Garner, L. E.; Scherf, U.;

Bazan, G. C.; Burrows, H. D. Self-Assembly of Poly{1,4-Phenylene-[9,9-bis(4-Phenoxy-Butylsulfonate)]fluorene-2,7-Diyl} with Oppositely Charged Phenylenevinylene Oligoelectrolytes. *J. Phys. Chem. B* **2014**, 613–623.

(14) He, Z.; Zhong, C.; Su, S.; Xu, M.; Wu, H.; Cao, Y. Enhanced Power-Conversion Efficiency in Polymer Solar Cells Using an Inverted Device Structure. *Nat. Photonics* **2012**, *6*, 591–595.

(15) Lutkenhaus, J. L.; Hammond, P. T. Electrochemically Enabled Polyelectrolyte Multilayer Devices: From Fuel Cells to Sensors. *Soft Matter* **2007**, *3*, 804.

(16) Wang, D.; Gong, X.; Heeger, P. S.; Rininsland, F.; Bazan, G. C.; Heeger, A. J. Biosensors from Conjugated Polyelectrolyte Complexes. *Proc. Natl. Acad. Sci. U. S. A.* **2002**, *99*, 49–53.

(17) Shu, S.; Zhang, X.; Wu, Z.; Wang, Z.; Li, C. Gradient Cross-Linked Biodegradable Polyelectrolyte Nanocapsules for Intracellular Protein Drug Delivery. *Biomaterials* **2010**, *31*, 6039–6049.

(18) O'Connell, M. J.; Chan, C. K.; Li, W.; Hicks, R. K.; Doorn, S. K.; Wang, H.-L. Polyelectrolyte Platform for Sensitive Detection of Biological Analytes via Reversible Fluorescence Quenching. *Polymer (Guildf).* **2007**, *48*, 7582–7589.

(19) Tai, B. C. U.; Wan, A. C. a; Ying, J. Y. Modified Polyelectrolyte Complex Fibrous Scaffold as a Matrix for 3D Cell Culture. *Biomaterials* **2010**, *31*, 5927–5935.

(20) Chakraborty, T.; Ghosh, S.; Moulik, S. P. Micellization and Related Behavior of Binary and Ternary Surfactant Mixtures in Aqueous Medium: Cetyl Pyridinium Chloride (CPC), Cetyl Trimethyl Ammonium Bromide (CTAB), and Polyoxyethylene (10) Cetyl Ether (Brij-56) Derived System. *J. Phys. Chem. B* **2005**, *109*, 14813–14823.

(21) Hennink, W. E.; van Nostrum, C. F. Novel Crosslinking Methods to Design Hydrogels. *Adv. Drug Deliv. Rev.* **2002**, *54*, 13–36.

(22) Luo, Y.; Kirker, K. R.; Prestwich, G. D. Cross-Linked Hyaluronic Acid Hydrogel Films: New Biomaterials for Drug Delivery. *J. Control. Release* **2000**, *69*, 169–184.

(23) Peppas, N. a.; Hilt, J. Z.; Khademhosseini, a.; Langer, R. Hydrogels in Biology and Medicine: From Molecular Principles to Bionanotechnology. *Adv. Mater.* **2006**, *18*, 1345–1360.

(24) Campoccia, D.; Doherty, P.; Radice, M.; Brun, P.; Abatangelo, G.; Williams, D. F. Semisynthetic Resorbable Materials from Hyaluronan Esterification. *Biomaterials* **1998**, *19*, 2101–2127.

(25) Prestwich, G. D.; Marecak, D. M.; Marecek, J. F.; Vercruysse, K. P.; Ziebell, M. R. Controlled Chemical Modification of Hyaluronic Acid: Synthesis, Applications, and

Biodegradation of Hydrazide Derivatives. *J. Control. Release* **1998**, *53*, 93–103.

(26) Shaw, P. E.; Ruseckas, A.; Samuel, I. D. W. Exciton Diffusion Measurements in Poly(3-Hexylthiophene). *Adv. Mater.* **2008**, *20*, 3516–3520.

(27) Kroeze, J. E.; Savenije, T. J.; Vermeulen, M. J. W.; Warman, J. M. Contactless Determination of the Photoconductivity Action Spectrum, Exciton Diffusion Length, and Charge Separation Efficiency in Polythiophene-Sensitized TiO 2 Bilayers. **2003**, 7696–7705.

(28) Dicker, G.; de Haas, M. P.; Siebbeles, L. D. A.; Warman, J. M. Electrodeless Time-Resolved Microwave Conductivity Study of Charge-Carrier Photogeneration in Regioregular poly(3-Hexylthiophene) Thin Films. *Phys. Rev. B* **2004**, *70*, 45203.

(29) Piris, J.; Kopidakis, N.; Olson, D. C.; Shaheen, S. E.; Ginley, D. S.; Rumbles, G. The Locus of Free Charge-Carrier Generation in Solution-Cast Zn1–xMgxO/Poly(3-Hexylthiophene) Bilayers for Photovoltaic Applications. *Adv. Funct. Mater.* **2007**, *17*, 3849–3857.

(30) Ferguson, A. J.; Kopidakis, N.; Shaheen, S. E.; Rumbles, G. Quenching of Excitons by Holes in Poly(3-Hexylthiophene) Films. *J. Phys. Chem. C* **2008**, *112*, 9865–9871.

(31) Savenije, T. J.; Ferguson, A. J.; Kopidakis, N.; Rumbles, G. Revealing the Dynamics of Charge Carriers in Polymer:Fullerene Blends Using Photoinduced Time-Resolved Microwave Conductivity. *J. Phys. Chem. C* **2013**, *117*, 24085–24103.

(32) Israelachvili, J. N.; Mitchell, D. J.; Ninham, B. W. *Theory of Self-Assembly of Hydrocarbon Amphiphiles into Micelles and Bilayers*; 1975; pp. 1525–1568.

(33) Beaucage, G. Small-Angle Scattering from Polymeric Mass Fractals of Arbitrary Mass-Fractal Dimension. *J. Appl. Crystallogr.* **1996**, *29*, 134–146.

(34) Svergun, D. I.; Koch, M. H. J. Small-Angle Scattering Studies of Biological Macromolecules in Solution. *Reports Prog. Phys.* **2003**, *66*, 1735–1782.

(35) Choudhary, S.; Bhatia, S. R. Rheology and Nanostructure of Hydrophobically Modified Alginate (HMA) Gels and Solutions. *Carbohydr. Polym.* **2012**, *87*, 524–530.

(36) Svergun, D. I. Restoring Low Resolution Structure of Biological Macromolecules from Solution Scattering Using Simulated Annealing. *Biophys. J.* **1999**, *76*, 2879–2886.

(37) Fairclough, J. P. A.; Norman, A. I. Structure and Rheology of Aqueous Gels. In *Annual Reports Section "C" (Physical Chemistry)*; 2003; Vol. 99, pp. 243–276.

(38) Shaw, M. T. *Introduction to Polymer Rheology*; 2012.

(39) Shah, J. V.; Janmey, P. a. Strain Hardening of Fibrin Gels and Plasma Clots. *Rheol. Acta* **1997**, *36*, 262–268.

(40) Tirtaatmadja, V.; Tam, K. C.; Jenkins, R. D. Superposition of Oscillations on Steady Shear

Flow as a Technique for Investigating the Structure of Associative Polymers. *Macromolecules* **1997**, *30*, 1426–1433.

(41) Hyun, K.; Wilhelm, M.; Klein, C. O.; Cho, K. S.; Nam, J. G.; Ahn, K. H.; Lee, S. J.; Ewoldt, R. H.; McKinley, G. H. A Review of Nonlinear Oscillatory Shear Tests: Analysis and Application of Large Amplitude Oscillatory Shear (LAOS). *Prog. Polym. Sci.* **2011**, *36*, 1697–1753.

(42) Hyun, K.; Kim, S. H.; Ahn, K. H.; Lee, S. J. Large Amplitude Oscillatory Shear as a Way to Classify the Complex Fluids. *J. Nonnewton. Fluid Mech.* **2002**, *107*, 51–65.

(43) Mason, T. G.; Bibette, J.; Weitz, D. A. Yielding and Flow of Monodisperse Emulsions. *J. Colloid Interface Sci.* **1996**, *448*, 439–448.

(44) Evans, R. C. Harnessing Self-Assembly Strategies for the Rational Design of Conjugated Polymer Based Materials. *J. Mater. Chem. C* **2013**, *1*, 4190.

(45) Ferguson, A. J.; Kopidakis, N.; Shaheen, S. E.; Rumbles, G. Dark Carriers, Trapping, and Activation Control of Carrier Recombination in Neat P3HT and P3HT:PCBM Blends. *J. Phys. Chem. C* **2011**, *115*, 23134–23148.

(46) Aguirre, J. C.; Arntsen, C.; Hernandez, S.; Huber, R.; Nardes, A. M.; Halim, M.; Kilbride, D.; Rubin, Y.; Tolbert, S. H.; Kopidakis, N.; et al. Understanding Local and Macroscopic Electron Mobilities in the Fullerene Network of Conjugated Polymer-Based Solar Cells: Time-Resolved Microwave Conductivity and Theory. *Adv. Funct. Mater.* **2014**, *24*, 784–792.

(47) Liang, Z.; Reese, M. O.; Gregg, B. A. Chemically Treating poly(3-Hexylthiophene) Defects to Improve Bulk Heterojunction Photovoltaics. *ACS Appl. Mater. Interfaces* **2011**, *3*, 2042–2050.

(48) Gregg, B. A. Transport in Charged Defect-Rich Π -Conjugated Polymers. *J. Phys. Chem. C* **2009**, *113*, 5899–5901.

(49) Prins, P.; Grozema, F.; Schins, J.; Patil, S.; Scherf, U.; Siebbeles, L. High Intrachain Hole Mobility on Molecular Wires of Ladder-Type Poly(p-Phenylenes). *Phys. Rev. Lett.* **2006**, *96*, 146601.

CHAPTER 7

Long-Lived Photoinduced Polaron Formation in Conjugated Polyelectrolyte/Fullerene Assemblies

7.1 Introduction

In biological photosynthetic systems, energy cascade structures promote the spatial separation of photogenerated charges created at the reaction center, preventing their recombination. These energy cascade structures require close proximity of the electron donors and acceptors, on the scale of ~1 nm, and the corresponding electron transfer (ET) processes take only a few picoseconds.[1] Similarly, photoexcitation in artificial organic photovoltaic (OPV) cells generates dissociated charges at a donor-acceptor interface on sub-picosecond time scales. However, OPVs suffer a large degree of recombination because they rely on phase separation of the conjugated polymer donor and fullerene acceptor into domains on the length scale of 10 to 20 nm to facilitate efficient exciton diffusion and charge transfer.[2,3] The high charge densities present in OPVs, coupled with the low dielectric constant of organic materials, favor carrier recombination before the charges can be extracted through external electrodes. If OPVs could be designed to use ET cascade structures that are reminiscent of photosynthetic complexes, it should be possible to greatly improve charge separation and reduce recombination losses.[4]

In this chapter, we describe how molecular self-assembly can enable dissolved OPV materials (conjugated polymers and fullerenes) in aqueous solution to mimic the ET cascade structures of biological complexes and allow us to 'spatially' control photogenerated charges. We demonstrate efficient long-time charge separation following photoexcitation: the ET cascade

produces separated polarons that are exceptionally stable for weeks, a lifetime that is unprecedented for OPV materials. Although long polaron lifetimes have been observed in covalently linked donor-acceptor dyads and triads[5] and micellar structures,[6] it is the fact that we are using standard organic photovoltaic materials that sets this work apart. In addition, our use of self-assembly provides potential future advantages in reproducibility and scalability, both of which are major hurdles for conventional OPVs with kinetically-controlled structures.[7–9] Finally, the photoinduced charge separation we achieve takes place in water, opening possibilities for the 'green' production of artificial photosynthetic devices.

7.2 Results and Discussion

The particular materials used in this study are a combination of a conjugated polyelectrolyte, poly(fluorene-alt-thiophene) (PFT),[10] and several regioisomers of the charged fullerene derivatives C_{60}-*N*,*N*-dimethylpyrrolidinium iodide ($C_{60}(PI)_n$), where *n* is the number of charged pyrrolidinium iodide groups[11] (Figure 7.1, (a) through (c)). PFT is a water-soluble semiconducting polyelectrolyte whose bis-alkylated sp^3-hybridized fluorenyl carbon forms a wedge-shaped monomer that facilitates the assembly of the charged polymer into rod-like micelles, as shown in Figure 7.1(b); details of how this polymer assembles have been published previously.[10] Because of the charged nature of the polymer, the electron acceptor(s) must also carry cationic charges to avoid heterocoagulation. The synthesis of $C_{60}(PI)_n$, depending on the reaction conditions, produced multiadducts with *n* ranging from 2 to 5, including multiple regioisomers for each *n*. To avoid confusion, we will refer to $C_{60}(PI)_n$ with *n* = 3-5 as 'higher' adducts, and fullerenes with *n* = 2 will be referred to as 'mixed-bis' adducts.

We achieved control over the solution-phase aggregation of these materials by exploiting

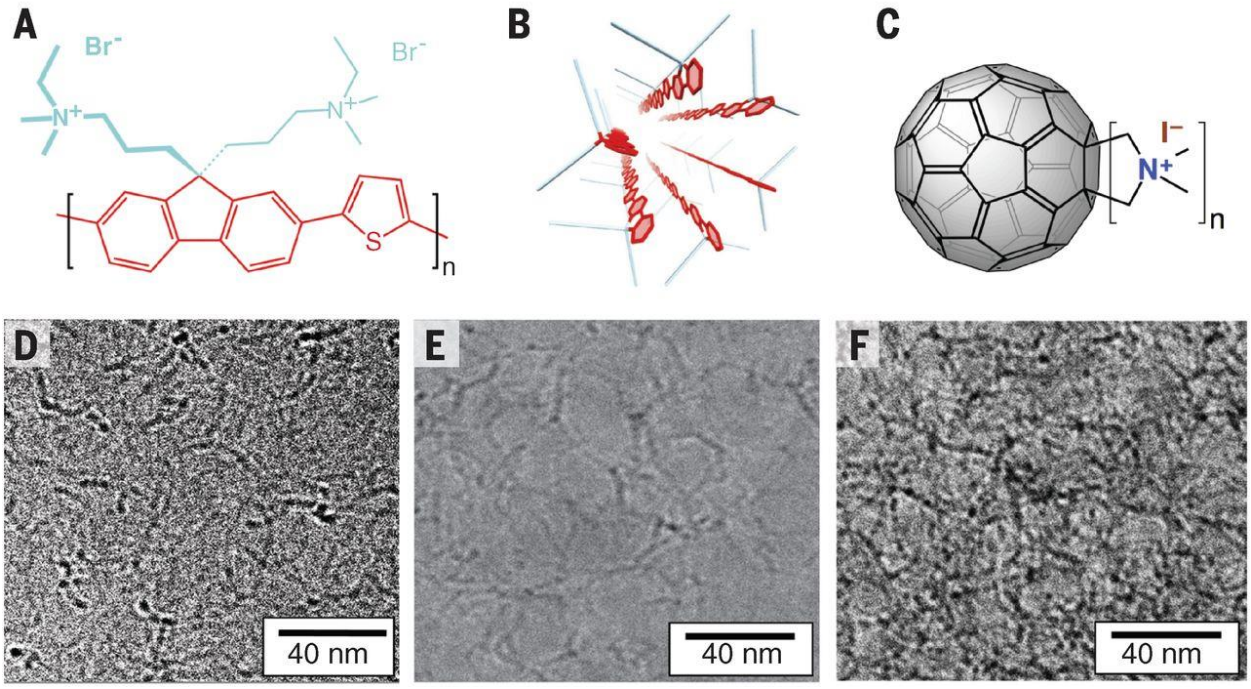

Figure 7.1. PFT and charged fullerene structure and assembly. PFT structure (a); cartoon of a PFT micelle (b); charged fullerenes (c). CryoEM images of pure PFT (d), PFT:mixed-bis adducts (e) and PFT:high adducts (f).

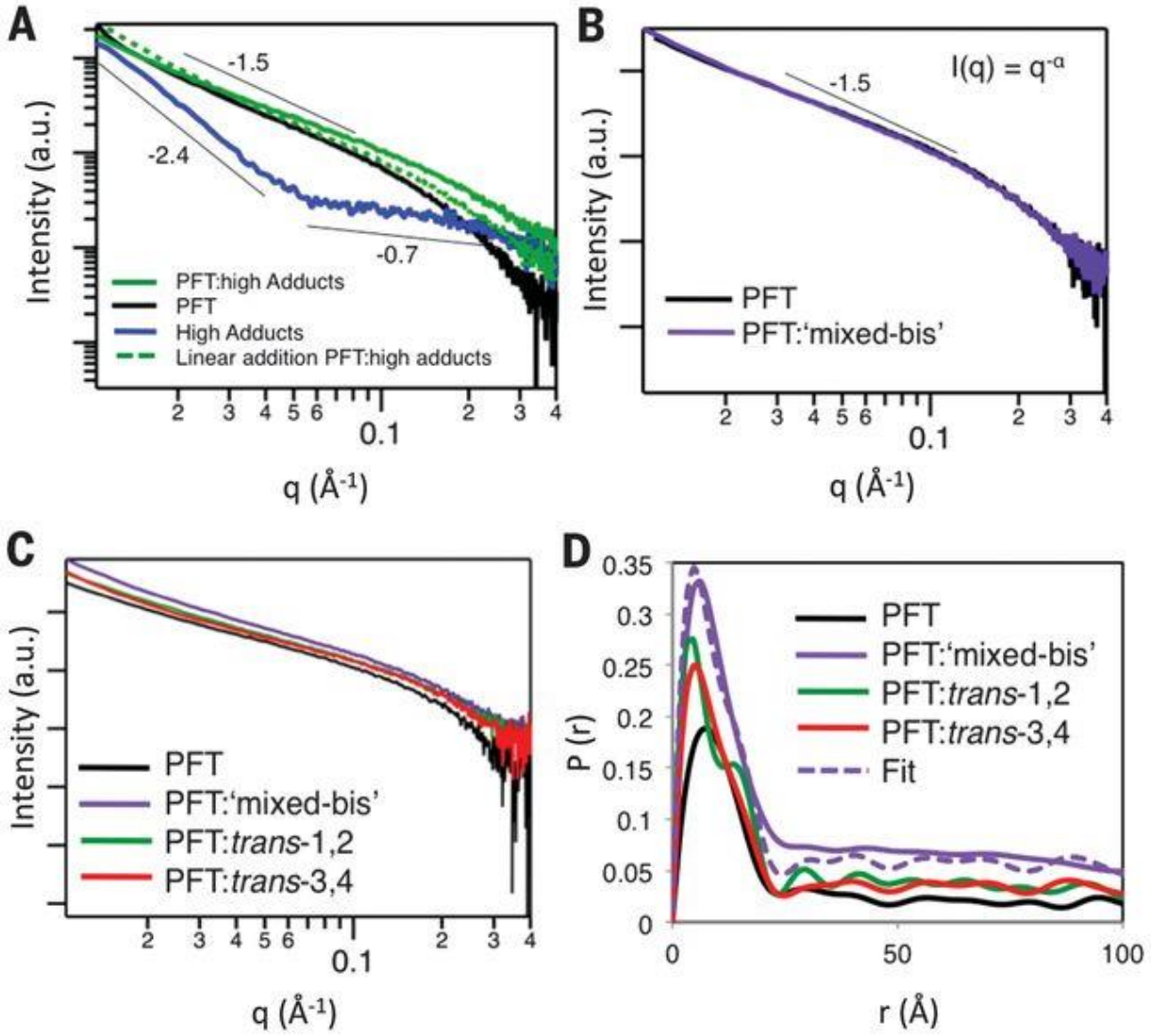

Figure 7.2. SAXS data for PFT and PFT/fullerene mixtures. (a) Data for PFT:high-adducts is reasonably approximated by a sum of PFT + high-adducts. (b) The PFT:mixed-bis profile overlap mass-scaled PFT data. (c) Raw data for all PFT and PFT:bis-fullerene samples are similar. (d) Fourier transformed P(r) data for the samples in (c) shows different fullerene environments for *trans*-1,2 and *trans*-3,4, with PFT:mix-bis corresponding to the sum of the two.

the different solubility properties of the conjugated polyelectrolyte and charged fullerene derivatives. Mixed-bis adducts show limited solubility (without PFT) in aqueous solution, while higher adducts are water soluble at high concentration. This difference suggests that the mixed-bis adducts should co-assemble in aqueous solution with PFT, a result we confirmed by cryogenic electron microscopy (cryoEM), small-angle X-ray scattering (SAXS), and luminescence quenching studies. CryoEM images of pure PFT, PFT:mixed-bis adducts and PFT:high adducts are shown in Figure 7.1 (d) through (f). Pure PFT samples self-assemble into branched micelles that are roughly 4 ± 0.5 nm in diameter and 30 to 50 nm in length. CryoEM images of PFT assembled with mixed-bis adducts are visually similar to the pure PFT, indicating association of the $C_{60}(PI)_2$ with the PFT micelles. In contrast, cryoEM images of PFT:high adducts appear blurry because these solutions contain separate PFT and fullerene agglomerates.

This interpretation of co-assembly of PFT with 'mixed-bis' adducts is also supported by SAXS measurements shown in Figure 7.2 (a) and (b). We radially averaged the SAXS data and fit it to a power law to extract the exponent α, which is related to the polymer fractal structure.[12,13] Values of α = 1, 2 and 4 correlate to rigid rod, lamellar, and spherical structures, respectively, although interactions between molecules cause deviations from these ideal slopes. Analysis of SAXS data for pure PFT yielded α = 1.5 at low *q* (rod-like at large size), increasing to α = 3.7 at high *q* (sphere-like at small size). Deviation from α = 1 arose from the branched network seen by cryoEM in Figure 7.1(d).[14] SAXS power-law slopes for $C_{60}(PI)_n$ high-adducts correspond to a percolation network at low *q* and rod-like behavior at high *q*, indicating aggregation.[12,15] SAXS data from the combined PFT:high adducts solution was well approximated as the mass-scaled sum of the pure PFT and pure fullerene scattering, suggesting a non-assembled mixture, similar to that seen by cryoEM. By contrast, mass-scaled SAXS from solutions of PFT and mixed-bis adducts is

nearly identical to the pure PFT. These results provide strong evidence that $C_{60}(PI)_2$ and PFT coassemble into a single micellar aggregate.

Finally, electronic interactions in the polymer-fullerene assemblies were confirmed with luminescence quenching, which provides an indirect measure of the photo-induced charge transfer from the polymer to the fullerenes.[16] Solutions of PFT:high adducts showed relatively little PL quenching, presumably because the donors and acceptors were not in close physical proximity, but aqueous solutions of PFT with the mixed-bis adducts had significant PL quenching, indicating both physical and electronic contact, as seen by the data in Figure 7.3(a). The data indicate that over 75% of the PFT excitations were quenched in the presence of the mixed-bis adducts.

We determined the dynamics of charge separation in these donor-acceptor assemblies using ultrafast broad-band transient absorption spectroscopy on dilute aqueous solutions of co-assembled PFT with mixed-bis adducts. Representative transient absorption spectra at different probe delays following excitation at 470 nm are shown in Figure 7.3(b). We assigned the negative transient absorption peak near 520 nm to stimulated emission, as the spectral features and the lifetime (Figure 7.3(c)) matched the fluorescence emission. Interestingly, the 690-nm absorption of the PFT hole polaron (P^+) appeared on a sub-picosecond time scale after photoexcitation.[17,18] This ultrafast appearance of P^+ confirmed that the $C_{60}(PI)_2$ adducts must be co-assembled with PFT, because other geometries would require diffusion or other structural rearrangements that could not occur so quickly. Once formed, Figure 7.3(c) shows that about 75% of the PFT polarons in these dilute samples decayed back to the ground state in ~200 ps. The remaining polarons survived past the nanosecond time scale.

To mimic biological charge-separation systems, co-assembly and rapid charge separation are required, but if they are followed by rapid recombination, the charges cannot be extracted. A

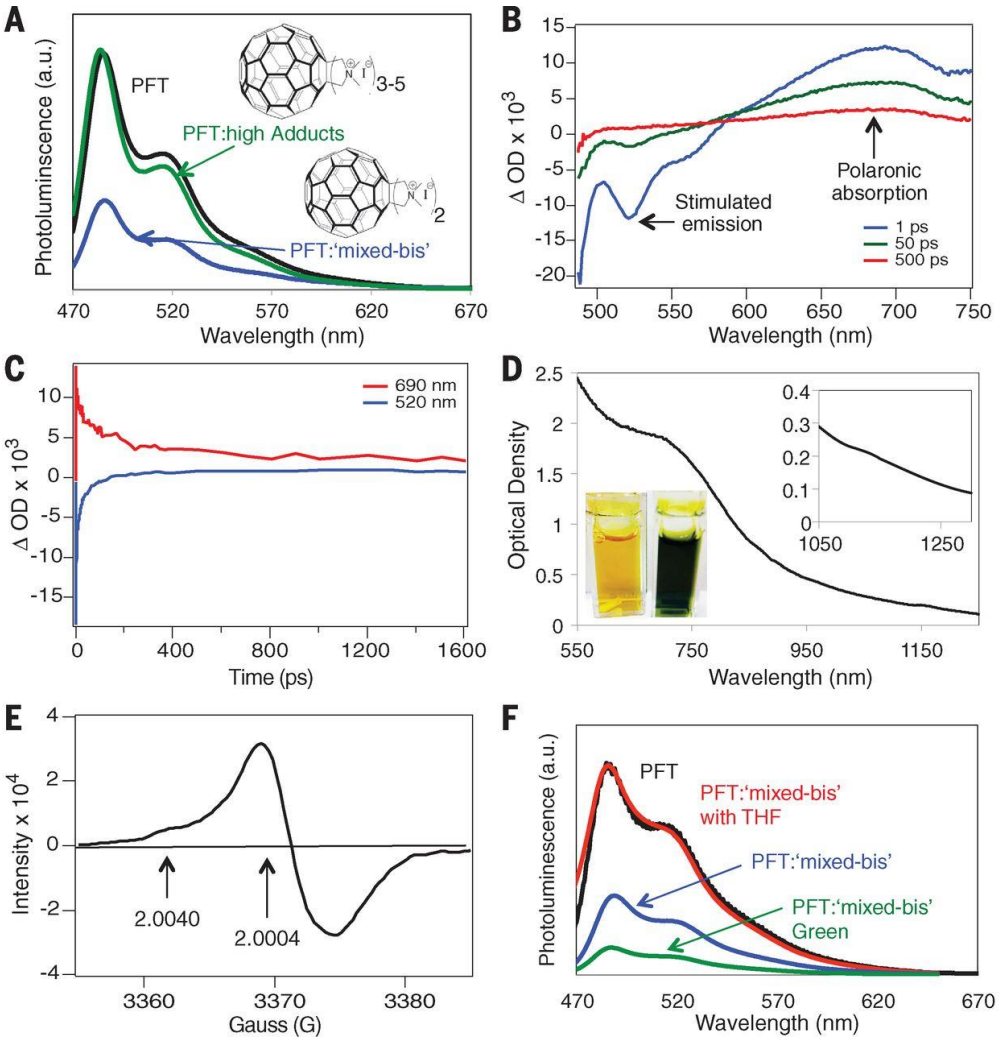

Figure 7.3. Formation of P^+ and N^- polarons requires intimate assembly of the polymer and fullerene. (a) PL of PFT, PFT:high adducts, and PFT:mixed-bis; (b) pump-probe spectroscopy for dilute PFT:mixed-bis solutions excited at 470 nm showing the rapid formation of both excitons and polarons; (c) time decays for the stimulated emission and the polaronic absorption from (b). Absorption from a green concentrated PFT/fullerene solution showing both P^+ and N^- polarons (d). EPR from a similar green solution, again showing both P^+ and N^- polarons (e). PL for various concentrated PFT:mixed-bis solutions showing that polarons quench luminescence, but the addition of THF, which, destroys the PFT/fullerene assembly, restores PL intensity (f).

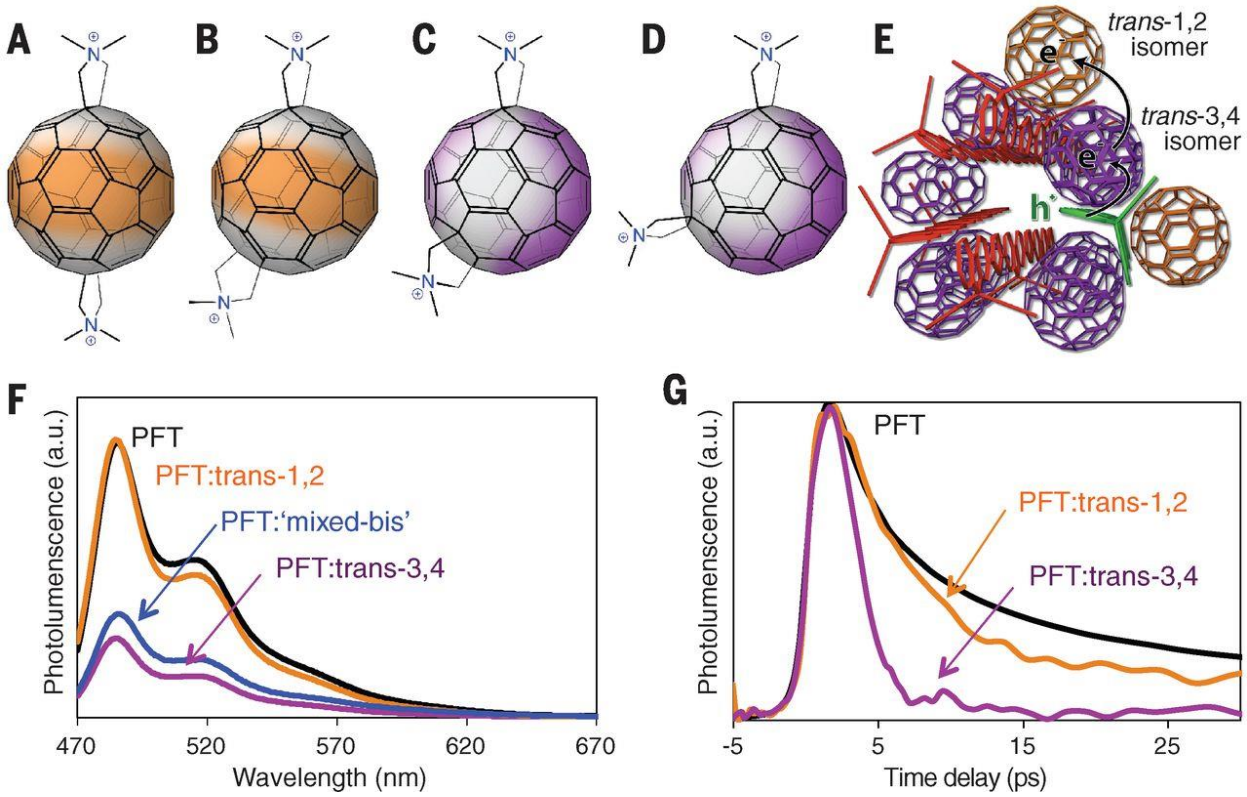

Figure 7.4. Spectroscopic evidence for a spatially defined electron transfer cascade. Chemical structure of *trans*-1 bis (a), *trans*-2 bis (b), *trans*-3 bis (c) and *trans*-4 bis (d) fullerene derivatives with color emphasizing hydrophobic regions. (e) Cartoon depicting the assembly of *trans*-1,2 (orange) and *trans*-3,4 (purple) bis fullerenes with PFT (red). Photoexcitation of the PFT backbone leads to charge transfer first to *trans*-3,4 and then to *trans*-1,2, where the electron remains due to stabilization by the reorganization of water. The hole (green, h^+) remains on PFT. (f) PL of dilute PFT, PFT:mixed-bis, PFT:*trans*-3,4, and PFT:*trans*-1,2. (g) Time-resolved luminescence for concentrated PFT:*trans*-3,4, and PFT:*trans*-1,2 samples.

fullerene acceptor that is optimized for charge separation thus needs to contain one class of compounds that can assemble intimately with the PFT for efficient charge transfer, and a second class of compounds that can assemble more loosely, allowing us to pull the electron away from the PFT and prevent recombination. Fortunately, both types of compounds were already available within our mixed-bis sample, and their properties could be examined simply by separating $C_{60}(PI)_2$ regioisomers. Our mixed-bis samples were primarily composed of four isomers (10% *trans*-1, 39% *trans*-2, 44% *trans*-3 and 7% *trans*-4). Structures of each of the isomers are shown in Figure 7.4 (a) to (d). We partially separated these isomers by silica gel column chromatography of the neutral pyrrolidine precursors (prior to quaternization), producing fractions that we refer to as *trans*-1,2 (29% *trans*-1 and 71% *trans*-2), and *trans*-3,4 (14% *trans*-2, 74% *trans*-3 and 12% *trans*-4). The *trans*-1,2 fullerenes have charges on nearly opposite sides of the buckyball, and can be viewed as isotropically-charged molecules that should not easily insert into a PFT micelle. By contrast, the angle between charges in *trans*-3 is ~145º and *trans*-4 is 103°, suggesting more amphiphilic molecules that could insert into the PFT micelle.

The co-assembly of PFT with *trans*-1,2 and *trans*-3,4 was examined via SAXS. Raw scattering data, in Figure 7.2(c), for all of the samples looked similar to pure PFT, but Fourier analysis using cylindrical boundary conditions showed subtle variations. In Figure 7.2(d), PFT and PFT:*trans*-3,4 showed similar probability distributions, supporting the model of insertion of fullerene into the PFT micelle. Interestingly, PFT:*trans*-1,2 shows two peaks, reminiscent of a polymer micelle with a partial "shell" of fullerenes surrounding the outside. The PFT:mixed-bis data were well fit by a simple linear combination of the PFT:*trans*-1,2 and PFT:*trans*-3,4 probability distributions, further supporting the idea that *trans*-3,4 assembles on the inside of the polymer micelle while *trans*-1,2 surrounds the outside. The relative locations of the two different

sets of fullerenes were also confirmed via solvatochromic absorption measurements, which are shown in Figure 7.5 (a) through (c). These measurements show that the UV absorption of *trans*-1,2 fullerenes assembled with PFT matches that of the fullerenes in pure water, indicating that *trans*-1,2 sits outside of the PFT micelle. In contrast, the absorption of the *trans*-3,4 fullerenes assembled with PFT matches that of the fullerenes in organic solvents, indicating that *trans*-3,4 sits in a lower dielectric environment like the micelle interior.

Figure 7.4 (f) and (g) show luminescence quenching measurements that further support the idea that different isomers of $C_{60}(PI)_2$ assemble in different places in the PFT micelle. The luminescence decays shown in Fig. 4G were taken using a Kerr-gated time-resolved fluorescence set-up using CS_2 as the gate medium, providing a time resolution of ~1 ps.[19] Clearly, the PFT fluorescence is quenched nearly to the instrument limit in concentrated solutions when assembled with *trans*-3,4 fullerenes, verifying that the photoinduced charge transfer to these fullerenes is ultrafast. In contrast, there is almost no fast quenching of the PFT emission with an equal amount of *trans*-1,2 fullerenes, reflecting their assembled position predominantly on the outside of the micelle, out of range for fast ET. Figure 7.4(f) shows steady-state luminescence measurements on these same samples. Consistent with the time-resolved data, assemblies of PFT with *trans*-1,2 fullerenes showed little luminescence quenching, whereas PFT assembled with *trans*-3,4 fullerenes had strong quenching. These quenching results suggested that not only can we selectively associate fullerenes with polymer micelles using the number of charges, we can also control the position of the fullerene within the micelle by the placement of the charges (Figure 7.4(e)).

Given this degree of control, the next step was to examine long lived excitations in assemblies of PFT and mixed-bis adducts containing both intimately assembled *trans*-3,4 and more

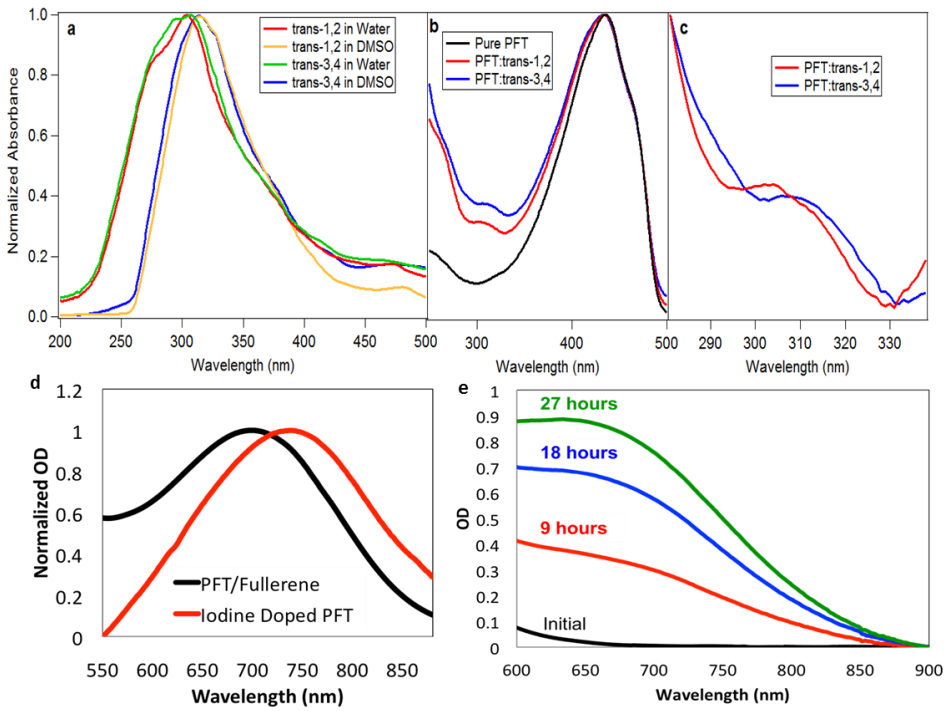

Figure 7.5. UV/Vis Absorbance spectra. (a) Pure *trans*-1,2 and *trans*-3,4 fullerenes, *not* assembled with PFT, in both water and DMSO; a clear blue-shift of the primary UV absorption peak near 300 nm can be seen for both samples dissolved in water (ε=80), compared to the same materials in DMSO (ε=47). Panels (b) and (c) show the same fullerene absorption peaks (with different scalings); a blue-shift of the *trans*-1,2 absorption relative to the *trans*-3,4 absorption is observed, indicating that the two types of fullerenes are in different dielectric environments. (d) PFT:mixed-bis adduct solution in water following exposure to light (black curve) and iodine-doped (i.e. hole doped) PFT (red curve). Similar absorption peaks indicate that the green color in the PFT:mixed-bis solution arises from the formation of long lived hole polarons on the PFT. (e) Dilute PFT:mixed-bis fullerene sample irradiated with 514-nm laser light for increasing longer periods of time. The polaron absorption increases upon exposure to light, but stops when the light is turned off, confirming that polaron formation is an excited-state electron transfer process.

isotropically-charged *trans*-1,2 fullerenes. Ideally, this co-assembly should permit rapid photo-induced electron transfer from PFT to the *trans*-3,4 fullerenes, followed by a second electron transfer step to the *trans*-1,2 fullerenes. If this type of directed ET cascade occurs, electrons on the *trans*-1,2 fullerenes would then be stabilized in the high dielectric environment of the water surrounding the micelle, preventing recombination with the PFT. Indeed, we found that photoexcitation of aqueous PFT:mixed-bis adduct solutions caused a dramatic color change from yellow to dark green over time, shown in Figure 7.3(d); once exposed to light, and the color change was essentially permanent, lasting days to weeks. Dilute solutions, like those used to collect the data in Figure 7.3 (b) and (c) required extensive light exposure (Figure 7.5(e)), but when higher concentrations were used, the color change took place in just a few seconds under room lights, indicating that the quantum yield for long-lived charge separation is much higher than the ~25% in dilute solutions (*cf.* Figure 7.3(b)).

PFT is a blue-absorbing polymer with an absorption maximum at 430 nm in water and little to no absorbance past 550 nm.[10] The color change from yellow to green was confirmed to arise from the appearance of the PFT hole polaron (P^+) by comparing steady-state data in Figure 7.3(d) with both transient absorption data in Figure 7.3(b) and absorption from PFT oxidized with iodine, both of which shows absorbs in the sub-gap region at ~690 nm, Figure 7.5(d).[20] The inset in Figure 7.3(d) shows that simultaneously, a substantially weaker negative (N^-) polaron absorption peak caused by the $C_{60}(PI)_2$ molecular anion was observed at 1180 nm. The low intensity of the N^- absorption has several origins: 1) the absorption cross-section of fullerene anions is much smaller than that of the polymer polarons;[21] 2) the weak N^- absorption peak sits on top of a broad scattering background from the co-assembled micelles in solution; and 3) the N^- polaron might react with impurities in the water, despite our best efforts to deoxygenate the solutions by freeze-pump-thaw

techniques.[22]

To further confirm the formation of stable, separated N^- and P^+ polarons after exposure to light, we performed electron paramagnetic resonance (EPR) experiments. Figure 7.3(e) shows the EPR signal from the green PFT:mixed-bis adducts solution; the *g*-factors for the N^- and P^+ polarons are 2.0004 and 2.0040, respectively, in good agreement with reported values for many other polymer-fullerene systems.[23] The N^- polaron line width we observed is broader than that in other polymer-fullerene systems, both because of the interaction of the water dipoles with the polarons and because of different spin-relaxation times for the electron and hole.[24,25] The critical difference between our co-assembled system and previous systems, however, is that the previous EPR work required active photoexcitation (light-induced EPR) in order to observe the polaron signals. In contrast, once exposed to light, the polarons created in our PFT:$C_{60}(PI)_2$ solutions remained stable essentially indefinitely.

Final confirmation that the long-lived separated charges resulted from a self-assembled ET cascade comes by examining the details of absorption and luminescence for a range of samples in different solvents. As discussed above, aqueous solutions of PFT and *trans*-1,2 fullerenes show little PL quenching in Figure 7.4 (f) and (g), but they did briefly turn green during the course of the dissolution, indicating polaron formation (possibly from disordered polymer that transiently allowed the fullerene to partly insert into the micelle). By contrast, despite the efficient luminescence quenching in solutions of PFT co-assembled with the *trans*-3,4 fullerenes (Figure 7.4 (f) and (g)), the solutions did not turn green and ultrafast experiments (data not shown) indicate that polarons are formed on sub-ps time scales, as in Figure 7.3(b), but recombine with 100% yield over the next few hundred ps. These results indicate that controlling the spatial position of the fullerenes can dramatically affect carrier dynamics. Moreover, photoexcitation of green-colored

PFT:mixed-bis fullerene solutions results in increased luminescence quenching because PFT excitons are further quenched by P^+-polarons, Figure 7.3(f). However, when tetrahydrofuran (THF), which is known to disassemble the polymer micelles,[26] was added to the co-assembled green system, the luminescence signal regained its intensity, indicating a fully reversible system (Figure 7.3(f)). These results further support the idea that intimate assemblies with well-controlled molecular positions are required to facilitate a charge transfer cascade and avoid recombination. When nanoscale architecture is optimized, the result is stable polarons that could potentially be applied to improve organic photovoltaic cells via suppression of charge recombination.

7.3 Conclusions

The self-assembly of the PFT polymer with a combination of *trans-1,2* and *trans-3,4* charged bis-fullerene isomers forms an ET cascade that promotes the creation of long-lived charge species. Upon photoexcitation of PFT, an electron is transferred to *trans-3,4* fullerenes sitting within the micelle; the electron is then funneled to the adjacent *trans-1,2* fullerene sitting the gallery region of the micelle, where it is stabilized by reorganization of the surrounding water. The electron and hole are now spatially separated, decreasing the probability of recombination to near zero, so that the separated charges are stable in aqueous solution for weeks. The key to producing these stabilized, separated charges lies in controlling the nanoscale structure of the polymer/fullerene assemblies. Now that the general principles of designing artificial self-assembled ET cascades have been established, it should be possible to apply these principles to the production of water-based OPV devices.

7.4 Experimental

Synthesis of PFT has been previously reported by our groups.[10]

7.4.1 Synthesis of Bis-*N,N*-dimethylfulleropyrrolidinium Iodide Isomers: Bis-N-methylpyrrolidine adducts were synthesized according to published methods[28,29] and were separated according to the following procedure. The crude product was dry loaded onto a silica column pre-treated with 2% triethylamine in toluene with an unusually large ratio of silica gel to product 1:~500 and the column was run with an extremely slow elution rate (~1-2 mL/min). The column was first eluted with toluene to yield a purple fraction of C_{60} followed by a second brown fraction containing the monoadduct (r_f = 0.70 2/10/88 TEA/Et_2O/PhMe). After elution of the monoadduct, the eluent was changed to 2/10/88 TEA/Et_2O/PhMe and two closely spaced fractions. The first fraction gives two spots by TLC corresponding to the *Trans-1* and *Trans-2* isomers (r_f = 0.50 and r_f = 0.43 2/10/88 TEA/Et_2O/PhMe) and the second fraction gives two spots by TLC corresponding to the *Trans-2* and *Trans-3* isomers (r_f = 0.43 2/10/88 TEA/Et_2O/PhMe r_f = 0.33 2/10/88 TEA/Et_2O/PhMe). Subsequent fractions contain many spots with r_f ranging from 0.2 to 0.33 (2/10/88 TEA/Et_2O/PhMe) corresponding to a complex mixture of *Trans-3*, *4*, *e*, and *cis-3* isomers which can be separated by HPLC using published methods.[28] ^{1}H NMR, ^{13}C NMR and MALDI-TOF spectra for the *Trans-1* and *Trans-2* and *Trans-2* and *Trans-3* mixtures match with previously reported spectra for the pure compounds.[28, 29] Bis-N,N-dimethylpyrrollidinium adducts were synthesized from the corresponding bis-N-methylpyrrolidine adducts according to published methods.[30]

7.4.2 Cryo-Em: For cryoEM, grids were prepared by placing a small drop (~4 μl) of

sample solution onto glow discharged holy carbon mesh Quantifoil 200 mesh grids with 3.5 μm holes spaced 1 μm apart. The grids were then blotted and plunged immediately into liquid nitrogen cooled liquid ethane to rapidly freeze the samples in vitrified ice. The cryo grids were visualized with an FEI Tecnai F20 transmission electron microscope at an accelerating voltage of 200 kV. Images were collected on a 16 megapixel CCD camera at ~50,000× magnification with a defocus value of approximately 3 μm.

7.4.3 Small-angle X-ray Scattering (SAXS): Small-angle X-ray scattering (SAXS) experiments were conducted at the Stanford Synchrotron Radiation Laboratory (SSRL) Beamline 4-2. Using a syringe, 100 μL of each sample was loaded in a quartz capillary and held at 25 ºC. Scattered X-rays (at 12 keV) were collected with a Rayonix MX225-HE detector (sample to detector distance = 1.7 m). The two-dimensional data was radially averaged to obtain one-dimensional scattering curves.

7.4.5 Spectra and Electron Paramagnetic Resonance: UV-vis absorption spectra were taken on a Perkin-ElmerLambda25spectrometer in a 0.1-cm glass cell in DMSO. ^{1}H and ^{13}C NMR spectra were taken on a 500 MHz Bruker Avance AV 500 spectrometer equipped with a 5-mm dual cryoprobe.

Electron paramagnetic resonance was performed at UCLA in the Molecular Instrumentation Center (MIC). Experiments were performed on the Bruker EMX EPR spectrometer in a nitrogen finger dewar to keep the sample frozen at 95 K. The microwave frequency was 9.437 GHz, amplitude of 4 G, microwave power of 0.02 mW and a scan time of 20.972 s for 32 accumulated scans.

7.4.6 Pump-probe Transient Absorption and Fluorescence Spectroscopy: A femtosecond Ti:Sapphire amplifier (Coherent, Legend Elite) seeded with a broadband Ti:Sapphire oscillator (Coherent, Mantis) was used for ultrafast pump-probe transient absorption experiments. Spectral and kinetic data acquisition was accomplished using a commercially-built spectrometer (HELIOS, Ultrafast Systems LLC). The amplifier output consisting of 40-fs, 3-mJ pulses centered around 800 nm (at a 1-kHz repetition rate) was split into two beams of roughly equal power. One of the beams was directed to an Optical Parametric Amplifier (Light Conversion, TOPAS-C) to create 470 nm pump pulses. A small portion of the amplifier output was focused onto a sapphire crystal to generate white-light continuum (WLC) probe laser pulses. The probe beam was directed onto a computer-controller translation stage so that the time delay between the pump and the probe could be varied. The pump and probe pulses were focused into the sample in a non-collinear geometry, making it possible to select only the WLC probe pulses for detection. The probe beam was focused onto the sample such that the spot size of the probe beam was smaller than that of the pump beam in order to ensure that the data collected came from a uniformly-excited region. Solution-phase samples of a concentration of 1 mg/ml were filled in glass cuvettes with a 1-mm path length to ensure sufficient transmission of the probe light. The transmitted probe beam through the sample was collimated onto a fiber optic cable using a telescope and then dispersed onto a one dimensional CCD detector. We chopped the pump beam at a frequency of 500 Hz and recorded the pump on/pump off signals for each consecutive pair of pulses to calculate the normalized transient absorption spectrum for a particular probe delay. We used a modest pump pulse energy of 60 nJ (spot size ~5 mm) for excitation and ensured that we were safely in the linear regime.

The same laser system was used for time-resolved fluorescence measurements. In this case, a 400-nm pulse was still used to excite the samples, but instead of generating WLC, the original 800-nm pulse was used to open the Kerr gate in CS_2.[19] The fluorescence from the samples was collected at 90° from the excitation pulse and passed through crossed-polarizers with the CS_2 cell between them and imaged onto a CCD detector. Control experiments on dye molecules indicate that the instrument response with this set-up is ~1 ps.

7.5 References

(1) Rutherford, A. W. Photosystem II, the Water-Splitting Enzyme. *Trends Biochem. Sci.* **1989**, *14*, 227–232.

(2) Piris, J.; Dykstra, T. E.; Bakulin, A. A.; Loosdrecht, P. H. M. Van; Knulst, W.; Trinh, M. T.; Schins, J. M.; Siebbeles, L. D. A. Photogeneration and Ultrafast Dynamics of Excitons and Charges in P3HT/PCBM Blends. *Journal of Physical Chemistry C* **2009**, *113*, 14500–14506.

(3) Shaw, P. E.; Ruseckas, A.; Samuel, I. D. W. Exciton Diffusion Measurements in Poly(3-Hexylthiophene). *Adv. Mater.* **2008**, *20*, 3516–3520.

(4) Gélinas, S.; Paré-Labrosse, O.; Brosseau, C.-N.; Albert-Seifried, S.; McNeill, C. R.; Kirov, K. R.; Howard, I. A.; Leonelli, R.; Friend, R. H.; Silva, C. The Binding Energy of Charge-Transfer Excitons Localized at Polymeric Semiconductor Heterojunctions. *Journal of Physical Chemistry C* **2011**, 7114–7119.

(5) Verhoeven, J. On the Role of Spin Correlation in the Formation, Decay, and Detection of Long-Lived, Intramolecular Charge-Transfer States. *J. Photochem. Photobiol. C Photochem. Rev.* **2006**, *7*, 40–60.

(6) Miura, T.; Maeda, K.; Murai, H.; Ikoma, T. Long-Distance Sequential Charge Separation at Micellar Interface Mediated by Dynamic Charge Transporter: A Magnetic Field Effect Study. *J. Phys. Chem. Lett.* **2015**, *6*, 267–271.

(7) Lungenschmied, C.; Dennler, G.; Neugebauer, H.; Sariciftci, S. N.; Glatthaar, M.; Meyer, T.; Meyer, A. Flexible, Long-Lived, Large-Area, Organic Solar Cells. *Sol. Energy Mater. Sol. Cells* **2007**, *91*, 379–384.

(8) Yasuda, T.; Shinohara, Y.; Ishi-i, T.; Han, L. Use of Benzothiadiazole–triphenylamine Amorphous Polymer for Reproducible Performance of Polymer–fullerene Bulk-Heterojunction Solar Cells. *Org. Electron.* **2012**, *13*, 1802–1808.

(9) Costa, T.; Marques, A. T.; Se, J.; Melo, S. De; Thomas, A. W.; Garner, L. E.; Scherf, U.; Bazan, G. C.; Burrows, H. D. Self-Assembly of Poly{1,4-Phenylene-[9,9-bis(4-Phenoxy-Butylsulfonate)]fluorene-2,7-Diyl} with Oppositely Charged Phenylenevinylene Oligoelectrolytes. *J. Phys. Chem. B* **2014**, 613–623.

(10) Clark, A. P.-Z.; Shi, C.; Ng, B. C.; Wilking, J. N.; Ayzner, A. L.; Stieg, A. Z.; Schwartz, B. J.; Mason, T. G.; Rubin, Y.; Tolbert, S. H. Self-Assembling Semiconducting Polymers-Rods and Gels from Electronic Materials. *ACS Nano* **2013**, *7*, 962–977.

(11) Cassell, A.; Asplund, C.; Tour, J. Self-Assembling Supramolecular Nanostructures from a C60 Derivative: Nanorods and Vesicles. *Angew. Chemie …* **1999**, *38*, 2403–2405.

(12) Beaucage, G. Small-Angle Scattering from Polymeric Mass Fractals of Arbitrary Mass-Fractal Dimension. *J. Appl. Crystallogr.* **1996**, *29*, 134–146.

(13) Choudhary, S.; Bhatia, S. R. Rheology and Nanostructure of Hydrophobically Modified Alginate (HMA) Gels and Solutions. *Carbohydr. Polym.* **2012**, *87*, 524–530.

(14) Li, Y.-C.; Chen, K.-B.; Chen, H.-L.; Hsu, C.-S.; Tsao, C.-S.; Chen, J.-H.; Chen, S.-A. Fractal Aggregates of Conjugated Polymer in Solution State. *Langmuir* **2006**, *22*, 11009–11015.

(15) Jeng, U.; Lin, T.-L.; Hu, Y.; Lin, J.-M.; Huang, Y.-S.; Liang, K. S.; Fan, L.; Thiyagarajan, P. Complex Structure of Fullerene Star Ionomers and Sodium Dodecyl Sulfate Resolved by Contrast Variation with SANS and SAXS. *Nucl. Instruments Methods Phys. Res. Sect. A Accel. Spectrometers, Detect. Assoc. Equip.* **2009**, *600*, 294–296.

(16) Park, Y.; Park, Y.; Gao, J.; Grey, J.; Wang, C. PPV and C 60 Nanocomposite with Enhanced Miscibility and Enhanced Photo-Induced Charge Transfer through Ground State Electrostatic Interactions. *Polymer (Guildf).* **2014**, *55*, 855–859.

(17) Österbacka, R.; An, C. P.; Jiang, X. M.; Vardeny, Z. V. Two-Dimensional Electronic Excitations in Self-Assembled Conjugated Polymer Nanocrystals. *Science (80-.).* **2000**, *287*, 839–842.

(18) Paquin, F.; Latini, G.; Sakowicz, M.; Karsenti, P.-L.; Wang, L.; Beljonne, D.; Stingelin, N.; Silva, C. Charge Separation in Semicrystalline Polymeric Semiconductors by Photoexcitation: Is the Mechanism Intrinsic or Extrinsic? *Phys. Rev. Lett.* **2011**, *106*, 197401.

(19) Arzhantsev, S.; Maroncelli, M. Design and Characterization of a Femtosecond Fluorescence Spectrometer Based on Optical Kerr Gating. *Appl. Spectrosc.* **2005**, *59*, 206–220.

(20) Chiang, C.; Fincher, C.; Park, Y.; Heeger, a.; Shirakawa, H.; Louis, E.; Gau, S.; MacDiarmid, A. Electrical Conductivity in Doped Polyacetylene. *Phys. Rev. Lett.* **1977**, *39*, 1098–1101.

(21) Kato, T.; Kodama, T.; Oyama, M.; Okazaki, S.; Shida, T. ESR and Optical Studies of the Radical Anion of C60. *Chem. Phys. Lett.* **1991**, *186*, 35–39.

(22) Guldi, D. M.; Prato, M. Excited-State Properties of C(60) Fullerene Derivatives. *Acc. Chem.*

Res. **2000**, *33*, 695–703.

(23) Krinichnyi, V. I. Dynamics of Charge Carriers Photoinduced in poly(3-Dodecylthiophene)/fullerene Bulk Heterojunction. *Sol. Energy Mater. Sol. Cells* **2008**, *92*, 942–948.

(24) Savenije, T. J.; Sperlich, A.; Kraus, H.; Poluektov, O.; Heeney, M.; Dyakonov, V. Observation of Bi-Polarons in Blends of Conjugated Copolymers and Fullerene Derivatives. *Phys. Chem. Chem. Phys.* **2011**, *13*, 16579–16584.

(25) Ceuster, J.; Goovaerts, E.; Bouwen, a.; Hummelen, J.; Dyakonov, V. High-Frequency (95 GHz) Electron Paramagnetic Resonance Study of the Photoinduced Charge Transfer in Conjugated Polymer-Fullerene Composites. *Phys. Rev. B* **2001**, *64*, 195206.

(26) Kelley, E.; Smart, T.; Jackson, A. Structural Changes in Block Copolymer Micelles Induced by Cosolvent Mixtures. *Soft Matter* **2011**, *7*, 7094–7102.

(27) Maggini, M.; Scorrano, G.; Prato, M. Addition of Azomethine Ylides to C60: Synthesis, Characterization, and Functionalization of Fullerene Pyrrolidines. *J. Am. Chem. Soc.* **1993**, *115*, 9798–9799.

(28) Lu, Q.; Schuster, D. I.; Wilson, S. R. Preparation and Characterization of Six Bis(N-methylpyrrolidine)−C60 Isomers: Magnetic Deshielding in Isomeric Bisadducts of C60. *J. Org. Chem.* **1996**, *61*, 4764–4768.

(29) K. Kordatos, et al. Isolation and Characterization of All Eight Bisadducts of Fulleropyrrolidine Derivatives. *J. Org. Chem.* **2001**, *66*, 2802–2808.

(30) Guldi, D. M. Probing the Electron-Accepting Reactivity of Isomeric Bis(pyrrolidinium) Fullerene Salts in Aqueous Solutions. *J. Phys. Chem. B* **2000**, *104*, 1483–1489.

CHAPTER 8

Conclusions

While there are many challenges in creating highly efficient organic photovoltaics, one of the main issues is controlling the morphology of the active layer. Creating the ideal interpenetrating network of polymer and fullerene in a bulk heterojunction necessary for both efficient exciton separation and charge extraction can be a difficult task if only spontaneous phase separation of the two components is utilized. This work focused specifically on controlling the polymer component to drive a system to an optimal morphology. By taking advantage of intrinsic polymer properties and processing methods, the blended system can be specifically tuned. Additionally, by using self-assembly techniques, the polymer morphology can be precisely directed.

To start, we used regioregularity differences in two batches of P3HT to see what effect the propensity to crystallize has on the processing technique in Chapter 2. Since the blend cast films rely on demixing of the P3HT and PCBM, a high degree of regioregularity was needed to drive the phase separation of the two components. On the other hand, a sequentially processed film creates a more optimal network with a low regioregularity polymer due to the fullerene intercalation into the amorphous polymer regions. This work can further contribute to the OPV field because it shows that the processing techniques can be chosen to match the intrinsic polymer properties. Many of the high performing polymers synthesized by research groups are much more amorphous than P3HT, due to a combination of a donor and acceptor block that do not stack as easily. Since these polymers do not have the propensity to crystallize that is needed for blend casting, sequential processing could be a route to further improve these systems in the future.

In order to further stress the importance of polymer regioregularity in OPVs, we looked at a system in which both the average side-chain length and the regioregularity were varied. In Chapter 3 we used a series of random thiophene co-polymers (RBOs) in which the ratio of octyl to butyl side-chains was changed. Rather than seeing the average side-chain length as the dominate factor for sequential processing and blend casting, it was actually the regioregularity that correlated the best with the efficiency trends. This work demonstrates that since regioregularity dictates the phase separation and final morphology, future work on comparing efficiency changes within a series of polymers must hold the regioregularity constant. Additionally, we were able to illustrate the way in which polymer swelling can be used as a predictor of demixing in blend casting and fullerene intercalation in sequential processing. Here, a polymer that swells easily is good for driving fullerene intercalation in sequential processing, but prevents the phase separation needed for blend casting. Thus by looking at the pure polymer characteristics, such as crystallinity and swelling, the final morphology could be predicted. This could be extended as a way to screen polymers even before creating BHJs to optimize the overall performance.

In addition to looking at changes in polymer regioregularity and crystallinity, this work also looked at the effect of polymer orientation and the ways in which it can be maintained. In Chapter 4, a polymer that is face-on in pure films was used to make BHJs by blend casting and sequential processing. We determined that when the polymer is mixed with PCBM in solution, there is too much of a favorable interaction between the two components to allow the polymer to stack face-on; the face-on orientation could only be preserved by sequential processing. The preservation of the orientation created a much more efficient device, even without the use of any additional solution additives, since the holes could travel through the π-conjugation. This again could be extended to future face-on polymers as a means to keep the favorable polymer orientation.

Additionally, sequential processing could possibly be expanded to an end-on polymer, in which the highest mobility direction could be used to further increase carrier extraction.

In Chapter 5, we moved from tuning the morphology of a blended system to controlling the morphology within a pure polymer system. Here, we sought to disentangle whether amorphous polymers suffer from low mobility due to intrinsic properties or due to the presence of a large number of traps due to kinks in the conducting backbone. By using a self-assembled silica host matrix, we were able to elongate the chains of a highly crystalline polymer, P3HT, and an amorphous polymer, MEH-PPV, to remove any kinks. What we observed was that both polymers actually have very similar mobilities in this morphology, confirming that the low mobility typically observed for MEH-PPV is due only to the presence of traps, not to poor intrinsic conduction. Additionally, the measured mobilities were as high as that of amorphous silicon, showing that semiconducting polymers do indeed have fairly good intrinsic hole mobility. Although this system makes use of an inorganic host matrix to force the polymer alignment, it does show that by utilizing methods to straighten polymer backbones can decrease traps and increase mobility.

The reduction of kinks in the polymer backbone was fully exploited by using self-assembly of the conjugated polyelectrolyte PFT. Since PFT forms rod-like micelles in solution, with its semiconducting backbone along the long-axis of the rod, the polymer chains were straightened in solution. In addition to forming these micelles, PFT forms a hydrogel at moderate concentrations. In Chapter 6, we determined that this hydrogel was formed by polymer chains bridging micelles, thus creating a 3D, interconnected conductive network, which could be strengthened through the use of THF annealing. Being able to create a 3D network has a wide range of potential uses, but in OPVs it would enable the creation of optimal polymer pathways for charge extraction. Since the network is preserved even in the solid state, it could be used as a scaffold for additional

fullerene intercalation, possibly through the use of sequential processing.

In Chapter 7, we explored adding a fullerene electron acceptor to the PFT 3D network. By using water soluble fullerene derivatives, we were able to co-assemble the PFT and fullerene in solution. In addition, we were able to tune the location of the fullerene in the co-assembled structure to either be inside or outside the PFT micelle by simply changing the location of the solubilizing adducts on the fullerene ball. This had profound effects as we demonstrated the creation of an energy cascade using both fullerene derivatives that not only efficiently split the excitons formed but also prevented back recombination, yielding long-lived polarons. Although this system is in solution, if such an energy cascade were translated to the solid state, it could help OPV performance, since electron recombination would be greatly limited. Current efforts at creating a solid-state OPV have not been successful as the co-assembled structure is not maintained with drying. However, the use of smaller electron acceptors could enable the preservation of the architecture and the creation of a working device that not only improves efficiency, but also is water processable to reduce the use of harmful solvents.

Overall, this work demonstrated a number of ways in which the morphology of a polymer could be controlled, both in the solid state and in solution. By utilizing self-assembly, intrinsic polymer properties can be taken advantage of to help advance the OPV field even further. Although fairly high efficiencies have been reached in laboratories, these devices are often not scalable nor stable for long periods of time. Further use of self-assembly can help solve both of these problems and opens the door for a wide range of potential polymer:fullerene morphologies.

APPENDIX A

Composition Effect in BC-BHJ Solar Cells

For BC-BHJ solar cells, in addition to polymer regioregularity, we also investigated the effect of varying the P3HT:PCBM composition on device performance. Figure A.1 and Table A.1 compares the *J-V* curves for BC devices made with the same polymer batches used in Chapter 2 but with different P3HT:PCBM ratios. For the LR P3HT, the best device performance was obtained with a P3HT:PCBM ratio of 1:0.9, which was inside the optimal P3HT:PCBM range for common commercially-available P3HT.[1] Increasing the PCBM loading to a P3HT:PCBM ratio of 1:1.3 causes a drop in both J_{sc} and V_{oc}.[2] For our in-house synthesize HR P3HT, however, we found that a P3HT:PCBM ratio of 1:1.3 yields both higher *FF*, J_{sc} and PCE than a 1:0.9 ratio. The observation that extra fullerene can be supported by the HR P3HT in BC devices indicated that the P3HT lamella formed in BC films must differ from that of SqP films.

To help understand the differences in BC device performance with different polymer:fullerene compositions, we compare the PL quenching of the BC films made from out different polymer batches in Figure A.3. We find that a 1:1.3 BC HR P3HT:PCBM active layer has slightly better PL quenching than a 1:0.9 HR P3HT:PCBM BC film, with quenching ratios of 83% and 81%, respectively. The opposite is true for LR P3HT, with the 1:0.9 LR P3HT:PCBM BC film haing 83% PL quenching while the same film with a 1:1.3 composition has only 80% quenching. This again indicates that more crystalline P3HT requires additional fullerene to form a more ideal morphology in BC films.

We also investigated the morphology of BC films by GIWAXS experiments, and obtained

the results shown in Figure A.4. When the P3HT:PCBM ratio is compared between BC BHJs, an interesting trend is observed. For the LR P3HT, increasing the fullerene ratio from 1:09 to 1:1.3 causes a decrease in overall crystallinity, and this crystallinity decrease does not recover even after annealing. This is expected since PCBM incorporation into the P3HT prevents crystallization, creating an overall more amorphous polymer:fullerene network, which is slightly detrimental to the device performance. On the other hand, the opposite trend is seen for the HR P3HT. In this case, the higher 1:1.3 composition ratio still starts out more amorphous as-cast than the 1:0.9 composition, but becomes more crystalline than that of the 1:0.9 mixture upon thermal annealing. This also matches the observed increase in device performance for the 1:1.3 BC film over the 1:0.9 BC film. We believe that upon thermal annealing, the high regioregularity enables this polymer to form a larger number of small crystallites instead of increasing the size of the as-cast crystallites. A comparison of the peak width between the samples shows that indeed, the 1:1.3 HR BC crystallites do not grow in size as mish as in other samples, allowing for high crystallinity even in the presence of a large amount of fullerene.

In out BC films, annealing also changes the fullerene crystallinity. In LR P3HT films, the fullerene peak increased upon annealing, indicating the formation of some fullerene crystallites. In the HR P3HT:PCBM 1:0.9 BC-BHJ, the fullerene crystallinity decreases upon annealing, which means that some of the fullerene crystallites are broken up to help form a more mixed network. on the other hand, the PCBM crystallinity remains relatively unchanged in the case of the 1:1.3 BC active layer since the phase separation is mainly being driven by the high propensity of the P3HT to crystallize.

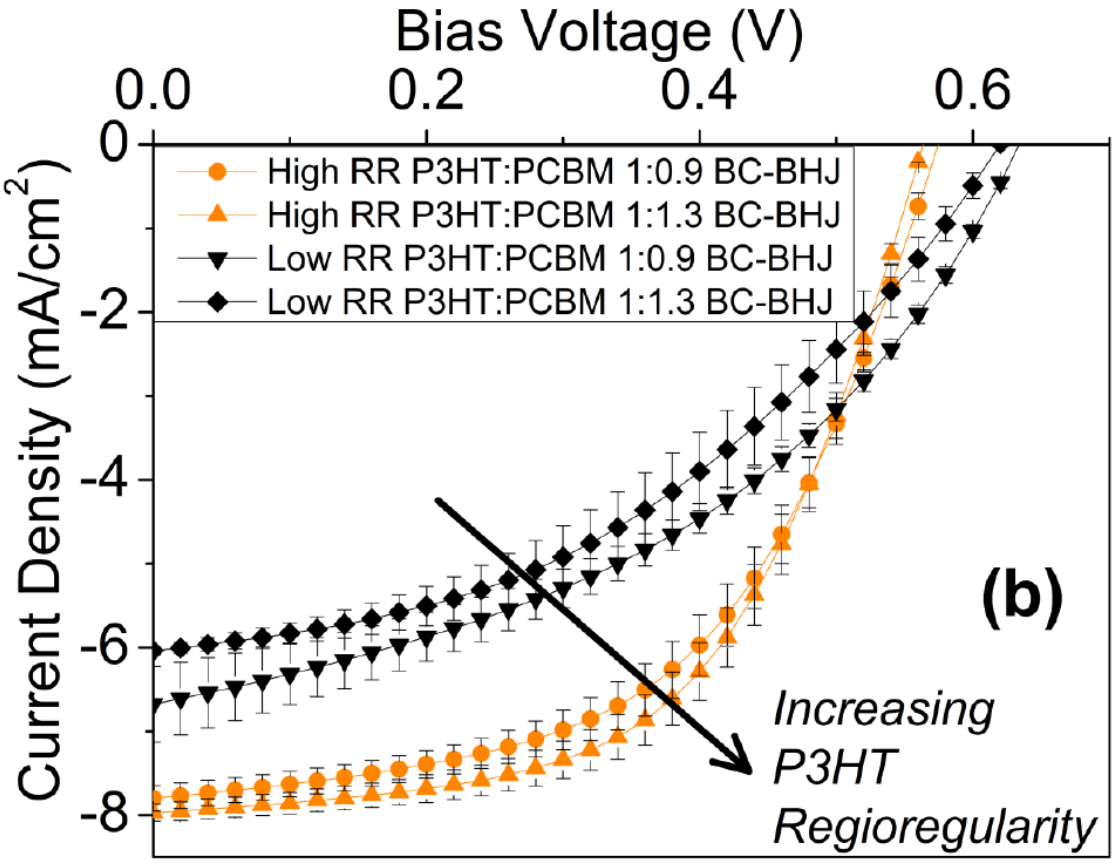

Figure A.1. *J-V* characteristics of BC-BHJ solar cells made from 16k HR P3HT (orange) and LR P3HT (black) with two polymer:fullerene weight ratios.

Table A.1. Summary of Solar Cell Parameters for the Devices in Figure A.1.

	V_{oc} (V)	J_{sc} (mA/cm^2)	*FF*	*PCE* (%)
Low RR P3HT:PCBM 1:0.9 BC-BHJ	0.64±0.01	6.68±0.45	0.42±0.01	1.79±0.07
Low RR P3HT:PCBM 1:1.3 BC-BHJ	0.62±0.01	6.04±0.05	0.42±0.04	1.58±0.17
High RR P3HT:PCBM 1:0.9 BC-BHJ	0.58±0.01	7.80±0.15	0.53±0.03	2.39±0.14
High RR P3HT:PCBM 1:1.3 BC-BHJ	0.56±0.01	7.97±0.10	0.56±0.02	2.52±0.13

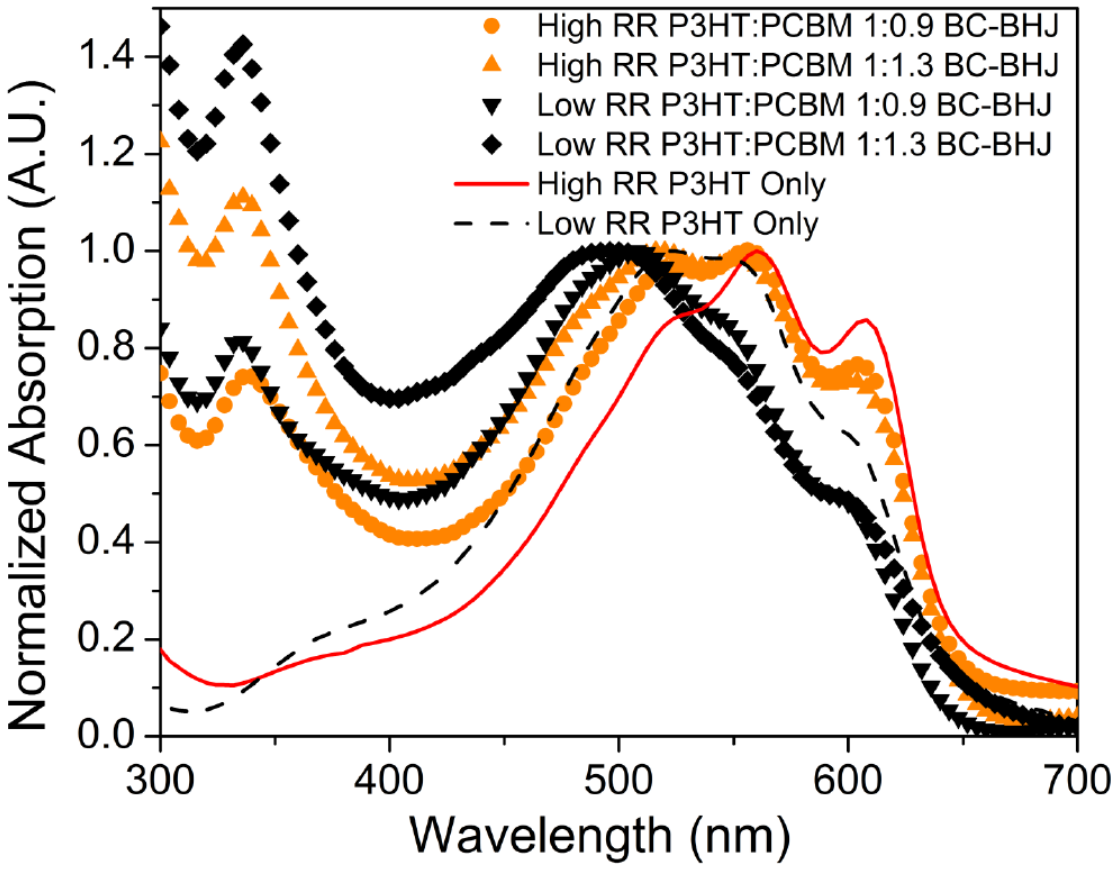

Figure A.2. UV-Visible absorption spectra of thin BC-BHJ P3HT:PCBM films made from the same P3HTs as in Figure A.1. All of the BC-BHJ films were thermally annealed at 150 °C for 20 minutes. The spectra were normalized to their highest polymer optical densities (OD) for ease of comparison.

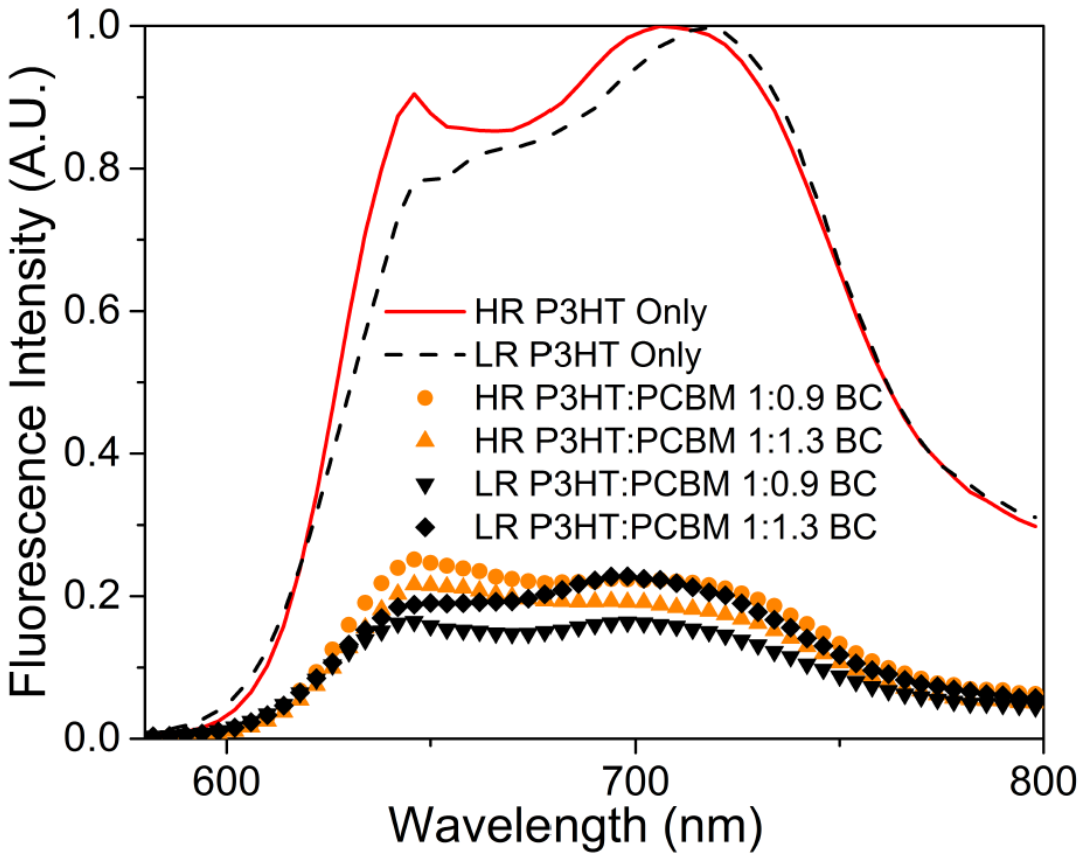

Figure A.3. PL Spectra of thin films made from: pure P3HTs and P3HT:PCbM BC-BHJ films (same as those in Figure A.2). The measured PL intensities were all divided by their optical densities at 530 nm, the excitation wavelength used in this experiment, and further normalized to the highest value of the pure HR P3HT film to best illustrate the extent of PL quenching in different samples.

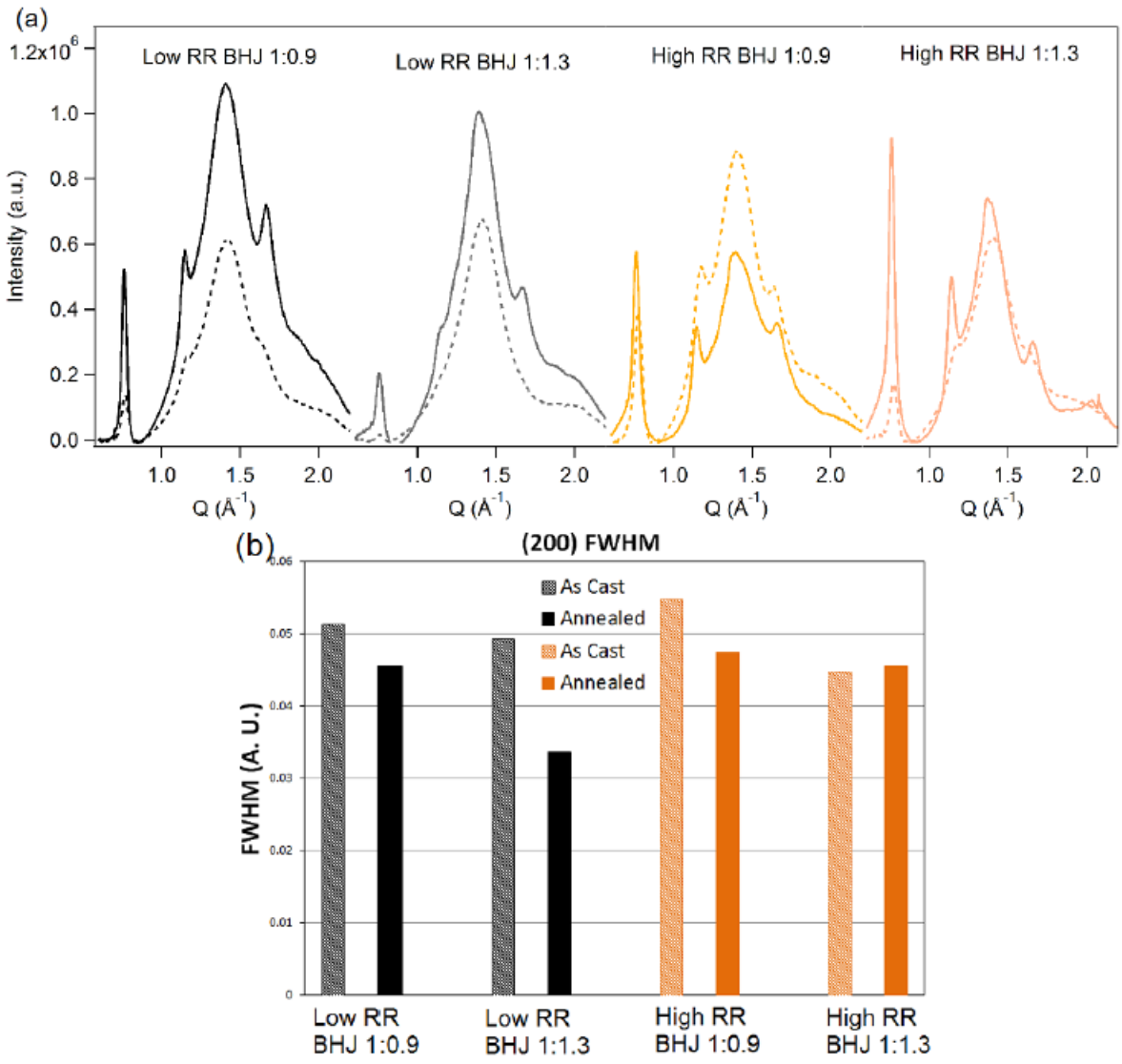

Figure A.4. (a) Integrated GIWAXS intensity for P3HT:PCBM BC-BHJ films. Dashed lines indicate as-cast films and solid lines are after 20 minutes of thermal annealing at 150 °C. (b) Full width at the half maximum (FWHM) for the polymer (200) peaks.

A.1 References

(1) Dang, M.; Hirsch, L.; Wantz, G. P3HT:PCBM, Best Seller in Polymer Photovoltaic Research. *Adv. Mater*. **2011,** *23*, 3597-3602.

(2) Müller, C.; Ferenczi, T. A. M.; Campoy-Quiles, M.; Frost, J. M.; Bradly, D. D. C.; Smith, P.; Stingelin-Stutzmann, N.; Nelson, J. Binary Organic Photovoltaic Blends: A Simple Rationale for Optimum Compositions. *Adv. Mater.* **2008,** *20*, 3510-3515.

APPENDIX B

Detailed Synthesis of Silica Nanopores and Preparation of FETs

B.1 Hydrothermal Synthesis of Nanopores

Before the addition of polyimide (by Cannon), 200 nm of SiO_2 must be thermally grown on N-type silicon using the oxidation-oxidation furnace in the Nanolab. For the oxidation, the wet method has been used at 1050 °C. The time can be calculated using a thermal oxide growth calculator assuming 25 Å of native oxide. No preliminary steps must be taken for the quartz substrates, and Cannon will provide those. Once the polyimide is coated, the arrow marked by Canon points in the direction of the rubbing direction. The pores are oriented perpendicular to the arrows and the rubbing direction. Before the substrates are cut, remark the arrow in several places to assure the pore direction is known.

B.1.1 Cover Glass and Bomb Preparation: To begin the hydrothermal synthesis, the quartz cover glass must be prepared. The quartz cover glass needs to be the same size or larger than the sample, old quartz samples can be used for this if the previous film is fully removed. To clean the cover glass, first wash with soap/water/acetone to remove any residue. Then, soak cover glass in 10% w/v KOH solution for 5 days, do not soak for more than 2 weeks since the KOH will begin to harmfully etch the cover glass. After KOH soaking, rinse cover glass well with DI water and rewash with soap/water/acetone.

On the same day (within several hours) of the hydrothermal synthesis, the cover glass must be treated with HF to improve its water wettability. HF is an acute toxin, so proper care must be

taken throughout the HF etching procedure. To HF treat the cover glass, first set-up 3 plastic petri dishes on a clean and dry surface. Fill one petri dish with buffered oxide etch (BOE), 6:1 NH_4F:HF (concentrated), and the other two petri dishes with Millipore water, cover each dish when not in use. Carefully soak each cover slip in the BOE petri dish for 3-5 minutes, the longer the better. Using clean tweezers, move the coverslip to the 1st water petri dish and again soak for 3-5 minutes. Move the cover glass once more to the 2nd water petri dish and soak for a final 3-5 minutes. Finally, rinse fully with Millipore water and dry the cover glass using either canned air or air/nitrogen from a gas cylinder in lab. Do not dry with lab air from the hoods as this air contains small amounts of oil that will hurt film formation. Once finished, the BOE can be saved and reused for future syntheses and the water from the 1st petri dish should be disposed of as waste with trace HF. The water in the 2nd petri dish can be disposed of down the sink.

Now that the cover slips are clean, a spacer must be added to each one. Carefully place 5 pieces of Kapton tape on 2 parallel sides of each cover slip. The Kapton should be applied so that no air bubbles or dust are trapped between the layers. Additionally, if your cover glass is significantly larger than your sample piece, the Kapton should be placed so that it can act as a spacer, so the space between the two Kapton lines should be smaller than the polyimide coated substrate.

Before the assembly of the samples with the cover glass spacers, the Teflon bomb should be cleaned by sonicating in soapy water and rinsing well with DI water. Ensure no dirt or particulates are adhering to the bomb. Clean off each polyimide coated substrate by blowing with clean air or nitrogen (no lab air, same as with the cover glass). The films should then be assembled with the cover glass spacers with the substrate facing downwards in the bomb and the indicator arrow pointing parallel to the Kapton tape. The films are then screwed between two Teflon pieces

and stacked within the bomb. The threads of the bomb should also be wrapped at least 5 times with Teflon tape to ensure a good seal with the cap. Do not put on the cap at this point.

B.1.2 Solution Preparation: Immediately before the synthesis, the precursor solution needs to be prepared. For one bomb add 3.75 g of Brij 56 to a clean (oven dried) flask and heat beifly with a heat gun to melt. Add 80 mL of Millipore water followed by 13.2 mL of concentrated HCl. Heat at about 45 °C with stirring until the Brij is fully dissolved (on the older hotplates, this is about level 2 for the heat), this may take a couple of hours. The solution must then be cooled to *exactly* 27 °C. The most efficient way to do this is to cool the flask to 30 °C in an ice bath, then remove the flask from the ice bath and let the flask cool on the bench top to 27 °C. Monitor the temperature carefully, as soon as the solution reached 27 °C, add 1.12 mL tetraethyl orthosilicate (TEOS) to the flask using two 1-mL syringes. Stir the solution for 2.5 minutes (as monitored by a stop watch). Now add the solution to the bomb by first tilting the bomb about 45° and pouring in about a quarter of the solution, slowly. Tap the outside of the bomb with a rubber mallet to remove air bubbles. Repeat this procedures of pouring one quarter of the solution followed by tapping until all of the solution has been added. Continue tapping the outside of the bomb for about 10 minutes to remove *all* air bubbles from between the sample and coverslips, no film will form in the places with air bubbles. Once all the air bubbles have been removed, seal the top onto the bomb tightly (using the vice if needed) and then seal the outside with electrical tape. Place the bomb in an oven at 80 °C for 5 days. The best ovens to use are one of the muffle furnaces (if not in heavy use or need) or the small oven. If the small oven is to be used, be sure it is not opened during the 5-day synthesis period. After the 5 days, remove the bomb from the oven and allow to cool. Remove each film and wash gently with Millipore water.

B.1.3 Calcination, Silylation, and Polymer Incorporation: For calcination, place all samples to be calcined in one of the tube furnaces (without a tube) or in the muffle furnace. Heat samples to 450 °C at a rate of about 1°C per minute (set for a 6 hour ramp). Hold at 450 °C for 4 hours. Cool down at a rate of ~1 °C per minute. Since muffle furnace cools down slower than it's programed tom set the ramp down time to 4 hours. If using one of the tube furnaces, set the ramp down time to 6 hours. Since this is a long calcination, it is recommended to do this overnight.

After calcination, the films must be silylated to create a hydrophobic surface for polymer incorporation. Since the calcined films are hydrophilic, they will readily collect water from the air, so it is best to perform the silylation immediately after calcination. To silylate the films, soak the samples in a solution of 1:1 hexamethyldisilazane (HDMS):chlorotrimethyl silane for 2 hours. The solution is water reactive and fumes in air, so this should be done in a fume hood. Take the films out of the solution and put on a glass petri dish in an oven at 80 °C for 30 minutes. Remove the films and wash with water, acetone, ethanol, and then water again. Blow dry (no lab air) and put back in 80 °C oven for 30 minutes.

Once silylation is complete, the films are ready to be incorporated with polymer. Prepare a 1-3% solution of the desired polymer in solvent that does not have a very low vapor pressure. 3% is ideal if ample polymer is available. The best solvent/polymer combinations for the common polymers are: MEH-PPV in chlorobenzene, F8T2 in xylenes, P3HT in *o*-dichlorobenzene (ODCB). Place the samples in a glass petri dish and put a few drops of polymer solution onto each one. Ensure they are each fully covered with solution. Cover petri dish with aluminum foil by folding the edges of the aluminum foil together to make a packet. Place aluminum foil-covered petri dish in the oven at 80 °C and leave it overnight. Remove the films and place on the shaker in

a solvent filled jar. Sonicate in jar briefly to remove excess polymer. Move films to a jar filled with water and sonicate briefly. The films are now complete, any optical studies can be done at this point using the polyimide on quartz samples.

B.2 Photolithography and FET Fabrication

In the Nanolab yellow-room, prepare the photomask by cleaning it in photoresist stripper. Once clean, blow the mask dry using nitrogen. Prepare to deposit the photoresist by take the AZ5214 photoresist out of the fridge and allow to warm to room temperature. Set a hot plate to 110 °C for later use. Place a substrate onto the spin coater chuck and fully coat with photoresist, avoid air bubbles. Set the spin ramp to 500 rpm, spin speed to 5000 rpm, and time to 30 seconds. The ramp down can be set to 1000 rpm. Spin coat photoresist onto each substrate.

Once all samples are coated with photoresist, back on hotplate. Be sure the temperature is exact and the time on the hot plate is exact; photoresist is very sensitive to bake time. Bake photoresist at 110 °C for 90 seconds for silicon substrates or for 3 minutes for quartz substrates. Now, take the samples to the Karl Suss to expose the photoresist. Align the mask using a straight edge of the wafer/substrate. The gaps between the large holes in the mask should be perpendicular to the pores, so that the FET source-drain gap is parallel to the pores. Expose photoresist in vacuum contact/contact mode. Expose for 6.7 seconds for silicon substrates or 5.2 seconds for quartz substrates. Develop the photoresist using 4 parts water and 1 part AZ400k developer. Put films in developer and swirl gently, it takes about 90 seconds to fully develop. Wash films well with water, blow dry with nitrogen and place in an aluminum foil-wrapped container.

Using the advanced oxide etch machine (STS-AOE) in the Nanolab to etch the polymers and pores. First, perform an O_2 clean on the chamber until the % clean is above 92%. Apply cool

grease in as smooth a layer as possible to the back of each sample, anywhere not in contact with the cool grease will cause a burn in the photoresist. Etch in manual mode using the program CTAS1, which is a combination of NH_4F and HF gas. Check the film thickness with profilometry, the thickness should be 300-350 nm. Scrape off the cool grease with a razor blade. To selectively etch into the SiO_2 to make contact with the polymer, immerse each sample in BOE for 5 seconds. Rinse each sample with water and dry. Finally, evaporate about 350 nm of metal to completely fill the trenches created by etching. Sonicate films in acetone to remove the photoresist along with excess metal.

For bottom gate electrodes, the films must be on n-type silicon with an oxide layer. Etch the back of the silicon with BOE (1-3 minutes) or scratch with a scribe to remove the native oxide and make contact. With either technique, be careful not to scratch the film. Make contact with the silicon with a piece of copper tape. These devices are now ready to be measured.

For top gate electrodes, the films must be on quartz and polystyrene can be used as the gate dielectric. Dissolve 256 mg of 250k MW polystyrene in toluene to make a 5% solution. Spin polystyrene onto samples at 3000 rpm for 200 seconds with 5 second acceleration to make a 500 nm film or at 5000 rpm to make a 400 nm film. Using a shadow mask, evaporate top electrode. These top gate devices are now ready to be measured.

APPENDIX C

Dammin Bead Models

The modeling program Dammin was used to create the bead models shown in Chapter 6. The software can be downloaded from the ATSAS website. Dammin requires the .out files produced from GNOM that contain the raw SAXS data and the GNOM fits to the data. The Irena program in Igor unfortunately does not produce .out files that can be successfully read by Dammin. Also, the data must be fit using the spheroid setting in GNOM rather than the cylindrical setting. The expert setting should be used in Dammin to enable precise control over the parameters. A description of each parameter can be found in the help files of the software, but the specific parameters used for Chapter 6 can be found below.

The main parameters to adjust at the sphere diameter, which sets the total size of the structure, and the packing radius of dummy atoms, which sets the size of the bead. The radius was chosen to be 5 Å to try to match the diameter of a single polymer chain, which is about 1 nm. Increasing the size of the structure may give more information, but each run will take significantly longer. Also, changing the number of knots and harmonics to fit will increase how good the fit is, but again will take significantly longer. For PFT, the parameters used seemed to be the maximum needed for the best fit, not improvement was seen past the ones listed. For future systems, higher numbers may be needed.

To begin any analysis, first use the “fast” setting on Dammin to get an initial idea of the structure. During the fast setting, it will automatically choose parameters based on the .out file, but will generally use fairly large beads. Once this has been run a few times, it can give an idea of how

large the sphere size needs to be to encompass the structural differences. The “slow” setting is also an option for running automatically, but it does use smaller bead sizes and it set to fit a larger number of harmonics. Running both the fast and slow setting helps to get an idea of where to start for the expert parameters. To compare multiple samples, the same expert parameters should be used on all to ensure the size scale is the same. Once each Dammin run in finished, the saved .log files is a record of the parameters used. The other data, however, is not as easy to plot. Screen captures are the easiest method for retaining the images and the graphs.

C.1 Dammin Expert Parameters

Bold values indicate parameters that were input into the program, non-bold values were calculated by the program based on the given inputs and data.

Computation mode ..... : **Expert**
Maximum diameter of the particle ..... : 300.0
Solution at Alpha = 0.221E+01 Rg : 0.105E+03 I(0) : 0.175E+05
Radius of gyration read ..... : 105.0
Number of GNOM data points ..... : 343
Maximum s value [1/angstrom] ..... : 0.3235
Number of Shannon channels ..... : 30.89
Number of knots in the curve to fit ..... : **22**
A constant was subtracted ..... : 9.234
Maximum order of harmonics ..... : **10**
Point symmetry of the particle ..... : **P1**
Sphere diameter [Angstrom] ..... : **140.0**
Packing radius of dummy atoms ..... : **5.000**
Radius of the sphere generated ..... : 70.00
Number of dummy atoms ..... : 1985
Number of equivalent positions ..... : 1
Expected particle anisometry ..... : **Unknown**
Excluded volume per atom ..... : 707.6
Radius of 1st coordination sphere ..... : 14.10
Minimum number of contacts ..... : 5
Maximum number of contacts ..... : 12
Looseness penalty weight ..... : **6.000e-3**
No of non-solvent atoms ..... : 1985
Initial DAM looseness ..... : 7.571e-3

Disconnectivity penalty weight ..... : 6.000e-3
Initial DAM # of graphs ..... : 1
Discontiguity value ..... : 0.0
Center of the initial DAM: 0.0000 0.0000 0.0000
Peripheral penalty weight ..... : 0.3000
Peripheral penalty value ..... : 0.6029
Looseness fixing threshold ..... : 0.0
R-factor fixing threshold ..... : 0.0
*** **The structure was randomized** ***
No of non-solvent atoms ..... : 989
Randomized DAM looseness ..... : 0.1057
Randomized DAM # of graphs ..... : 3
Discontiguity value ..... : 2.024e-3
Randomized peripheral penalty value ..... : 0.6110
Weight: 0=s^2, 1=Emphas.s->0, 2=Log ..... : **1**
*** Porod weight with emphasis at low s ***
Initial scale factor ..... : 2.285e-8
Scale factor fixed (Y=Yes, N=No) ..... : **N**
Initial R^2 factor ..... : 0.7585
Initial R factor ..... : 0.8709
Initial penalty ..... : 0.1840
Initial fVal ..... : 0.9424
Variation of the target function ..... : 3.045e-4
CPU per function call, seconds ..... : 6.875e-4
Initial annealing temperature ..... : **1.000e-3**
Annealing schedule factor ..... : 0.9500
# of independent atoms to modify ..... : 1
Max # of iterations at each T ..... : **138950**
Max # of successes at each T ..... : **13895**
Min # of successes to continue ..... : **46**
Max # of annealing steps ..... : **200**

C.2 Additional PFT Bead Models

Each bead model in Chapter 6 was preformed several times to ensure the trend in the results were significant, the additional models are shown on the following pages.

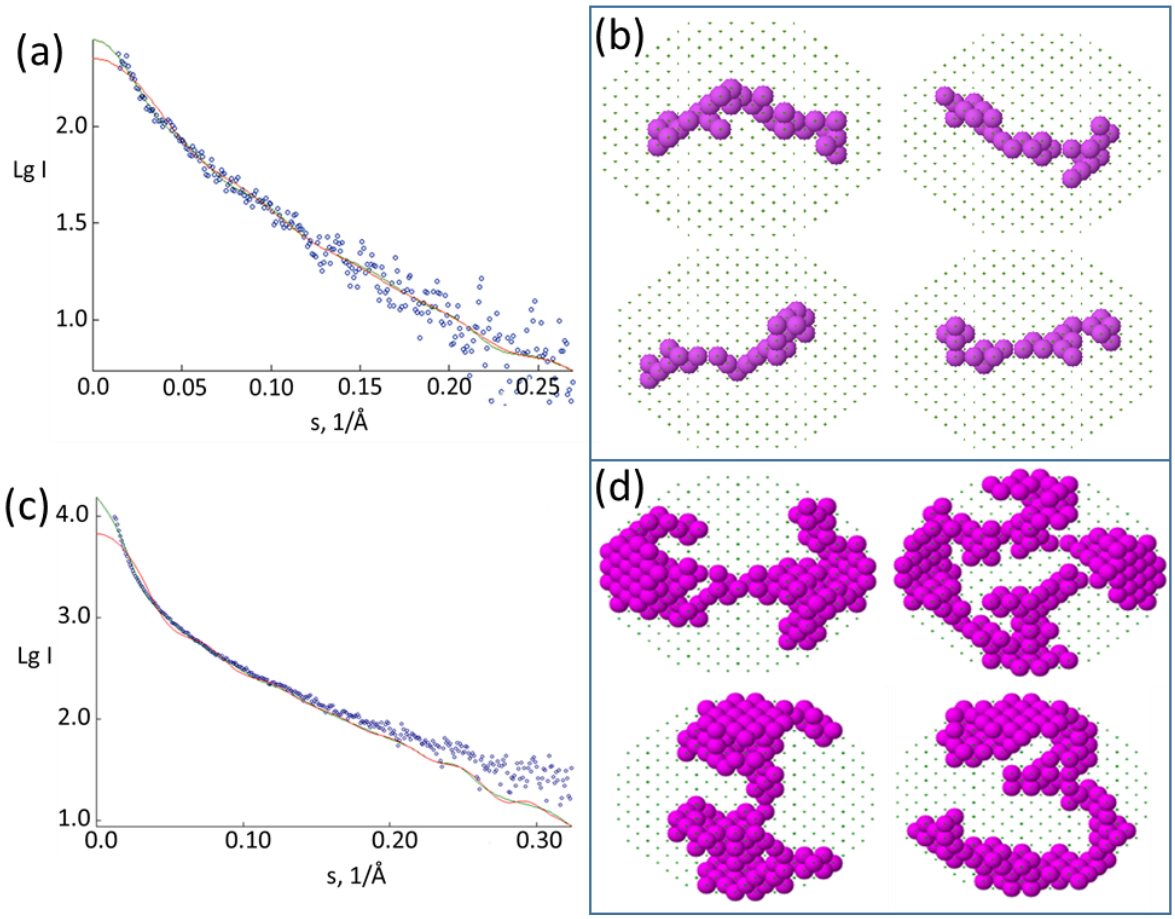

Figure C.1. Raw SAXS data with Dammin fits and additional bead models for high MW PFT with THF (a, b) and after THF annealing (c, d).

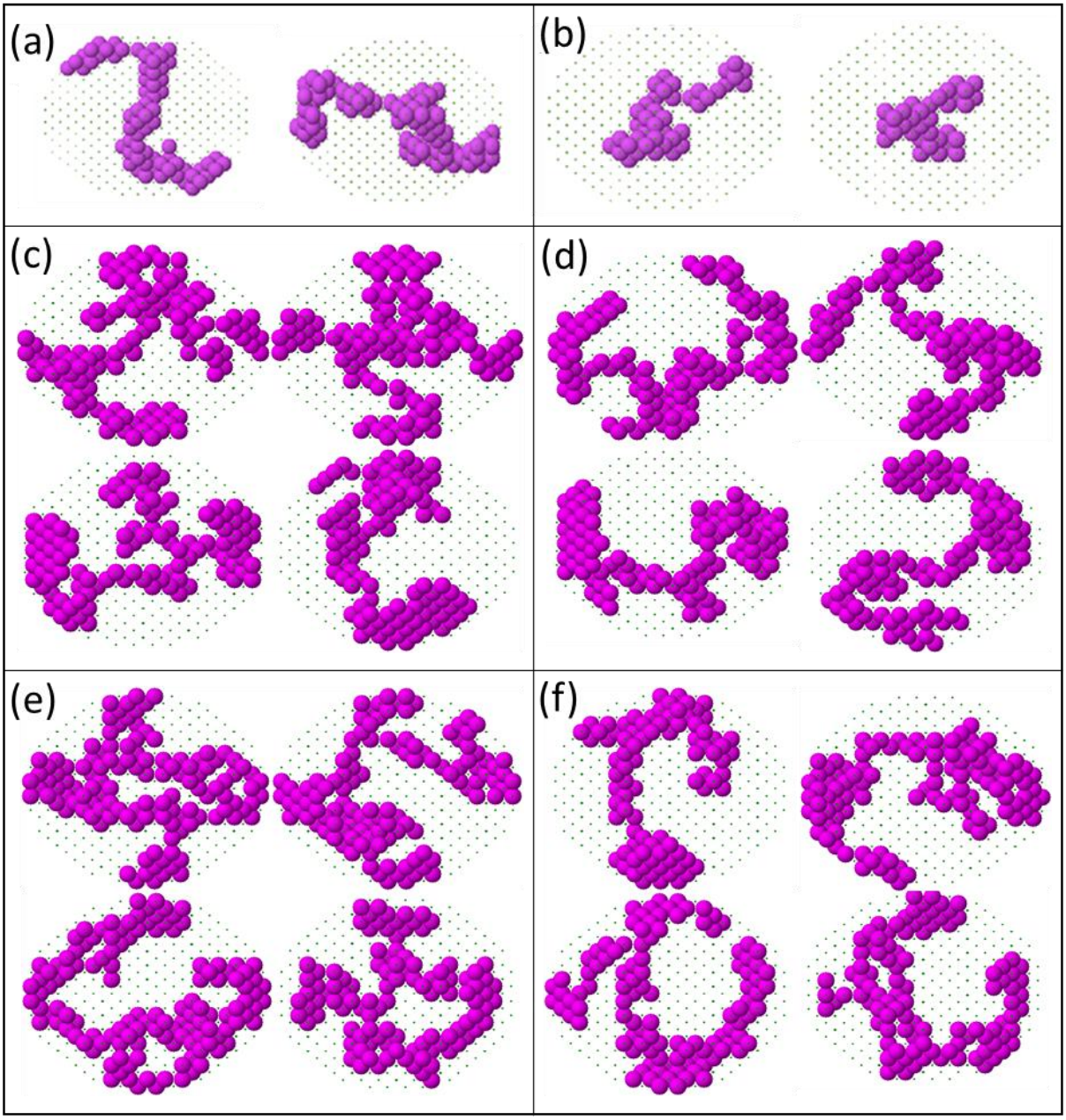

Figure C.2. Additional Dammin bead models for high MW PFT (a), low MW PFT (b), 9:1 High:Low MW (c), 7:3 High:Low MW (d), 10:1 High:Low MW (e) and 10:3 High:Low MW PFT.

APPENDIX D

Additional PFT Information

Poly(fluorine-alt-thiophene) (PFT) has been synthesized by Chenjun Shi, Daniel Kilbride, and Robert Thompson in the past. The synthesis involves first marking an uncharged version of the polymer and subsequently quaternizing it. However, the unchaged version of PFT has a very low solubility in any organic solvent, so obtaining molecular weight and any other comparative data has been very difficult. Additionally, since the solubility decreases during monomer polymerization, the molecular weights vary from batch-to-batch and each batch is very polydisperse. Any comparisons made with PFT should be done using the same batch, if possible, to decrease molecular weight differences. Using a PFT batch with a higher or lower molecular weight will change the concentration needed to form a gel.

D.1 Size Selective Precipitation

Since each PFT batch is very polydisperse, it needs to be divided into low and high molecular weight fractions. This can easily be done using size selective precipitation, in which the largest molecular weight polymer will precipitate out of solution first. To begin the process, dissolve PFT at a very high concentration in DMSO. I have typically dissolved about 250 mg un-fractioned PFT in 10 mL of DMSO. If you start with too much DMSO, it become difficult to fit all of the solution in the 250 mL centrifuge tubes. It may be necessary to heat the PFT solution at a low temperature to dissolve it all of the way.

After the PFT is fully dissolved in the DMSO, pour the solution into a plastic centrifuge tube and dropwise add ethyl acetate. In between drops, gently shake or swirl the tube. A precipitate often begins to form at the top where to ethyl acetate firsts hits the DMSO, but

upon swirling, the precipitate will re-dissolve in the beginning. Continue adding the ethyl acetate dropwise until the precipitate does not re-dissolve. Depending on how concentrated the original solution is, this will take 1-5 mL of ethyl acetate. Centrifuge the solution at 4000 rpm for about 5 minutes, or until the solid is all at the bottom of the tube. The solid is the high molecular weight fraction, which typically is the largest fraction that will be obtained.

Pour off the supernate into a new centrifuge tube. Follow the same procedure as before by slowly adding ethyl acetate until a precipitate forms. This time it will take 20-50 mL of ethyl acetate and the liquid may need to be split into two centrifuge tubes. If not solid forms even at this point, set the tubes aside and the low molecular weight fraction should precipitate out slowly over a few days. The amount of ethyl acetate needed and whether or not a precipitate forms depends on the batch. Recent batches have been much less poly disperse, so the remaining PFT is still rather soluble in the ethyl acetate.

It is necessary to wash the solids collected several times with ethyl acetate to remove residual DMSO, otherwise it will be difficult to obtain dry PFT. To wash, add 10-20 mL ethyl acetate to the solid in the centrifuge tube and shake vigorously (the vortex mixer helps). Centrifuge to collect the solid and pour of the supernate. For best results, repeat this at least two more times. The final product can either be transferred to a septa-capped vial and dried either under a flow of air or in the vacuum oven (with the heat off).

D.2 Pure PFT

Once the PFT is dried, it can be used in an endless number of experiments. For experiments involving gels, solutions should be made at 10-15 mg/mL. The exact concentration at which a gel will form depends on the molecular weight of the batch. To enable

all of the PFT to dissolve and to form a gel, heating must be used in addition to stirring while making the solutions. Since they are all in water, 80 °C is the hottest they should be heated and they should not be left for extended periods of time, otherwise the water will still evaporate out of the vials. Once the liquid is cooled, a gel should remain in the vial; if it does not, increase the PFT concentration. For stronger gels, THF annealing can be performed by adding 1 drop of THF to the sample vial (containing about 1 mL of gel). Upon stirring without heat, the gel should liquefy. To remove the THF, simply heat the vial at 80 °C with the cap removed until all of the THF has evaporated. The best way to gauge this is by marking the solution level in the vial before adding THF and then heating until the same level is obtained again. The new gel will be stiffer and is often less cloudy than the original.

To create films out of PFT, there are two main options. To create a thick film, a PFT gel can be doctor-bladed onto a substrate. In the water box, there is a premade sample holder with spacers that can be used to make reproducible films. To doctor-blade the film, put a substrate onto the sample holder a scoop some of the PFT gel onto it. Using even pressure, slide a razorblade across the sample to scrap off the excess. The film can now be dried on a hot plate to remove the water. For thinner films, spin coating can also be used, however it is difficult to get even thickness films. You must start with a more dilute/liquid solution, however as the solution dries, it will still go through the gel transition and cause rings of thick and thin regions on the substrate. The best way to prevent this is to spin coat out of a more concentrated solution containing THF. It will create a more even film, but the PFT morphology may not be preserved.

The micelle structure of PFT can be studied using solution SAXS on beamline 1-4. For all of these studies, much more dilute solutions must be used because the gel cannot easily

pass through the capillary flow cell. We have found that 1 mg/mL PFT is the most ideal concentration for these studies, but it is best to have 2 concentrations of each sample to ensure adequate signal can be obtained. Samples may be run in pure water or with additives, such as THS or isopropanol. If you want to run samples containing additives, be sure to also have a solution blank that has the same additive ratio. If this is not done, the background scattering cannot be properly subtracted. Even if running only water containing samples at the synchrotron, a new solvent blank should be collected every 5-10 samples to account for beam drift. All samples must be made ahead of time in septa-capped vials. Since only 0.1 mL of sample is necessary, GC vials with screw topped caps have worked the best in the past.

Solution SAXS data can be analyzed either using the ATSAS software package, which is already installed on the computers at beamline 1-4, or using the Irena macro for Igor. The ATSAS package can be downloaded for free online, but is only for PC or Linux. There are three main programs that are useful in the package. Primus is used for plotting the raw data. While at the beamline, you will use this software to double check your data for signal-to-noise and for any oddities that indicate the sample should be re-run. To fit the data, GNOM can be used to perform the Fourier transforms and create the probability distribution functions. The resultant .out files from the program can be saved and used by the Dammin program, as mentioned in Appendix C. The Irena macro, on the other hand, can be used to not only plot the data and obtain the probability distribution functions, but can also be used to fit the slope in regions of the raw data. Fitting the slopes is especially useful for high molecular weight PFT gel samples, as they do not always give the characteristic rod-like data in the probability distribution.

D.3 Mixtures with Electron Acceptors

As the pure PFT samples have been fairly well characterized, more future work will involve mixtures with electron acceptors. There is still a lot yet to be studied, such as novel water-soluble fullerenes, PDI-small molecules, and combinations of both. As discussed in Chapter 7, these solutions can form stable polarons, but they are highly reactive with oxygen. Because of this all solutions should be made using water that has been degassed by freeze-pump-thaw techniques at least five times. All samples should also be made and stored in the water-box.

To make polaron-containing (or green) solutions, a solution should be made with a PFT:acceptor ratio of at least 1:0.5 wt/wt, with the higher the better. If enough acceptor is available, a 1:1 wt/wt ratio is ideal for fullerenes. Additionally, these solutions should be made starting from solid PFT and acceptor mixed together rather than mixing two separate solutions. This helps facilitate the transfer of the acceptor into the interior of the micelle. Since there is not a balance located in the water box, the samples should be weighed outside of the box and the powders pumped into the box afterwards. To create a system that forces the acceptor into the interior of the micelle, the solubility of the electron acceptor also needs to be fairly low. As in Chapter 7, the solubility of the bis-fullerene was very low, so the PFT acted as a surfactant. To create a cascade, the molecule on the outside also needs very low solubility, such that it will still self-assemble with the polymer.

As far as concentration of the solutions, it should be tuned based on the experiment needed. In order to measure the polaron characteristics by absorbance or EPR, the concentration needs to be at least 1 mg/mL or higher. The PFT absorbance peak at these concentrations will be too high to see, so measurements will only be of the polaron rather than

the polymer. Depending on the batch of PFT, solutions of high concentration (ideally closer to 5 mg/mL) will start to turn to green on their own in the room lights. This does not always happen though, so if not, the formation of polarons can be induced by irradiating them with 514 nm wavelength laser light. If you want to cause the polaron formation in a vial, be sure to actively stir the solution and increase the spot size of the laser (with a lens) to avoid the evaporation of water in the process.

For ultra-fast pump-probe studies (done by the Schwartz group), 1 mg/mL solutions can be used, but 1 mm cuvette should be used instead of the standard 1 cm ones in the Tolbert lab (the Schwartz group can provide these). For photoluminescence quenching, dilute solutions are required. Since PFT has a very high extinction coefficient, solutions should be diluted to 0.01 mg/mL polymer. Absorbance at these concentrations should yield a PFT peak with an optical density less than 1. The fluorescence signal will still be high and can be obtained on our laser set up. A fluorescence water blank should be used to subtract the stray laser light. Additionally, a notch filter can be purchased to help remove the laser light.